Universidade de Évora - Instituto de Investigação e Formação Avançada

Programa de Doutoramento em Ciências da Terra e do Espaço

Área de especialização | Processos Geológicos

Tese de Doutoramento

Innovative Conservation Techniques for Bio-deteriorated and Soiled Ornamental stone in Urban Areas: Laser versus Plasma Vapour Cleaning

Yufan Ding

Orientador(es) | Emma Angelini

Jose Mirao

Nicola Schiavon

Évora 2023

Universidade de Évora - Instituto de Investigação e Formação Avançada

Programa de Doutoramento em Ciências da Terra e do Espaço

Área de especialização | Processos Geológicos

Tese de Doutoramento

Innovative Conservation Techniques for Bio-deteriorated and Soiled Ornamental stone in Urban Areas: Laser versus Plasma Vapour Cleaning

Yufan Ding

Orientador(es) | Emma Angelini

Jose Mirao

Nicola Schiavon

Évora 2023

A tese de doutoramento foi objeto de apreciação e discussão pública pelo seguinte júri nomeado pelo Diretor do Instituto de Investigação e Formação Avançada:

Presidente	|	Maria João Costa (Universidade de Évora)
Vogais	|	Brunetto Giovanni Brunetti (Universidade de Perúgia) Emma Angelini (Politecnico di Torino) (Orientador) Luis Roso Franco (Universidad de Salamanca) Mauro Francesco La Russa (Universidad de Cantabria) Nicola Schiavon (Universidade de Évora) (Orientador) Tilde de Caro (National Research Council of Italy)

Évora 2023

Declaration

I hereby declare that the contents and organization of this dissertation constitute my own original work and does not compromise in any way the rights of third parties, including those relating to the security of personal data.

Yufan Ding

2022

* This dissertation is presented in partial fulfillment of the requirements for **Ph.D. degree** in the University of Évora and the Graduate School of Politecnico di Torino (ScuDo).

I would like to dedicate this thesis to my loving family, friends, and people that helped me, as well as those working in this field.

Acknowledgments

This PhD project has been carried out under the European Joint Doctorate in "Archaeological and Cultural Heritage Materials Science" - ED-ARCHMAT, awarding a joint Double Doctorate degree in *Earth and Space Sciences (Ciências da Terra e do Espaço)* by University of Evora (UEVORA), in cotutelle with the degree in *Materials Science and Technology (Scienza e Tecnologia dei Materiali)* by Polytechnic of Turin (POLITO).

This project has received funding from the European Union's Horizon 2020 research and innovation programme H2020-MSCA- ITN-2017- EJD: Marie Skłodowska-Curie Innovative Training Networks (European Joint Doctorate) – Grant agreement nº: 766311 – ED-ARCHMAT.

Sample collection in the research was by special permission of the Direção-Geral do Património Cultural and the Mosteiro da Batalha authorities. The research presented in this paper was carried out mainly using data collected at Universidade de Évora, Politecnico di Torino, and Direção-Geral do Patrimonio Cultural, as part of H2020-MSCA-ITN-2017, ED-ARCHMAT (ESR1).

The laser instruments used in this research were from and the laser ablation experiments were carried out in Instituto de Nanociencia y Materiales de Aragón, CSIC in Zaragoza, Spain. Special thanks to the contribute in Chapter 5 by Prof. Luis Alberto Angurel and Prof. Xerman de la Fuente Leis, for their precious training in laser technology applied to cultural heritage material.

The bio-chemical analysis in this research was conducted in the Departamento de Química e Bioquímica in University of Evora with the assistance from Prof. Ana Teresa Cardeira and Doc. Catia Salvador. Special thanks to them for their professional support in assessing the cleaning results of microorganisms.

The optical particle sizer (OPS) used in this research was supported by the Institute of Earth Sciences (Group 1 – Atmospheric Sciences, Water and Climate) of the University of Évora. Thanks to Prof. Maria João Costa, and Prof. Daniele Bortoli for providing the access to the OPS equipment.

The climatic data (temperature, humidity, sun irradiation) of the Batalha region was provided by the IPMA (Instituto Português do Mar e da Atmosfera).

Special thanks to Prof. Pedro Redol for supporting the sample collection as well as offering help in accessing the document reports in the Masteiro da Batalha,

Many thanks to the professors and researchers in the Hercules Lab and University of Evora for sharing the knowledge and training the instruments – Prof. Patricia Moita, Prof. Cristina Barrocas Dias, Prof. Teresa Ferreira, Margarida Nunes, Massimo Beltrame, Sandra Velez, Luis Dias, Ines Lemos Cardoso, Sriradha Bhattacharya, Silvia Scardina, Joao, Pedro Barrulas, Ana Manhta, Fabio Sitzia, Carla Lisci, Ana Cardoso, Dulce Valdez, and many students come and go in our lab.

Many thanks to the professors and co-workers in Politecnico of Torino for the help in research and the support in life – Prof. Marco Parvis, Leonardo Iannucci, Alessio Gullino, Leila Es Sebar, Camilla Noe, Amina Vietti.

Thanks to the professors for passing on knowledge – Prof. Porcelli Francesco, Prof. Matekovits Ladislau, Prof. Barbara Bonelli, Prof. Bento Caldeira, Prof. Jose Borges.

Special thanks to my friend Aditya Goyal, for his generous help in my living in Europe.

Sincerest thanks to my supervisors – Prof. Nicola Schiavon, Prof. Emma Angelini, Prof. Sabrina Grassini, Prof. José Mirão, for their great effort and selfless support in my study and research during this PhD.

In the end, gratefulness to my family and friends, for cheering up and accompanying with me in any difficult times.

Abstract

Innovative Conservation Techniques for Bio-deteriorated and Soiled Ornamental Stone in Urban Areas: Laser versus Plasma Vapour Cleaning

This project aims to investigate the application of two innovative technologies - laser cleaning and plasma treatment for the conservation of limestone materials in urban environment, the Batalha Monastery, one of the most iconic monuments in Portugal was used as a case study. The thesis is divided into two parts. The first part (chapters 1-3) describes the stone, the degradation processes and their causes. The second (chapters 4-6) investigates the effectiveness of stone cleaning with plasma and laser technologies, proposing a method of preserving limestone by deposition of SiOx films. In particular, chapter 1 focuses on the mineralogical-petrographic characterization of the limestones used in the construction and restoration of the monastery, identifying the quarries. Chapter 2 characterizes the orange surface patinas present on the facades and on architectural reliefs of the monastery, identifying the mechanisms of formation. Chapter 3 investigates the nature of the microbial colonization of the monastery's limestones, revealing the process of formation, and the synergistic contribution of urban pollution in the biodegradation processes of stone monuments. Chapter 4 reports the results of plasma treatments on limestone tablets subjected to accelerated microbial colonization, evaluating their ability to inhibit bio-deterioration. Chapter 5 reports the results of treatments with four types of lasers with different irradiation modes used for ablating the lichen crust present on the limestone of the monastery, as well as for the cleaning of stone tablets exposed on the roof of the monument, comparing their efficacy and safety. Chapter 6 evaluates the effectiveness in terms of stone protection from environmental attack by pollutants and biological agents of the surface deposition by plasma of a thin-film of SiO_x on limestone samples. Preliminary results show how the SiO_x film helps protect it from acid rain and slows down bio-colonization processes, by forming a resistant coating on the stone surface.

Resumo

Técnicas Inovadoras de Conservação para Pedra Ornamental Bio-deteriorada e Suja em Áreas Urbanas: Limpeza de Vapor a Laser versus Plasma.

Este projeto visa investigar a aplicação de duas tecnologias inovadoras - limpeza a laser e tratamento por plasma - para a conservação de materiais calcários em ambiente urbano, utilizando o Mosteiro da Batalha, um dos monumentos mais emblemáticos de Portugal, como caso de estudo. A primeira parte (capítulos 1-3) descreve os materiais pétreos, os processos de degradação e as suas causas. A segunda parte (capítulos 4-6) investiga a eficácia das técnicas de limpeza de pedras com tecnologias de plasma e laser, propondo um método de preservação de calcário através da deposição de películas protetoras de SiO_x. Em particular, o capítulo 1 incide sobre a caracterização mineralógico-petrográfica dos calcários utilizados na construção e restauro do mosteiro, identificando as pedreiras originais. O capítulo 2 caracteriza as pátinas de cor laranja, presentes nas fachadas e nos relevos arquitetónicos do mosteiro, identificando os respetivos mecanismos de formação. O capítulo 3 investiga a natureza da colonização microbiana dos calcários do mosteiro, revelando o processo de formação correspondente e demonstrando a contribuição sinérgica da poluição urbana nos processos de biodegradação dos monumentos pétreos. O capítulo 4 relata os resultados dos tratamentos com plasma em provetes de calcário submetidos à colonização microbiana acelerada, avaliando a sua capacidade de inibir a biodeterioração. O capítulo 5 relata os resultados de tratamentos com quatro tipos de lasers com diferentes modos de irradiação utilizados para a ablação da camadas de liquen presentes no calcário do mosteiro, bem como para a limpeza das superficies de pedra expostos no telhado do monumento, comparando eficácia e segurança. O capítulo 6 avalia a eficácia em termos de proteção da pedra contra o ataque ambiental por poluentes e agentes biológicos da deposição superficial por plasma de um filme fino de SiO_x em amostras de calcário. Os resultados preliminares mostram como o filme SiO_x, ao formar um revestimento resistente na superfície da pedra, ajuda a protegê-la da chuva ácida e retarda os processos de biocolonização.

Riassunto

Tecniche innovative di conservazione per pietre ornamentali biodeteriorate e sporche nelle aree urbane: pulizia laser contro vapore plasmatico

Questo progetto mira a indagare la applicazione di due tecnologie innovative – pulizia laser e trattamento al plasma, per la conservazione di materiali lapidei calcarei in ambiente urbano utilizzando come caso studio il Monastero di Batalha, uno dei monumenti più iconici del Portogallo. La tesi è divisa in due parti. La prima parte (capitoli 1-3) descrive i materiali lapidei, i processi di degrado e le loro cause. La seconda parte (capitoli 4-6) indaga l'efficacia di tecniche di pulizia della pietra con tecnologie al plasma e al laser proponendo un metodo di conservazione della pietra calcarea tramite deposizione di film protettivi di SiO_x. In particolare, il capitolo 1 si concentra sulla caratterizzazione mineralogica-petrografica dei calcari utilizzati nella costruzione e nel restauro del monastero, individuandone le cave di provenienza originali. Il capitolo 2 caratterizza le caratteristiche patine superficiali di colore arancione presenti sulle facciate e e su rilievi architettonici monastero, individuandone i meccanismi di formazione. Il capitolo 3 indaga la natura della colonizzazione microbica dei calcari del monastero, svelandone il processo di formazione, e rivelando il contributo sinergico dell'inquinamento urbano nei processi di biodegrado dei monumenti in pietra. Il capitolo 4 riporta i risultati di trattamential plasma su tavolette calcaree sottoposte a colonizzazione microbica accelerata, valutandone la capacità di inibire il bio-deterioramento. Il capitolo 5 riporta i risultati di trattamenti con quattro tipologie di laser con diverse modalità di irradiazione utilizzati per l'ablazione della crosta lichenica superficiale presente sulla pietra calcarea del monastero, nonché per la pulizia di tavolette di pietra esposte sul tetto del monumento, comparandone l'efficacia e sicurezza. Il capitolo 6 valuta l'efficacia in termini di protezione della pietra dall'attacco ambientale da parte di agenti inquinanti e biologici della deposizione superficiale tramite plasma di un film sottile di SiO_x su campioni di pietra calcarea. I risultati preliminari mostrano come il film di SiO_x, formando un rivestimento resistente sulla superficie della pietra, contribuisca a proteggerla dalle piogge acide e ne rallenti i processi di bio-colonizzazione.

Contents

List of Figures

List of Tables

Chapter 1

Provenance study of the limestone used in the construction and restoration of the Batalha Monastery

Part of the work in this chapter has been previously published in [1]

1.1 Introduction

1.1.1 Building Limestones in Portugal

Limestones (calcário in Portuguese) have been used extensively in the construction of many ancient Portuguese monuments, due to its bright colour and "soft", carvable texture. This building lithotype is a perfect choice to be used as both ornamental and decorative stone. There are several limestone producing regions in Portugal which provide ornamental material nowadays and in the past [2][3][4]:

(a) *Maciço Calcário Estremenho (MCE)* – a Jurassic limestone massif around 150 km north of Lisbon that belongs to the Lusitanian Basin in Portugal. It is a mountainous region raised relatively to the surrounding areas as a result of compressive tectonic phenomena that followed the opening of the Atlantic Ocean around 20 million years ago. *MCE* is now the largest limestone extraction district in Portugal. The massif is made of thick Mesozoic carbonated rocks; some species could be dated back to Bathonian and Callovian ages in Middle Jurassic. This region includes several quarrying centres: *Pé da Pedreira* which has the well-known Moca Creme variety; *Codaçal* that produces a homogenous limestone named Semi-Rijo Codaçal; *Moleanos*,

where Vidraço de Moleanos with excellent properties was exploited; *Fátima* from which the typical "Creme de Fatima" limestone comes; and *Alvados* area that has the most traditional and valuable limestone variety called Alpinina. The other two are *Salgueiras (Arrimai)* and *Cabeça Veada* [4] [5] [6].

(b) *Pêro Pinheiro* – the region located 30 km north of Lisbon, brings out many traditional limestones (the first quarrying began six centuries ago) valuable for their vivid colours: the yellow "Amarelo Negrais", red "Encarnado Negrais", deep red "Encarnação de Lameiras" and "Abancado", blue "Azul Cascais", together with the famous ivory "Lioz" mentioned in many studies are all from this region. Lioz limestone is a late Cretaceous limestone of Turonian age. The commonly seen colour is ivory and beige, pink with other colour is relatively rare, its unique pattern is caused by the occurrence of compositional veins of fossiliferous content. It is medium-grained, exclusively composed of sparitic calcite, hence its mechanical behaviour is better than other sedimentary limestones. Due to its mechanical properties and decorative appearance, Lioz limestone was considered a good quality construction material and it is probably the most widely used limestone in Portuguese monuments and official buildings, such as the famous Belém Tower, the Jerónimos Monastery and some of the delicate of São Roque church in Lisbon, as well as some decorative elements at Convent of Christ in Tomar [7] [8].

(c) *Serra de Sicó* - lies between Tomar and Coimbra, here the rocks are mainly from the Jurassic era. It has a high production potential although the quarrying is now sporadic [4] [6].

(d) *Algarve basin* - at the southern end of Portugal, produces the light brown Brecha Algarvia, confined in Mesquita and Santo Estevão areas. Portugal has 76 million cubic meters of limestone resources in its territory. Nowadays limestone is the most required Portuguese product in the international market [4] [6].

(e) *Other areas* – close to Coimbra region in western Portugal, in the middle of the northern branch of the Lusitanian basin, there is the famous *Ançã* limestone formed in the Bajocian–Bathonian age in the middle Jurassic epoch. It is a homogeneous, fine-grained and oolitic-tendency limestone, containing > 96.5 wt% of $CaCO_3$. Its colour ranges from white to grey with some yellowish variations. Its mechanical features are low compressive strength and low hardness. This limestone is composed of a micrite matrix, with abundant bioclasts (fibrous calcite < 500 mm), also very little spathized micritic cement could be found. Due to its easy workability, *Ançã* limestone has been used in the Santa Cruz Church and in the Porta Especiosa of Coimbra Old Cathedral [8]. Besides that, there is a limestone tuft that is potential for further extraction in the Pleistocenic area at Condeixa-a-Velha, near Coimbra [6].

For human beings, natural stones are one of the oldest construction materials. Though being known as durable and eternal, stones are actually very sensitive to environment and thus the ambient conditions in urban areas and industrial zones cause severe decay of the stone monuments nowadays. In order to find compatible stone resources with the same or similar appearance and properties (mechanical, chemical etc.) for preserving the heritage, it is essential to carry out the stone testing and provenance study for the purpose of identifying the possible sources from existing quarries for replacing the weathered stones, when conservation is no longer possibe [9].

Some important Portuguese building limestones have been studied systematically, such as *Lioz* and *Ançã*. To better understand the decay pattern of Batalha Monastery and develop a suitable conservation strategy, it is necessary to study the properties of the building limestone. Another aim is to assess whether the Batalha monument was constructed with one of the building limestones quoted above, which is essential for finding possible restoration materials in the future.

1.1.2 Common methodology and tools for provenance studies

Along with the development of analytical techniques, the methodologies for stone provenance study have also been improved. Petrographic image analysis (PIA) was firstly applied by a German geologist in 1890s, and since then it has been the most widely used mineralogical method. PIA is usually carried out by optical microscopy (OM) or scanning electronic microscopy (SEM), and it provides information about the lithologies and microfossils that help to find the source-stone for monumental building materials [10]. Sometimes thin-section petrography is the only way to trace the stone provenance, such as in the study of Roman and medieval monuments in Tongeren, Belgium. The recycled "Roman" sandstone ashlars were proved to be weathered sublitharentic / subarkosic sandstone via PIA [11], by collecting the information of a mass of stone species and building the petrographical atlas, this is a useful tool for the identification of natural stones, providing suggestions for possible stone replacements. Since 1990s, cathodoluminescence (CL) has been added to optical microscopy, which allows the identification of accessory minerals in order to distinguish the cathodomicrofacies and to reveal the chemical and volume composition in the carbonate grains [12]. CL has helped to distinguish carbonate stones that contain various trace element, and has been applied in the determination of marbles from historical quarries in Czechia [12], to identify the Goktepe marble exploited in antiquity in Turkey [13]. Nowadays, CL is coupled with SEM to carry out quantitative CL for the marble provenance study [14].

In the 1990s, advances in instrumental techniques were employed together with the communication between archaeologists and archaeometrists, who attempted to unravel archaeological issues via geochemical approach in the research of stones sources [15]. In stones, there are different mineral phases which contain typical trace elements, and these can be detected by various elemental analytical techniques, i.e., X-ray fluorescence (XRF), X-ray luminescence (XRL), particle induced X-ray emission (PIXE), ion luminescence (IL), radio luminescence (RL), inductively coupled plasma-mass spectrometry (ICP-MS) [16] [17]. Those techniques were applied in many provenance studies. For example, the provenance of the volcanic obsidian from Transylvania, Romania was defined by drawing Ti/Mn – Rb/Zr, Ba/Ce – Y/Zr two-dimensional scatter plots [18].

There are also techniques that assist mineralogical analyses. X-ray diffraction (XRD) enables the identification of different mineral phases in stones and defines the composition, if not too low [19]. Loss-on-ignition (LOI) measures the loss in weight of ignited sample due to the release of CO_2, H_2O and other volatiles. After obtaining the general composition of the samples, LOI justifies the purity of specific minerals [20]. Thermogravimetric analysis (TGA) is similar to LOI, it is able to evaluate the presence of particular volatile compounds, essentially hydraulic or carbonate minerals in the stone samples, i.e., calcite, dolomite, portlandite, kaolinite, illite etc. [21], and measures the percentage of them [22] [23].

In addition, stable isotopic analyses (SIA) can also be used to assess geochemical similarities or differences, this is usually carried out with inductively coupled plasma-mass spectrometry (ICP-MS), and inductively coupled plasma-optical emission (ICP-OES) [24] [25] [26]. For sandstones in Gotland, it was found that the $\delta^{13}C$ values go downwards in stratigraphic sequence and decrease from north to south if, at the same stratigraphic level. This distinct geographical pattern makes it possible to determine the stone origin [27]. For the marbles from Moldanubian Zone in Cezchia, a lower $\delta^{15}O$ value of metacarbonates indicate interactions with metamorphic / magmatic fluids during metamorphism, and lower $\delta^{13}C$ is related to decarbonation process. The shifts to lower isotopic O and C values were also found in silicate-enriched marbles [28]. Besides isotopes of C and O, the isotopes of some trace elements are also effective to distinguish rocks because they help to differentiate sediments produced by the erosion of different source lands. For instance, the isotopic Nb-Sr data was a means to elucidate the sedimentary provenance such as the Upper Carboniferous in Britain and Germany [29].

In spite of the chemical and elemental approach, there are also physical analytical methods such as the uniaxial compressive strength (UCS) and ultrasonic pulse velocity

(UPV) tests; by measuring the mechanical and intrinsic properties, it helps to identify limestones [20]. Electron spin resonance (ESR) could identify the provenance of marbles by characterizing the Mn^{2+} impurity presented in the stone [30].

Based on the principles for preserving precious cultural heritage objects, intact analytical protocols have been developed along with the advances of portable and non-destructive instruments, among which, the portable XRF (pXRF) is the most commonly used instrument. Compared to the laboratorial analytical techniques, pXRF is portable, rapid, and requires no sample preparation [31]. For some trace element such as Rb, Sr and Zr, pXRF provides data consistent with that obtained from INNA and ICP-MS in the study of obsidian provenance in Japan [31]. The pXRF has proved its high potentiality in distinguishing decorative stone samples from different provenance, including Egypt, France, Italy, Australia, India, Portugal and so on [32]. It was also applied in the definition of the limestone material of sculptures in Chichén Itzá, Mexico [33]. Saleh et al. set up a joint portable system based on radio-luminescence that obtains X-ray luminescence (XRL) spectra simultaneously with XRF data, and they successfully determined the lapis lazuli stones, both historical and modern, from different classified provenances and speculated the origin of unknow samples [34]. The portable infrared mineral analyser (PIMA) was proved to be also capable of detecting all common clay minerals, sulphates, hydroxides and carbonates by reflectance spectroscopy, thus it could be a non-destructive and reliable technique for identifying sandstones from architectures [35]. Prompt Gamma activation analysis (PGAA) is another powerful bulk chemical method that meets the non-destructive requirements; it quantifies all the major components and a few trace elements in rock samples, including igneous, metamorphic and some sedimentary stones. PGAA was found to have good matching values compared with XRF, ICP-MS and INA, thus becoming a proposing technique for characterizing cultural heritage materials [36].

Provenance determination of stones is a challenging task because stones from individual localities could exhibit different properties (due to secondary veining, various deformation intensities etc.) or stones of different localities may have similar petrographic characteristics. Moreover, the international trading of valuable stones makes them transported over huge distances [12]. Therefore, provenance study is usually a combination of the above-mentioned petrographical, mineralogical, geochemical and physical-mechanical approaches. For example, in the study of Antas site in Sardinia, Italy, minero-petrographical (thin-section, OM, petrographic atlases) and physical-mechanical (dry-wet masses, real-bulk volumes, porosity calculating and strength test) characterization were applied on the Punic and Roman temples to define the metadolostone and sandstone used as their construction materials and their conservation state [37]. To define the origin and composition of the granitic stone that

was used to build Casas de Paredes in A Coruña, Spain, SEM, XRD, XRF, DTA-TGA were all applied [38]. In another case study about the granite used in the Roman theatre in Merida, Spain, PIA was carried out by OM together with the elemental geochemistry obtained by ICP-MS. Moreover, ultrasonic pulse velocity (UPV) and hardness rebound tester (HRT) were applied both in situ and on the quarry rocks to reveal the structure, allowing to identify the granite's provenance [39]. These provenance techniques could also be worthwhile for commercial purposes: to certify the origin of the commercial limestone Comblanchien from Bourgogne, France, macroscopic and microscopic observation were applied in addition to chemical composition measured by ICP-AES and ICP-MS, oxygen, carbon, neodymium isotopes analysed by mass spectrometers, thus discriminate the mined limestones from different quarries and provide the feasibility to attach identity cards and commercial labels to them [40].

Therefore, in order to obtain accurate and thorough information about the stone of the Batalha Monastery, multiple analytic methodologies will be applied.

1.1.3 Construction and restoration history of the Batalha Monastery

Figure 1.1 The Monastery of Batalha

The Mosteiro de Santa Maria da Vitoria (Figure 1.1), known internationally as the "Monastery of Batalha", was constructed to commemorate the victory over Castile. It

is considered an architectural masterpiece, demonstrating a perfect mixture of the Gothic and Manueline styles. Initial construction began in 1386 and took two centuries to complete. In 1840, after the monastery had been nearly abandoned due to the suppression of religious orders in 1834, a first restoration programme began [41]. The Batalha Monastery has been added to the list of World Heritage sites by UNESCO. A satellite view of Batalha is shown in Figure 1.2, the monastery being highlighted by white dash lines. It can be seen that the Portuguese national road IC2 (N1) runs north-south about 50 meters west of the monument building. Vineyards are located less than 200 meters in the northwest direction, and farm lands can be found less than 300 meters eastwards from the monastery.

Figure 1.2. Satellite map of Batalha county, the Batalha Monastery is marked by the dash circle. Picture from Google map ©

Over a century has now passed since the last large-scale restoration was completed. The Batalha Monastery shows a high degree of stone decay, mainly due to bio-deterioration processes, which are known to play an ever-increasing role in stone decay both in urban and rural environments [42]. In order to plan an appropriate conservation strategy for the protection of the monastery, it is necessary to obtain petro-geochemical

data from the stone used in its construction and successive restoration interventions [43].

According to Aires-Barros and reports from the Batalha City Council, the two original limestone quarries used for the construction of Batalha Monastery in the 15th century were the Pidiogo and Valinho do Rei quarries, located respectively 8 km and 7.5 km to the east of the monastery [44] [45]. Soares et al. indicated that four quarries served as the main source of building stone for the restoration during the 19th century: a) the Reguengo do Fetal quarry provided the stone from 1840 to the mid-1880s; b) from 1854 until the end of the restoration activities, the Carvalhos quarry was the one mainly used; c) in the last decade of the 18th century, the Cabeço do Roxo and the Outeiro de Sebastião quarries have also been reported to supply stone materials for the restoration of the monastery [46]. Despite the somewhat scarce historical documentary evidence, no detailed petrographic/geochemical study has ever been carried out to test the accuracy of the assignment of these historical quarries as the suppliers of the carbonate stones for the building and the restoration of the monastery. To contribute to this open discussion, a multi-analytical approach has been adopted for the first time in this study, combining a) sampling of selected original stones from the monastery, b) a field survey to identify the location of and collect samples from the ancient quarries mentioned in the literature and c) petrographic and geochemical analyses using thermal-gravity analysis (TGA), X-ray diffraction (XRD), optical microscopy (OM) and scanning electronic microscope + energy dispersive X-ray fluorescence (SEM + ED-XRF).

1.2 Methods and Materials

1.2.1 Field investigation and sample collection

With special permission from the Direção-Geral do Patrimonio Cultural and the Mosteiro da Batalha authorities, 12 pieces of detached stone fragments were collected for destructive and/or non-destructive characterisation, depending on the signed agreement with the monastery curator. The collected stone fragments came from various parts of the monastery, as labelled in Figure 1.3.

The location of the Pidiogo and Valinho do Rei quarries was indicated in a document released by Batalha Municipality [45]. The approximate location of Reguengo do Fetal, Cabeço do Roxo and Outeiro de Sebastião quarries were recorded in the book “O restauro do Mosteiro da Batalha” [41], although their exact location had been lost and only rediscovered in the course of the current doctoral research. Despite

considerable efforts, it was not possible to find one of the restoration quarries mentioned in the historical documents, i.e., the Carvalhos quarry, because it had been renamed during the last century. Field trips were made to five quarries (Figure 1.4), and the latitude and longitude were recorded with the help of Google Earth. More than 20 kg of samples were collected and marked with their corresponding origin, of which 18 samples were from Valinho do Rei and Pidiogo, believed to be the original quarries used in the construction of the monastery in the 15th and 16th centuries, and 16 samples were from Reguengo do Fetal, Cabeço do Roxo and Outeiro de Sebastião, used as the restoration quarries in the 19th century.

1.2.2 Thin-section petrography (OM)

Thin-sections of the stone samples were obtained using the following procedure: stones were cut into cuboids with a cross-sectional area of 2 cm × 3 cm, and the cross-sectional surface was polished with 220# sandpaper and 400# and 1000# SiC powder, with water added sequentially. The polished stone surface was glued to the glass slide with epoxy resin and epoxy hardener mixed at the weight ratio of 2:0.9. After the epoxy glue had set, the stones were cut and ground to a thickness of 0.1~0.2 mm, and polished using 400# and 1000# SiC powder with water until the thickness of the stone section reached 0.025 mm. Thin-sections were observed by OM using a LEICA DM2500P using transmitted light.

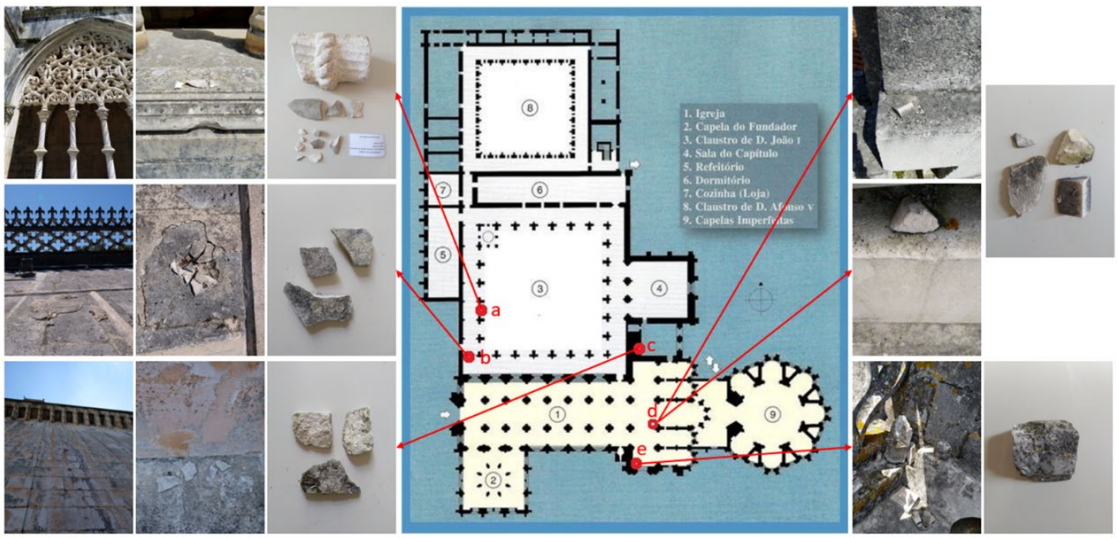

Figure 1.3. Locations of samples collected from Batalha Monastery: a. west gallery of the Royal Cloister, outside the 3rd window (ground-floor level); b. Royal cloister roof top (roof level); c. Church north-aisle eaves arch (roof level); d. Church roof railing (roof level); e. Church south carved baluster (roof level).

a

b

c

d

e

f

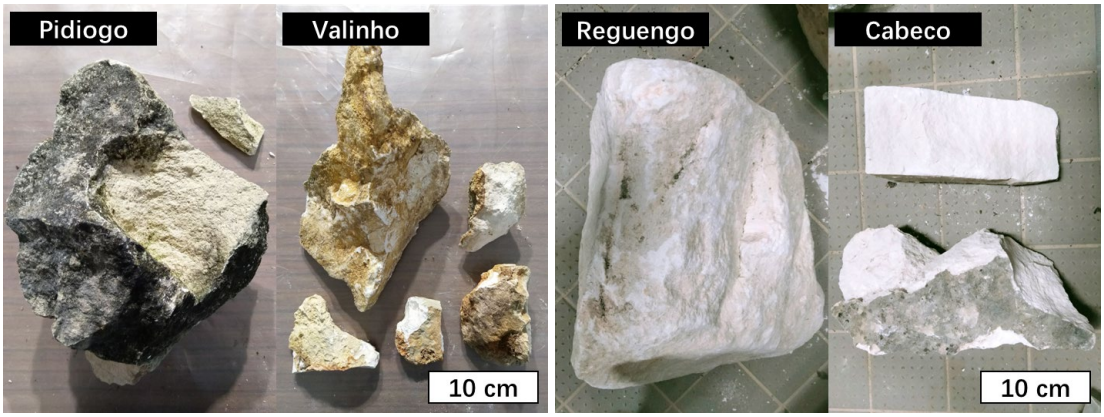

g h

Figure 1.4. Photo records of field investigation to quarries: a. Pidiogo (39°39'15.7"N 8°44'27.9"W); b. Valinho do Rei (39°39'32.5"N 8°44'58.1"W); c. Reguengo do Fetal (39°38'43.64"N 8°45'16.19"W); d. weathered outcrop of Valinho do Rei e. Cabeço do Roxo (39°35'39.84"N 8°51'27.19"W), f. Abandoned quarry of Outeiro de Sebastião (39°35'38.89"N 8°51'27.49"W), g and h. stone samples taken from quarries.

1.2.3 Powder X-ray diffraction (PXRD)

The characterisation was carried out using a BRUKER D8 Discover X-ray diffractometer, with a CuKα source and operating at 40 kV and 40 mA. Scans were run from 3 ° to 75 ° 2θ, with a 0.05 º 2θ step and a measuring time of 1 s/step per point. The DIFFRAC.EVA software package (BRUKER/AXS GmbH, Germany) and the PDF-2 database files (ICDD, Denver, USA) software with the PDF-2 mineralogical database were utilised to interpret the XRD patterns. The semi-quantification was carried out using the reference intensity ratio method of Hubbard et al. [47]. The specimens used to conduct the characterisation were stone powders hand milled in an agate mortar.

1.2.4 Thermogravimetric analysis (TGA)

The TGA analysis was carried out using a TG-DTA NETZSCH STA 449F3 Jupiter. The temperature of the sample was increased at a heating rate of 10 °C /min from 40 °C to 1,000 °C, under an N_2 protective atmosphere, while the mass of the powdered sample was monitored against time and temperature. TGA applied to stone allows the quantification of minerals that are decomposed by temperature, such as minerals with structural water content or carbonates. Thermal decomposition with gaseous evolution can be detected by measuring the weight change, thus, by using stoichiometry, the content of each corresponding mineral composition can be determined.

1.2.5 X-ray fluorescence spectroscopy (XRF)

XRF analyses were performed with a Benchtop EDXRF Bruker S2 PUMA, using a methodology similar to the one adopted by Georgiou et al. [48]. Quantifications were obtained using a regression method with 19 standard reference materials [49]. Spectra Elements 2.0 software was utilised for acquisition and data processing, reporting the final oxide/element (Na_2O, MgO, Al_2O_3, SiO_2, P_2O_5, SO_3, K_2O, CaO, TiO_2, MnO, FeO) concentration and the instrumental statistical error. Two sample preparation methods were used: (1) 1.2 g of sample powder was fused with 12 g of flux (Li-tetraborate) on a Claisse LeNeo to form fused beads; (2) 10 g of sample powder was compressed with 1 g of wax (N,N'-dioctadecanoylethylenediamine) on a Specac Manual Hydraulic Press to form pellets.

1.3 Results and discussion

1.3.1 Thin-section petrography

The micrographs of the thin sections are presented in Figure 1.5 and Annex 1A, in which oolites, calcite crystals and fossils may be clearly distinguished. Based on the classification scheme introduced by Flügel for identifying microfossils [50] and classifying carbonate grains in microfacies studies [51], [52], and referring to previous biostratigraphy of carbonate succession [53] [54], Table 1.1 summarises the petrography features of the samples.

The limestone samples from the Reguengo do Fetal and Cabeço do Roxo quarries and the limestone samples from the Batalha Monastery roof top, eaves arch and church baluster show oolites of relatively uniform size and with compacted dispersion. However, the Valinho do Rei samples show clear differences in carbonate clasts; there are peloids with small diameters (0.1 mm on average) and ooids that are ten times larger (1 mm). The Outeiro de Sebastião quarry, the Batalha Monastery royal cloister and church railing 1 contain abundant marine microfossils. Large-sized sparite crystals (up to 0.5~1 mm) can be identified as intergranular cement between oolite grains, some of which was recrystallised from micrites. According to Dunham's classification, all the limestones investigated can be classified as grain-supported [55]. The presence of sparry calcite cements and quasi-spherical oolites implies precipitation in a high-energy shallow marine depositional environment [56].

Foraminifera in the samples belonged mostly to four genera: *Miliolid*, *Kurnubia*, *Trocolina* and *Haddonia*. These foraminifera are found in inner shallow-water platforms from the late Jurassic and early-middle Eocene, indicating, respectively, the

sedimentary depositional environment and the age of these limestones [50]. This deduction matches that of the "Carta Geológica de Portugal" [57], see Figure 1.6, with the Pidiogo, Valinho do Rei and Reguengo do Fetal quarries showing limestone deposits of Bathonian age and Cabeço do Roxo and Outeiro de Sebastião of Callovian age, both of which belong to the middle–late Jurassic period.

Data in Table 1.1 and the features described above were summarised from the thin-section photos, which can be found in Annex 1A.

Pidiogo

Valinho do Rei

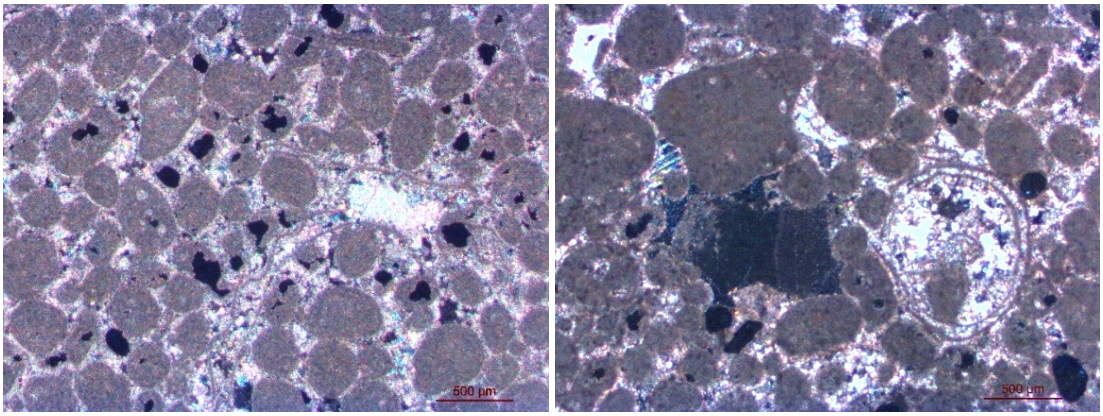

Reguengo do Fetal

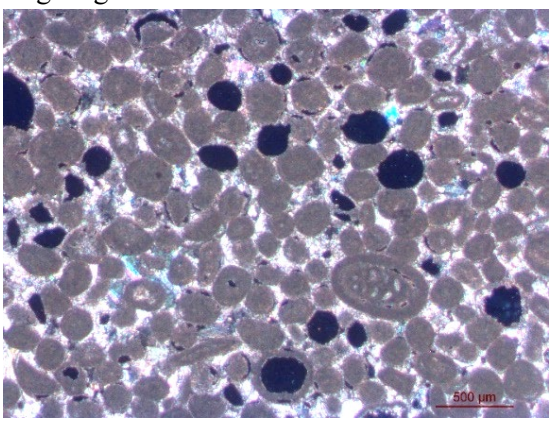

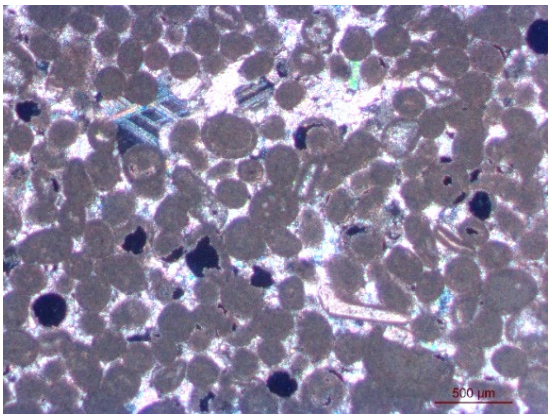

Cabeço do Roxo quarry

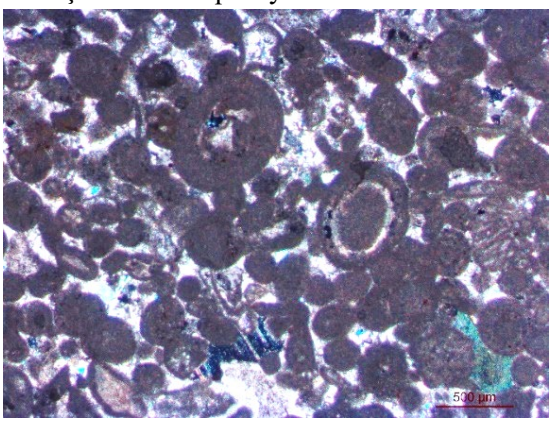

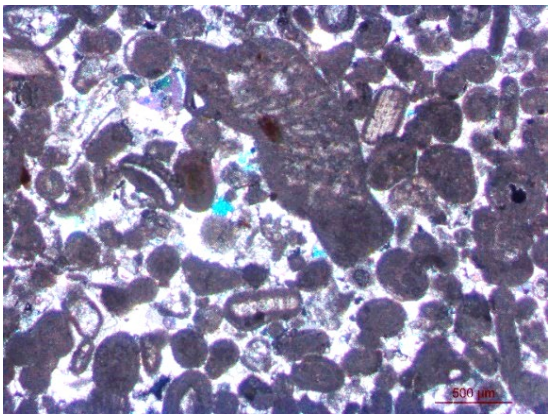

Outeiro de Sebastião

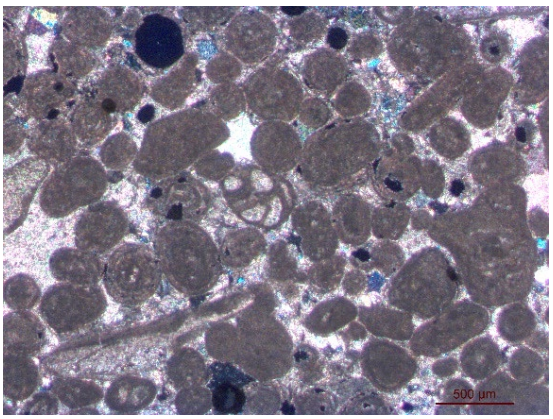

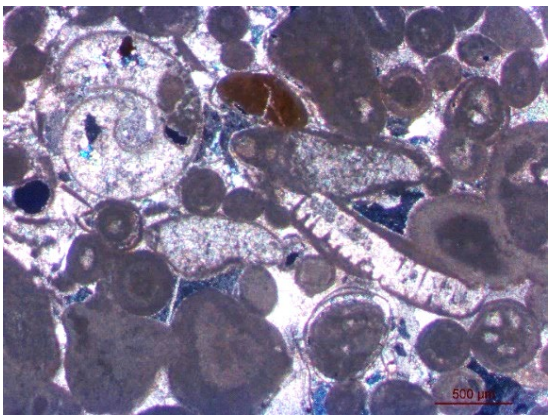

Batalha Monastery, royal cloister west gallery

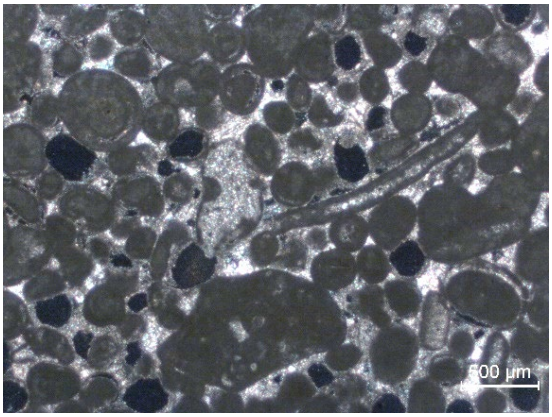

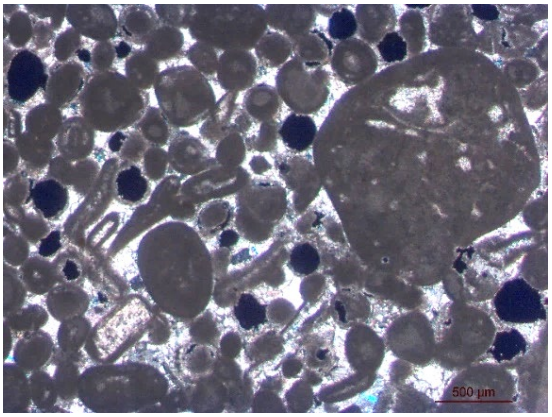

Batalha Monastery, north aisle eaves arch

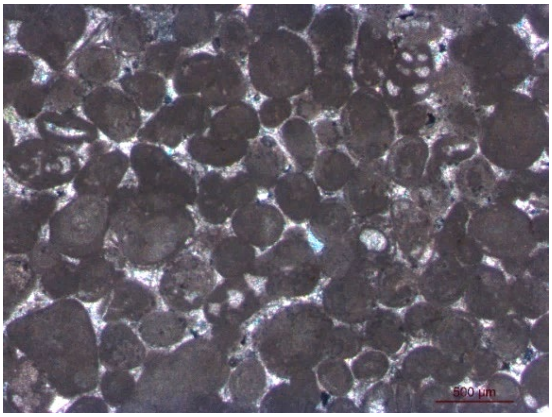

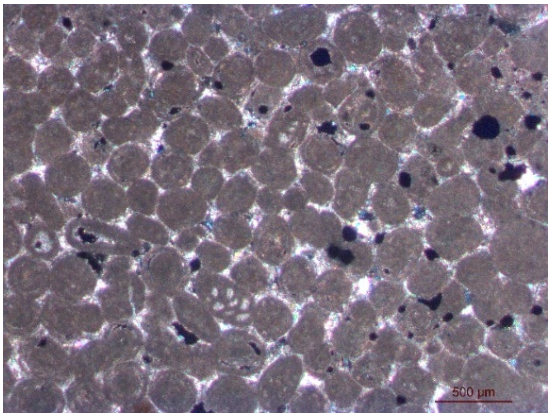

Batalha Monastery, roof top

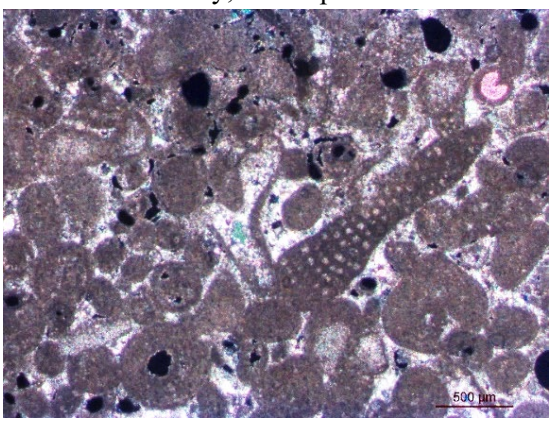

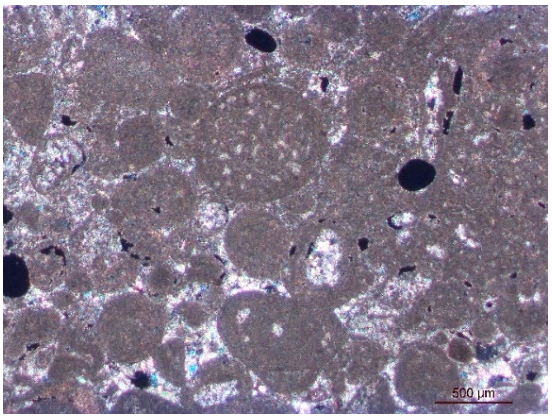

Batalha Monastery, church railing 1

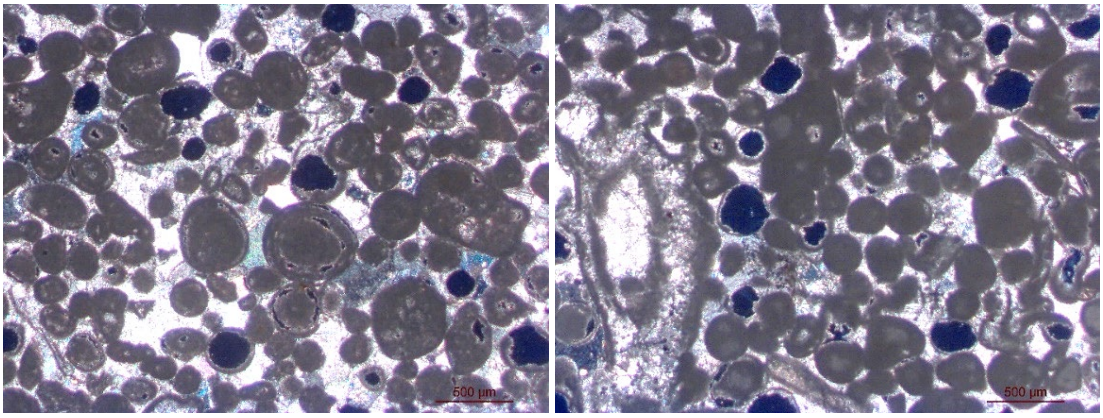

Batalha Monastery, church railing 2

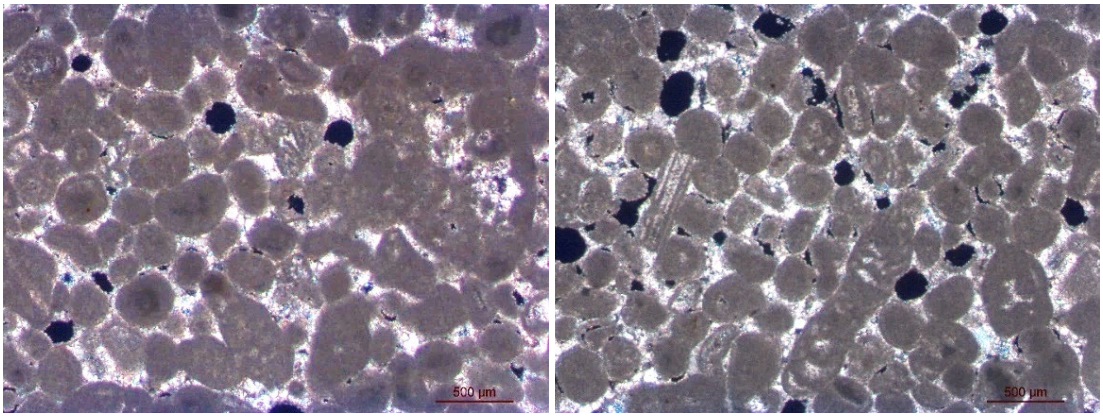

Batalha Monastery, baluster

Figure 1.5. OM thin section photos of stone samples from quarries and the monastery

Table 1.1. OM Petrography: summary.

Sample locations	**Oolite morphology and dimension**	**Calcite cement**	**Fossils**
Pidiogo	ooids 0.2~0.5 mm peloids ~0.1 mm	Micrite and sparite of 0.01~0.1 mm between oolites, pseudo spars can reach 0.5~0.8 mm.	Gymnocodiacean algae, trilobite, foraminifera, gastropod, ostracod, intraclast
Valinho do Rei	ooids 0.4~1 mm peloids 0.05~0.1 mm	Mostly small sparite and micrite between peloids, spars of 0.1~0.2 mm between large ooids and bioclasts.	Foraminifera (Trocholina, Kurnubia, Miliolina), intraclast, brachiopod, styliolinid, bivavle
Reguengo do Fetal	ooids 0.2~0.5 mm intraclasts 0.8~1 mm	Mostly sparite < 0.05 mm and micrite, spars of 0.2~0.5 mm are commonly seen alongside and inside fossils.	Ostracod, foraminifera (Miliolid, Alveospta, Haddonia), trilobite, echinoderms, brachiopod
Cabeço do Roxo	ooids 0.2~0.4 mm	Mostly spars < 0.06 mm and micrite, very few spars of 0.2~0.3 mm.	Wood, gymnocodiacean algae, foraminifera
Outeiro de Sebastião	ooids 0.2~0.5 mm	Some micrite, rich sparite of 0.01~0.1 mm, spars of 0.2~0.4 mm are commonly seen between ooids and fossils.	Pseudodonezella, foraminifera (Kurnubia), trilobite, echinoderm
Batalha Monastery, Royal Cloister	ooids 0.2~0.5 mm intraclasts > 1 mm	Small sparite inside fossils, big spars > 0.5 mm are commonly seen outside fossils and between ooids.	Gastropod, gymnocodiacean algae, bivalve, foraminifera (Miliolid), intraclast
Batalha Monastery, roof top	ooids 0.2~0.5 mm	Mostly small sparite and micrites between ooids and inside fossils.	Foraminifera
Batalha Monastery, eaves arch	ooids 0.2~0.5 mm intraclasts > 1.2 mm	Mostly small sparite and micrite between ooids, very few spars of ~0.2 mm.	Foraminifera (Trocholina alpina, Miliolina), echinoderms, intraclast, trilobite
Batalha Monastery, church railing 1	ooids 0.2~0.5 mm	Mostly small sparite and micrite, a few spars reach 0.5 mm.	Gymnocodiacean algae, foraminifera (Lepidorbitoides), trilobite, bivalve, echinoderm
Batalha Monastery, church railing 2	ooids 0.2~0.5 mm peloids 0.1~0.15 mm	Middle-sized spars of 0.1~0.5 mm are widely distributed between ooids, some small sparite and micrite can be seen inside fossils.	Salpingoporella istriana, foraminifera, trilobite
Batalha Monastery, church balustrade	ooids 0.2~0.4 mm	Mostly sparite < 0.1 mm between ooids and inside fossils.	Wood, gymnocodiacean algae, foraminifera

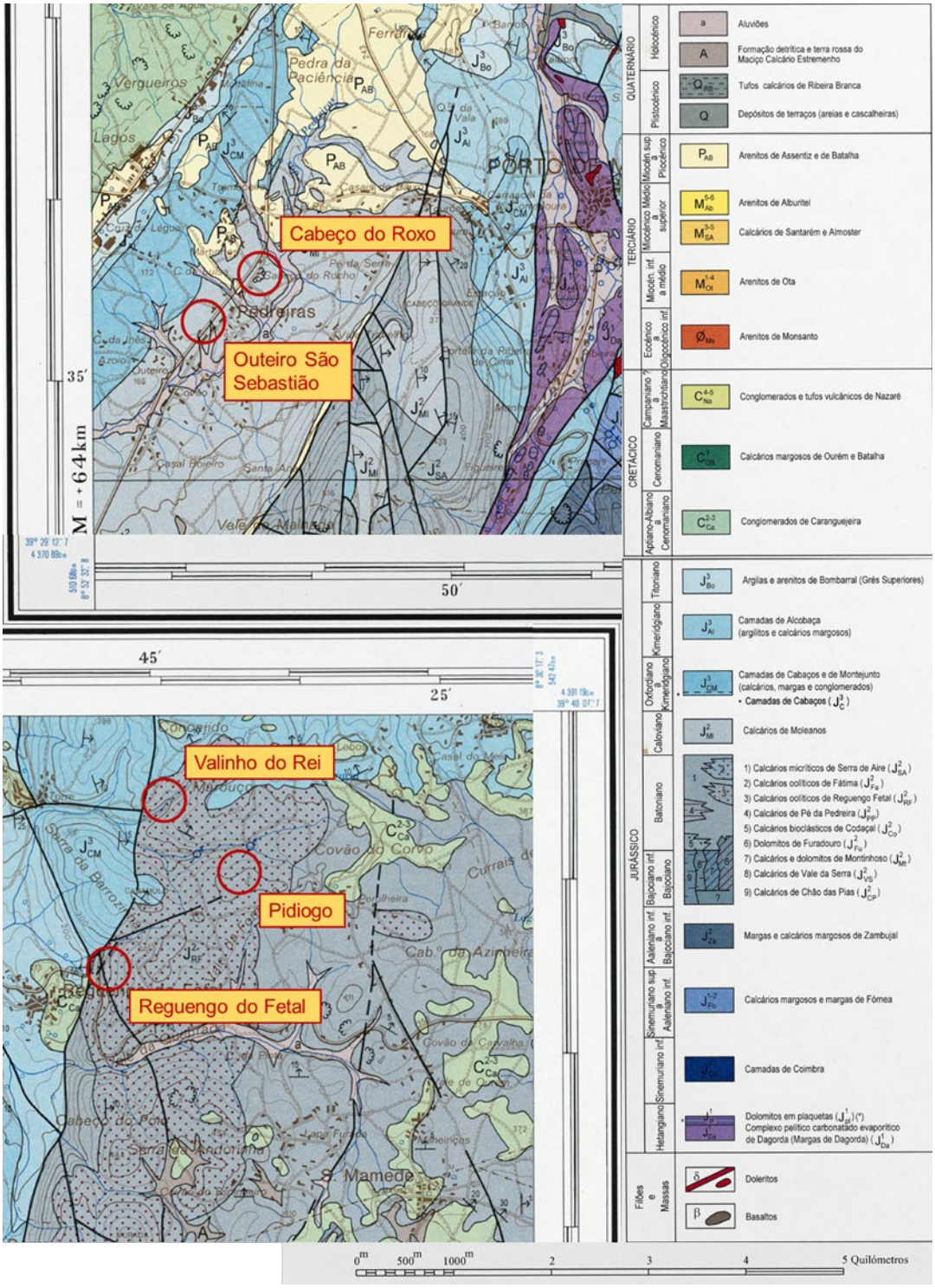

Figure 1.6. Quarries marked on the Carta Geologica de Portugal and their geological settings [25].

1.3.2 X-ray diffraction

Figure 1.7 shows the XRD diffractograms of all the stone samples from the quarries and the Batalha Monastery. The results indicate that all the samples have the same mineral composition: calcite ($CaCO_3$), magnesium calcite ($(Mg_{0.03}Ca_{0.97})CO_3$) and quartz (SiO_2). Semi-quantitative analysis shows that the content of calcite in these limestones is over 95 % ($CaCO_3$ 60~70 % and $Mg_{0.03}Ca_{0.97}CO_3$ 25~35 %), while the content of quartz is around or lower than 1 %.

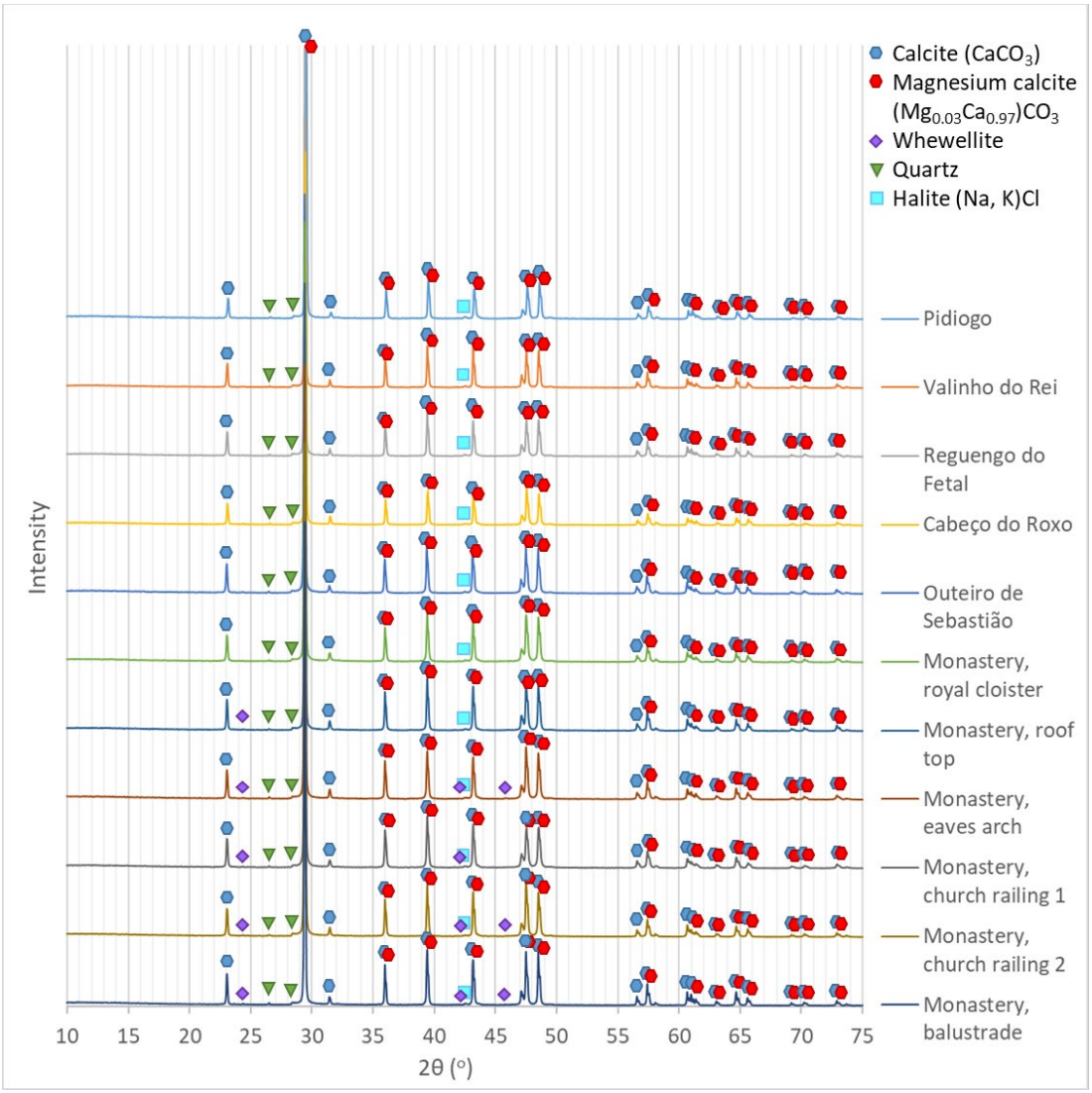

Figure 1.7. XRD results of the stone samples.

For the minor peaks, the minerals identified were whewellite ($CaC_2O_4•H_2O$), and sodium potassium chloride $(Na_{0.5}K_{0.5})Cl$. Whewellite was especially presented in the stones from the monument, implying the calcite underwent some chemical alteration.

The sodium potassium salt was presented in all limestone samples. However, due to the weak intensity of this peak (less than 0.5 %) and the possible overlapping of the major mineral peaks, this identification is inconclusive.

1.3.3 Thermogravimetric analysis

Figure 1.8 shows the weight loss of one sample according to temperature increase. A mass loss in the temperature range of 650 °C–850 °C was observed, indicating the decomposition reaction of calcite [58]: $CaCO_3 \rightarrow CaO + CO_2$. The differential of the thermal gravity curve showed the reaction to be single stepped. There is no mass change in the other temperature ranges, demonstrating no absorbed water, gypsum, portlandite, illite or muscovite which provide different thermal-gravity performance [59] [60]. As seen in Table 1.2, the calculated results show that the concentration of calcite in all the samples as ranging between 97.2 wt%~99.2 wt%. It should be noted that the molar mass of $CaCO_3$ was used in the calculation, thus the actual percentage of calcite would be lower than this number; this minor inaccuracy originates from the presence of the magnesium calcite.

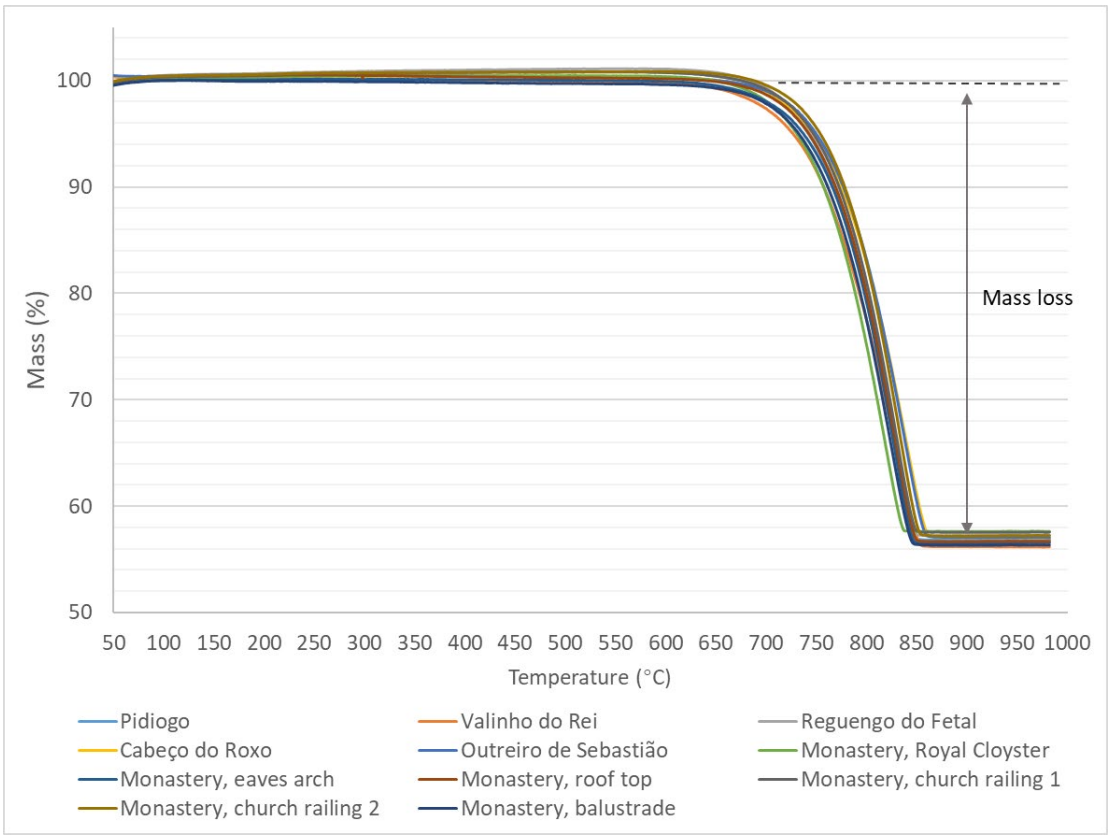

Figure 1.8. TGA curve of stone from the Batalha Monastery baluster.

Slight differences could be seen by comparing the curves of all the samples. For example, limestone from the Valinho do Rei quarry showed obvious weight change after the temperature reached 600 °C, while for the sample from Outeiro de Sebastião, it was after 630 °C. A feasible thermodynamic explanation for this phenomenon is that a larger particle size causes the activation energy to be higher, thus requiring more thermal energy to initiate the decomposition process [61]. Grain size can also affect the reaction kinetics; limestone, with small grain size, has a higher thermal decomposition rate [62]. This is in accordance with thin-section observation, as the major component of the Valinho do Rei limestone is characterised by micritic cement between small peloids, while the Outeiro de Sebastião limestone has larger ooids, more fossils and larger recrystallised sparite cements.

Table 1.2. Calcite proportion from TGA calculation

Sample	Weight loss (wt%)	Calcite (wt%)
Pidiogo	43.93	99.9
Valinho do Rei	43.58	99.1
Reguengo do Fetal	43.85	99.7
Cabeço do Roxo	43.24	98.3
Outeiro de Sebastião	43.23	98.3
Batalha Monastery, Royal Cloister	42.77	97.2
Batalha Monastery roof top	43.48	98.9
Batalha Monastery eaves arch	43.39	98.6
Batalha Monastery church railing 1	43.21	98.2
Batalha Monastery church railing 2	43.64	99.2
Batalha Monastery church baluster	43.28	98.4

1.3.4 X-ray fluorescence analysis

Table 1.3 lists the concentration of essential elements in each limestone sample, Annex 1B shows the complete concentration of all the detected elements. Besides calcium, in the limestone there are also silicon, phosphorous, sulphur, strontium, magnesium, sodium, potassium, chlorine and barium.

Figure 1.9 illustrates the relative intensity of each element. The overall ratio of these elements is rather homogeneously distributed, with the exception of the Batalha Monastery baluster sample, which shows apparent higher counts of P, S and Cl, while the naturally weathered Valinho do Rei stone has the highest counts of Na and Cl. This could be explained by the effect of salt weathering [63]. In addition, there is a noticeable disparity in the strontium peak intensity between some samples.

Table 1.3. Element concentration of limestone samples by XRF analysis.

	Na_2O	MgO	Al_2O_3 (ppm)	SiO_2	P_2O_5	S (ppm)	K_2O	CaO	Fe_2O_3 (ppm)	Rb (ppm)	Sr (ppm)	Ba (ppm)	Cl (ppm)
Monastery. Royal Cloister	0.22%	0.83%	647	0.92%	1.14%	1660	0.22%	61.50%	182	7	189	541	123
Monastery. roof top	0.18%	0.84%	597	0.91%	0.71%	557	0.22%	61.90%	529	4	221	384	44
Monastery. eaves arch	0.19%	0.81%	602	0.94%	0.71%	505	0.21%	62.40%	303	6	182	481	41
Monastery. church roof railing 1	0.21%	0.97%	771	0.90%	0.72%	590	0.22%	62.20%	246	5	268	336	45
Monastery. church roof railing 2	0.20%	0.83%	813	1.03%	0.72%	535	0.17%	62.20%	188	5	167	431	44
Monastery. baluster	0.27%	0.72%	710	0.89%	0.72%	475	0.22%	62.50%	229	6	110	370	47
Pidiogo	0.18%	0.92%	830	0.91%	0.71%	620	0.20%	62.50%	207	4	183	455	45
Valinho do Rei. lower layer	0.20%	0.77%	594	0.89%	0.71%	430	0.20%	62.60%	167	6	93	440	41
Valihno do Rei. upper layer	0.21%	0.80%	875	0.90%	0.72%	449	0.22%	62.60%	120	7	100	436	42
Valinho do Rei. weathered	0.32%	0.75%	749	0.90%	0.70%	527	0.25%	62.00%	105	4	119	410	174
Pidiogo (repeat)	0.13%	0.86%	452	0.89%	1.00%	939	0.31%	64.50%	121	3	157	417	50
Valinho do Rei (repeat)	0.15%	0.67%	559	0.91%	1.01%	914	0.39%	64.70%	115	6	110	489	61
Reguengo do Fetal	0.14%	0.76%	585	0.89%	0.99%	878	0.33%	64.90%	263	3	111	364	52
Cabeco do Roxo	0.17%	0.79%	485	0.92%	1.00%	913	0.30%	64.50%	440	4	163	505	50
Outreiro de Sebastiao	0.15%	0.76%	719	0.91%	1.00%	930	0.31%	64.40%	466	5	146	460	50

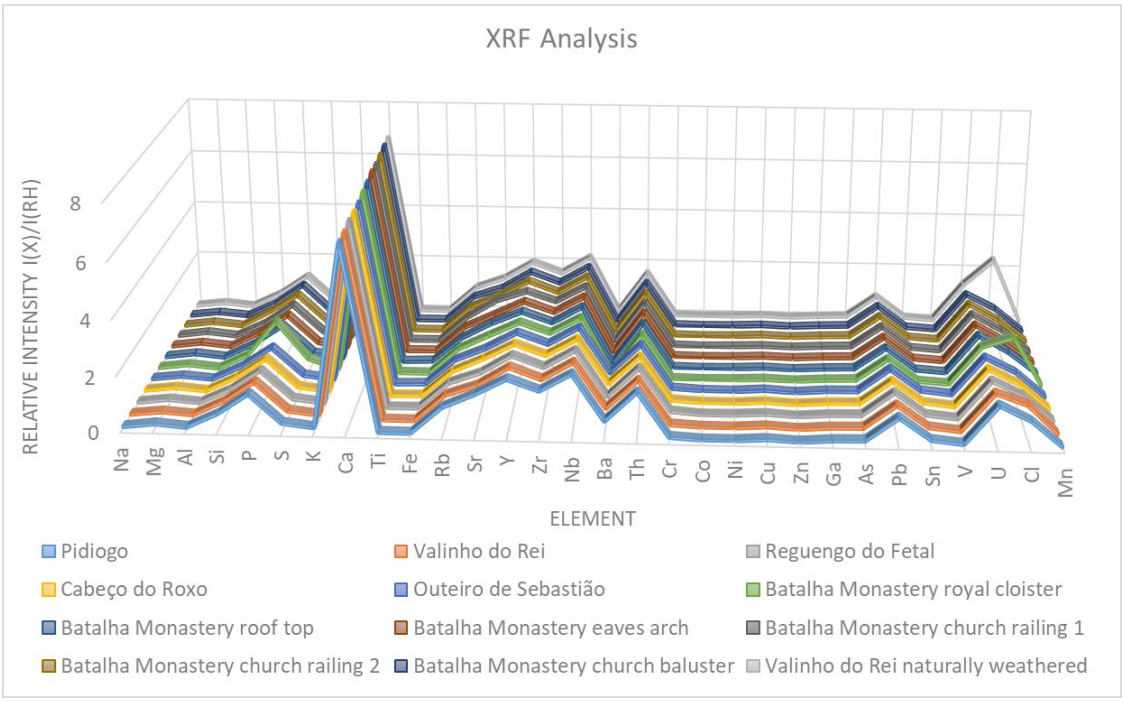

Figure 1.9. XRF elemental results.

It is well known that Sr^{2+} may substitute for Ca^{2+} in calcium minerals (i.e., calcite, dolomite, aragonite, gypsum) due to their same coordination number and similar ion radius [64]. The strontium concentration in sedimentary carbonate rocks is affected by various environmental factors, such as the Sr/Ca ratio in seawater, the continental weathering mass balance, hydrothermal circulation, carbonate deposition, or even biological effect [65] [66]. Therefore, the Sr/Ca ratio has long been a useful geochemical method for obtaining the correlation between stone artefacts and quarries, distinguishing the stones and identifying the origin [67] [68]. From the Ca-Sr element alignment scatter plot (Figure 1.10), it can be seen that the plots that represent the Batalha Monastery baluster, Valinho do Rey and Reguengo do Fetal are similar, suggesting a Sr/Ca concentration ratio around 1.7 (ppm/%). However, limestones from the Batalha Monastery Royal Cloister, eaves arch and church railing 2 have similar Sr/Ca ratios to the Pidiogo and Cabeço do Roxo quarries of around 2.8. The plots for the Batalha Monastery roof top (Sr/Ca ratio 3.6) and church railing 1 (Sr/Ca ratio ~4.3) are not close to any existing quarry samples; a possible explanation is that these stones were from the lost Carvalhos quarry.

River water (RW) and mid-ocean ridge (MOR) are the two major contributors for the seawater composition, and the MOR flux drastically affects the mole ratios of Mg/Ca, Na/K, Cl/SO_4 and defines the mineralogy of limestones [69]. Mg/Ca ratio also reflects some of the conditions during the limestone precipitation, including the sea

water evaporation rate, the Mg/Ca concentration, the pH and the salinity of seawater, or the algal abundance in the brine [70] [79] [80]. Faster evaporation of the sea water, capillary concentration, the Mg-enriched algal sheath and other specific conditions would result in higher magnesium content in the sediments, thus forms magnesium limestone or dolomite limestone [70] [79] [80]. It is shown in Figure 1.11 that the Mg/Ca ratio of all the limestone samples are concentrated in values, indicating there were no big differences in the sedimentary conditions of all the quarry limestones in accordance with the factors that would affect the magnesium concentration. The average Mg/Ca value is 0.0126, thus all the stones from quarries and the site could be classified as "pure" limestone [70] suggesting a possible low magnesium content or low evaporation rate of the seawater where the limestone was sedimented.

Since the seawater chemistry has primary control on the formation of carbonate rocks, the minerals in limestone also report the seawater chemistry and its fluctuations [71] [72]. Figure 1.12 illustrates a linear correlation between chloride and sulphur in all the limestone samples except the salt decayed one, such positive relation suggests that the S and Cl elements existed in these limestones were from the same or similar sources [73]. In other words, sulphates and chlorides were present in the marine environment where these limestones were formed [74] [75], and as a result the comparable anionic concentration of Cl^- and SO_4^{2-} are presented in the stone samples. The explanation for the linear correlation between Na_2O+K_2O and Cl (Figure 1.13) of most analysed samples is analogous, the sodium and potassium halite are indigenous in marine environment [76] [77].

The sharp increase of Cl concentration in the weathered quarry sample indicates the stone decay is related to salt, and the higher content of Na+, K+ and Cl- in this sample added credibility to it. Another observation is that the fragment from the royal cloister on the ground floor of the Batalha Monastery contains higher amount of NaCl and KCl than the stones on the higher floors, the reason of this phenomenon could also be the possible factor causing stone deterioration in the Valinho do Rei quarry: the absorption of saline-contained groundwater from the stone foundation through capillary rising and the swelling-shrinking and crystallization-hydration circles along seasonal temperature changing leads to the salt decay of limestones [78]. One step further, the linear correlation between Na_2O+K_2O and Cl in the two samples from the monastery ground floor and the weathered part of Valinho do Rei gives rise to the assumption that the underground aquifers of these two locations are connected.

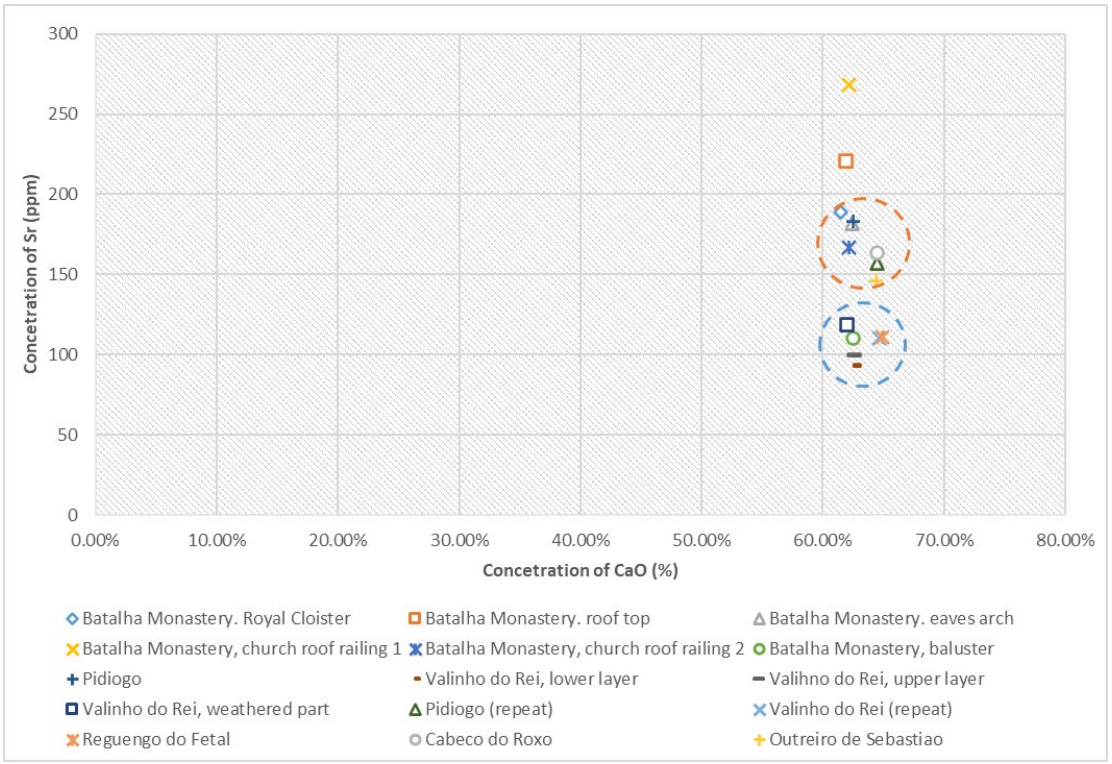

Figure 1.10. Sr-Ca element alignment based on XRF data

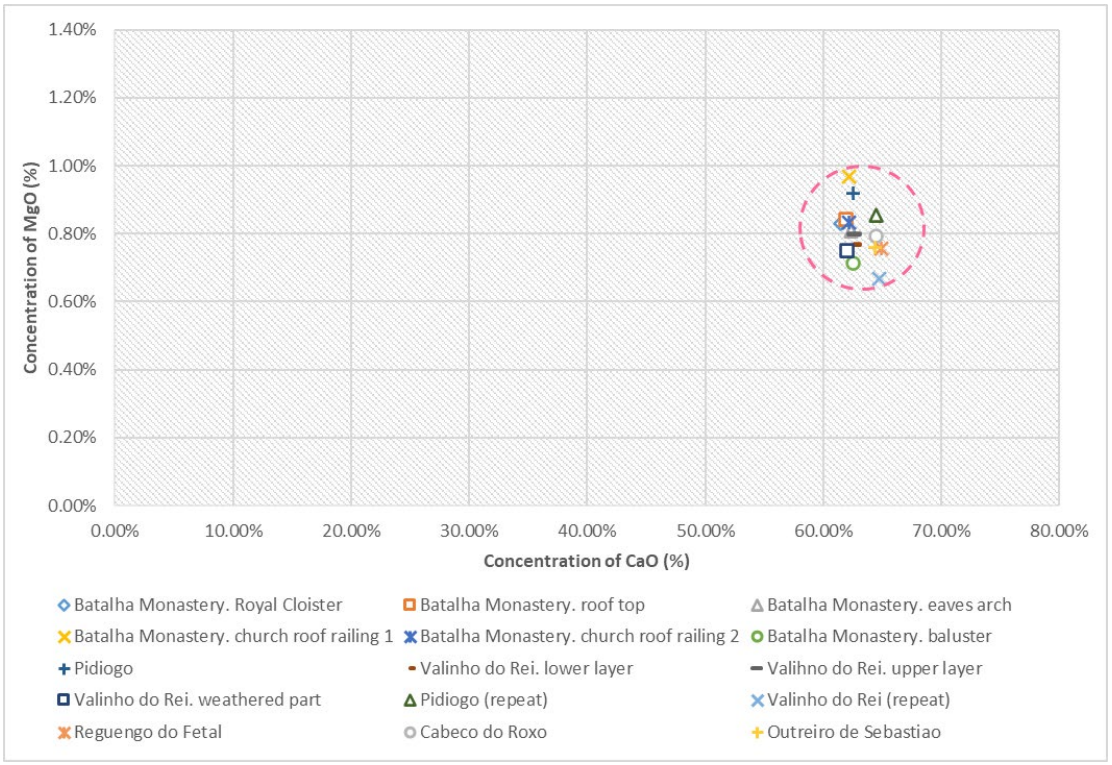

Figure 1.11. Mg-Ca element alignment based on XRF data

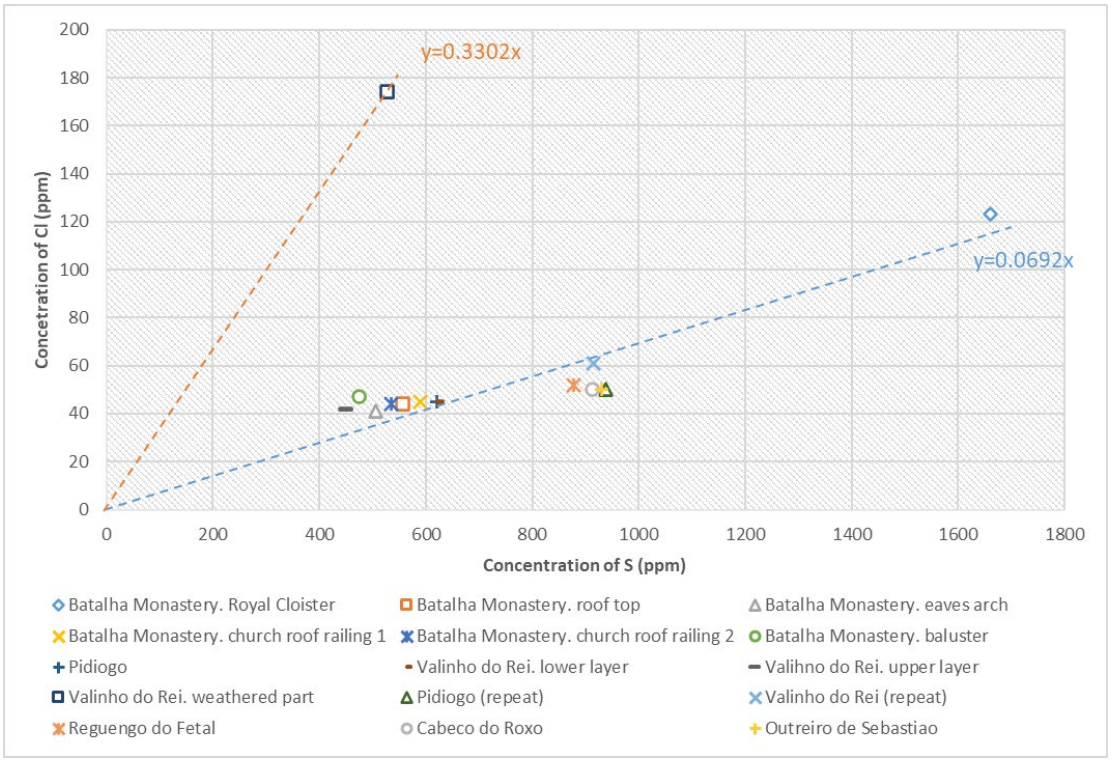

Figure 1.12. Cl-S element alignment base on XRF data

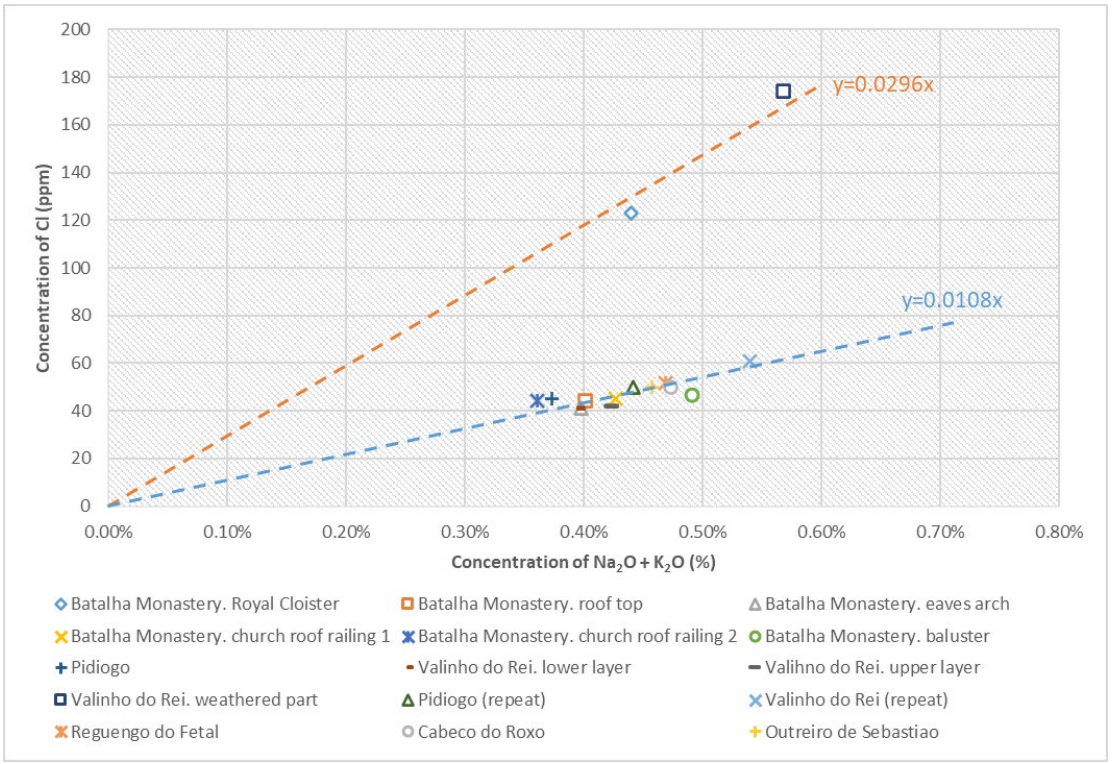

Figure 1.13. (Na_2O+K_2O)-S concentration alignment base on XRF data

1.4 Conclusions

A combined multi-analytical approach was used to establish the quarries of provenance for the Batalha Monastery. Since considerable historical evidence can be drawn from the study of material provenance, these techniques have provided a powerful tool for the collection and analysis of valuable information of special interest to conservation research. The petrographic study confirmed that stones from the Batalha Monastery and the quarries that were used for construction and restoration are all oolitic limestones, dating back to the middle–late Jurassic period and deposited on inner shallow-water platforms at the edge of the continental shelf. The results as well demonstrated these oolitic limestones are species different from the limestones exploited in other regions of Portugal.

Nevertheless, according to the classification made by Carvalho et al. [4][6] and comparing the present limestone exploit regions with the geological map [57], the five investigated quarries (Pidiogo, Valinho do Rei, Reguengo do Fetal, Cabeço do Roxo, Outeiro de Sebastião) are either inside, on the edge of or nearby the MCE region, which is also a Jurassic limestone massif. Actually, Reguengo do Fetal fault was once mentioned in an article by Carvalho et al. in recent years [81] as one of the outcrops parallel to the western limit of the São Mamede Plateau, which belongs to the Pé da Pedreira Member in MCE. It was reported that the limestone is cream coloured and homogenous fine-grained in the northernmost region of Reguengo do Fetal, thus it is valued as a potential area that suits for producing large lithologically homogeneous blocks for ornamental purpose [81]. Therefore, although the other four quarries have not yet been officially included in the MCE [4] [5] [6] [81], the possibility of them being in the same massif and sedimented from similar seawater 20 million years ago is likely high. Additionally, the highly aligned ratios of Mg/Ca, Cl/S and N,K/Cl obtained by XRF in these investigated limestones from quarries and monastery support this hypothesis.

XRD and TGA showed a high content of calcite (> 97 wt%) and a small amount of quartz (≤ 1 wt%). Furthermore, to correlate each quarry with the different sections of the monastery from where samples were collected, a Ca-Sr correlation chart was developed based on the ED-XRF result, suggesting that the monastery baluster was made of stone from the Valinho do Rei or Reguengo do Fetal quarries, while part of the church railing, the north-aisle eaves arch and Royal Cloister were built using stones from the Pidiogo or Cabeço do Roxo quarries. To precisely distinguish the limestones' provenance, inductively coupled plasma-mass spectroscopy (ICP-MS) analyses can be conducted to obtain minor and trace element data on samples from both the monastery and the quarries identified in this study to further confirm the results [82]. These

analytical results confirm the quarry-source attribution for the Batalha building materials found in the historical documents of the Batalha Monastery. For possible conservation and restoration in the future, this research can provide a reference for the selection of stones in order to obtain equivalent physicochemical and mechanical properties to maintain the consistency and integrity of the historical monument.

Chapter 2

Surface orange patinas on the limestone of the Batalha Monastery

Part of the work in this chapter has been previously published in [85]

2.1 Introduction

As mentioned in chapter 1, the monastery located in the small town of Batalha in Central Portugal was built and restored using Jurassic oolitic limestones extracted from several quarries in the region surrounding the monument [44][1]. Although originally white in colour, the monastery limestone is now extensively covered with orange patinas which can be seen on the surface of facades, ornaments, columns and walls (Figure 2.1). Few previous studies in the literature addressed the problem of the nature and origin of these coloured patinas. Rattazzi and co-workers examined two statues stored in the monastery museum showing orange patinas at their surface [86]: the external orange layers were found to show a rather homogeneous texture with traces of gypsum and clay minerals with FTIR analysis showing bands of Al-silicates and iron oxides, interpreted as Earth of Sienna natural and Red Ochre pigments. Aires-Barros et al. investigated the original 15th century Saint Matthew statue and the external walls of the main façade [87]: the statue showed the presence of calcite with minor nitrate, silicate and organic products like benzoic acid, while on the external walls the orange patinas were found to be predominantly composed by calcium oxalates such as whewellite ($CaC_2O_4.H_2O$) with minor weddellite ($CaC_2O_4.2H_2O$), together with hydroxyapatite ($Ca_5(PO_4)_3(OH)$), halloysite and nitrates.

Figure 2.1. Facade and ornaments with orange patina at the Imperfect Chapel, Batalha Monastery

These authors interpreted these patinas on the Batalha limestone surface as representing what conservators called “scialbatura”: a superficial film often found as a surface coating on calcareous Greek and Roman monuments in urban areas, displaying colours ranging from yellow, brown, pink to red and often associated with pitting phenomena [88]. In the late 1980’s, researchers demonstrated that the principal components of the “scialbatura” were Ca-oxalates (mainly weddellite and whewellite), iron oxides (ochres), calcite from the underlying marble substrate, quartz and feldspars as a result of dry deposition of windborne soil dust, and gypsum originated from the sulphation reaction between atmospheric SO_2 in gas and liquid phase (derived from

fossil fuel, oil and coal burning processes) and the calcitic substrate [89]. In fact, the origin of oxalate minerals found on calcitic stone surfaces in urban environments has been the subject of intense debate for decades with researchers claiming as being due to different chemical and biogenic processes, namely: a) oxalate mineral precipitation associated with chemical attack on calcite-rich substrates of oxalic acid due to metabolic activity of encrusting epilithic lichens [90][91][92]; b) non-bio-mediated chemical reactions between the calcareous stone substrate and a number of natural and manmade organic pollutants found in the urban atmosphere from volcanic activity and industrial production activities [93], and/or vehicle exhaust emissions [94]; and c) organic compounds used in past decorative or protective treatments and responsible for oxalate formation, such as calcium caseinate, egg, milk, etc. [88][95], "Scialbatura" patinas has been also considered to represent intentionally added "sacrificial" coating for the monuments eventually leading, though, to further stone decay [96]. In other studies, Fassina [97] considered lime as being the main component of the traditional "scialbatura", with, in addition, titanium oxide detected in the yellow-pink layer. The yellow colour was interpreted as related to the presence of fluorite probably formed during the superficial consolidation using fluorosilicate treatments or alternatively to acid cleaning interventions.

Nearly 15 years have passed since the last research was carried out on this topic. As part of the research carried out in this thesis, two fragments from the Batalha Monastery – an ornament section and a window tracery section, as well the patina powders from the monastery wall have been investigated. This study aimed to determine the composition of the orange layers present at their surface, make a comparative study between each other and with previous research. Another aim was to assess the possible interactions between the oolitic limestone substrate, the orange surface patinas and the urban environment surrounding the Monastery.

2.2 Methods and Materials

2.2.1. Sampling

By special permission of the Direção-Geral do Patrimonio Cultural and the Mosteiro da Batalha authorities, samples were collected with a scalpel from sections of the monastery external walls and facades where orange colour alterations were particularly severe (Figure 2.2). In Figure 2.2, photos in a), b), c) and d) show orange patinas with different colour shades, e) is the same window frame as shown in d), but the area without distinct orange colour, f) is the archway with black patina.

In addition, two ornamental fragments from the monastery storage were also sampled: one was an ornament from the west portal of the church - “S-116” (Figure 2.3) dating from the 15th century, the other was an ornament from a window tracery in the Royal Cloister (Figure 2.4). These samples were both located outdoor and occasionally exposed to the sun and rain.

For the ornamental fragments, complying with the principle of non-destructive detection, the following analytical methods were used.

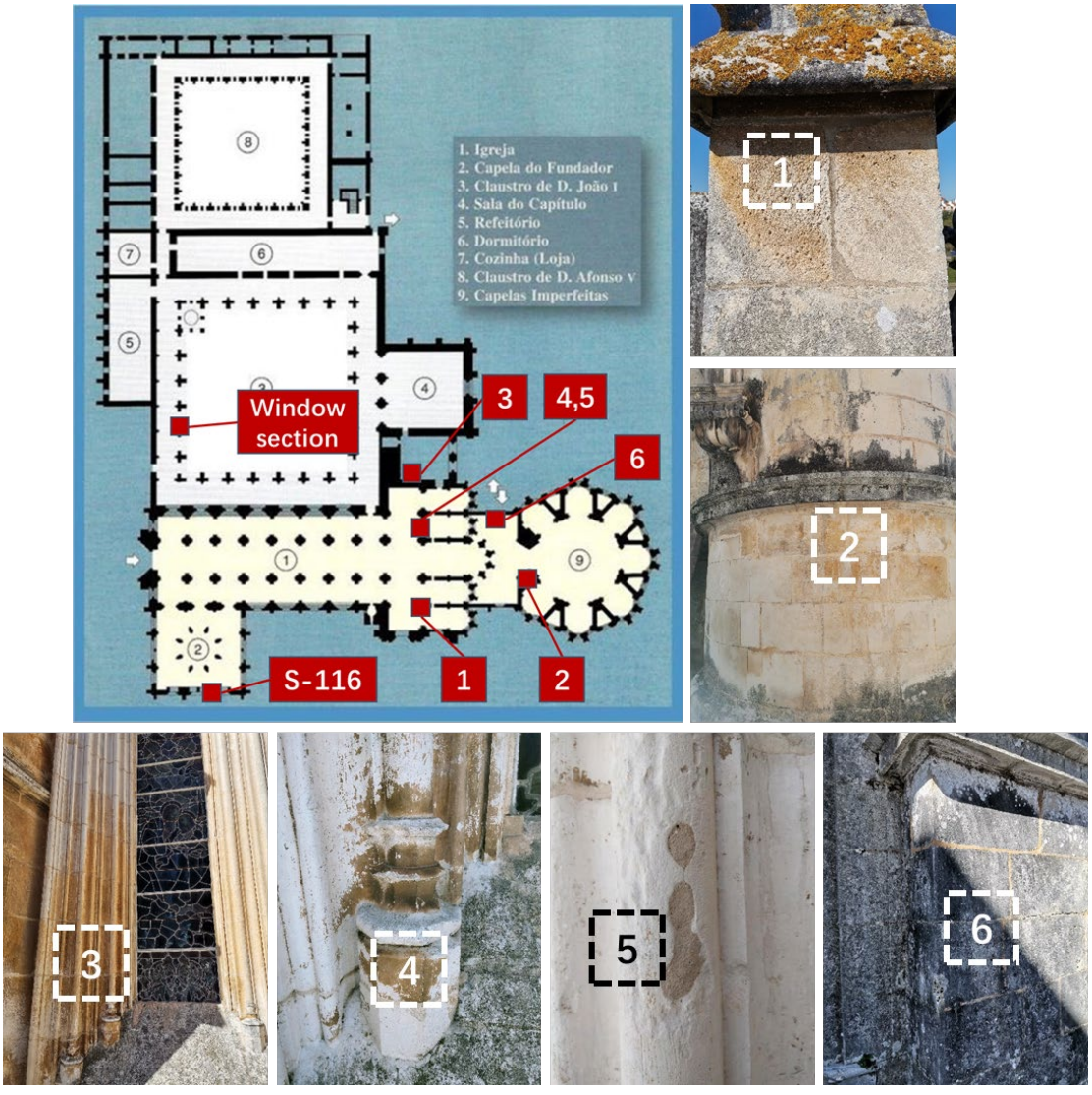

Figure 2.2. Locations in Batalha Monastery where samples were collected: 1). external wall on the roof, top floor; 2). big column on the imperfect chapel, second floor; 3). window frame of the church (bright saturated orange), second floor; 4). window frame from the church (dark brown orange) second floor; 5). window frame from the church (white), second floor; 6). archway on the imperfect chapel covered by black crust, second floor.

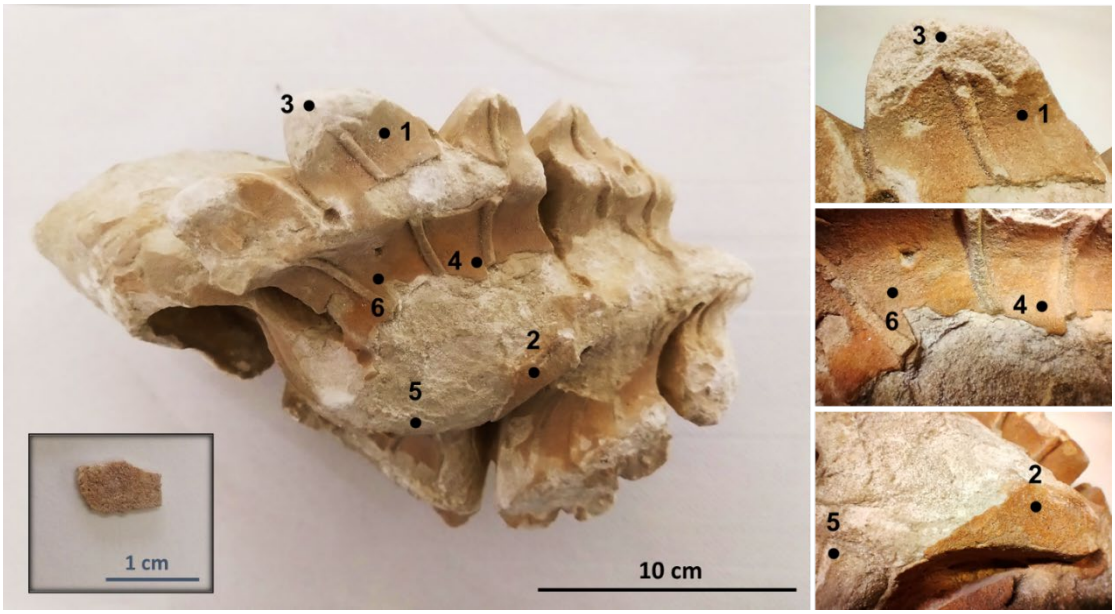

Figure 2.3. Ornament “S-116” and the peeled off surface fragment

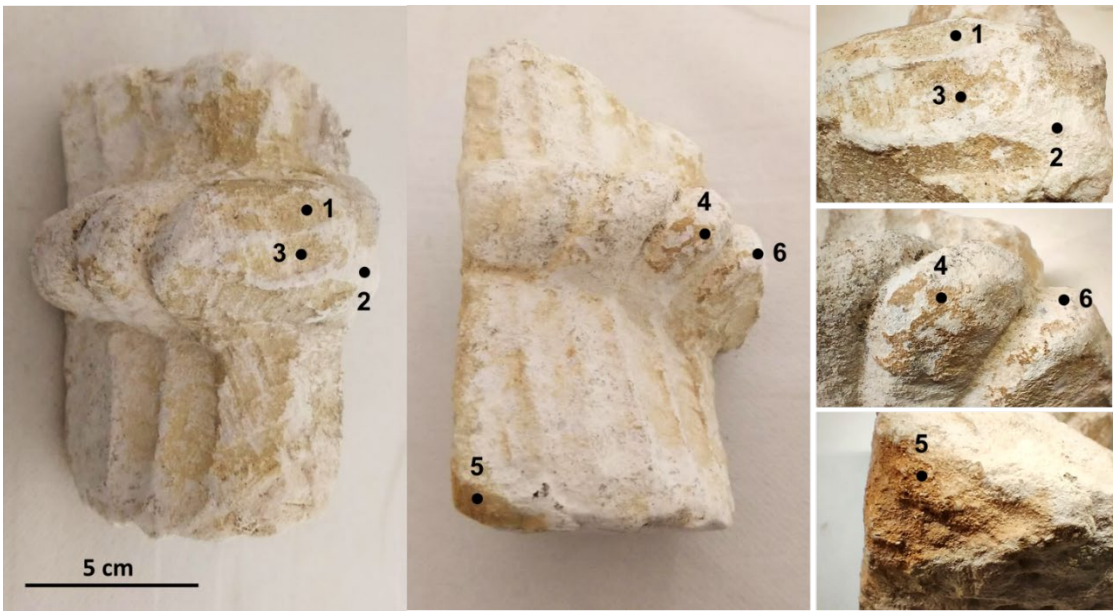

Figure 2.4. Window tracery piece from the Royal Cloister of the Monastery

2.2.2 Colour evaluation

Datacolour CHECK II PLUS Spectrophotometer was used to determine the colour of the patina, by selecting the CIELabCH system, the colour evaluation was illustrated as *L*, *a*, *b*, *C*, *H* (see Figure 2.5). L^* represents the lightness, the value of which is 100 for white and 0 for black; a^* describes the axis of green (-*a**) to red (+*a**), and b goes

from blue (-*b**) to yellow (+*b**). *H** (hue) is the colour tone, while *C** (chroma) is the saturation of a colour.

By comparing the appearance of the samples with the Munsell colour chart and taking *L**, *a**, *b** values as references, colour number that is most similar to the presented patinas is selected.

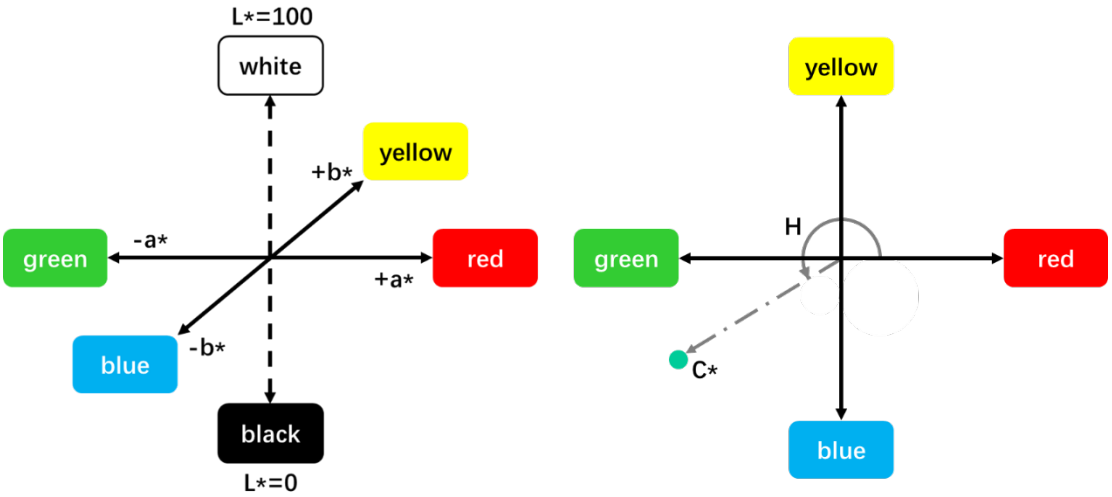

Figure 2.5. Illustration of index in CIELabCH system.

2.2.3 Optical Microscope

Samples were observed under LEICA M205C Stereo Microscope (Leica, Wetzlar, Germany). A peeled-off fragment of sample S-116 was consolidated with resin and polished, for the observation of the cross-section.

2.2.4 X-ray micro-diffractometry (µ-XRD)

Multiple points on the orange layer and the substrate of the samples (Figure 2.3 and Figure 2.4) were characterized by µ-X-ray diffraction using a commercial Bruker AXS D8 Discover diffractometer with Cu Ka radiation, Lynxeye detector, interval 3–70° 2µ, and step of 0.028/s. DIFFRAC.SUITE EVA and Highscore Plus software were used to identify the mineralogical composition and to perform a semi-quantification by the RIR method [98].

2.2.5 Variable-pressure scanning electron microscopy coupled with energy dispersive spectrometry (VP-SEM + EDS).

Scanning electron microscopy coupled with energy dispersive X-ray spectrometry was carried out using a Hitachi S3700N (Tokyo, Japan) SEM coupled to a Bruker

(Karlsruhe, Germany) XFlash 5010 SSD Detector system [99]. The samples were characterized at a chamber pressure of 40 Pa, without any sample preparation, with an accelerating voltage of 20 kV, using a working distance 10 mm and a BSEM detector.

2.3 Results and Discussion

2.3.1 Mineral characterization of the coloured patina samples from monastery outdoor areas

The μXRD results of the samples collected from walls are shown in Figure 2.6, with the semi-quantification of each mineral is reported in Table 2.1. From the results, it can be seen that the composition and relative mineral concentration in region 1 (Figure 2.2 a) (stone wall on the monastery roof) and region 2 (Figure 2.2 b) (stone column on the imperfect chapel) were similar: the content of calcite were between one third to a half with a minor content of quartz; around one fifth of gypsum, which is a typical product of the reaction between carbonate stone and acid rain; around 10% of weddellite and a quarter of whewellite, although region 2 had slightly more calcium oxalate and less calcite than region 1.

In region 3 and region 4 (Figure 2.2 c and d, correspondingly), which are the window frames on the church, the calcite amount was reduced to only ~ 20%, while the calcium oxalates reached a total amount of 63%~75%; worthy of note, the major difference between the composition of region 4 and region 3 was the gypsum, region 4 had higher gypsum quantity (16%) than the 5% of region 3, that might be the factor from which darker orange colour was originated. Region 5 was the white part of the same church window frame, in which only calcite and small amount of weddellite were detected. Combining with the appearance shown in Figure 2.2 e, it can be deducted the window frame was painted with lime. This could be the reason why the window frame showed higher quantity of calcium oxalates transformed from calcite than the stone pieces – the porosity of calcium carbonate obtained from lime paste can reach up to 65% [100], on contrast, porosity of the limestones consisting the Batalha Monastery were 1.1% ~ 16.9% [44]. The open pores would facilitate the reaction between calcite and the environment.

No gypsum or oxalates in the black-coloured region 6, however, 3% of potassium sulphate was detected in its patina powders, which could be possibly related with the black crust on this area. Cyanobacteria and cyanophilous lichens were proved to be one origin bringing about the grey and black colours on limestone monuments [101], and K_2SO_4 is a typical fertilizer promoting plant growth which could be applied in the vineyards and farms surrounding the Batalha Monastery (Figure 1.2). Inorganic

mineral particles were considered to be nutrient source for microorganisms, the potassium and sulphate ions as well as sunlight and high temperature were found to be associated with the increasing biovolume of algae and cyanobacteria communities [102]. Seen from Figure 2.2 f, this sampling area was also directly exposed to sun. Therefore, the agricultural industry in conjunction with sunlight, led to abundant microbial colonization on region 6 and thus ends in such black patina.

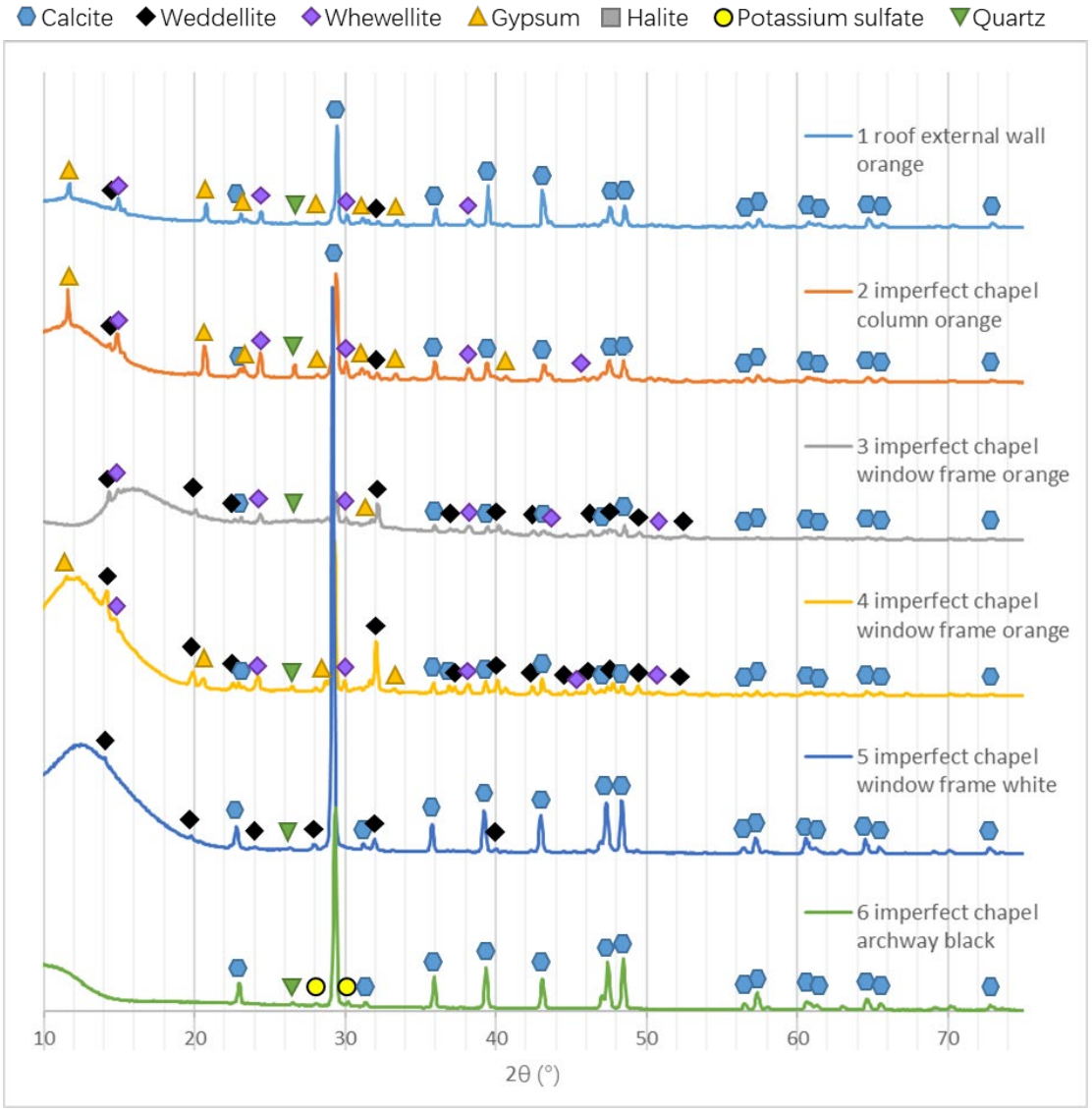

Figure 2.6. XRD results of the powders from the Batalha Monastery external walls.

Table 2.1. Qualitative and semi-quantitative list of minerals and compounds in the powders from the Batalha Monastery walls.

	Region 1	Region 2	Region 3	Region 4	Region 5	Region 6

Appearance **Composition**	orange stone wall	orange stone column	orange window frame	dark orange window frame	white window frame	black archway
Calcite ($CaCO_3$)	46%	35%	18%	21%	81%	95%
Gypsum ($CaSO_4•2H_2O$)	19%	20%	5%	16%	-	-
Quartz (SiO_2)	1%	5%	2%	1%	-	2%
Weddellite ($CaC_2O_4·2H_2O$)	8%	11%	39%	40%	19%	-
Whewellite ($CaC_2O_4·H_2O$)	26%	28%	36%	23%	-	-
Potassium Sulphate (K_2SO_4)	-	-	-	-	-	3%

2.3.2 Colour evaluation of the two artefact fragments from the monastery museum

The photographs of the sample S-116 and window tracery piece are presented in Figure 2.3 and Figure 2.4, respectively. Microscopy was performed on these two samples and the pictures are shown in Figure 2.7. It can be seen that the orange colour of the patina on S-116 is more saturated than that of window tracery sample. The patina on the window tracery surface is unevenly distributed and its colour also shows variegation over the area (Figure 2.7 b). On the contrary, the patina on the ornament S-116 is much more homogenous, the colour is consistent over the patina covered region (Figure 2.7 a). Cross-section observation revealed that the peeled-off fragment consists of a 0.1~0.2 mm orange layer and 1~1.2 mm oolitic limestone substrate, and the fragment has thickness of ~1.3 mm (Figure 2.7 c), implying that the detachment of this coating happens under the limestone surface.

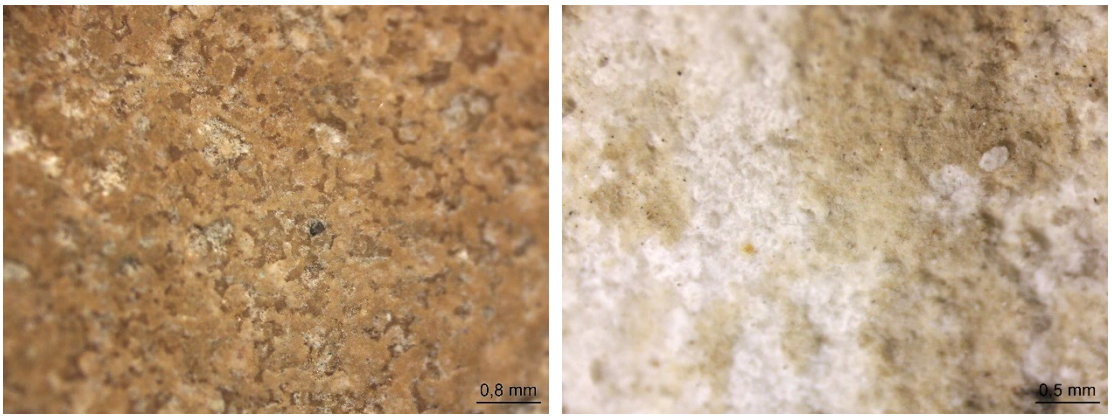

a b

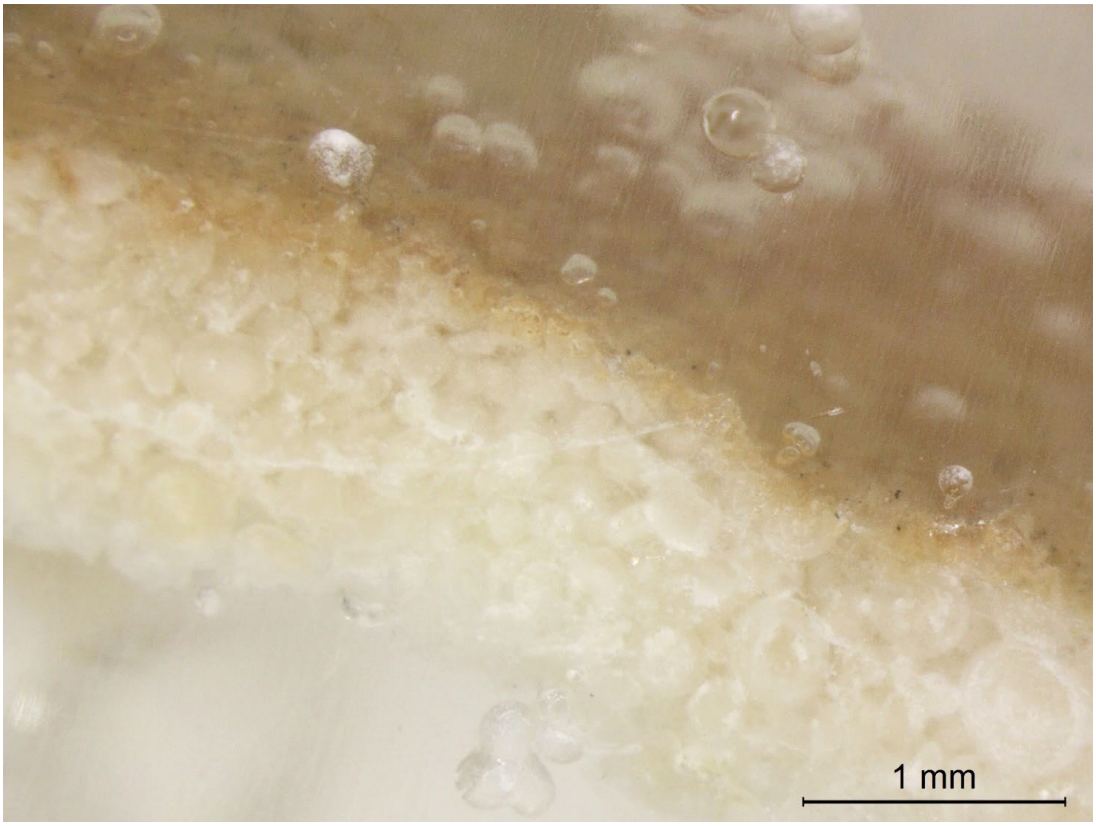

c

Figure 2.7. Optical microscope photos of a. sample S-116 surface; b. the window tracery sample surface; c. cross-section of the peeled-off fragment from sample S-116.

The colour evaluation of sample S-116's patina is *L**: 68.63, *a**: 9.66, *b**: 15.67, *C**: 16.56, *H**: 66.04. MUNSELL 2.5YR/6/6 is very close to this colour. While the patina on the cloister window tracery is detected as *L**: 85.24, *a**: 3.97, *b**: 15.46, *C**: 15.96, *H**: 75.58, which is close to MUNSELL 5YR/8/6.

2.3.3 Mineral and chemical characterization of the patina on ornament "S-116"

μ-X-ray diffraction patterns were acquired on six points of the ornament "S-116" and a peeled off fragment, as shown in Figure 2.3. Points 1, 2, 4 and 6 were acquired on the orange surface patinas whereas Points 3 and 5 were acquired on the substrate where the orange surface had already peeled off with the limestone substrate showing extensive decay. The XRD pattern and peaks are presented in Figure 2.8, and a semi-quantitative evaluation is given in Table 2.2.

In both samples, the stone substrate is an oolitic limestone consisting mainly of calcite and quartz [1]: accordingly, peaks of both minerals are seen at all points

analysed. A considerable amount of gypsum can be detected at points 1, 2, 4, 6 and in the detached fragment, in areas corresponding to the orange surface, while at points 3 and 5 where the coating is completely removed, gypsum is absent. Halite was present in all analysed spots, with its content being significantly higher at points 3 and 5, indicating that halite was concentrated on the substrate surface underneath the orange layer. Feldspar peaks were present particularly at point 1, confirming the presence of soil dust deposition in this area. A minor amount of hematite was detected in all orange patinas which could indicate the presence of red ochre pigment or "Terra Rosa" like material.

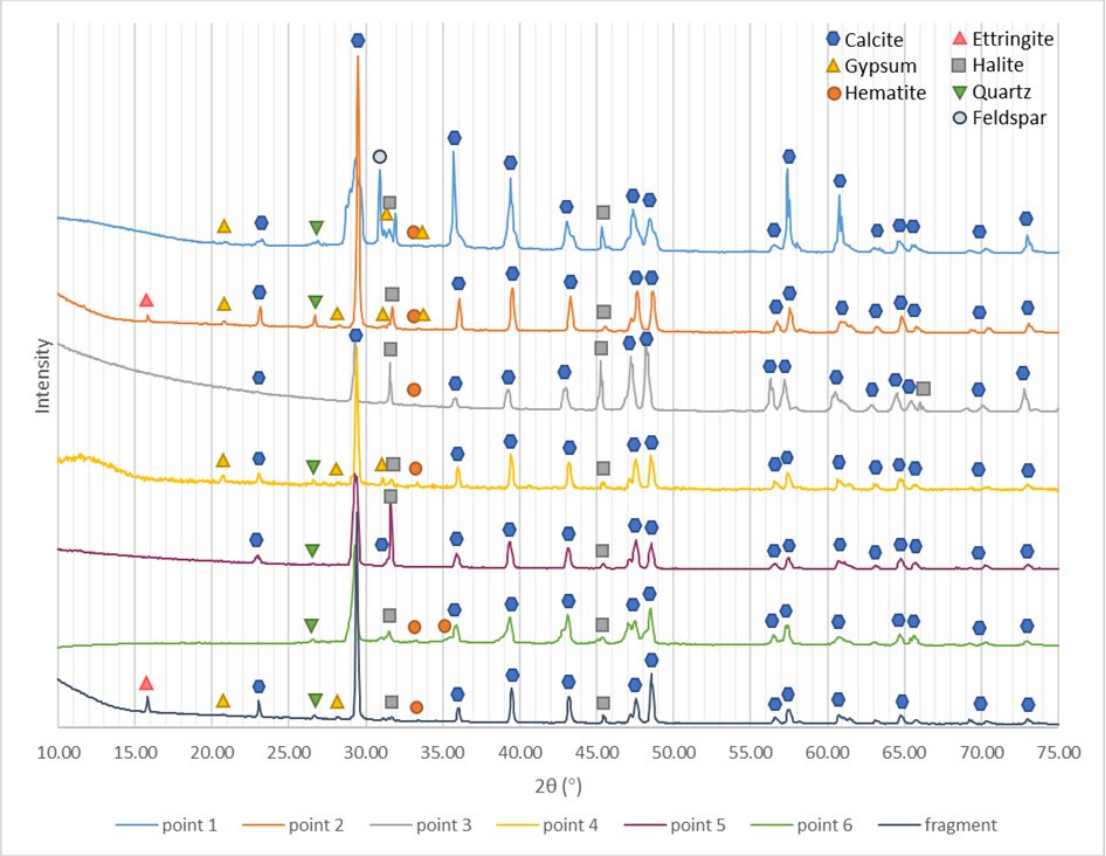

Figure 2.8. XRD results of multiple points on ornament "S-116" and the peeled-off fragment

The minor presence of ettringite peaks in the XRD results is somewhat intriguing. Ettringite [$Ca_6Al_2(SO_4)_3(OH)_{12}\cdot 26H_2O$] is commonly found in modern Portland cement concrete and supplementary cementitious materials where it can occur as primary ettringite, i.e. intentionally added and homogeneously distributed within the Portland cement in order to improve the quality of the concrete with regards to its stiffness. Ettringite and gypsum may also represent the results of sulphate attack: calcium aluminate hydrates and calcium silicate hydrates mixed with lime, can react

with water and gypsum or other sulphate salts, to produce ettringite [$Ca_6Al_2(SO_4)_3(OH)_{12}\cdot 26H_2O$] and thaumasite [$Ca_3Si(OH)_6(CO_3)(SO_4)\cdot 12H_2O$] [103]. The application of cement-based mortar in the Batalha monastery during past restoration interventions [46] could therefore explain the presence of ettringite on the ornament surface.

Table 2.2. Qualitative and semi-quantitative list of minerals and compounds detected on the ornament "S-116" surface

	Fragment	**Point 1**	**Point 2**	**Point 3**	**Point 4**	**Point 5**	**Point 6**
Appearance Composition	**Orange surface**	**Orange surface with dust**	**Orange surface**	**Weathered white substrate**	**Orange surface**	**Weathered white substrate**	**Orange surface**
Calcite ($CaCO_3$)	81%	40%	74%	70%	73%	72%	68%
Gypsum ($CaSO_4\bullet 2H_2O$)	7%	20%	8%	-	19%	-	9%
Quartz (SiO_2)	2%	4%	5%	7%	3%	7%	6%
Hematite (Fe_2O_3)	1%	5%	2%	2%	3%	-	14%
Halite (NaCl)	1%	5%	4%	21%	2%	21%	3%
Ettringite	8%	-	7%	-	-	-	-
Feldspar ($KAlSi_3O_8$)	-	26%	-	-	-	-	-

The peeled-off fragment was observed under the VP-SEM+EDS: results are shown in Figure 2.9. There is a correlation between the distribution of sodium and chloride, confirming the presence of halite (NaCl) grains. Potassium (K), aluminum (Al) and silicon (Si) peaks pointing to the presence of quartz, feldspar and clay minerals probably as soil dust. The peak of calcium (Ca) is weak where the NaCl and feldspar / soil dust / clay grains are present, which means halite was precipitated and aluminosilicates were deposited subsequently on the top of the limestone substrate. This could also be seen from SEM images, the halite (up left) and feldspar (down central) show a well-formed crystalline habit with relatively large dimension grains (>50 μm), in contrast with the poorly crystallized gypsum grains.

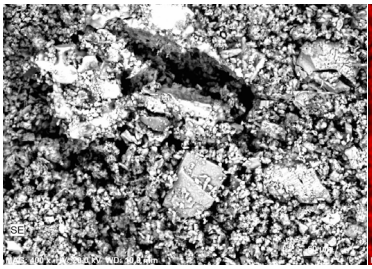

BSE

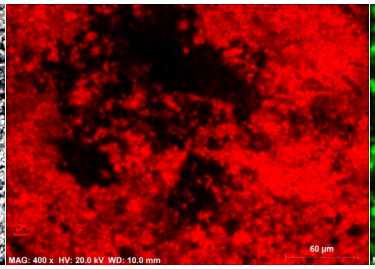

Ca

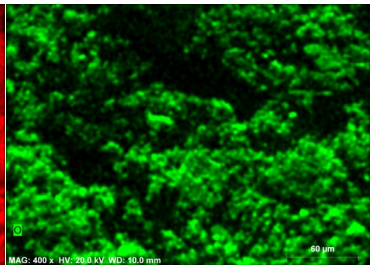

O

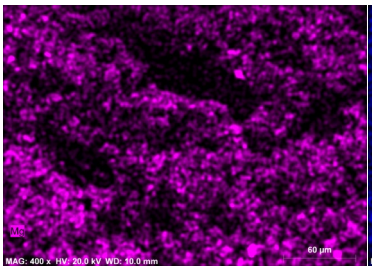

Mg

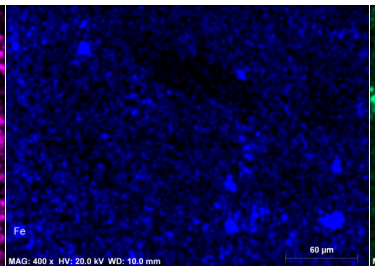

Fe

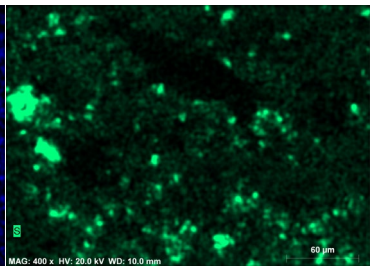

S

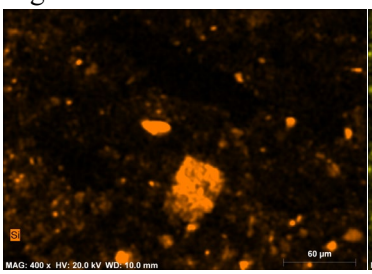

Si

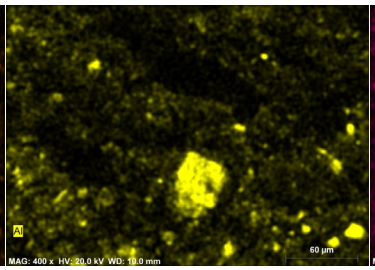

Al

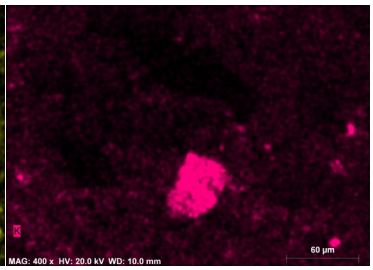

K

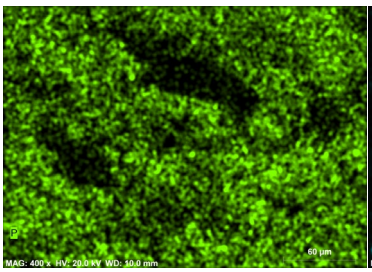

P

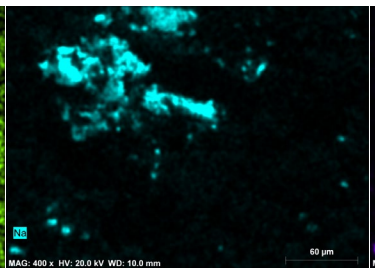

Na

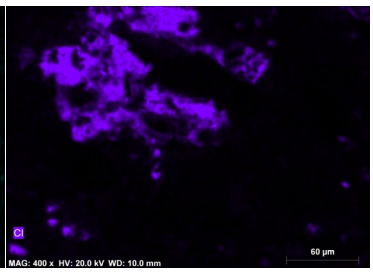

Cl

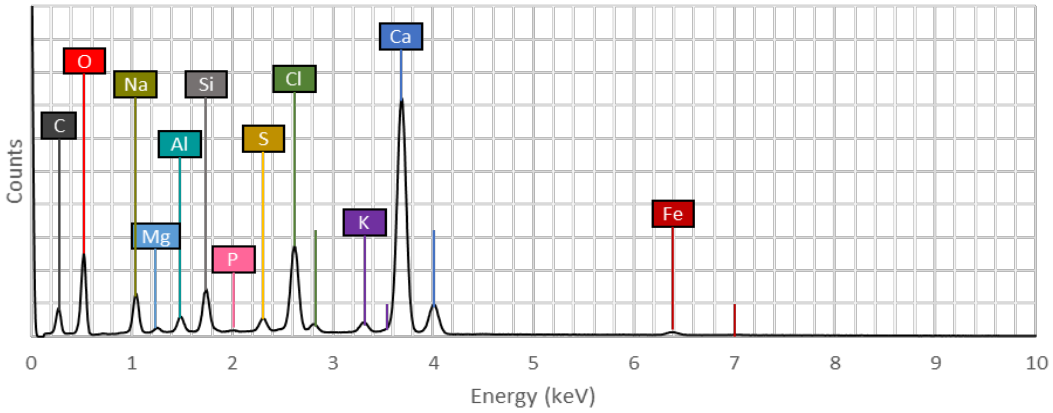

Figure 2.9. SEM-EDS element mapping of ornament “S-116” fragment

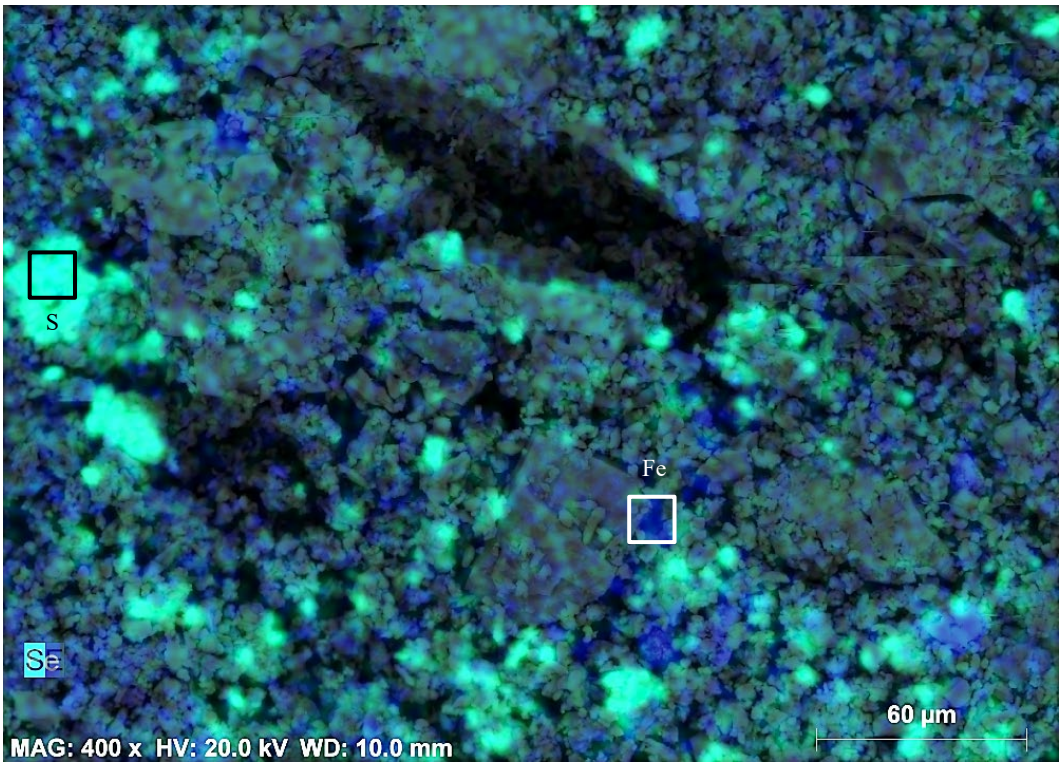

Figure 2.10. Overlapped element map of Fe (blue) and S (neon green) with the SE morphology image.

The distribution of iron (Fe) was homogenous over the whole analysed area, supporting the interpretation of a pigment surface application, although hematite grains are also present as an accessory mineral in the original limestone. The presence of sulphur (S) can mainly be ascribed to the presence of gypsum ($CaSO_4 \cdot 2H_2O$); its distribution again is rather homogeneous and some aggregated gypsum mineral grains

can be seen. By comparing the distribution of Fe and S (Figure 2.10) in the EDS map, it can be seen that hematite was likely to be mixed and applied together with gypsum in the uppermost layer. This hypothesis can be supported by the recorded use of red and yellow ochre: in ancient Macedonian paintings, one of the main means of using ochre was to mix them with lime to produce tint plasters which were then applied to the surface of monuments [104]. Gypsum plaster might have been applied in the lime to achieve faster setting time. Therefore, the colour on the ornament "S-116" surface could be by reason of the same procedure. It is noteworthy the presence of phosphorous (P), which was also detected by Lazzarini and Salvatori on the "scialbatura" of Cathedral and church of S.Zeno, Verona [88], and interpreted as an artificial protective coating made with calcium caseinate, which comes either from the phosphoproteins in milk, or from the collagen in animal skin or serine in egg yolk [105].

2.3.4 Window tracery from Batalha Monastery Royal Cloister

The window tracery sample was analyzed only by micro-XRD to prevent causing any damage. Figure 2.11 shows the XRD pattern, and in Table 2 the main minerals are listed together with their semi-quantitative evaluation. At point 1, where an orange surface is still visible, abundant calcium oxalate was present including weddellite and whewellite, together with feldspar and hematite. Gypsum was detected where the orange surface was worn-out and detached revealing the underlying white substrate. In these areas, the main composition was calcite with minor amount of gypsum and calcium oxalate and no detected hematite. Point 3 has a different appearance than point 1, the surface showing a dark orange colour and the texture being loose and powdery in this area, the XRD results revealed calcite, some weddellite, feldspar, and minor hematite. Halite was present at point 3 and absent at points 1 and 2.

Calcium oxalate is itself colourless, but when mixed with organic and inorganic fragments like lichens, fungi and bacteria, or quartz, feldspars mineral grains and iron oxides from soil dust, the patina may acquire a yellowish-brown hue [106]. Thus, the colour of this window tracery could possibly originate from calcium oxalate mixed with other mineral grains such as soil dust. The stone surface oxalates were generally considered to be the result of lichen excreted oxalic acid that reacts with the calcium carbonate substrate [90]. However, recent studies have reported that various bacteria such as, for instance, Pseudomonas fluorescens, Burkholderia, Bacillus and C. jiangningensis JN53, etc. can also produce oxalic acid even without the presence of lichen microbiomes, [107][108][109]. In fact, Bacillus (phylum Firmicutes) and Burkholderia (phylum Beta-Proteobacteria) were found in the Batalha Monastery bio-deteriorated stone and the atmospheric environment in this study (see Chapter 3) [110]. Thus, although no lichen crust was present on the Window tracery sample, the

possibility of bacteria producing oxalic acid and causing mineral weathering cannot be excluded.

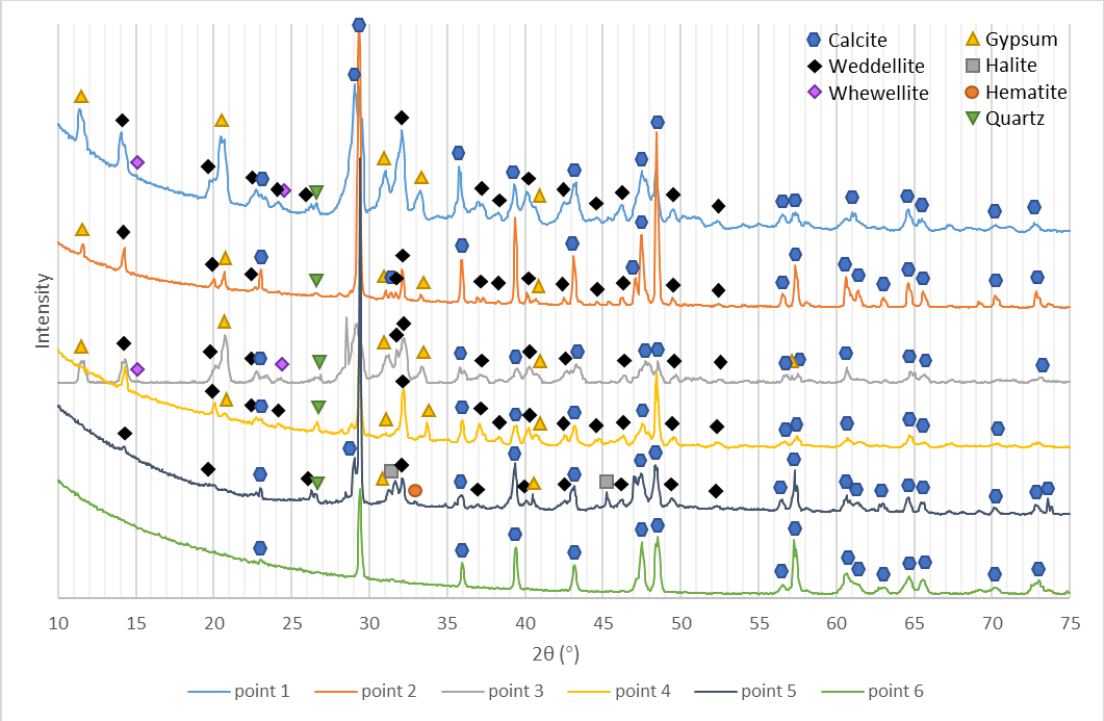

Figure 2.11. XRD results of multiple points on the Royal Cloister window tracery

Calcium oxalates may also be deriving from vehicular exhaust emissions by incomplete combustion of aromatic hydrocarbons (such as benzene, toluene, naphthalene) in the engines, generating diacids including oxalic acid, cis-unsaturated acids and aromatic acids [94]. Due to the polar nature of these dicarboxylic acids, they preferentially adsorb water in environments characterized by high values of relative humidity and could react with calcareous stone to form calcium oxalates. As a matter of fact, the Portuguese national highway IC2 runs through Batalha only 50 meters west of the monastery, there are over 14000 cars passing daily in front of its west façade and the traffic noise has been damaging the glasses and stones [111]. With such a huge volume of traffic, not only the sound pollution, but also the atmospheric vehicular pollution could not be ruled out as an accessory cause for the development of oxalate patinas on the limestone surfaces of the monastery. The benzoic acid found by Aires-Barros et al [87] on the external walls of this monument, makes this hypothesis more plausible.

Table 2.3. Qualitative and semi-quantitative list of minerals and compounds detected on the window tracery

	Point 1	Point 2	Point 3	Point 4	Point 5	Point 6
Appearance **Composition**	**Orange surface**	**White substrate**	**Orange surface**	**Orange surface**	**Orange surface loose texture**	**White substrate**
Calcite ($CaCO_3$)	54%	80%	15%	38%	85%	100%
Gypsum ($CaSO_4•2H_2O$)	18%	9%	39%	19%	3%	-
Weddellite ($CaC_2O_4·2H_2O$)	17%	10%	31%	37%	7%	-
Whewellite ($CaC_2O_4·H_2O$)	9%	-	12%	-	-	-
Quartz (SiO_2)	2%	1%	3%	6%	2%	-
Hematite (Fe_2O_3)	-	-	-	-	1%	-
Halite (NaCl)	-	-	-	-	2%	-

2.3.5 Comparison among the samples

Though all named "orange patinas", there are significant differences among the samples investigated. Table 2.4 lists these differences with respect to composition, appearance and decay patterns.

For the monastery external surfaces showing colour alteration, the orange patina was developed on the substrate without causing any delamination or flaking. The chemical composition contains both calcium oxalates and gypsum, no minerals associated with a pigmental function were found. For the ornament "S-116", the orange layer follows the external geometrical shape of the object, for example, the ridging stripes spreading out from the centre, which also was observed on the substrate. In the case of the Royal Cloister window tracery, the orange patina appears to be closely adhering to the limestone substrate as opposed to the visible separate layering observed on "S-116". Moreover, there was an abundant weddellite on the Window tracery surface, which was not found on the sample "S-116".

The decay pattern of the orange layers on the two samples investigated was also distinct. On the ornament "S-116", the surface layer was flaking, on the white substrate under the peeled-off lamination, higher content of halite was detected. This indicates a typical salt decay process: salt solution evaporates and crystallizes at the interface between the coating and the substrate, leading to detachment eventually [112]. In this case, the salt responsible for decay is mainly halite (NaCl), its precipitation leading to salt decay in the monastery may probably derive from ground-moisture capillary rise

processes. Considering the Royal Cloister window tracery, the patina was lost preferentially at the ridges and bulges but was more preserved in flat areas where marks of scratches can also be seen. Three possible explanations can be suggested: a) the evaporation rate of salt solutions is higher at the geometrically protruded parts due to a larger specific surface area, resulting in higher crystallization pressure inside the stone pores and more severe decay [113]; b) protruded areas endure more mechanical abrasion from rain, wind, sands, and human activities, thus accelerating the decay processes and associated loss of material; or c) the orange patina was originally formed irregularly on the limestone substrate. For the external walls with orange appearance, generally, the limestone substrate showed decay such as pitting or holes which could be due to the acid rain attack, however this does not appear to be related with the distribution of the orange patina; it is difficult to illustrate the decay mechanism of the dark orange colour on the window frame painted with lime plaster for the lack of evidence proving whether the patina was formed as it presented or the patina was lost partially due to environmental factors.

Table 2.4. Comparison between the orange patinas on the sample "S-116" and on the Royal Cloister Window tracery

	S-116	**Window tracery**	**External walls**
Composition	Gypsum and hematite, with minor ettringite and aluminosilicates. No calcium oxalates.	Abundant weddellite and whewellite on the surface, gypsum was also detected.	Abundant weddellite and whewellite in the surface powder, gypsum was also detected.
Appearance	The orange layer has an *imprint of shaping,* homogenous in colour and thickness, it shows obvious lamination from the substrate.	The orange patina is *closely adherent* to the limestone substrate, *no visible separate lamination,* the colour is not uniform on the surface.	The orange patina is *closely adherent* to the limestone substrate, *no visible separate lamination,* the colour is not uniform on the surface.
Decay Pattern	Surface layer is *flaking*, a higher content of halite and nitratine were detected from the white substrate under the peeled off lamination, indicating a typical *salt decay* process.	Patina is lost preferentially at the *ridges* and *bulges,* scratches can be seen. It could be due to a higher crystallization pressure of salt solution at protruded parts, or the protrusion endures more natural and artificial mechanical attack.	Patina is inhomogeneous. On the limestone bricks the orange colour is darker on the top and lighter in the bottom; for lime plaster surface, orange colour was more remained on the vertical side, and lost preferably on the horizon stages,

Combining the results obtained, a preliminary sketch diagram (Figure 2.12) was made to illustrate the different characteristics of the two samples investigated.

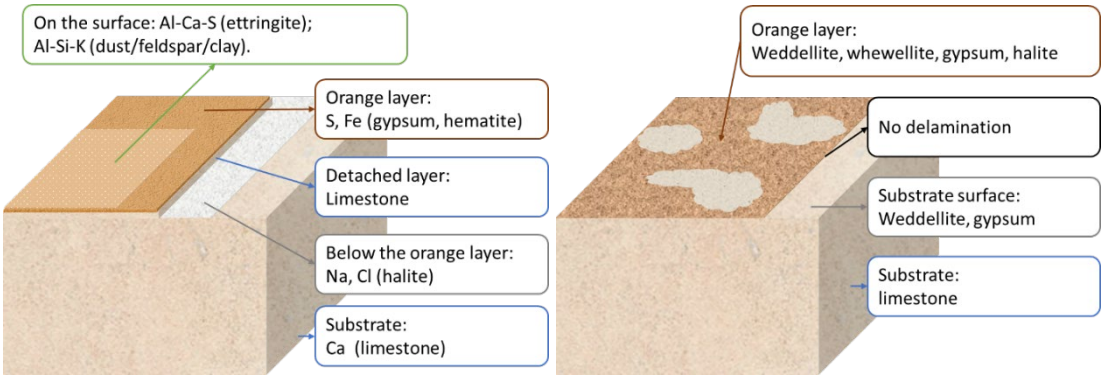

Figure 2.12. Sketch of the sample "S-116" (left) and the Window tracery (right)

2.3.6 Comparison with previous research

Through the above-mentioned results and analysis, it can be concluded that the orange layers on the Royal Cloister Window tracery and the external walls are similar to the findings by Aires-Barros et al [87]. Such patina is compatible with a "scialbatura" nature for its composition, texture and colour, as described by Lazzarini and Salvatori, i.e., an intentionally added protective patina [88]. No titanium oxide and fluorite presence as reported in previous research by Fassina [97]. The results of the present study are in line with the conclusion that the presence of calcium oxalates in this monastery could be linked to either vehicular exhaust emissions [94] or to bacterial activity [107], but not to oxalic production by lichenous colonization and its reaction with the calcite-rich stone surface [89][114].

The orange coating on the ornament "S-116" sample matches the description of that on the original apostle statues from the church doorway [86]. Considering the ornament "S-116" and the apostle statues were both crafted in the 15th century, it is feasible to consider that the same coating procedure was used, despite them being located in different sites of the Batalha Monastery. Although it is commonly believed that in this type of surface layers, the gypsum occurring on calcareous stones is a reaction product of calcareous or silicate stones in a SO_2 polluted urban atmosphere [91], the possibility of artificial gypsum coating cannot be completely excluded [115]. In fact, the homogeneity of the layers and the presence of hematite may support the conclusion of the intentional application of a pigmented plaster.

2.4 Conclusions

In this chapter, a chemical / mineralogical characterization was carried out on orange surface patinas found in external walls and two different limestone artifacts from Batalha Monastery in Portugal. The homogenous and decorative layer on

ornament “S-116” is mainly composed of gypsum and hematite with traces of K-feldspars possibly originating from soil dust deposition and/or mortar joints in the monument. It is highly likely to be applied intentionally, using the same craft procedure as the apostle statues of the monastery. Its delamination is a typical phenomenon of salt decay, for a high concentration of halite was found on the substrate under the exfoliated surface.

The coloured surface of the Royal Cloister Window tracery and the external walls contains abundant calcium oxalate including weddellite and whewellite, gypsum was also detected. The surface colour was not homogeneous on the window tracery piece where erosive episodes led to surface loss, while the reason why that colour on the monastery walls present various shades was undetermined. Based on the above results, this surface layer was compatible with the description of “scialbatura”, as it shows evidence of substrate stone reacting with the environment. This patina was likely generated due to air pollution and bacterial metabolic activities.

Chapter 3

Biodegradation and Microbial Contamination on the Limestone Surfaces of Batalha Monastery

Part of the work in this chapter is published in [110]

3.1 Introduction

The microbial contamination of stone surfaces in buildings and monuments leads to the formation of biofilms which are in turn responsible for physical and chemical bio-deterioration processes that may severely affect the preservation of Cultural Heritage assets in both urban and rural environments. Several types of autotrophic and heterotrophic microorganisms may colonize stone surfaces such as bacteria, fungi, algae, and lichens. Lichens may be described as an association between a fungus, usually an ascomycete (MYCOBIONT) and one or more photosynthetic partners, generally green algae or cyanobacteria (PHOTOBYONT) with the fungus forming a thallus or lichenized stroma that may penetrate deeply within the stone substrate through the action of fungal hyphae [116][117]. In recent studies, with the help of molecular assays, it was revealed that besides the photobiont algae and cyanobacteria, a high diversity of bacteria such as Proteobacteria, Actinobacteria, Acidobacteria, Bacteroidetes and Firmicutes are also associated with the lichen symbiotic system. These bacteria play multiple roles: nutrient supply (especially nitrogen, phosphorus, and sulphur), resistance against biotic and abiotic stress factors, detoxification of metabolites, provision of vitamin B_{12} for photosynthesis, production of hormones to

support fungal and algal growth, and degradation of older parts of the lichen thallus [118]. Lichens are active agents in the biodegradation of minerals in building stone and natural stone. In a research of fungal diversity and distribution on stone surfaces in the old cathedral of Coimbra, both traditional cultivation and modern NGS (Next Generation Sequencing) techniques were used to establish a relationship between the identified fungal populations and different biodeterioration processes active at the surface of the cathedral [119]. A review paper described the microbial agents identified as responsible for stone biodeterioration processes on several famous Portuguese cultural heritage monuments in Lisbon, Coimbra, and Tomar [120]. For instance, the St. Cruz Church in Coimbra was constructed with Ançã limestone and presented various species of algae and phylum cyanobacterium (Gloeocapsa novacekii Komarek & Anagnostidis and kuetzingiana Nageli, *Myxosarcina sp*., *Nostoc sp*., *Phormidium sp*., *Scytonema sp*., *Tolypothrix sp*.) [121]. In the Cathedral of Guarda, which was also built with Ançã limestone, several species of fungi (*Botrytis cinerea, Cladosporium sp., Engyodontium album, Penicillium sp., Trichoderma viride*) were identified [122]. In the Belem Tower and Jeronimos Monastery located in Lisbon and built with Lioz limestone, Phylum Cyanobacteria and several lichens species (*Aspicilia sp., Caloplaca aurantia, Lecanora sp., Squamarina crassa, Thyrea, Verrucaria* and *Xanthoria parietina*) were identified [123][124]. The limestone of the Convent of Christ in Tomar was unspecified; in this site, algae, bacteria, fungi, and lichens were confirmed, but the species were not determined [125]. Methods used for the identification of microbial communities included Optical Microscopy, Scanning Electron Microscopy combined with Energy-Dispersive X-ray Spectroscopy, Transmission Electron Microscopy, X-ray Diffraction Spectroscopy, the identification of bacteria, and molecular biology protocols.

It has been shown that different atmospheric air pollutants present in urban environments may interact with the microbial community in the weathering of building stones: for instance, pioneering bacteria may use hydrocarbon from air pollution as a source of nutrients [126]; a lichenous cover may facilitate the deposition of particulate airborne pollutants on the stone surface [127]; sulphate or non-sulphate soiling layers from urban air pollution may also act as localized sites of intense desegregation of the stone underneath [127]. Previous studies also revealed that air pollution can affect the nature and distribution of bacterial communities in biofilms growing on building stone [128].

Figure 3.1. (**left**) The external wall of Batalha Monastery, covered by dark brown/gray biofilms and crusts; (**right**) Balustrade on the roof of the monastery showing thick biofilms and lichenous crusts.

The Batalha Monastery (Figure 1) is listed as a UNESCO World Heritage Site and is located in central Portugal. The monastery was built using a Middle–Late Jurassic oolitic limestone that was extracted from several ancient quarries located in sites not far from the monument itself: Pidiogo, Valinho do Rei, Carvalhos, Reguengo do Fetal, Cabeço do Roxo, and Outeiro de Sebastião [129]. The outer surfaces of the oolitic limestone in the walls of the monastery show extensive coating by biofilms and lichenous crusts leading to intense biodeterioration and aesthetical disfigurement effects. The aim of the current study was threefold: (a) assess whether microbial colonization and the formation of lichenous crusts is responsible for the decay of the limestone used in the Batalha Monastery: (b) identify the microflora colonizing the limestone surface of the Batalha Monastery, in order to provide a microbial database that could help restorers in the selection of the correct cleaning procedure to be adopted for the conservation of the Monastery; and (c) assess the relative importance of biodeterioration versus anthropogenic air pollution in the limestone weathering in Batalha.

3.2 Methods and Materials

3.2.1 Location and sampling

Samples (Figure 3.2 a and b) were collected from stone façades and roof areas of the Batalha Monastery (GPS latitude 39°39′32″ N, longitude 8°49′30″ W). The

temperature at the site often reaches 30 °C (rarely 40 °C) in summer and minus 3 °C in winter with an average daily humidity of 81%. The maximum solar radiation in summer can reach 30,000 kJ/m^2, while in winter, it averages around 5000 kJ/m^2 (meteorological data from the Instituto Português do Mar e da Atmosfera, monitored in the meterological station in Leiria, Portugal, 13 km from Batalha).

The microbial sampling was carried out on representative areas of the stone materials, including areas showing evidence of weathering and stone decay such as flaking and granular desegregation. Sterile microinvasive (chisel and scalpels) and noninvasive (swabs) tools were used during the sampling under semi-aseptic conditions. Sterile swabs were placed in a suspension of transport MRD medium (Maximum Recovery Diluent) and preserved at 4 °C until utilization.

3.2.2 Air monitoring

An optical particle sizer (Optical Particle Sizer Spectrometer Model 3330, TSI, Min-neapolis, USA) was located outdoor at the roof level of the Batalha Monastery to sam-ple particulate air pollutants. Particle collection campaign was carried out continuously for 1 week starting January 20th and ending January 27th 2020. Sterilized paper filters with pore size 0.45 µm (GN-6 Membrane, 47 mm, White, Gridded, Gamma Irradiated, Pall Coorperation) were used. Then, collected filters (Figure 3.2 c) were stored in a sterile box for microbial characterization and Scanning Electron Microscopy with Energy Disper-sive Spectroscopy (SEM + EDS) observations.

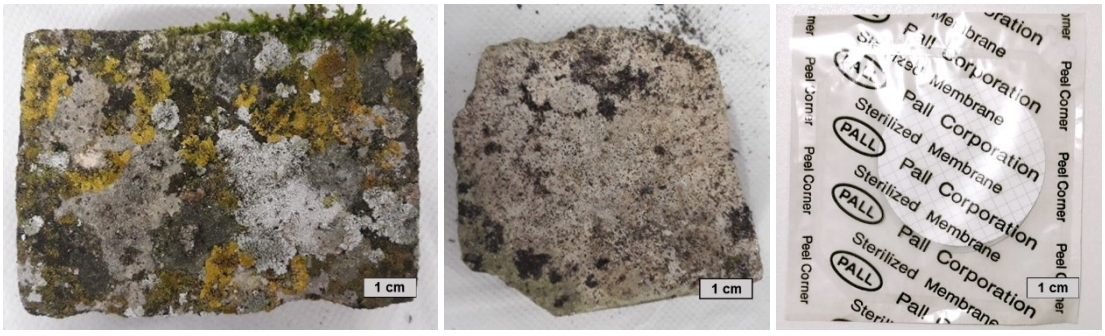

a b c

Figure 3.2. Microbial colonized stone samples from the Batalha Monastery: (a) sample MB-R3; (b) sample P2-5; (c) filter paper from the optical particle sizer.

3.2.3 Molecular Analysis of Bacterial Communities

High-throughput sequencing (HTS) based on 16S rRNA gene analysis was conducted for the identification of bacterial communities present within biofilms on

the limestone surface of the Batalha Monastery and deposited on the optical particle sizer filter.

Microsamples were collected from limestone facades of the monastery, and the metagenomic DNA was extracted using the QIAmp DNA Stool Mini Kit (Qiagen, Limburg, Netherlands) with slight modifications from the manufacturer's instructions [130]. The bacterial communities were characterized by the 16S rRNA V3-V4 region us-ing the Illumina Sequencing platform. The analytical procedure was the same as thor-oughly described by Dias et al. and Rosado el al. [131][132].

3.2.4. Morphology Observation, Mineralogical, and Chemical Characterization of the Bio-Deteriorated Stone

Optical Microscopy (OM)

Samples were observed under LEICA M205C Stereo Microscope (Leica, Wetzlar, Germany), photos were taken by a uEyeUI 149xSE-C industrial camera (IDS, Obsesulm, Germany).

X-Ray Micro-Diffractometry (µ-XRD)

The mineralogical characterization of the stone surface was carried out by µ-X-ray diffraction using a commercial Bruker AXS D8 Discovery diffractometer (Bruker,Karlsruhe, Germany) with the DaVinci design and Cu Ka radiation, Gadds detector, interval 3–708 2µ and step of 0.028/s. The EVA code and Highscore Plus software were used for the identification of the peaks using the PDF-2 International Centre for Diffraction Data (ICDD) mineralogical database.

Low-Vacuum Scanning Electron Microscopy Coupled with Energy-Dispersive Spectrometry (LV-SEM + EDS)

Scanning electron microscopy coupled with energy-dispersive X-ray spectrometry was carried out using a Hitachi S3700N (Tokyo, Japan) SEM coupled to a Bruker (Karlsruhe, Germany) XFlash 5010 SDD Detector system. Operating conditions were as follows: back-scattered imaging detector (BSEM); low-vacuum mode (pre-set pressure of 40 Pa) allowing the observation of non-coated biological samples; accelerating voltage—20 kV; current: 120 mA. For surface observation, a tablet (2 cm × 3 cm × 1 cm) with biofilm was cut from the stone sample and put into the chamber directly. For cross-section investigation, stone tablets were consolidated with resin, cut, and polished before observation.

3.3 Results and discussion

3.3.1 Optical microscope observation

Field photographs from the monastery sampling sites are shown in Figure 3.3. Macroscopical visual examination allowed the identification of the following lichens species: *Aspicilia sp.*, *Caloplaca sp.*, *Lecanora sp.*, *Verrucaria*, *Dirina massiliensis*, and *Xanthoria* [133]. These lichens are also found at other sites in Portugal and in Mediterranean countries such as Italy and Spain [134].

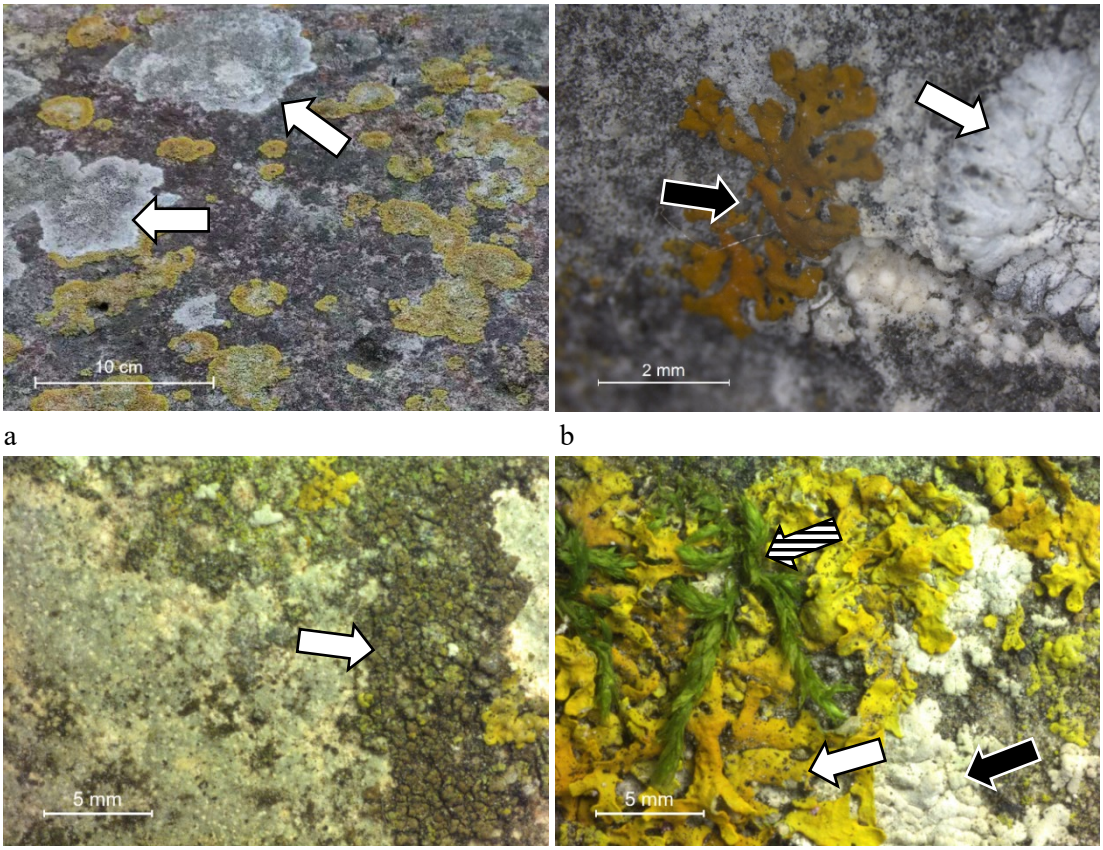

a b c d

Figure 3.3. Batalha Monastery, lichenous crusts on limestone: (**a**) Dirina massiliensis (white arrow); (**b**) Crustose Caloplaca sp. (black arrow) and Lecanora sp. (white arrow); (**c**) Aspicilia sp. (white arrow); (**d**) Foliose Xanthoria (white arrow), Lecanora (black arrow) and higher plant (stripe arrow).

3.3.2 XRD results

Point micro-XRD analyses (Figure 3.4) were performed on three areas characterized macroscopically by different colours, i.e., respectively white, black, and

greenish (the latter possibly suggesting the presence of cyanobacteria, i.e., blue–green algae). Diffractograms corresponding to white and black areas show the presence of Ca-oxalate mineral peaks of weddellite and whewellite, while in green areas, only calcite and quartz of the limestone substrate are detected. The building stone used in the construction of the Batalha Monastery was in fact an oolitic limestone with a mineralogical composition characterized by more than 97% calcite with minor amounts of quartz [129].

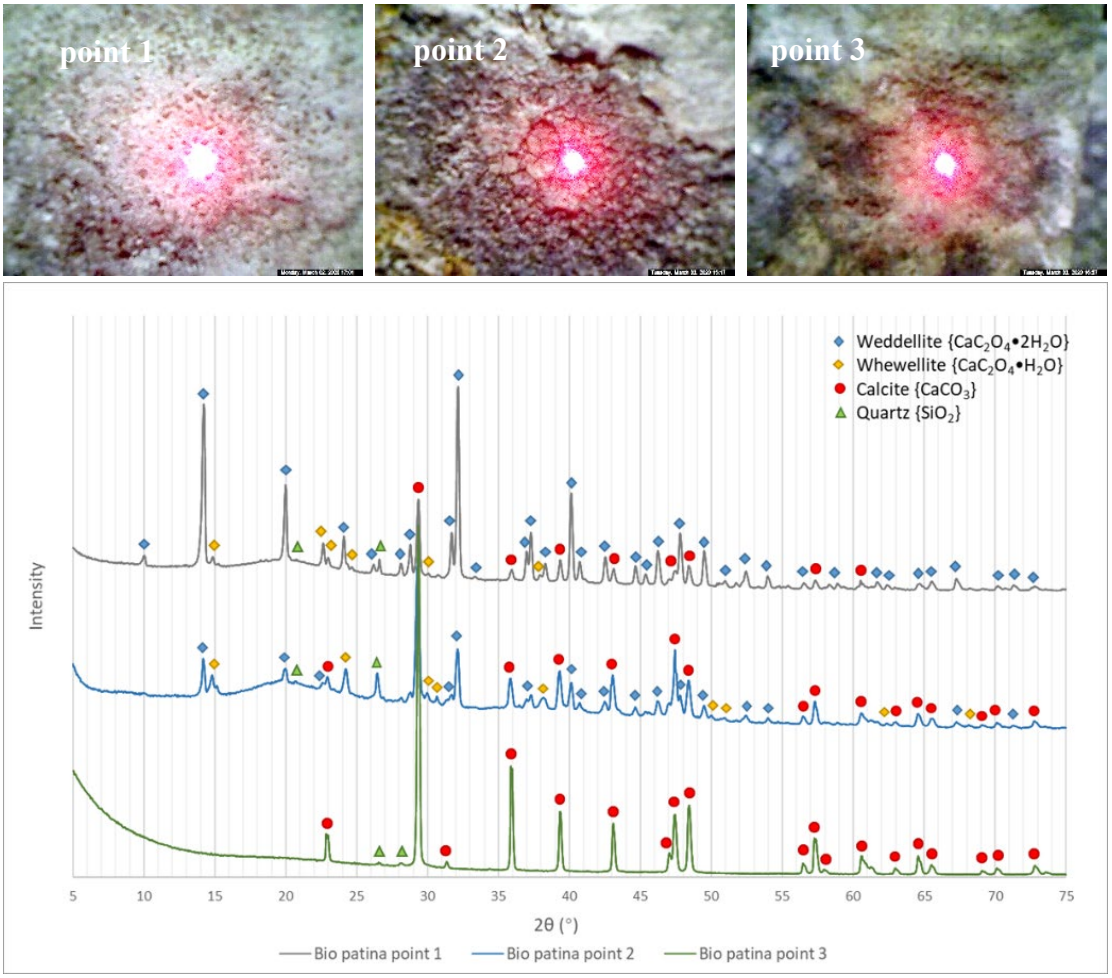

Figure 3.4. XRD result of the bio-colonized stone surface.

It is well known how fungi are able to excrete different organic compounds such as oxalic acid as a result of their metabolic activity, which may react with $CaCO_3$ -rich materials such as limestones, leading to the crystallization of secondary Ca minerals in limestones [135][136]. In this case, the whewellite and weddellite could be a product from the reaction between the limestone substrate and the microflora metabolic products.

3.3.3 SEM-EDS results

In Figure 3.5 SEM imaging of cross-sections of bio-deteriorated stone fragments shows (a) and (b) lichen hyphae mechanically penetrating inside the stone fabric up to a depth of 3 mm; (c) and (d) a close-up of hyphae progression preferentially along limestone oolite grain boundaries leading to the complete detachment and incorporation of stone substrate fragments within the advancing lichenous weathering crust.

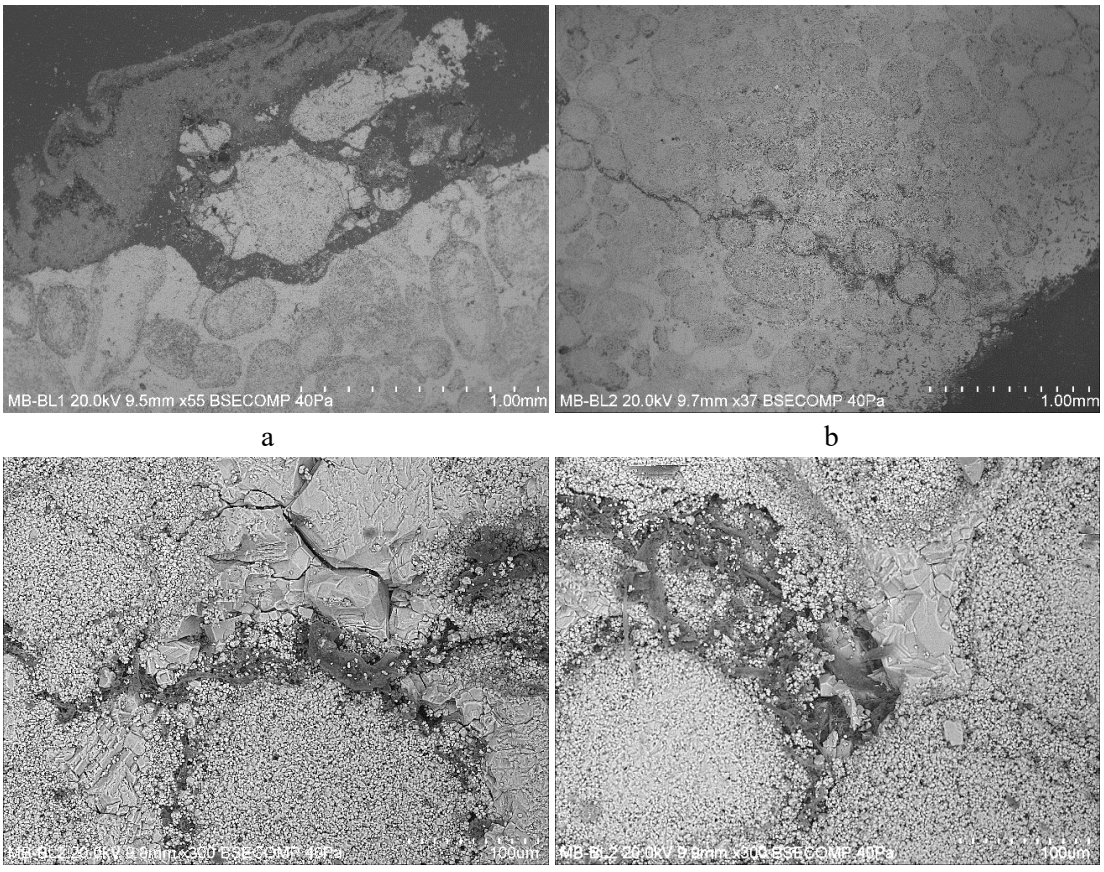

Figure 3.5. Back-scattered imaging detector (BSEM) micrographs of biodeteriorated Batalha oolitic limestone: (**a**) Detached stone fragments incorporated within the growing lichenous weathering crust; (**b**–**d**) Lichen hyphae penetrating deeply inside the limestone fabric using pre-existing intracrystalline cracks and/or porosity within the sparitic cement and leading to the detachment of the oolitic grains.

Figure 3.6 (a) shows an intermediate stage of stone fragmentation with evidence of chemical etching patterns on mineral faces by fungal hyphae exploiting intracrystalline cleavage planes of calcite. Some hyphae were able to desegregate the stone fabric into fragments with grainsize 1–10 μm (black arrow) with granular size 1–10 μm. Figure

3.6 (b) shows a close-up view of fungal hyphae and spores particles disrupting the inner stone microfabric. Figure 3.6 (c) shows an area where the limestone substrate was completely desegregated into micron-size fragments. Several crystals (with dimension around 10 µm) can be seen displaying a tetragonal crystalline habit typical of Ca-oxalates, the interpretation of which is confirmed by EDS elemental analysis (see Annex 3A). Figure 6d shows the re-precipitation of microcrystalline calcite crystals as confirmed by the EDS spectrum showing Ca peaks (Annex 3B). Figure 3.6 (e) shows again the presence of etching patterns (pit size 2–5 µm) on the stone surface. Hyphae here are septate and have a spherical shape. Figure 6f is an epitome of the above-mentioned degradation forms: dissolution cavities, pitting, penetrated hyphae, and oxalate precipitation can all be seen on this part of the stone. The increase in surface roughness and porosity favors adhesion and colonization by microorganisms, which in turn make the stone more prone to mechanical weathering [137].

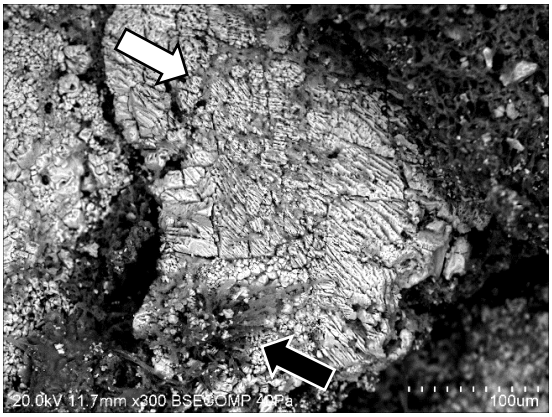

a

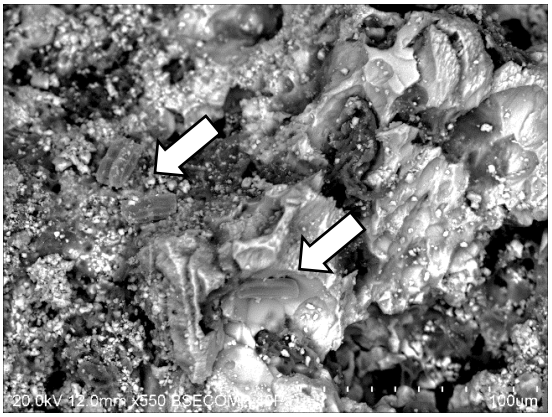

b

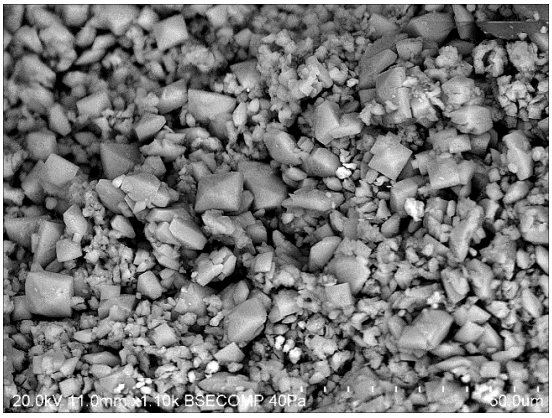

c

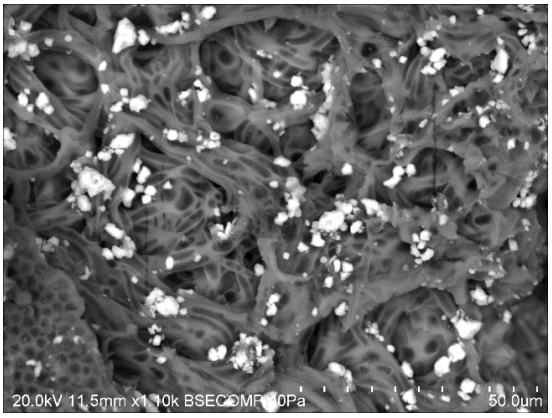

d

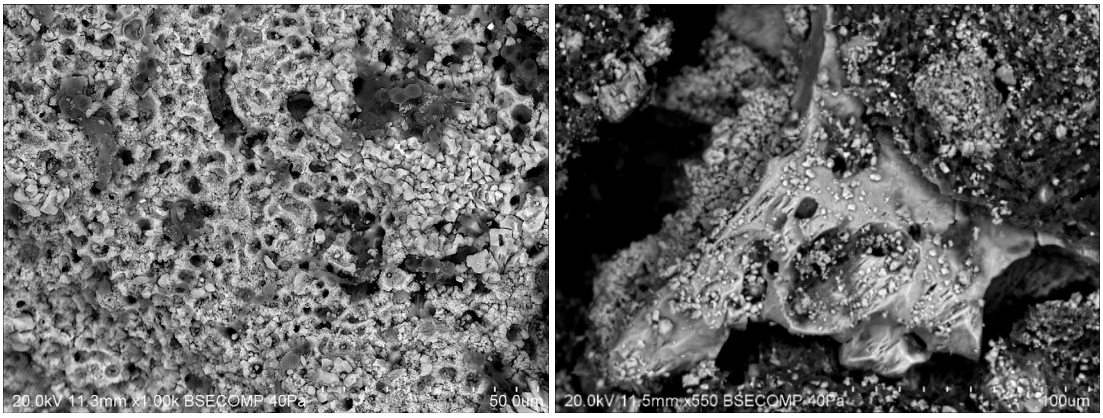

e f

Figure 3.6. BSEM photos of limestone specimen from Batalha Monastery, surface: (**a**) Stone full of rifts, hyphae penetrating (black arrow) and expanding across the calcite cleavage planes (white arrow); (**b**) Stone surface with fragmented granules and microbial spores (white arrow); (**c**) Calcium oxalate crystals (weddellite) showing typical tetragonal habit; (**d**) Microorganism tissues and cohesive calcium composite; (**e**) Pitting corrosion associated with hyphae penetration and Ca-oxalate precipitation; (**f**) A stone showing multiple degradation forms.

Element mapping of a lichen-covered area is shown in Figure 3.7. The strong signal of C and O correlating with the lichen represents the organism, while Ca is almost undetectable at the substrate covered by lichen except for some scattered grains on the lichen surface. Al, Mg, Na, and Si showed positive correlation with the lichen colonization, suggesting a silicate soil dust source. Cl and K are distributed evenly on the investigated area possibly from a fertilizer source. There are also a few Fe-Ni particles in this mapping, which are likely generated by vehicular traffic or industrial activity.

There is a noteworthy presence of P and S peaks associated with the presence of lichenous crusts. In other areas (Annex 3C), the element N also shows a distribution highly correlated with the presence of fungal hyphae. It is evident that the presence of a lichenous cover on the stone surface facilitates the deposition of soil dust and other airborne particles while at the same time increasing the retention of water and the wet deposition of gaseous and particulate pollutants containing N, P, and S derived from anthropogenic sources such as agricultural fertilizers (N and P) and combustion-related (S) processes [138].

SE

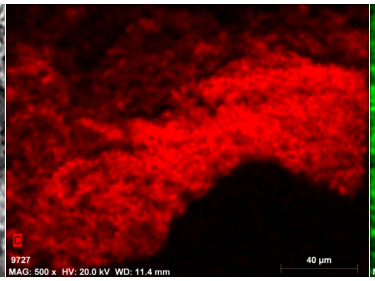

C

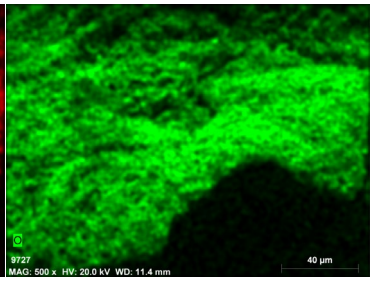

O

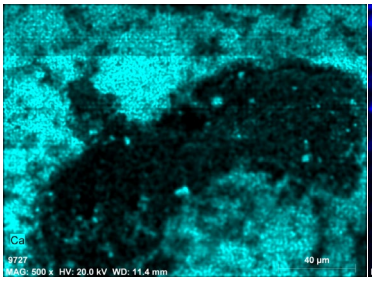

Ca

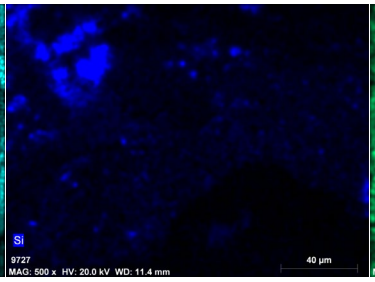

Si

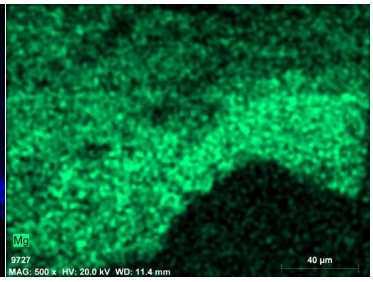

Mg

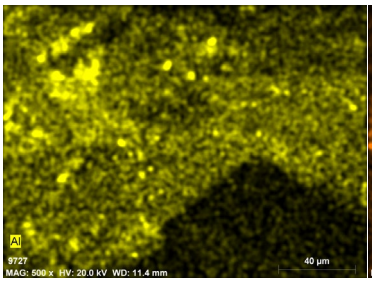

Al

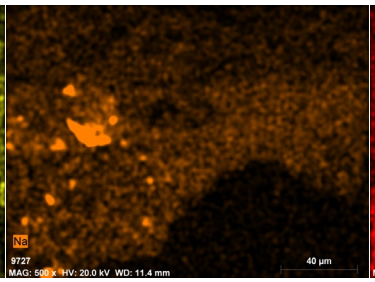

Na

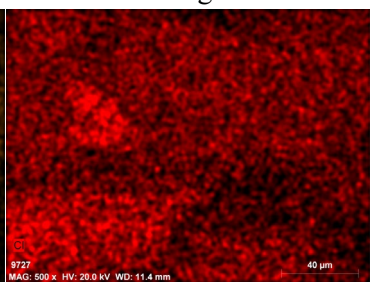

Cl

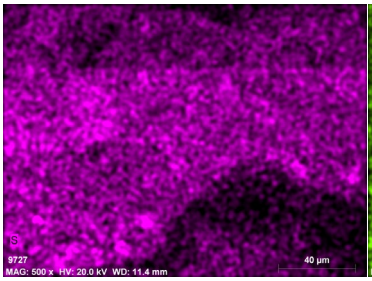

S

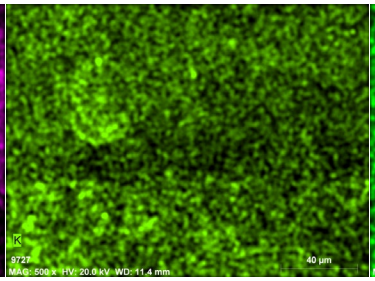

K

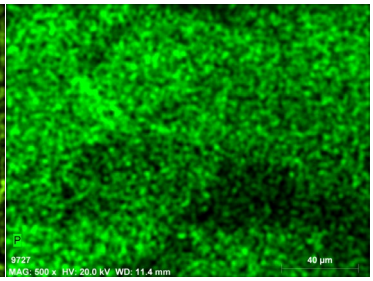

P

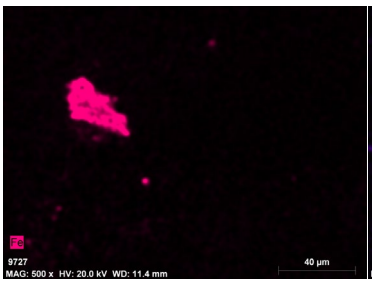

Fe

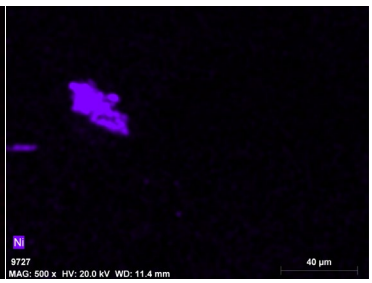

Ni

Figure 3.7. Scanning Electron Microscopy with Energy Dispersive Spectroscopy (SEM-EDS) element mapping of a lichen-covered area on the sample MB-R3.

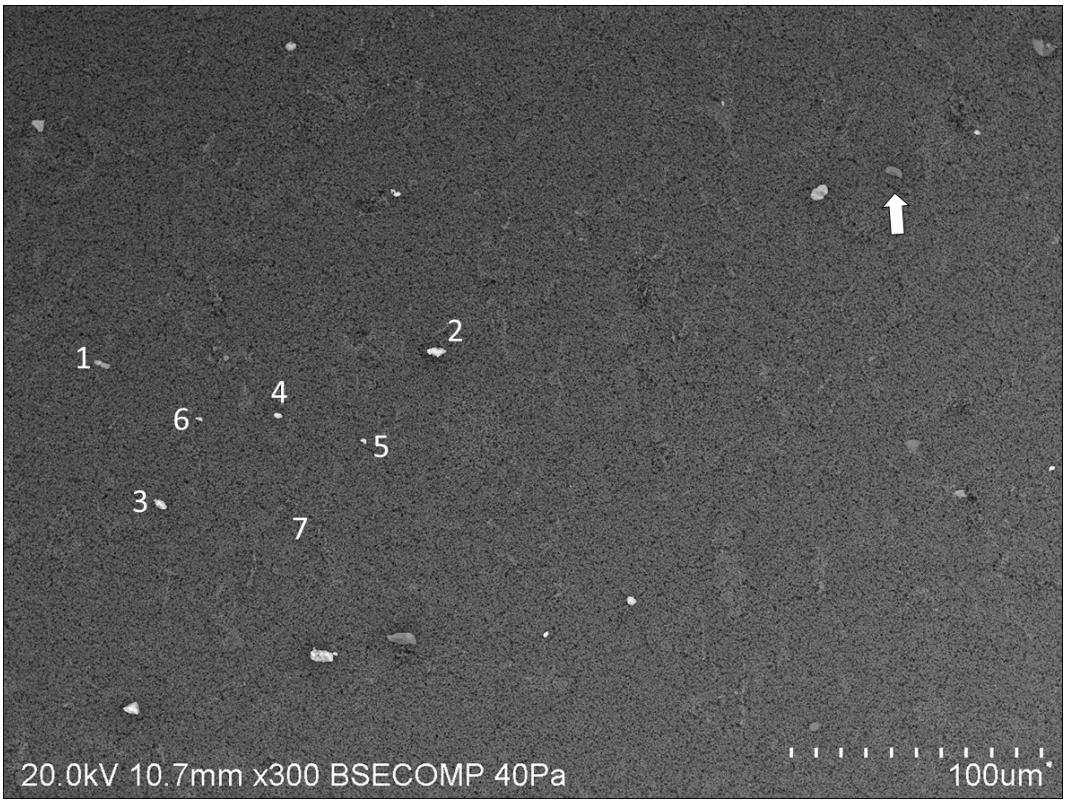

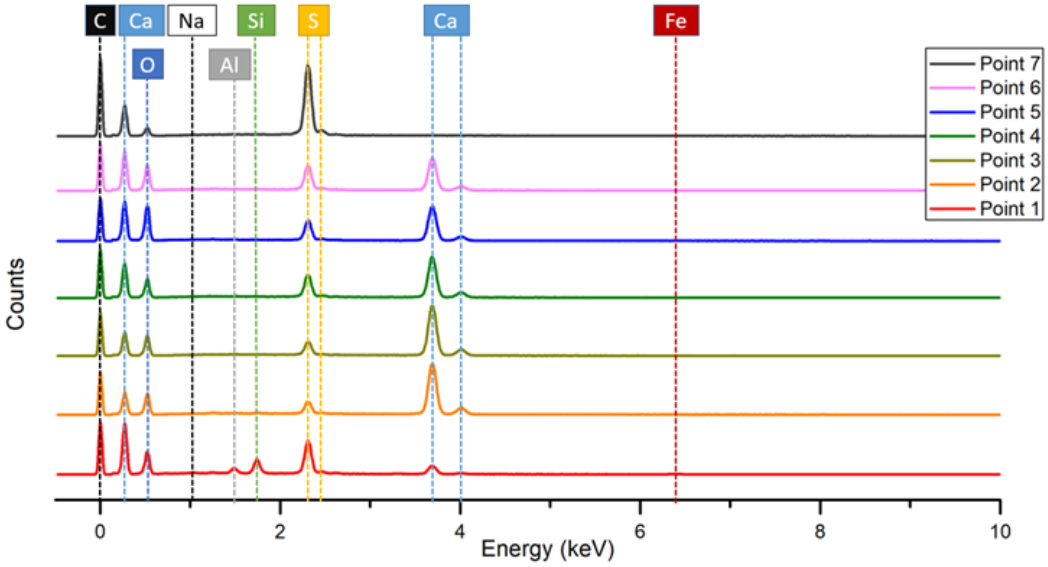

Figure 3.8. SEM-EDS analysis of filter paper. A spore particle is shown (white arrow).

SEM investigation on the filter papers from the optical particle sizer and the multi-point element analysis are shown in Figure 8. Particles are mostly of sizes less than 20 μm, and spores can also be seen (white arrow). Multi-point EDS analysis shows that the particles (point 1–6) are mainly Ca-C-O-S rich, suggesting the presence of $CaCO_3$, CaC_2O_4, and $CaSO_4$. Some particles show the presence of Na, Si, and Al, which are likely to be associated with deposited windborne silicate soil dust. The weak signal of Fe might come from oxidized iron products. A notable result is that on the filter paper where no particles are present (point 7), there is a significant peak of S, suggesting sulphur compounds are still affecting today's air quality in the outdoor environment surrounding the Batalha Monastery. The spores present on the filter papers proved that they have been deposited on the stone surface by dry and wet deposition as airborne atmospheric particles.

3.3.4 High-Throughput Sequencing

The identification of bacterial communities is shown in Figure 9. The dominant airborne bacteria from the surrounding atmospheric environment on the filter paper belong to phyla Proteobacteria (61.86%) and Firmicutes (25.46%); aside from that, Bacteroidetes (4.17%), Actinobacteria (2.53%), and Acidobacteria (1.67%) are also present. For the sample MB-R3, the dominant bacteria phyla are Proteobacteria (44.23%), Actinobacteria (14.59%), Cyanobacteria (11.52%), Bacteroidetes (7.68%), Acidobacteria (5.82%), Firmicutes (5.48%), Verrucomicrobia (3.10%), and Planctomycetes (2.85%). Sample P2-5 is characterized by analogous microbial communities but with different relative abundances: Proteobacteria (52.40%), Cyanobacteria (9.39%), Bacteroidetes (8.85%), Actinobacteria (6.92%), Acidobacteria (3.24%), and a small quantity of Deinococcus (1.44%) and Planctomycetes (1.23%).

It is noteworthy that Proteobacteria phylum is by far the most represented in all samples, with Gammaproteobacteria and Alphaproteobacteria as the two predominant classes. The percentage of Actinobacteria and Acidobacteria has increased from filter paper to sample P2-5 to MB-R3, while Firmicutes bacterial abundance reduces following this sequence. Considering the degradation level of the two stone specimens, MB-R3 has a massive lichen layer on the surface, while P2-5 has not yet formed an evident lichen crust. It can be speculated that the lichen flora has changed the microenvironment, which selectively benefits the growth and reproduction of certain bacterial species, thus rearranging the relative abundance of bacteria. In fact, a previous study illustrated that the metabolite production and phenoloxidase activity of lichens can affect the bacterial community structure [139].

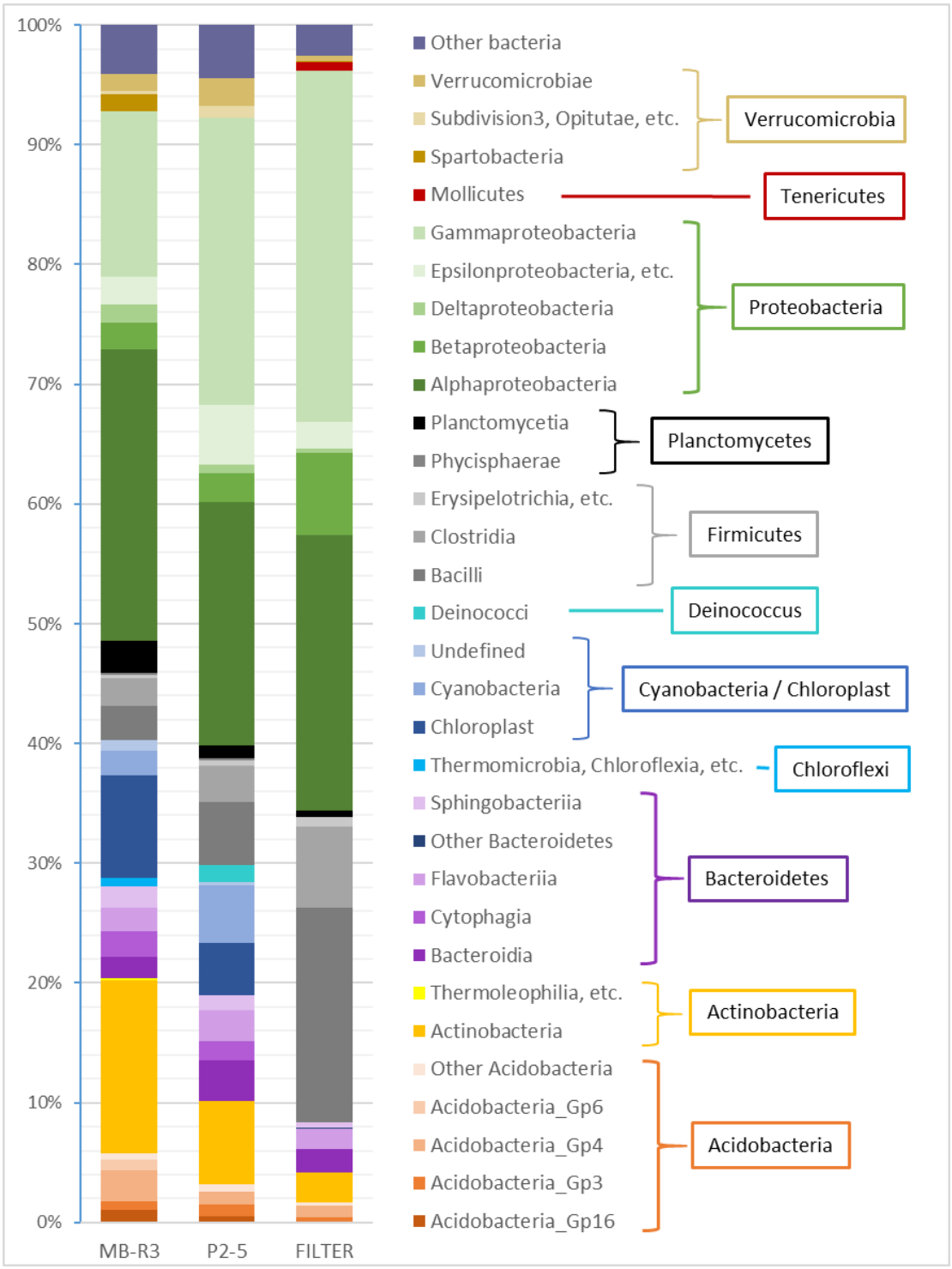

Figure 3.9. Relative abundance of the dominant bacterial classes in the stone samples and filter paper with corresponding phyla (on the right side).

Another significant discovery is that Cyanobacteria, while abundant on the stone samples, seem not to be present on the filter papers. In fact, cyanobacteria could be found present at a few millimeters of depth from the stone–atmosphere interface as they seek shelter from desiccation and intense UV radiation [121]. Therefore, the Cyanobacteria found on the stone samples could have already been present in the stone materials from the original quarries.

3.3.5 Discussion

Proteobacteria and Bacteroidetes are believed to provide nutrients, mobilize iron and phosphate, and fix nitrogen for the lichen symbiotic growth [140]. Firmicutes is also well known for symbiotic nitrogen fixation and their beneficial and endophytic interaction with plants resulting in plant growth promotion [141]. Actinobacteria play the leading role in cellulose degradation, promoting the decomposition of plant remains [142]. Cyanobacterial are the typical photolithoautotrophic organisms that synthesize carbohydrate. Planctomycetes reproduction has been reported to be associated with the enrichment of N and P [142]. Hence, the increase of Planctomycetes ratio from membrane filter to sample P2-5 to MB-R3 may be due to the growth of a lichenous cover which in turn facilitates the fixation of nitrogen and a phosphorus-rich compound, resulting in the abundance increase of Planctomycetes bacteria; the EDS analysis of the biofilm (Figure 3.7 and A3) is also in agreement with that.

The Nitrosomonas spp., Nitrobacter spp., and Thiobacillus spp. from Alphaproteobacteria and Betaproteobacteria class are chemolithoautotrophic bacteria that obtain energy from the oxidation of inorganic compounds (ammonia, nitrites, hydrogen sulfide, thiosulphates, or elementary sulfur), fixing CO_2 from the atmosphere and releasing nitrous acids, nitric acid, or sulfuric acid [118]. The above-mentioned bacteria detected on the stone samples microbiomes in this research, combined with the significant presence of S-rich compounds on the filter samples, may suggest that air pollution leads to a richness of nutrients for the chemolithoautotrophic bacteria and indirectly promotes lichen growth.

The presence of bacterial community in lichen microbiomes was also reported in other studies. For instance, Paramo lichen harbored microbiomes composed mainly of the phyla Proteobacteria, Acidobacteria, Verrucomicrobia, Bacteroidetes, and Actinobacteria [143]. In other research, four lichen species from SW-Norway were analyzed with the bacteria detected in the lichen–rock samples, which were affiliated with the major lineages Acidobacteria, Actinobacteria, Proteobacteria (Alpha-, Beta-, Gamma-), Bacteriodetes, Chloroflexi, Deinococcus, Firmicutes, Planctomycetes, Tenericutes, and Cyanobacteria [144]. Even in the Antarctic and Arctic, the lichens-

associated bacteria are Actinobacteria, Bacteroidetes, Deinococcus-Thermus, Firmicutes, and Proteobacteria (Alpha-, Beta-, and Gamma-) [145]. Regardless of the lichen species, there is some consistency in the bacterial phyla associated with lichens around the world, although the community structure can differ according to geographical location.

3.4 Conclusion

The biodegradation processes occurring on Batalha Monastery limestone constitutes a complex phenomenon involving different steps. At the beginning, photolithoautotrophic bacteria (e.g., cyanobacteria) present in the stone started to grow using sunlight as an energy source for photosynthesis. Airborne bacterial spores from the surrounding atmospheric environment were also deposited to the stone surface, some of which are chemolithoautotrophic; they grow by utilizing the sulphates, nitrates, phosphate, and metallic particles from the air as nutrients, and being responsible for the production of acidic substances attacking the stone substrate, the use of fertilizers and combustion of fossil fuel can promote this process. These primary colonizers accumulate biomass, forming a biofilm enriched with organic and inorganic substances and growth factors, providing an excellent nutrient base for the subsequent heterotrophic microflora. As a result of metabolic activity, a series of acid compounds and expansion of hyphae damage the stone substrate by making fissures and boreholes as well as pitting and detached fragments, which in turn increase the capillary adsorption and accelerate degradation from the environment and microbial activity [146]. The development of a lichen cover promotes the fixation of phosphorous and nitrogen, which is selectively beneficial to some bacterial species, and the secondary metabolites of lichens can affect the bacterial community structure. In this complicated process, contamination in the air plays an important role to exacerbate limestone deterioration in the Monastery of Batalha. Therefore, an effective conservation strategy to preserve the Batalha Monastery would be twofold: i.e., to reduce S, N, and P-based air pollution in the atmosphere surrounding the monument while at the same time eliminating (using the appropriate cleaning procedure) the microbial colonization on the stone.

Chapter 4

Plasma etching acts on the inhibition of incipient bio-colonization and biodegradation on building limestone

Part of the results in this chapter has been published in article [147]

4.1 Introduction

During the aging of cultural heritage objects, stone artifacts may undergo decay under the effects of different kinds of contamination. Through dry and wet depositional processes, soil dust, insects, mildew, fungi and gaseous and particulate air pollutants accumulate on stone surface building up patinas and crusts, which are difficult to remove without damaging the original substrate [148] [149] [150]. Conventional cleaning methods often fail to completely remove these surface soiled patinas and/or biofilms by using toxic and aggressive chemicals that may leave undesired residues [151] [152]. In the literature, the possible use of plasma cleaning for the restoration and preservation of various materials such as wood, paper, fabric, metals, glasses, ceramics and stones has been reported. Plasma etching, for instance, was used in an attempt to remove: a) varnish (lacquer) coating on paintings using oxygen plasma [153]; b) epoxy / acrylic resin on stones by using compressed air or mix of oxygen and argon plasma[154] [155]; c) cleaning patinas on metal artefacts using hydrogen plasma [156]. It was proved that plasma can successfully remove the above-mentioned contaminations without damaging the substrate.

Plasma removes the surface contamination via three different reactions: (a) ion sputtering – atoms on the surface can be sputtered non-selectively when the floating potential of the plasma ions is beyond substrate – surface binding threshold; (b) radicals etching – atoms or radicals from the plasma chemically react with the surface, volatile reaction products can be eliminated through pumping. The choice of the gas mixture used for etching is determined by the volatility and stability of the etched products. For Si-rich materials, halogen-, hydride-, and methyl compounds can be used. For an effective removal of organic compounds, oxygen can be used; (c) heating – the surface immersed in the plasma is heated mainly by electron, ion bombardment, and plasma radiation [157]. In the study of Liqing Yang et al [158], a self-designed radio-frequency (RF) glow discharge oxygen plasma was used to sterilize the Pseudomonas aeruginosa on the polyethylene terephthalate (PET) sheets, the germicidal effect is a function of treating time and distance from the induction coil. The sterilization mechanism study demonstrated that intense etching action of electrons and ions on cell membrane engenders bacteria death in the plasma active discharge area, while in the plasma afterglow area attacking polyunsaturated fatty acids in the cell membrane by high concentration oxygen radicals becomes the main factor of bacteria death.

The type of plasmas applied for cleaning can be classified into several categories depending on their operating principle: a) dielectric barrier discharge (DBD), in which the discharge is generated in a cylindrical system at the atmospheric pressure: it consists of a tube made with dielectric material (fused silica), the high voltage electrode (brass) is a ring placed over the tube and the rod ground electrode is placed in the middle of this tube with gas inlet, driving the plasma to the environmental air [159]; b) corona discharge initiates the plasma between the internal pin-shaped electrode and the cylinder/truncated cone shaped external electrode (nozzle) which is made with stainless steel and is replaceable, when the nozzle is open, coronal filaments brings out a gas flow with the leaving plasma flowing freely [160]. c) arc discharge generates thermal plasma by compressed air, it can reach working temperature exceeding 300 °C ~ 400°C, with short treating time [155] [161]; d) capacitive coupled plasma has a vacuum chamber, with inlet for selective gas (inert, oxidic or reductive) that generates ions and react with the sample, two discal-shaped electrodes are placed at the top and the bottom, with sample placed in between [162]. Atmospheric plasma treatment has been shown to be able to remove biofilms on artificial substrates such as polystyrene wafers and stainless steel [163] [164], while He/O2 plasma jet was found to have antimicrobial effects on some bacterial biofilms [165].

Figure 4.1. Bio-degradation on the inner wall of the “imperfect chapels” of the Batalha Monastery.

This study aims to investigate the effectiveness of plasma etching in the removal of microbials from bio-deteriorated limestone surfaces in monuments and buildings and in the prevention of microorganism growth, in order to provide conservators with a feasible and effective solution for preserving stone monuments in both urban and rural environments. The Batalha Monastery (Figure 4.1), a UNESCO listed World Heritage site located in central Portugal and built with locally quarried Jurassic oolitic limestone [1], was chosen for this investigation. The Monastery oolitic limestone has suffered and still is suffering from severe biodeterioration caused by extensive lichenous crusts and microorganism biofilms growing on the building surface: this promotes both physical and chemical attack on the limestone substrate via hyphae mechanical penetration along calcite inter-crystalline spaces, dissolution/leaching of

calcite minerals, and precipitation of secondary minerals such as Ca-oxalates within the stone porosity framework [150].

4.2 Materials and Methods

4.2.1 Preparation of Stone tablets

Limestones were collected from five quarries which supplied the oolitic limestone used in the building and restoration of the Batalha Monastery: Pidiogo (39°39'15.7"N 8°44'27.9"W), Valinho do Rei (39°39'32.5"N 8°44'58.1"W), Reguengo do Fetal (39°38'43.64"N 8°45'16.19"W), Cabeço do Roxo (39°35'39.84"N 8°51'27.19"W) and Outeiro de Sebastião (39°35'38.89"N 8°51'27.49"W) [1]. The stones were cut into 2 cm (width) × 2 cm (length) × 1 cm (height) tablets, washed and dried under 60 °C for 24 h, then sterilized.

4.2.2 Extraction, cultivation and incubation of microbials

Sampling was performed on representative areas of the stone materials of the Batalha Monastery, including areas with evidence of alterations. Microinvasive (chisel and scalpels) and non-invasive (swabs) methods were applied during the samples' collection, performed with sterile material but in outdoor environment. The extracted microorganism was stored in falcon tube, being immersed by saline solution.

For bacterial and fungal growth, malt extract (ME) medium was prepared with 20 g/L malt extract, 20 g/L glucose and 1 g/L peptone, then sterilized in autoclave for 20 min at 120 °C and 1.5 bars. 1 mL of saline medium which contains the collected microorganism and add it into 500 mL ME medium, this culture was then incubated for 72 h in an incubator with controlled temperature of 28 °C and with orbital agitation at 150 rpm. 1 mL of mixed culture was used to inoculate each limestone tablet in 2.1. Then all tablets were incubated in the ARALAB Plant Growth Chamber for 15 days, with controlled temperature at 28 °C, humidity at 81.0% rH, and 10% illumination of 4x18W fluorescent.

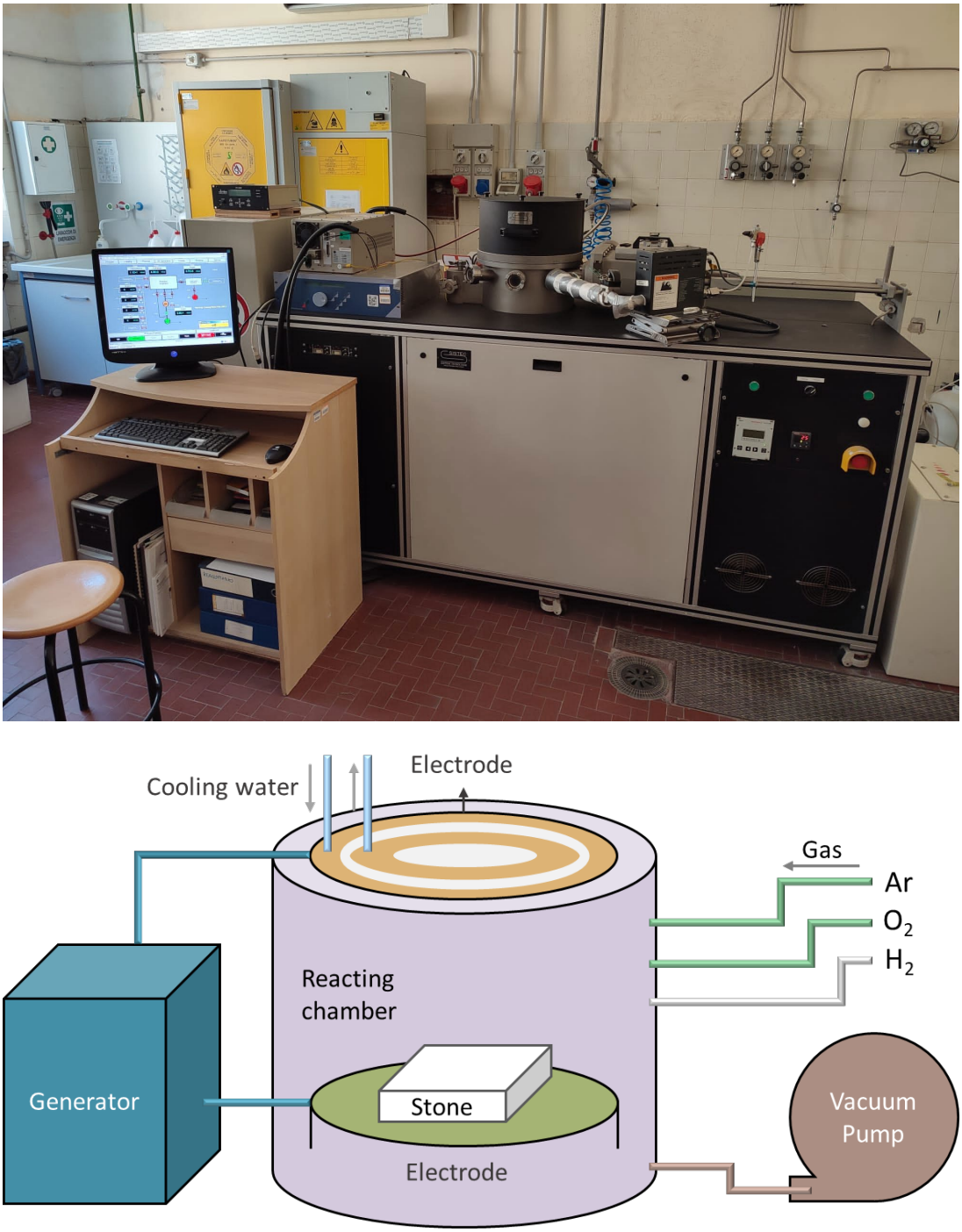

Figure 4.2. Photo of the coupled parallel-plate plasma reactor and schematic of the instrument structure.

4.2.3 Plasma etching of bio-incubated and exposed samples

The cleaning treatments were carried out in a lab-constructed capacitively coupled parallel-plate reactor (Figure 4.2). The reactor employs a two-electrodes configuration; the upper electrode is connected to a radio frequency (RF) (13.56 MHz) power supply through an impedance matching unit, while the bottom electrode is connected to the ground [166]. The etching treatments were performed by positioning the samples on the ground electrode in a plasma fed with Ar (99.99% purity) and O_2 (99.99% purity) in different ratios (with absolute flows in the range of 10 to 100 sccm - standard cubic centimeter per minute, respectively), at input power in the range of 15 W to 60 W, for a maximum treatment time of 120 minutes.

Figure 4.3 shows the tablet areas with corresponding treatment settings. An area of the sample surface is shielded from the plasma, in order to compare the surface chemistry and morphology with other areas exposed to the plasma, and before and after plasma etching.

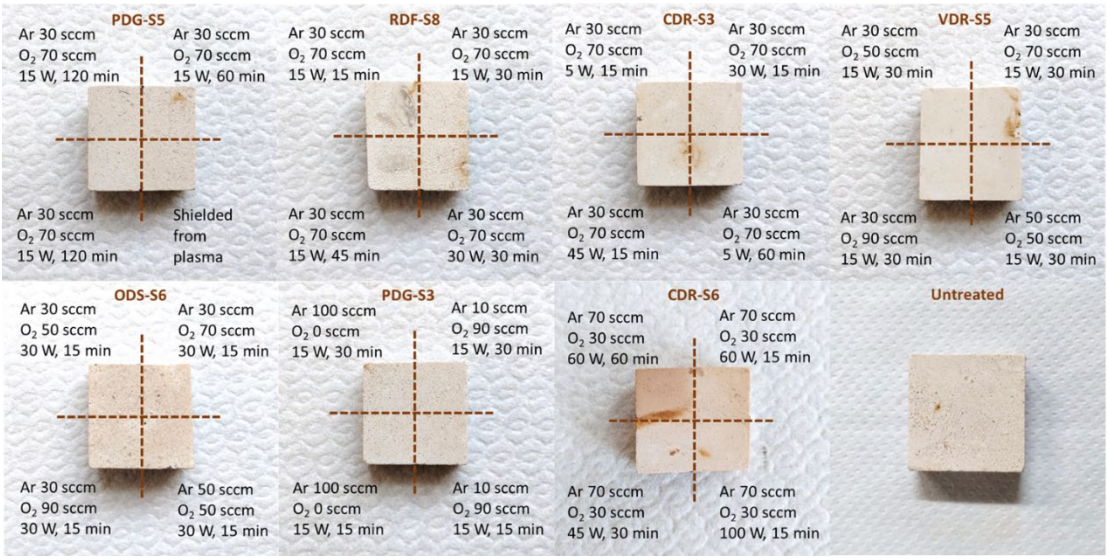

Figure 4.3. Different areas of the tablets treated by plasma in different experimental conditions.

4.2.4 Assessment of plasma treatment

Attenuated Total Reflectance-Fourier Transform Infrared Spectroscopy (ATR-FTIR)

The FTIR spectra were recorded by Perkin Elmer Spectrum 2000 FTIR spectrometer (Perkin Elmer, Norwalk, CT, USA) equipped with a single reflection

attenuated total reflectance (ATR) accessory. For each sample, 16 scans were recorded with resolution of 4 cm^{-1} [167].

SEM and Bright Field Microscope

Scanning electron microscopy coupled with energy-dispersive X-ray spectrometry was carried out using a Hitachi S3700N (Tokyo, Japan) SEM coupled to a Bruker (Karlsruhe, Germany) XFlash 5010 SDD Detector system. Operating conditions were as follows: backscattered imaging detector (BSEM); low-vacuum mode (pre-set pressure of 40 Pa) allowing the observation of non-coated biological samples; accelerating voltage: 20 kV; current: 120 mA. For surface observation, the plasma-treated and plasma-untreated tablets (2 cm × 2 cm × 1 cm) were put into the chamber directly. Samples were also observed under LEICA M205C Stereo Microscope (Leica, Wetzlar, Germany), photos were taken by a uEyeUI 149xSE-Cindustrial camera (IDS, Obsesulm, Germany).

Cell viability index (MTT assay)

Cell viability index (CVI) of the bio-contaminants present in samples was assessed by the 3-(4,5-dimethylthiazol-2-yl)-2,5-diphenyltetrazolium bromide (MTT) adapted for cultural heritage materials [168][169] [169], 500 µL sterile water to extract the microorganisms from the tablet surface, then 90 µL of each extracted suspension from stone were incubated with 300 µL of MTT solution (0.5 mg/mL) for 4 h, at 37ºC in the dark. After this, the suspensions were centrifuged at 10000 rpm for 15 min and the supernatants were removed and discarded. Then 100 µL of DMSO/ethanol (1:1) was added to promote the dissolution of the formazan crystals formed. The final suspension was determined by spectrophotometry at 570 nm. Each assay was performed in triplicate.

4.3 Results and Discussion

4.3.1 FTIR spectra and sugar decomposition

The FTIR spectra of plasma-treated and plasma-untreated samples are reported in Figure 4.4. Limestone tablets before bio-incubation are characterized by peaks at 2514 cm^{-1}, 1795 cm^{-1}, 1396 cm^{-1}, 872 cm^{-1}, 712 cm^{-1}, which are typical bands of low-magnesium calcite, and the small peak at 1072 cm-1 represents the minor amount of quartz in it [RRUFF ID: R040070.1] [170] [171] [172]. Peaks at 1070 cm^{-1} and 782 cm^{-1} represent quartz [RRUFF ID: R040031.1]. After bio-incubation, aside from the calcite and quartz, the presence of peaks at 3278 cm^{-1}, 2925 cm^{-1}, 1637 cm^{-1}, 1320 cm^{-}

[1], 1030 cm^{-1} can also be seen, the main peak of calcite at 1396 cm^{-1} has become wider, a peak at 1411 cm^{-1} can be seen after spectrum subtraction. Among the newly added peaks, 3278 cm^{-1} represents (O-H) stretching peak which belongs to carbohydrate, water or organic acids, 2925 cm^{-1} represents (C-H) stretching band in CH_2 and CH_3 group, 1637 cm^{-1} refers to (O-H) bending, the peak at 1320 cm^{-1} is due to O-H bending of the C-OH group, 1411 cm^{-1} is a combination of O–H bending of the C–OH group and C–H bending of the alkenes, peaks at 1031 cm^{-1} is due to carbohydrates and organic acid C-O, C-C stretching [173] [174]. According to the previous study, these are characteristic peaks of sugar (could be cellulose or glucose) [175].

The incubated tablets were treated by plasma in different experimental conditions: a (Ar 30 sccm, O_2 70 sccm, 5 W, 15 min); b (Ar 10 sccm, O_2 90 sccm, 15 W, 15 min); c (Ar 30 sccm, O_2 70 sccm, 30 W, 15 min); d (Ar 30 sccm, O_2 70 sccm, 15 W, 120 min). It can be seen that after plasma treatment condition b), c) and d), tablets have shown weakened or removed peaks at 3278 cm^{-1}, 2925 cm^{-1}, 1637 cm^{-1} and 1031 cm^{-1} (Figure 4.4), implying the removal of sugar. Area shielded from plasma does not show any weakening of the sugar related peaks, implying that only the eliminating of sugar can be realized only by exposure to plasma. Plasma etching under condition a) shows little difference than the untreated sample, because very short working time and very low working power was applied, however condition b) and c) lead to obvious weakening of the sugar peaks. Sample treated under condition d) has no characteristic peaks other than limestone.

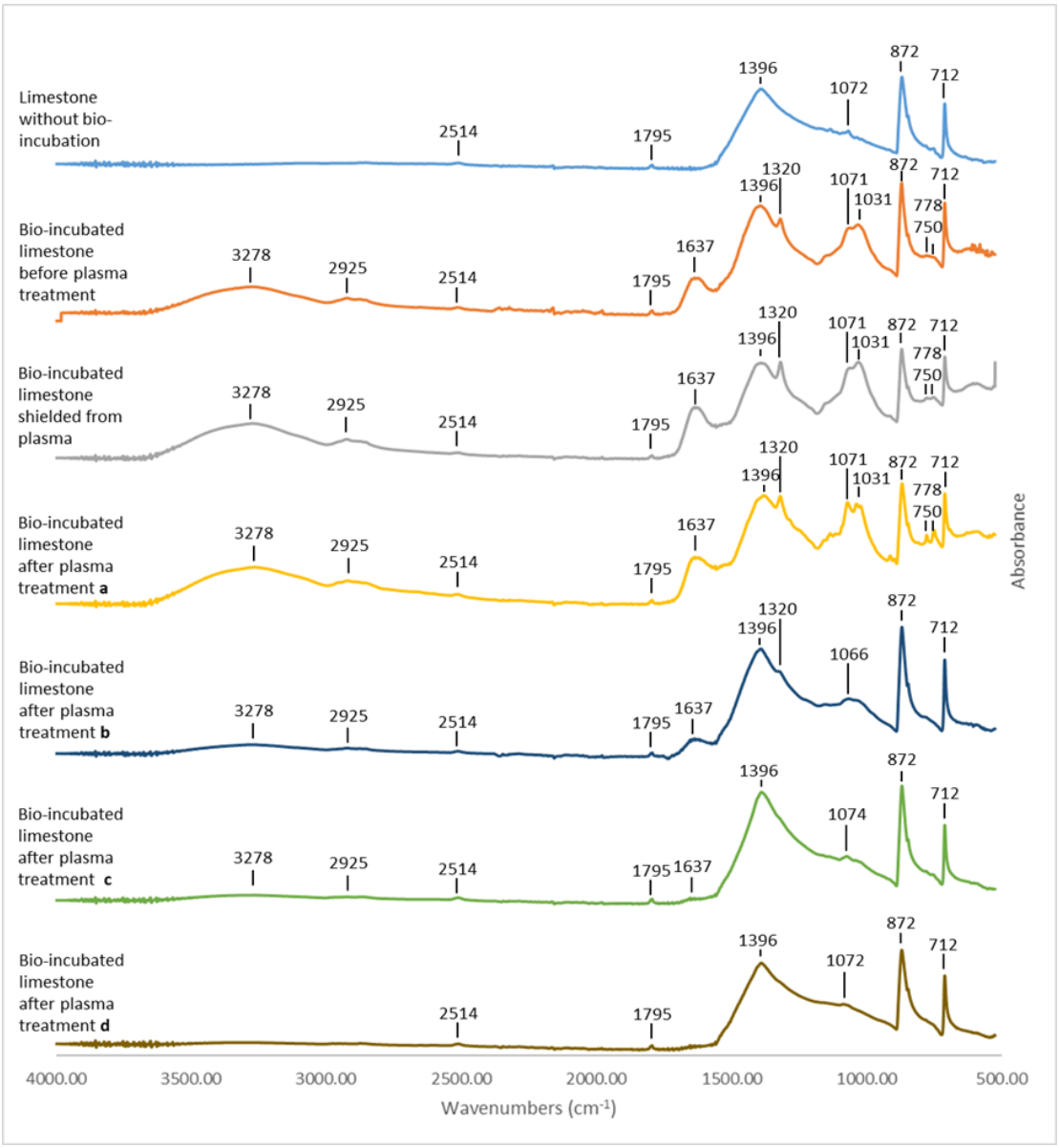

Figure 4.4. FTIR spectra of tablets before and after plasma etching under different experimental conditions.

To assess the factors that affect the cleaning results, incubated stone tablets were treated with various operating parameters of the coupled-capacitive plasma, including operation time, plasma power, gas ratio of oxygen and argon, as listed in Table 4.1 and Table 4.2. Semi-quantification of the organic substance can be done by using Beer-Lamber law:

$$A = -\log_{10}\frac{I_t}{I_0} = \log_{10}\frac{1}{T} = K \cdot l \cdot c\ ,$$

where A is the absorbance, K is the absorptivity, l is the optical path length, c is the concentration of the attenuating species. Because K and l are constant for all the samples in this experiment, the organic concentration is in direct proportion to the absorbance. Define the cleaning efficiency by the weakening of the organic-matter-related peaks: the ratio of peak intensity after treatment to the peak intensity before treatment are graded as: "○" completely removed (< 0.05), "●" mostly removed (0.05 ~ 0.3), "■" partially removed (0.3 ~ 0.8), "▼" presented (0.8 ~ 1.0). It can be seen that, under the same treating duration, higher power leads to better cleaning effect; under the same plasma power, longer working time performs better cleaning results. The surface cleaning effect was also influenced by the gas ratio, higher argon concentration in the plasma discharge has better performance of removing sugar, this may be due to the fact that the dry corrosion by ionized argon has more intense cleaning effect for the limestone surface, instead of oxidation reaction by oxygen.

Table 4.1. Effect of input power and etching time on sugar removal under fixed gas flow Ar 30 sccm and O_2 70 sccm.

Etching time / Input power	**15 min**	**30 min**	**45 min**	**60 min**	**120 min**
shield from plasma					▼
5 W	▼			●	
15 W	■	■	●	○	○
30 W	●	●			
45 W	●	○			
60 W	●				
100 W	●				

Table 4.2. Effect of different gas ratios in the plasma discharge on sugar removal.

Gas flow / Power and time	**Ar 100 O_2 0**	**Ar 50 O_2 50**	**Ar 30 O_2 50**	**Ar 30 O_2 70**	**Ar 30 O_2 90**	**Ar 10 O_2 90**
15 W, 15 min	●			■		■
15 W, 30 min	○	●	●	●	●	●
30 W, 15 min		●	●	●	●	

4.3.2 SEM observation

Samples with and without plasma treatment were observed by SEM and stereo microscope; SEM micrograph are shown in Figure 4.5. On samples not exposed to plasma discharge, a mass of clustered and filamentous microorganisms can be clearly seen on the limestone surface (a). Under higher magnification, interlaced filamentous microorganisms and circular cell structure (b, c, d) are clearly displayed. After plasma

etching, the filamentous microorganisms are mostly removed, some spotted microbial aggregation remains on the surface, mostly at the or inside of the oolites (e). This could be due to the loose structure inside or on the boundary of the oolites, where microbials are easy to aggregate in and difficult to remove at these inter-crystalline spaces. Circular cells are distorted and damaged (g), or completely lysed with no structure (h). The filamentous microorganisms are broken and no longer connected, leaving only remains of fractured debris (circled by the yellow dash lines in h).

The SEM investigation shows how the plasma is capable to effectively disrupt microbial structures and remove microorganisms with the cleaning effect particularly significant on stone regions characterized by low porosity and massive texture. However, due to the non-homogenous porosity distribution in oolitic limestones, microbials remaining in cavities are not easily removed.

4.3.3 Optical microscopy and appearance changing

Observed by bright field stereomicroscope, bio-contaminated limestone shows some distinct changes after plasma cleaning (Figure 4.6). Before plasma etching, yellow biofilms and black mold spots were present on surface areas where microbial growth is more severe (a, b). White filamentous organisms also were found widely distributed over the stone surface (c) with the tablet edge being a region where the biofilm is easier to form (d). After plasma etching, biofilms show cracking and detachment from the stone substrate (e), the colour of the microbial crust was lightened, black mildews were partially faded (f), white filaments were obviously removed (g) with the biofilm on the tablet edge also peeling off in some cases (h).

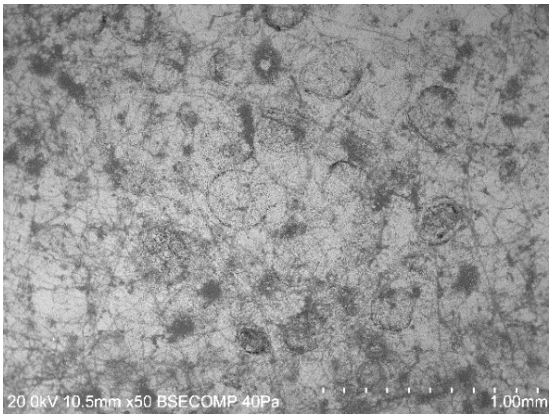

a b

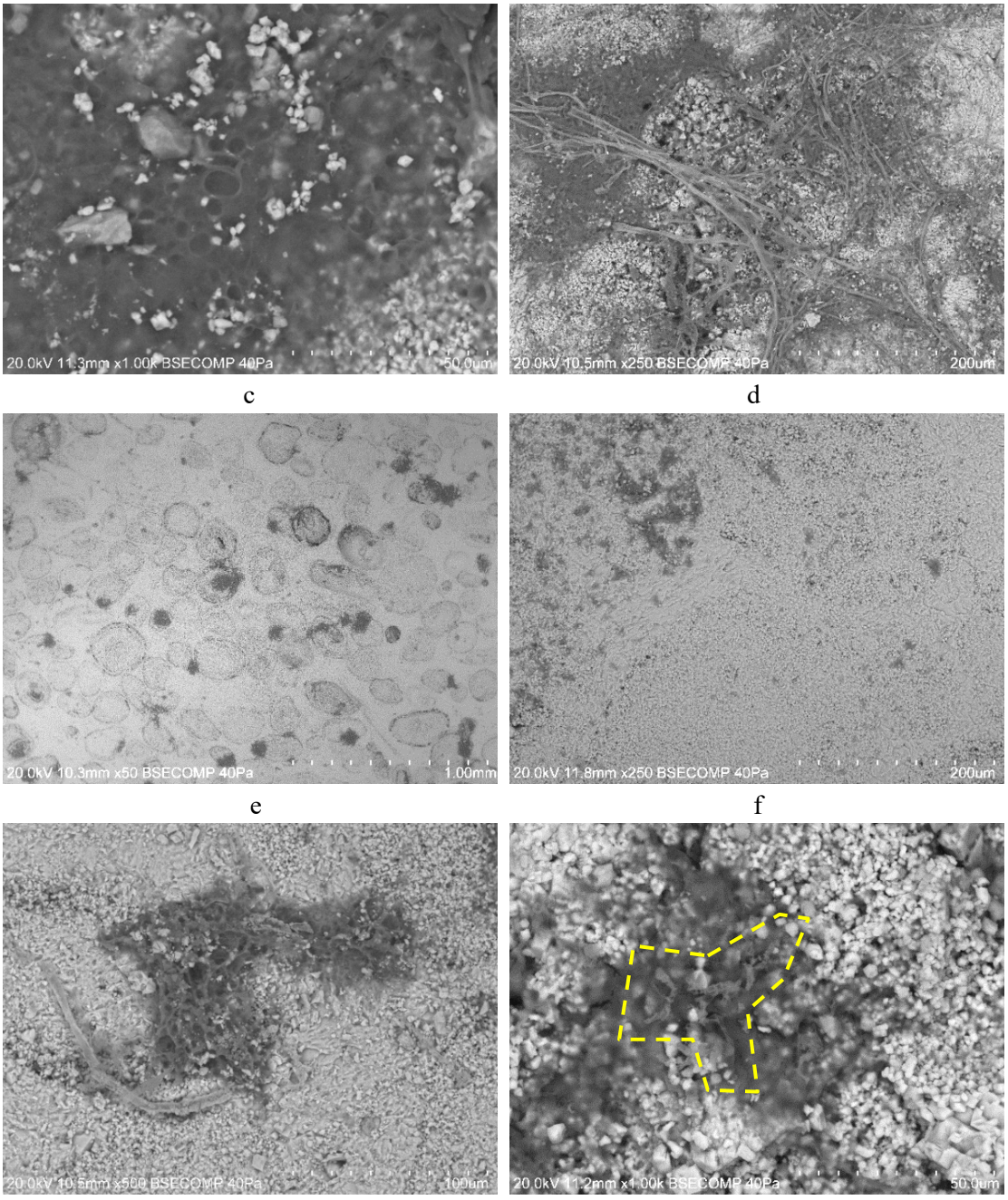

Figure 4.5. SEM of the tablets before and after plasma treatment: a. abundant microbes on the area shielded from plasma; b. various species of microbials on the untreated sample; c. circular structured cells on the untreated sample; d. filamentous microorganism on the sample shielded from plasma; e. sample treated with 15 W plasma for 30 min; f. sample treated with 30 W plasma for 15 min; g. tortured and damaged cells after 15 W 120 min of plasma treatment; h. microorganism debris (circulateed by yellow dash) on the sample treated with 45 W 30 min.

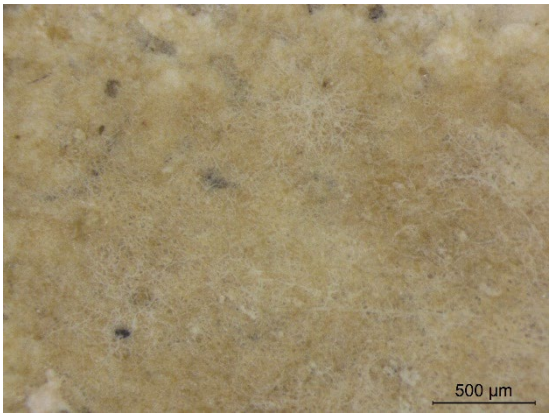

a

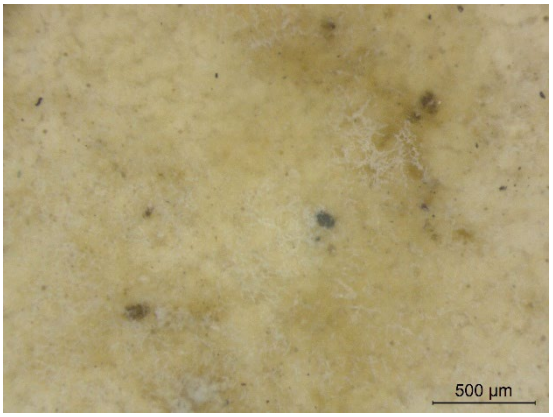

b

c

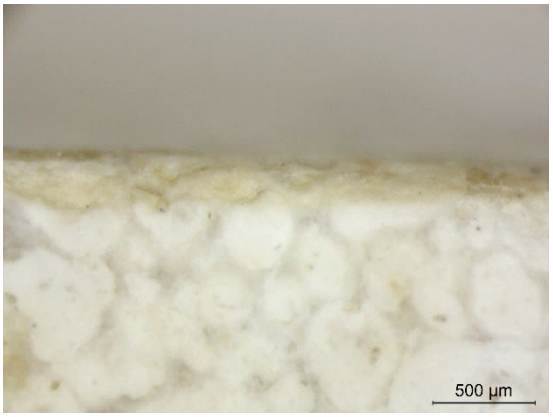

d

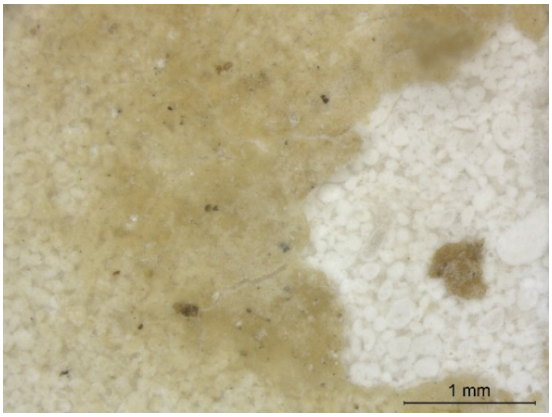

e

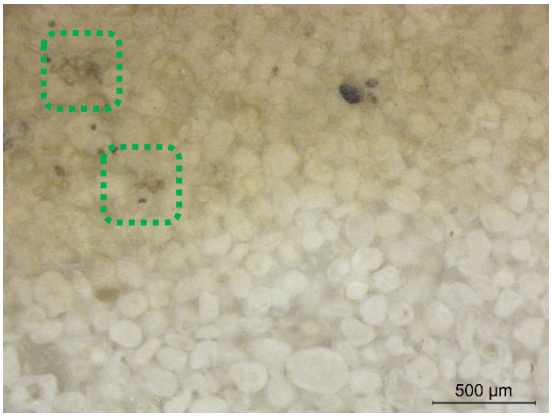

f

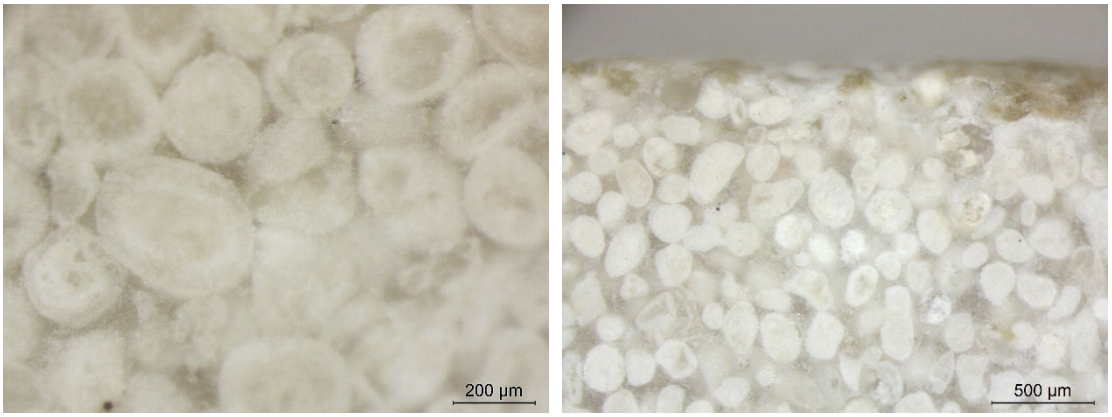

g h

Figure 4.6. Bright field microscope photo of the sample tablets: a. an area covered by thick biofilm before plasma treatment; b. coloured biofilm and black mildews on the stones before plasma treatment; c. filamentous microorganism on the limestone before plasma treatment; d. the edge of tablet before plasma treatment; e. thick biofilm cracked and detached from the substrate after plasma treatment (15 W, 30 min); f. lightened colour of the biofilm and partially faded mold spots (circled by green dash) after plasma treatment (100 W, 15 min); g. filamentous microorganism significantly diminished after plasma treatment (30 W, 15 min); h. the edge of tablet after plasma treatment (15 W, 30 min).

4.3.4 Cell Viability

Cell viability index test (CVI) was carried out on areas with the same size in treated and untreated samples. Results are shown in Table 3 where the % of cell viability is referring to the untreated sample. Another sample underwent sterilization by remaining in autoclave at 120 °C for 30 min, to compare with the effect of plasma cleaning.

Set the cell viability of the autoclave sterilized sample that went through the same CVI procedure as 0% and that of the untreated tablet as 100%, when the cell viability value is lower than the sterilized sample, they were justified to 0% as well. It can be seen that samples underwent the plasma etching with parameters of Ar 30 sccm, O_2 70 sccm for 15 min with input power 15 W, 30 W, 45 W, presented 2.5% ~ 3.5% cell viability, which are a bit higher than the autoclave sterilized tablets; but with the same etching time but with the input power being increased to 60 W - 100 W, the cell viability reduced to 0%, being lower than the sterilized ones.

Under 15 W input working power, when the plasma etching time was extended to 30 min and 45 min, cell viability was reduced to 0%, which were also lower than the one after autoclave sterilization. Of particularly interest, when the plasma input power and etching time both increased, the biocide effect was more obvious – for example, for sample under half hour etching at 30 W and sample treated under 60 W for one

hour, the cell viability were much lower than the sterilized one, here marked as 0% as well.

Table 4.3. Cell viability index of treated and untreated samples.

Plasma etching parameters of the sample	Cell viability (%)
incubated sample without plasma etching	100%
autoclave sterilized sample	0%
plasma etching Ar 30 sccm, O_2 70 sccm, 15 W, 15 min	3.34%
plasma etching Ar 30 sccm, O_2 70 sccm, 15 W, 30 min	0%
plasma etching Ar 30 sccm, O_2 70 sccm, 15 W, 45 min	0%
plasma etching Ar 30 sccm, O_2 70 sccm, 30 W, 15 min	3.50%
plasma etching Ar 30 sccm, O_2 70 sccm, 45 W, 15 min	2.55%
plasma etching Ar 30 sccm, O_2 70 sccm, 60 W, 15 min	0%
plasma etching Ar 30 sccm, O_2 70 sccm, 100 W, 15 min	0%
plasma etching Ar 30 sccm, O_2 70 sccm, 30 W, 30 min	0%
plasma etching Ar 30 sccm, O_2 70 sccm, 60 W, 60 min	0%

4.4 Conclusions

This research aims to discuss the performance of low-pressure plasma etching in the inhibition of biodegradation on limestone surfaces, FTIR, SEM, optical microscope, and CVI test were used to assess the etching results. Results indicated that, with an input power of 15 ~ 45 W and etching times of 30 ~ 60 min, plasma etching is able to efficiently remove sugar compounds from limestone surfaces, thus preventing micro-organisms growth on the stone by removing their main nutrients supplies. In addition, 15~100 W plasma discharge can damage the microorganism by destructing the cell structures, eventually causing the removal of filamentous microbes, rupture of circular microbial cells and detachment of biofilm. CVI test provides evidence that plasma cleaning is comparable with autoclave sterilization with respect to its ability to kill microbes. In the cleaning protocol used in this study, Ar functioned as dry etching source and O_2 contributes to the oxidation of organic substance.

However, plasma etching is not able to achieve significant cleaning effect on limestone suffering severe bio-colonization, i.e., surface covered by thick lichen crusts. Figure 4.7 shows the comparison of a limestone tablet colonized by various lichen species before and after plasma treatment (Ar 90 sccm, O_2 60 sccm, 100 W, 30 min), it demonstrates no obvious change.

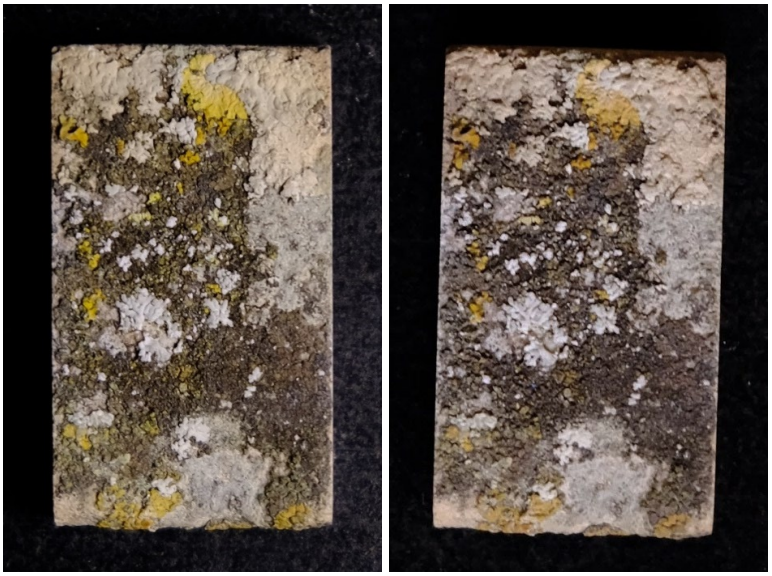

Figure 4.7. Lichen colonized limestone tablets before (left) and after (right) plasma etching.

Therefore, considering the short processing time, low input power, and the advantages of being non-toxic and eco-friendly, as well as its capability of removing initial-state microbial coatings and decomposing sugar substances, plasma etching can be considered a promising tool for reducing the risk of biodegradation of the stone monuments and other building materials. Nevertheless, the elimination of grave bio-crusts should be handed over to more intensive cleaning technique.

Chapter 5

The application of laser technologies for the removal of biofilms from limestone surfaces

5.1. Introduction

Laser ablation induced on optical absorbing substances is the foundation for conducting laser cleaning. When the laser irradiation fluence exceeds the intrinsic threshold of the material structure, the ablation occurs. This process could involve photothermal mechanism which leads to evaporation, or / and photomechanical and photochemical mechanism that leads to ablation and spallation [176]. Appropriate parameters are important for the laser cleaning effect, i.e., beam intensity can lead to surface ablation, local damage, melting to explosive vaporization along with the intensity and temperature increasing; shorter wavelength and wavelength differ from the object colour provides better absorption; smaller beam size has higher removal rate but the too small one can damage the object surface; long pulse duration produces high temperature and vaporization of substance, while ablation is originated by short-pulse lasers; dwell time (time between two pulses), if being too short, the ablated dust may interfere with the laser, being too long would prolong the cleaning process; by adjusting laser fluence and scanning speed, one can find balance between cleaning efficiency and surface damaging; laser incidence angle (glancing or parallel) is also an essential factor that defines angular laser cleaning or shock laser cleaning [177]. High temperature caused by long laser pulse would propagate heat inside the substance, the thermal diffusion length is positively correlated with the square root of the pulse duration multiply by the intrinsic material diffusivity [178]. Heat accumulation is also related to

the laser frequency, i.e., in a higher frequency, the second pulse will be released when the material's surface is not yet cooled down from the first pulse, the subsequent pulses would continue and yield a significantly higher heat accumulation comparing to a laser with lower frequency [179]. Other than these two main factors, repetition rate of the scanning laser, overlapping of the laser beam radius and materials' properties could all affect the temperature during laser treatment [180].

For the conservation of historical artworks, only pulsed laser systems have been used for their capability of limiting heat damages as compared with continuous-wave lasers. Even though, there are plenty variation of instruments. Divided by the lasing medium material, the most widely used is the Nd: YAG (neodymium-doped yttrium aluminium garnet; Nd: $Y_3Al_5O_{12}$), which emits wavelength at 1064 nm in the infrared zone and its harmonics by frequency doubling (waves with frequency at an integer multiple of 1064 nm), for example, 532 nm which is a green laser, and also 355 nm and 266 nm which are ultraviolet [181] [182]. Er (erbium): YAG was also considered promising for cleaning certain types of historical artefacts since 2001, it emits radiation at 2940 nm with low photon energy of 0.4 eV, functioning by photo-thermal disaggregation or micro-distillation with rare chemical changes, offering a gradual and better controlled cleaning process [183]. Other broadly used active laser mediums are: KrF (krypton fluoride) laser that generates wavelength at 248 nm, Ti:Sa (titanium-sapphire, Ti:Al_2O_3) fires 800 nm laser, TEA CO_2 emits infrared wavelength at 10.6 um, Yb (ytterbium): YAG laser and Nd: Van (vanadate, including YVO_4, $GdVO_4$, $LuVO_4$) lasers both are with wavelength of 1064 nm, GaAlAs laser emits 780 nm red light, XeCl (xenon monochloride) laser emits 308 nm ultraviolet light, etc [184]. Classified by operation mode, pulsed lasers could be divided into: mode-locked, Q-switched, pulsed-pumped and free-running. Q-switching (also named giant pulse formation or Q-spoiling) mode manipulates the cavity loss in order to accumulate energy in the lasing material, then release the energy to yield giant short pulses with hight peak power (up to gigawatt) and with pulse duration from nanoseconds (10^{-9} s) to microseconds (10^{-6} s) [185]. On the other side, mode-locking induces fixed phase relation among various laser cavity oscillating modes by interference, thus it is capable to produce extremely short pulses from picoseconds (10^{-12} s) to femtoseconds (10^{-15} s) with repetition rate of megahertz [186]. A pulsed laser beam can be generated also using the pulsed-pumping approach, which means the source itself is pulsed and can be tuned by controlling the pump modulation, without any costly and bulky intracavity modulators [187]. If the pulsed laser is not specified as the modes above, it is considered free-running, meaning that the laser emission lasts as long as possible for the pumping process, usually with a pulse duration of microseconds (10^{-6} s) to milliseconds (10^{-3} s) [188].

The earliest experiment showing the use of laser for artwork conservation (removing superficial black scabs from stone statuary) was carried out by Lazzarini et al. in the 1970s [189]. After 1990s, in line with the development of new laser systems and innovations in laser basic research and applications, laser cleaning has turned into a common restoration technique to be applied to a series of Cultural Heritage materials: a) paper - Nd:YAG laser and KrF laser were applied for removing inks, stamps, chalk and dirt from paper, it was found the lasers were effective when the materials to be removed did not penetrate the fibres too deep, and green laser had better removing performance and least side effects [190]. The Nb: YAG green laser was also experimented to clean the hyphae and mycelia of fungus that cause ancient paper discolouration, turning out to be more efficient than chemical bleaching [191]. b) metal - temperature-sensitive metal surfaces such as antique artworks made from copper, bronze, silver, and gold. Ti: sapphire femtosecond laser is a qualified technique to remove the corrosion and pigment coatings without damaging the objects [192]. KrF laser was proved to be a powerful tool for cleaning metal artifacts, i.e., by removing chlorine from bronze coins [193]. For the purpose for fine removal of the thin corrosion layer on the archaeological ironwork, liquid assisted cleaning process carried out with 1064 nm Nd: YAG laser could represent a fast and effective technique able to preserve fragile metal surfaces [194]. c) ceramics - Q-switched ruby laser was applied to clean the encrustation on the contaminated ceramic surface [195]. Dual sequential laser combined with biocide has been very effective in ablating cortical layers of the lichens colonizing ceramic roof tiles [196]. Besides cleaning, TEA CO_2 laser and Nd: YAG laser were also used for eliminating surface defects and strengthening objects by melting the superficial layers [197]. d) mural paintings – Er:YAG laser at 2940 nm wavelength was tested to clean the linseed oil or “beverone” from the mural paintings, the laser was able to remove the organic layers without surpassing the pigment damage threshold [198]. This laser has also been applied for removing aged shellac varnish from mural paintings: as compared with chemical cleaning, laser cleaning has been found to be more gradual and able to operate at a smaller localized scale [199]. e) stones - in Europe, there are large numbers of stone sculptures, monuments, historical buildings and facades. Laser has been widely applied on the stone artefacts restoration, to remove the old patina, pollution encrustation and decay crusts. For instance, Nb:YAG laser has been proved to be a fast and well-controlled technique to clean the black gypsum crust developing on limestones as results of sulphation in outdoor urban environments [200]; two wavelength methodology of combining 1064 nm and 355 / 535 nm lasers has been developed to remove, for instance the biological films and patinas developing in stone buildings and statues in Athens [201].

In order to better control the laser ablation process and check the possible associated damage occurring on the treated substrate, in-situ and portable monitoring / evaluation instrumental capabilities have been added to the laser cleaning protocols used for CH materials. One of the most widely used tools is the Laser-Induced Breakdown Spectroscopy (LIBS), a non-destructive technique that is able to obtain both qualitative and quantitative elemental compositional data of the treated substance. LIBS has already been successfully used for analysing a variety of Cultural Heritage materials such as pigments in paintings, pottery, metals, etc. [202]. Another laser-based monitoring workstation has been tested by exploiting the photomechanical effects: by tracing interference generated patters of the synchronized laser beam, it is possible to acquire the relevant displacement of the surface expressed in spatial coordinates during the laser ablation [203]. There is also a non-standard system which is the on-line optical diagnostics based on the shadow-graphic and spectroscopic analyses [204]. Besides those, an innovative technique is named photoacoustic (PA) monitoring: by integrating low noise photoacoustic amplitude measurements, it establishes correlations that enabled to differentiate discreet stages in laser cleaning process such as over-layer ablation, effective cleaning, and substrate damaging. This method could predict the onsets of effective cleaning and substrate's damage, improving the cleaning outcome [205]. The PA monitoring has been recently applied to various kinds of stone and solid paper objects [206] [207].

In the past decade, several research articles have started reporting the use of laser cleaning towards the effective removal of lichen patinas and crusts from building stones in monuments. Free-running infrared (2940 nm) Er: YAG laser, for instance, was shown to be able to destruct lichen cell walls [208]. Nanosecond infrared (1064 nm) Nd: YAG laser at 5 ns pulses and 2.0 J/cm^2 fluence proved to be effective in the removal of Verrucaria Nigrescens lichen thalli on dolostone and, at the same time, destroy the fungal and algal endolithic cells [209]. The efficacy of nanosecond Nd: YAG laser and Er: YAG laser for removing biofilm on granite were also tested: these lasers, though were found to induce biotite melting which might affect physical properties of the stone [210]. In another research, it was suggested how the sequential dual irradiation (1064 nm and 355 nm) Nd: YAG laser could represent and viable approach for removing bio-colonization crusts on the dolomite heritage stone [211]. A comparative study was carried out using nanosecond Q-switched Nd: YAG lasers of different wavelengths (1064 nm, 355 nm, 266 nm) together with the sequencing IR-UV laser, for cleaning lichens on the Valonsadero sandstone and Alpedrete granite, results showed the laser treatment to be clearly inducing substantial damage of the lichens, but without achieving their complete removal [212]. Ultraviolet (355 nm) Nd: YVO_4 laser was used for removing lichens from granitic stone, its cleaning performance being compared

with mechanical procedure by scalpel: results indicated that the effectiveness of laser treatment was higher than that of mechanical along, while combination of the two protocols proposed as the one providing even better results [213]. Industrial developments in shortening the laser pulse duration have opened up new applications also in the field of conservation and restoration. A comparative study between femtosecond Ti: Sapphire in 790 nm and 395 nm with the nanosecond Nd: YVO_4 355 nm laser in removing biological crusts from granite suggested that the femtosecond laser in both IR and UV wavelengths performed well and respected the original substrate morphology as compared to the nanosecond laser [214]. In another article focusing on laser-induced discoloration effects after cleaning stones and painted artefacts, the ultrashort femtosecond-based laser systems were shown to overcome the limitation of longer pulses lasers due to their minimisation of the photo-thermal, photochemical, and photo-mechanical phenomena, thus avoiding melting and bubbling effects and the formation of cracks on the ablated substrate [215].

From the above, one could see that the laser system, involving pulse duration, wavelength, repetition etc, and the intrinsic properties of the ablated materials are all parameters that could affect the cleaning outcome and effectiveness. Aim of this chapter was to test the efficacy of four irradiation-mode laser systems to remove the biological crusts and biofilms from the Batalha Monastery oolitic limestones, the effect of cleaning result and possible alteration of the substrate caused by different laser systems and operation conditions will be investigated.

5.2 Methods and Materials

5.2.1 Bio-deteriorated limestone samples

Two types of samples were used for the laser cleaning experiments: (I) First type (Figure 5.1 a) was the original severely deteriorated limestone from the Batalha Monastery roof showing at its surface a microbial crust consisting of lichens, fungi and bacteria (Figure 5.1 b) as discussed in Chapter 3. The thickness of the biocrust can reach 50 - 700 μm (Figure 5.1 c, d). (II) The second category were the limestone samples from the five quarries identified as the source of the building stone material for the Batalha construction and restoration (Chapter 1). All samples were cut into tablets of 5 x 5 x 1 cm and field exposed on the roof of the Batalha Monastery for 20 months from September 2019 to May 2021 (see Figure 5.2).

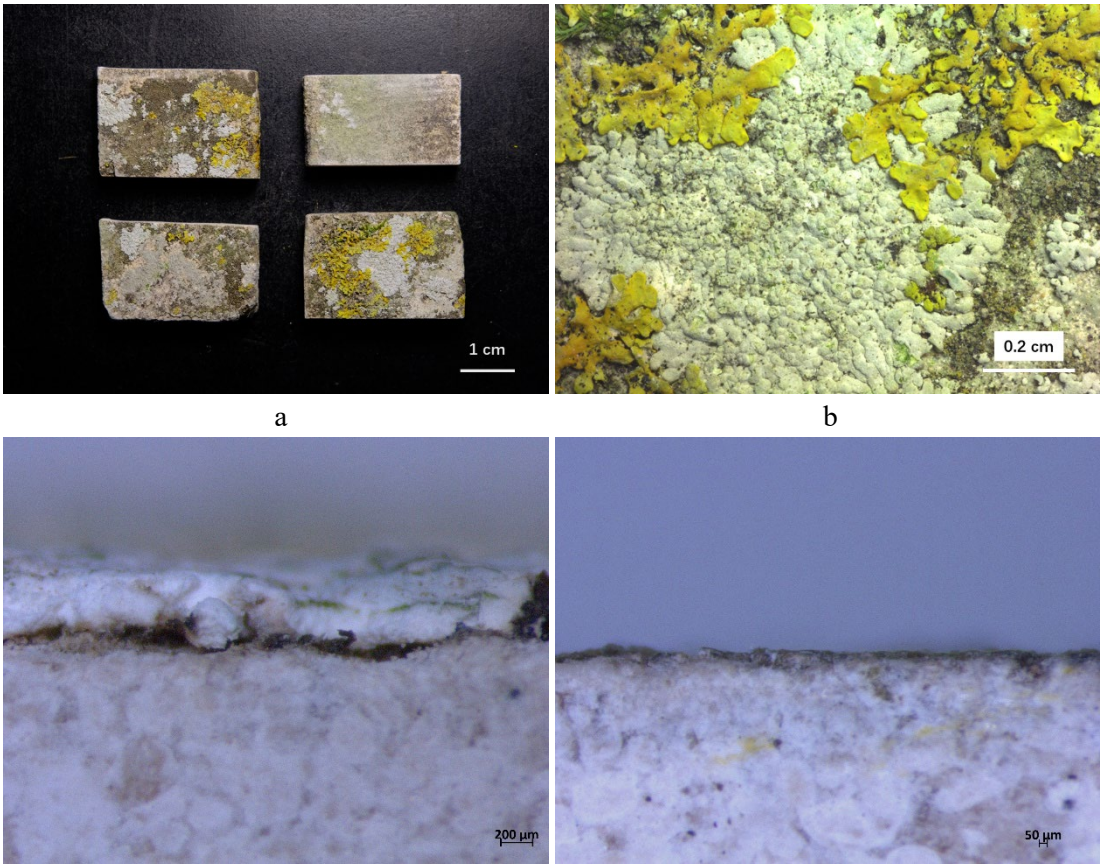

a b

c d

Figure 5.1. Bio-deteriorated limestone samples from the Batalha Monastery: a. overview; b. dino-light digital microscopy of lichenous patinas on the surface; c and d. side views of the tablets.

Figure 5.2. Natural exposed sample (left) and its surface under OM (right).

5.2.2 Laser cleaning using different irradiation modes

All the laser facilities (Figure 5.3) used in this research came from the Instituto de Nanociencia y Materiales de Aragón (INMA-CSIC- Zaragoza Spain). Laser cleaning tests using various parameters were firstly carried out on in small areas of 5 x 5 mm of the samples, as determined by preliminary analysis – optical microscopy and confocal microscopy. Cleaning operational conditions were then optimized and conducted on larger areas of the limestone samples.

Femtosecond UV laser

The femtosecond ultraviolet laser used (Figure 5.3 a) is a Yb:YAG laser (Carbide CB3-40W, Light Conversion, Vilnius, Lithuania), with average output power at 11 W, centre wavelength of 343 nm, beam size ~30 μm and pulse duration of 238 fs. The PPD (pump-probe depletion) of the laser is adjustable. In this research, cleaning tests were carried out at the following operating conditions: power attenuation ranging from 30% ~ 100%; frequencies 2 kHz – 200 kHz; distance between laser scanning lines at 0.005 – 0.030 mm; scanning speeds from 300 to 3000 mm/s.

Picosecond UV laser

The picosecond ultraviolet laser used (Figure 5.3 b) (Rofin-Sinar PowerLine Pico 10-355) had a maximum power of 3 W, laser wavelength of 355 nm, beam diameter of ~ 32 μm inferred using the D2 method proposed by Liu et al. [216] and pulse duration of 300 ps. In the tests presented in this chapter, the following operating conditions were used: frequencies ranging from 250 to 800 kHz at a pump power of 9A, scanning speed from 2000 – 5000 mm/s, distance between laser scanning lines from 0.002 to 0.020 mm. The scan process was repeated between 5 and 80 times.

Picosecond IR laser

This picosecond infrared laser (Figure 5.3 c) (PowerLine Pico 10-1064, Rofin-Sinar, Germany) had a maxim output power at 8 W with a galvanometer mirror system, laser wavelength of 1064 nm, pulse duration of 800 ps, the laser beam waist diameter (1/e 2 criterium) is approximately 79 μm as deduced following the D2-method [217]. In the experiments presented in this chapter, frequencies ranging from 200 to 800 kHz were setted at a pump power of 4.5 - 9A. Scanning speed was at 500 – 3000 mm/s, line width was from 0.001 to 0.020 mm, repeating 1 – 5 times.

Nanosecond IR laser

The nanosecond infrared laser (Figure 5.3 d) is an Ytterbium-pulsed fiber laser (model PEDB-400B, Perfect Laser, Co., Ltd., Wuhan, China), with central wavelength λ = 1060 ~1070 nm, under different pulse repetition frequencies (frep) and pulse duration (tp) values. The focusing of the laser beam was achieved by a flat field scanning lens system (effective focal length of 163 mm), resulting in a beam diameter of 65 μm [218]. Experimental conditions in this study were the following: power attenuation 60% - 100%, frequency 70 -600 kHz, scanning speed 500 – 1000 mm/s, pulse duration 5 ns and distance between laser scanning lines set at 3.6 – 7.1 μm.

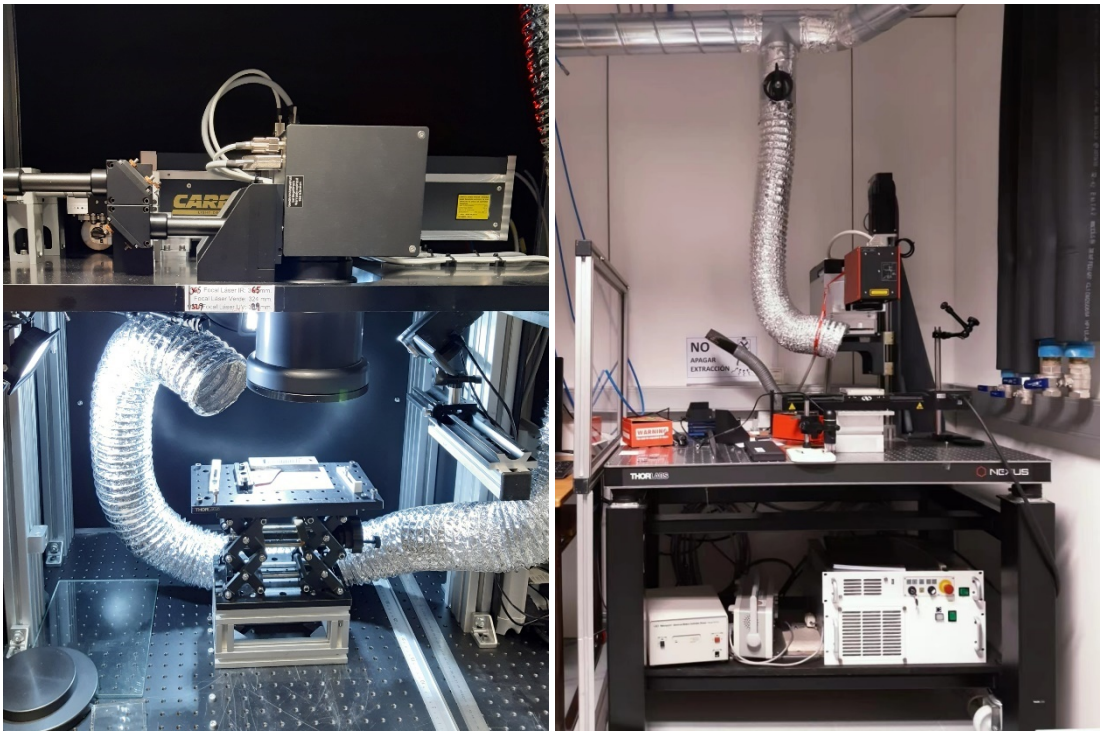

a b

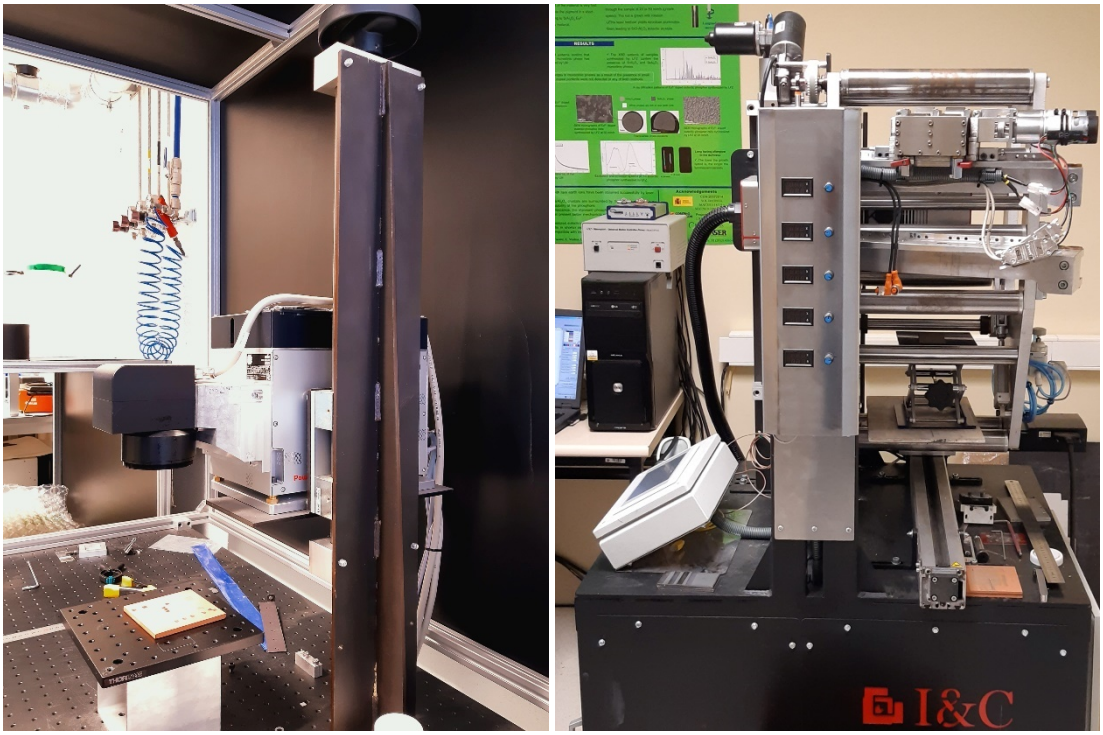

c d

Figure 5.3. Laser instruments used in the cleaning of stones: a) fs-UV laser; b) ps-UV laser; c) ps-IR laser; d) ns-IR laser.

5.2.3 Characterization of laser-induced surface alteration and cleaning effects

Optical microscopy

The stone surface after laser cleaning was observed by optical microscopy (MC80Dx OM, Zeiss, Jena, Germany) from INMA (CSIC-University of Zaragoza, Zaragoza Spain), in order to visually assess differences between pre- and after treatment areas.

Confocal Microscopy

A Sensofar PLμ2300 confocal microscope from INMA (CSIC-University of Zaragoza, Zaragoza Spain) was used to investigate the surface morphology and topography of the samples. The equipment was equipped with four confocal objectives (x10, x20, x50 and x100) and two interferometric ones (x10, x20). By combining the advantages of confocal technology on steep slopes and for rough surfaces with the compatibility to interference technique, this 3D optical profiler system was able to provide 3D topographic image of sample surface.

X-ray micro-diffractometry (μ-XRD)

Changes in substrate composition in the laser cleaned stone surfaces was characterized by μ-XRD. Instrument and operating parameters were the same as described in previous chapter 2, section *2.2.4 X-ray micro-diffractometry (μ-XRD).*

Cell viability index (CVI/MTT assay)

CVI measurements was aimed to assess the microbial viability remained on the limestones after laser cleaning. The instrument and process were the same as described in chapter 3, section 4.2.4 - *Cell viability index.*

Variable-pressure scanning electron microscopy (VP-SEM)

The laser cleaned stones were also observed by VP-SEM, both on the surface and resin-consolidated cross-section. The instrument and operating condition were the same as described in chapter 2, section *2.2.5 Variable-pressure scanning electron microscopy coupled with energy dispersive spectrometry (VP-SEM + EDS).*

5.3 Results and Discussion

5.3.1 Preliminary assessment and laser parameters optimization

The original stone from Batalha Monastery covered by biocrusts was assessed by μ-XRD and combined with results from *Chapter 3 Biodegradation and Microbial Contamination on the Limestone Surfaces of Batalha Monastery*, The bio-patina showed a distinct composition from the limestone substrate (>97% calcite and 1~2% quartz), as shown in *Chapter 1 Provenance study of the limestone used in the construction and restoration of the Batalha* Monastery. It could be seen that weddellite and whewellite were the major minerals on lichen and microorganism covered areas, the calcium oxalates (whewellite with the addition of weddellite) concentration ranging from 43% to 78%, with the calcite only less than 50%, evidencing the chemical attack on the carbonate stone induced by microbial colonization.

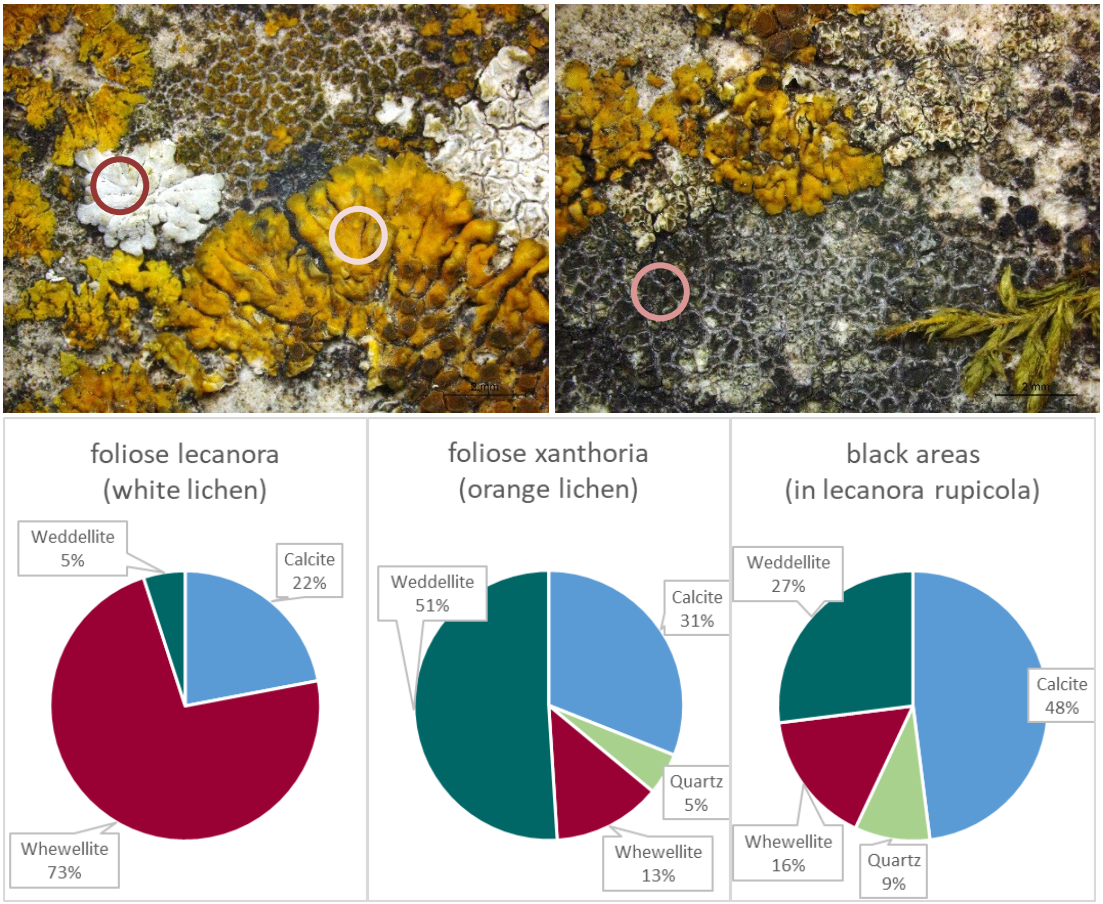

Figure 5.4. The mineral composition of lichen-covered areas on limestone from Batalha Monastery.

Summarizing from *Chapter 3 Biodegradation and Microbial Contamination on the Limestone Surfaces of Batalha Monastery* and combining the illustration by Geoffrey et al. [221], the stable microbial-films grown on rock substrate consist of a) feldspars, clay and/or windborne dust particles and mineral grains deposited at the outer surface parts of the biomass; b) oxalates and other secondary minerals formed in the lichen thallus, interface and subsurface; c) oxalates and secondary minerals also present in cavities, cracks and holes of the rock substrate penetrated by microorganism hyphae (Figure 3.5 and Figure 3.6). Thus, the mineral composition acquired by XRD could be used for evaluating how deep inside the substrate the laser cleaning was effective .

These lichen-covered tablets then went through various lasers cleaning modes for experimenting the optimized operating parameters. Figure 5.5 shows the 5 x 5 mm cleaned areas on the sample tablets, and Annex 5A illustrates the microscopic photographs of each area. The areas where specific operating conditions resulted in a better cleaning effect, i.e., by obtaining homogenous colour and removing most if not

all the lichenous debris, are marked with blue squares. The optimized laser operating conditions were then applied to larger areas in the next section.

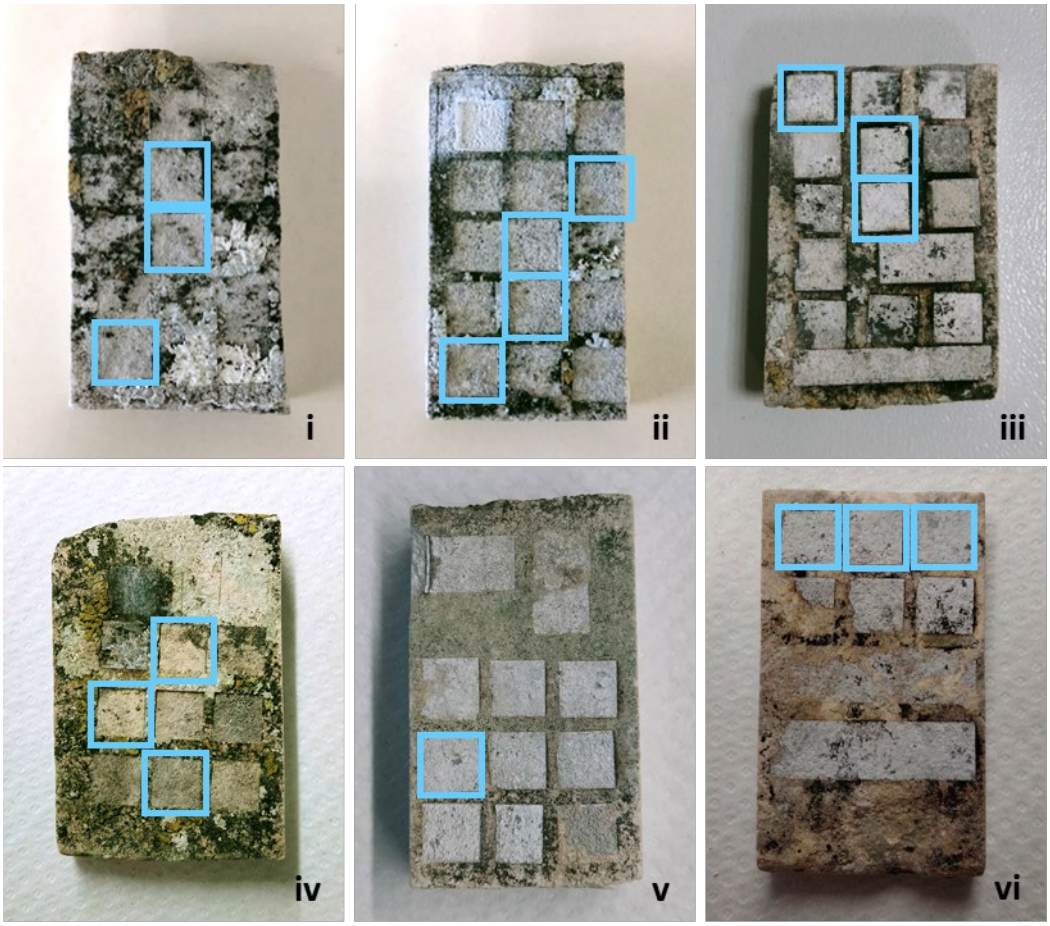

Figure 5.5. Stone tablets with 5 x 5 mm treated areas by different laser modes: (i) tablet C, treated by fs-UV laser; (ii) tablet E, fs-UV; (iii) tablet G, ps-IR laser; (iv) tablet H ps-UV; (v) tablet I, by ns-IR laser; (iv) tablet J, treated by ns-IR laser.

5.3.2 Laser cleaning effect on limestone showing severe bio-colonization

Stone samples treated by femtosecond UV laser

The bio-patina covered tablets before and after femtosecond (FS) UV laser ablation are shown in Figure 5.6, and the operating parameters are listed in Table 5.1, Laser parameters were selected in order to maintain a distance between laser pulses of 0.015 mm in the laser scanning direction and in the direction perpendicular to it. It is evident that different laser parameters led to different cleaning effect on each treated area. The

micrographs of the treated areas are presented in Figure 5.7, while Figure 5.8 illustrates the XRD data together with their semi-quantification results.

As observed under the OM in Figure 5.6, zone I of the fs-UV treated tablet showed effective cleaning results, with most of the lichen crusts ablated and the treated surface clean and smooth. By zooming up, a few black spots which are the residues of the lichens can still be seen present on the stone surface. The original morphology of the oolites in the limestone (see Figure 5.2) were replaced by amorphous and irregular grains in various shades of white colour. This matches the dissolution and reprecipitation of calcium minerals in the bio-decay as described in *Chapter 3*. As seen from SEM images (Figure 5.7), although bio-colonization were mostly removed, large amounts of pores and ditches were remained. Zone II had quite amount of lichen remnants. The compensation of lower speed and lower frequency in the operation parameters used for cleaning zone II ended in the same spacing as in zone I, but the laser scan direction was single, which made the cleaning effect inferior than that of zone I (which had two perpendicularly intersecting scan directions). Seen from microscopic and SEM graphs, the crustose lichen is partially damaged, revealing the green chloroplast from cyanobacterial or algae, and the black medullary fungal hyphae underneath the upper cortex or coming out from the cracks of the cortex [219]. From the cross-section microscopic image of zone II, hyphae roots can be seen 0.5 mm below the surface. Zone III was applied by fs-UV laser with faster scanning speed, higher power attenuation and more repeating times, however the cleaning effect was not as superior as zone I. From the SEM images of zone III, it can be seen more clearly that pores and ditches left by the microorganisms are at 5~20 μm (pore diameter) and 20~60 μm (ditch length), inside which there were microorganism residues remaining. Though being tiny in dimension, these pores would enhance the water retention, allow salt crystals grow inside, and alter the mechanical stress in the substrate [220] [221]. Therefore, the stone surface once been invaded by lichens and fungus, even if the colonization covering is removed, the substrate would still behave substandard than the intact one. Another observation is that on zone III, the cleaning process seems more effective in the left part than the right one, there are two possible explanations: the lichens grown on the left part have higher absorption of the laser energy, or the crustose lichen covered the right side has higher resistance against the damage than the foliose lichens on the left. Lichen specie could influence the laser cleaning effectiveness, such phenomenon was also observed by other researchers [222].

The semi-quantitative results acquired from XRD analysis show that the mineral composition of all the laser cleaned area are 95~96% calcite and 4~5% quartz. The relatively higher ratio of quartz to calcite comparing with the freshly cut limestone (1% quartz and ~98% calcite) could be due to the higher resistance against microbial-acid

attack of quartz, while calcite was more easily weathered and detached from the limestone substrate, quartz remained and possessed higher portion.

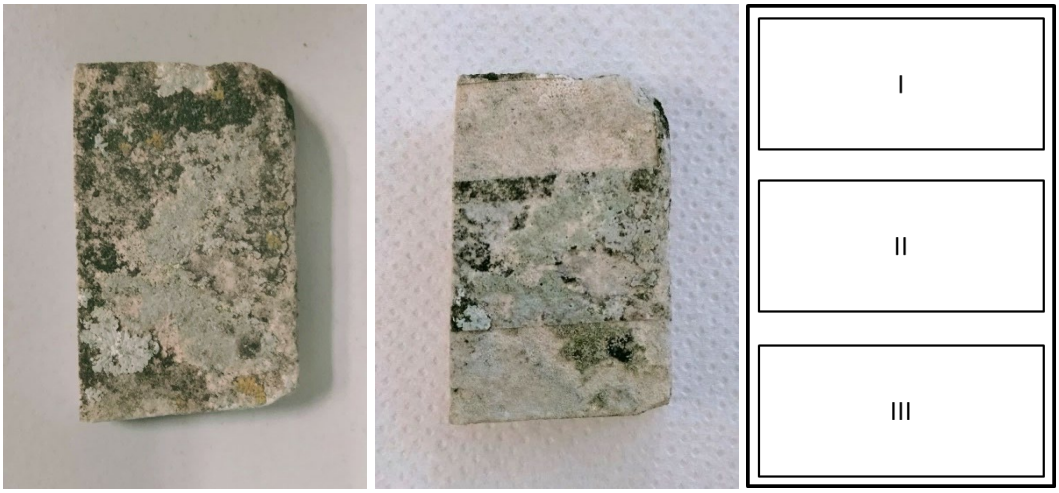

a b c

Figure 5.6. Sample tablet for fs-UV laser treatment. a. before cleaning; b. after cleaning; c. three cleaned zones treated with different laser parameters.

Table 5.1. Operation parameters of fs-UV laser for treating the sample.

Treated zone	**Unit**	**I**	**II**	**III**
Pulse duration	fs	238	238	238
Attenuation		45%	45%	60%
Actual power	W	1.749	1.749	3.244
Frequency	kHz	100	10	200
PPD		2	20	1
Energy per pulse	µ J	8.75	8.75	16.22
Fluence per pulse	J/cm^2	0.93	0.93	1.73
Irradiance	GW/cm^2	3925	3925	7281
Scan speed	mm/s	1500	150	3000
Laser dots distance	mm	0.015	0.015	0.015
Scanning line distance	mm	0.015	0.015	0.015
Average fluence	J/cm^2	3.9	3.9	7.2
Scan direction	-	0°+ 90°	90 °	45°+ 135°
Repetition	-	10 (*2)	10	15 (*2)
Total fluence	J/cm^2	78	39	216
Laser shots pattern		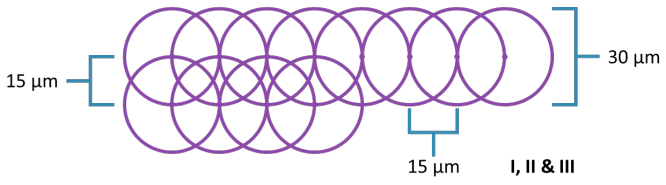		

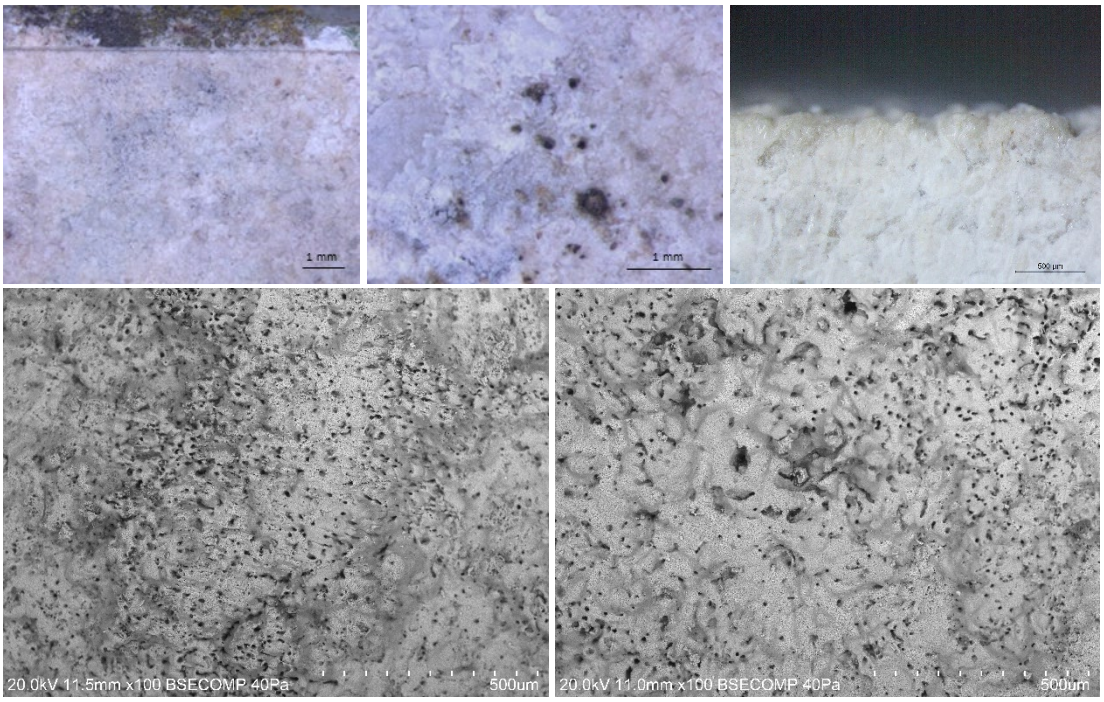

ZONE I (top: OM photos. bottom: SEM images)

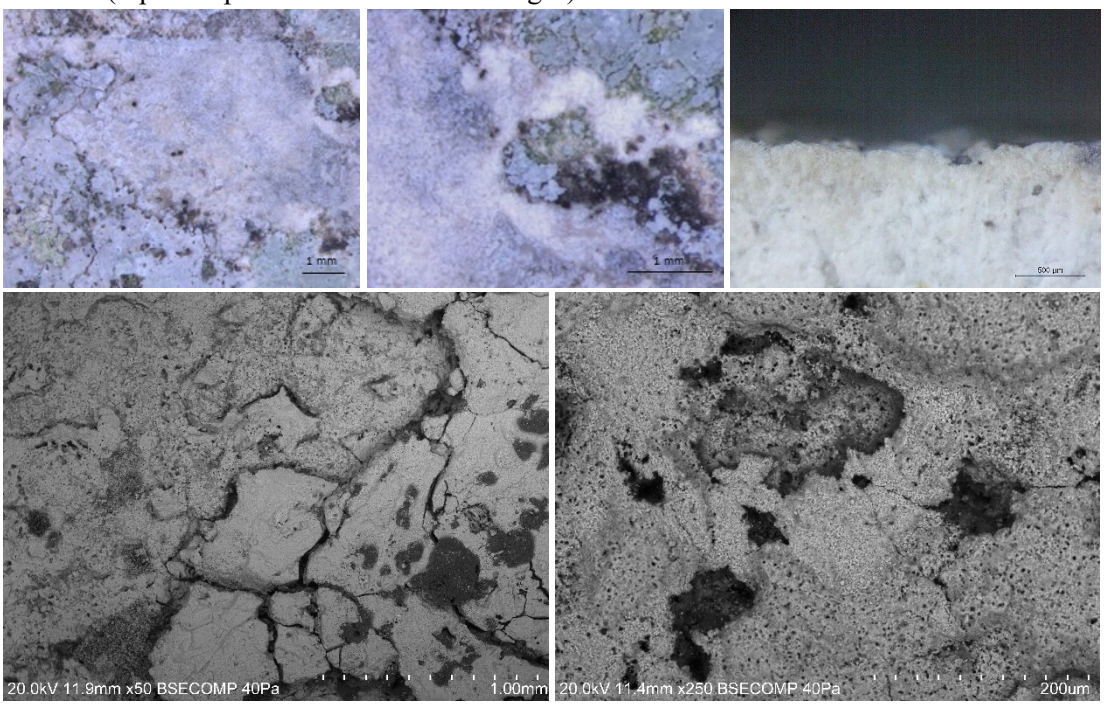

ZONE II (top: OM photos. bottom: SEM images)

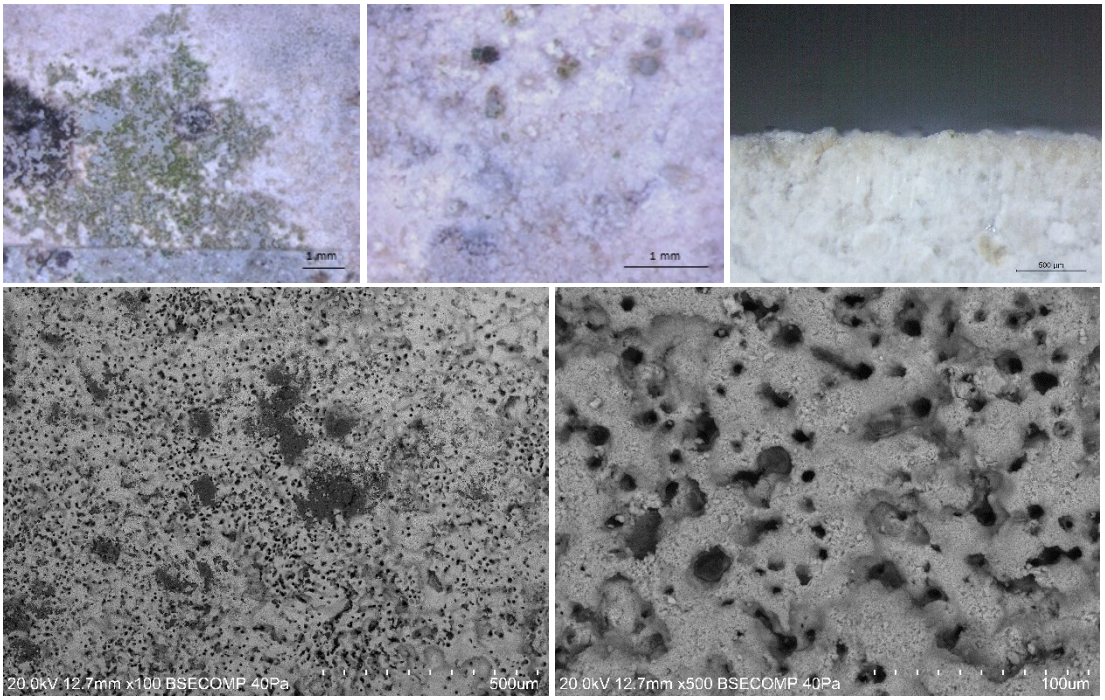

ZONE III (top: OM photos. bottom: SEM images)

Figure 5.7. Optical microscopy and SEM image of the fs-UV laser cleaned sample surface.

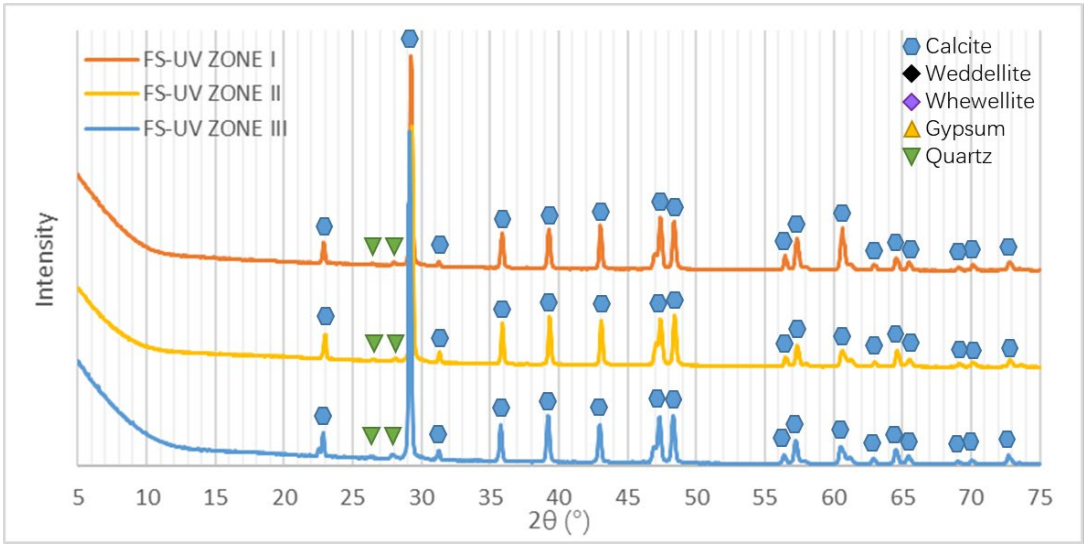

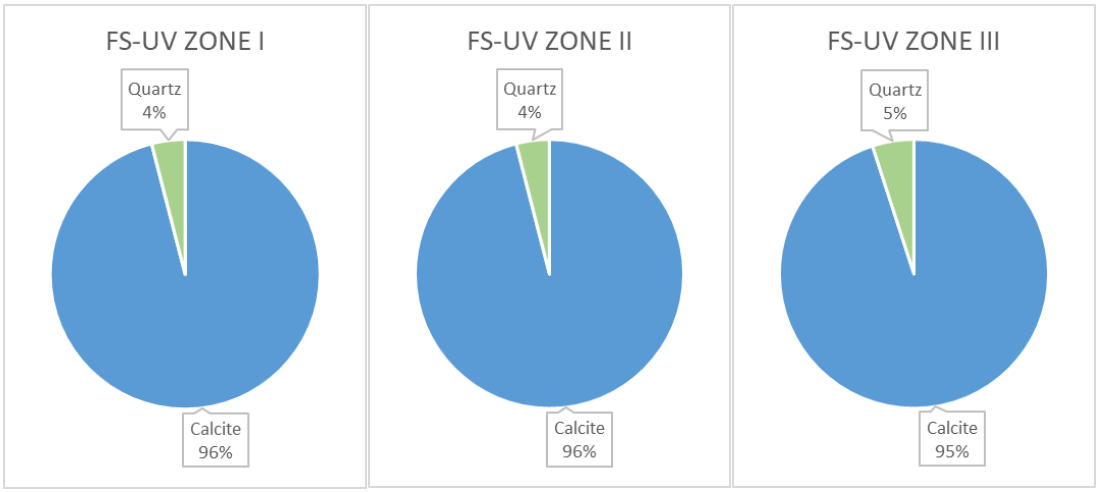

Figure 5.8. XRD and semi-quantitative results of the sample cleaned by fs-UV laser.

Stone samples treated by picosecond UV laser

The experimental data of the stone sample treated by ps-UV laser is listed below: Figure 5.9 shows the photo of sample before and after treatment, the operation parameter of laser applied on each zone is listed in Table 5.2.Then Figure 5.10 presents the OM and SEM images of each treated area, while Figure 5.11 presents the XRD results and mineral composition of each treated zone.

Evaluated from the sample photo and microscopic images, zone II of this ps-UV laser cleaned sample had the best appearance in which the lichens were mostly removed. Laser parameters applied on this zone II had narrower line spacing and lower scanning speed comparing to zone III, while other conditions (power, frequency, repeating times) were the same, resulting in a four-times higher average fluence from 2.8 to 11.2 J/cm2 over zone III, with a cleaning duration four times longer. In order to be able to ablate the bio-colonization, however, higher scan density is essential which would also require longer cleaning times. Zone II underwent intersecting scanning while zone I had only one scanning direction: it was obvious that orthogonal cleaning orientation resulted in a better cleaning effectiveness.

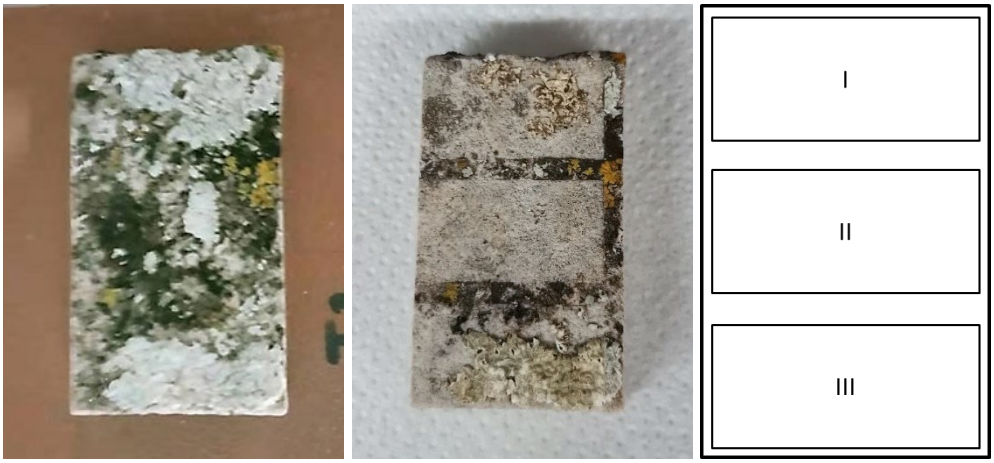

Figure 5.9. Sample tablet for ps-UV laser treatment: before cleaning (left), after cleaning (middle), and three zones with different treating parameters (right).

Table 5.2. Operation parameters of ps-UV laser for treating the sample.

Treated zone	**Unit**	**I**	**II**	**III**
Pump power	A	9	9	9
Actual power	W	1.79	1.79	1.79
Frequency	kHz	250	250	250
Energy per pulse	µ J	7.16	7.16	7.16
Fluence per pulse	J/cm^2	0.92	0.92	0.92
Irradiance	GW/cm^2	3.06	3.06	3.06
Scan speed	mm/s	2000	2000	4000
Laser dots distance	mm	0.008	0.008	0.016
Scanning line distance	mm	0.008	0.008	0.016
Average fluence	J/cm^2	11.2	11.2	2.8
Scan direction	-	0°	0° + 90°	0° + 90°
Repetition	-	20	10 (*2)	10 (*2)
Total fluence	J/cm^2	224	224	56
Laser spots pattern		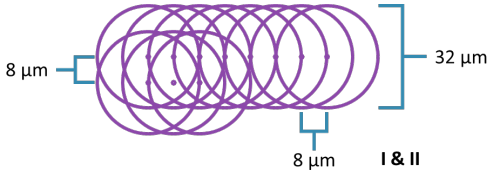		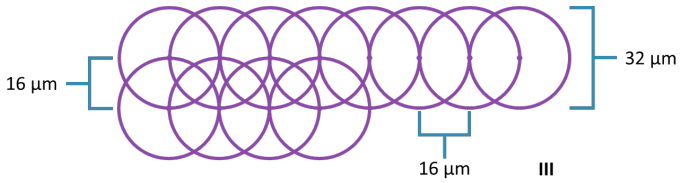

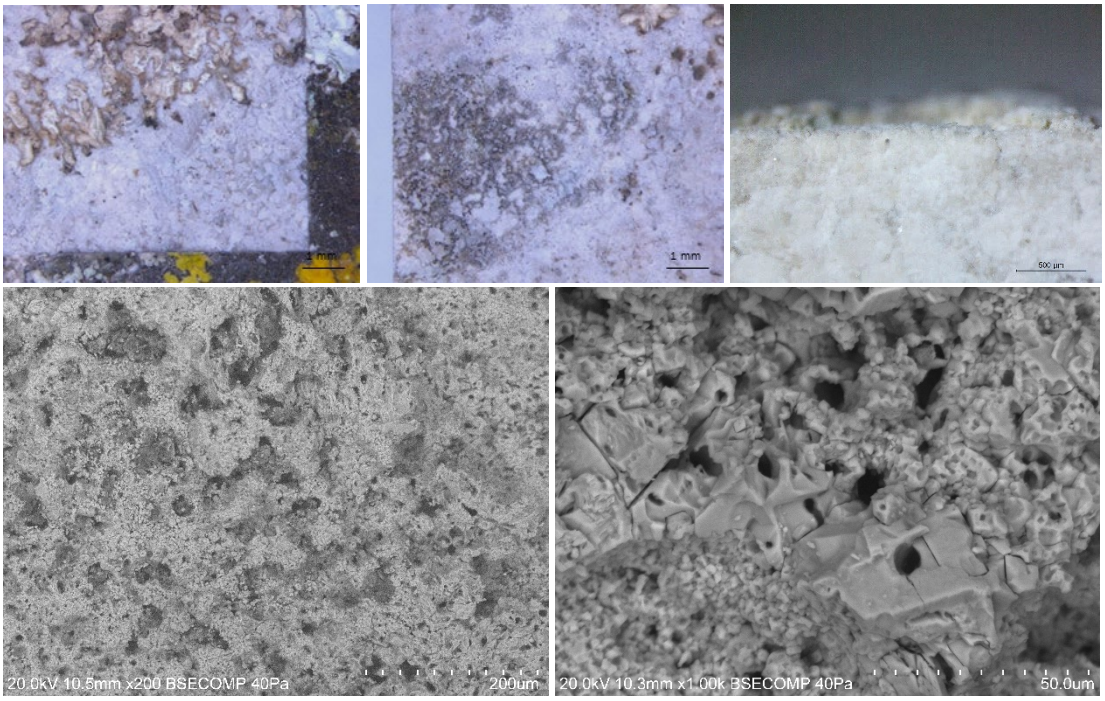

ZONE I (top: OM photos. bottom: SEM images)

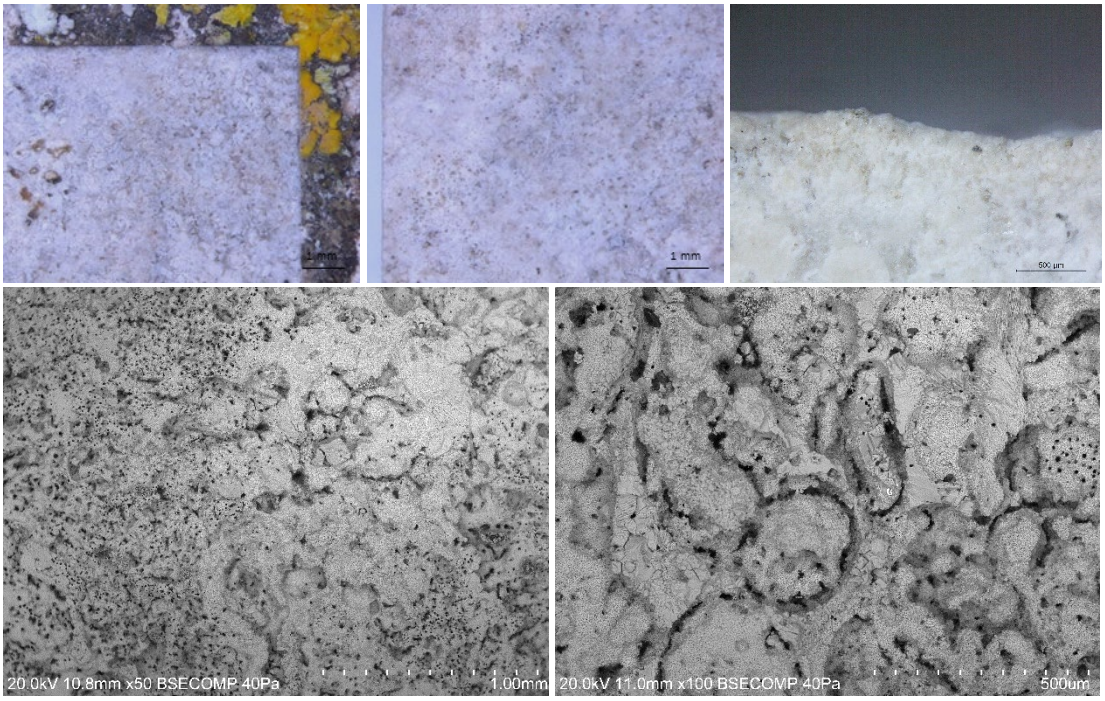

ZONE II (top: OM photos. bottom: SEM images)

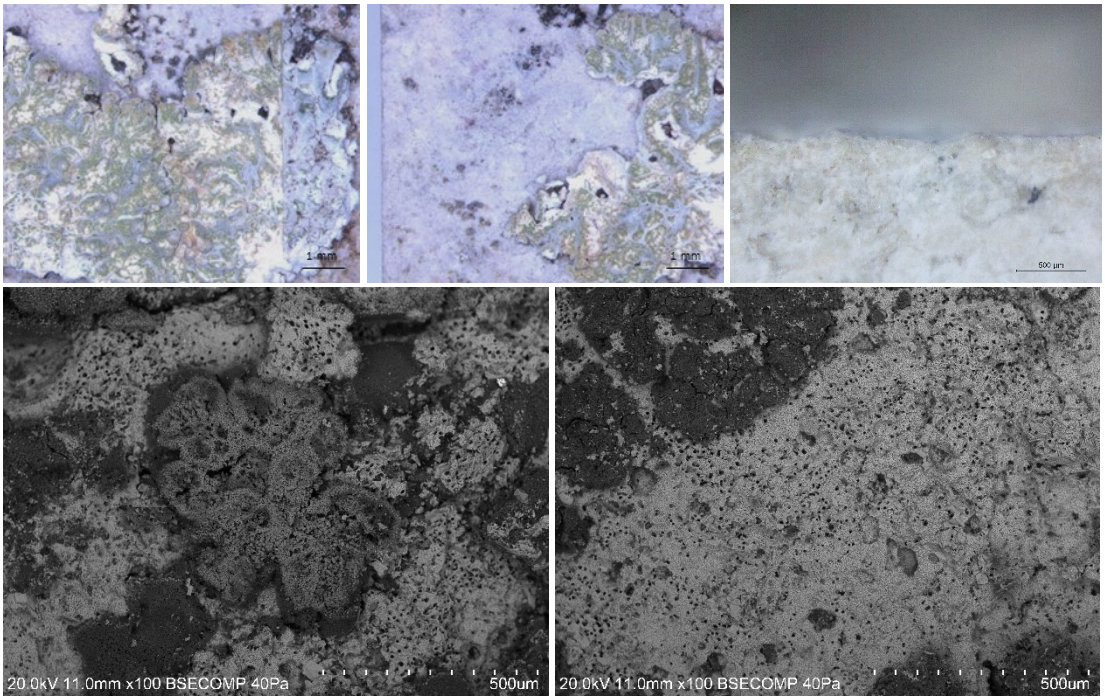

ZONE III (top: OM photos. bottom: SEM images)

Figure 5.10. Optical microscopy and SEM image of the ps-UV laser cleaned sample surface.

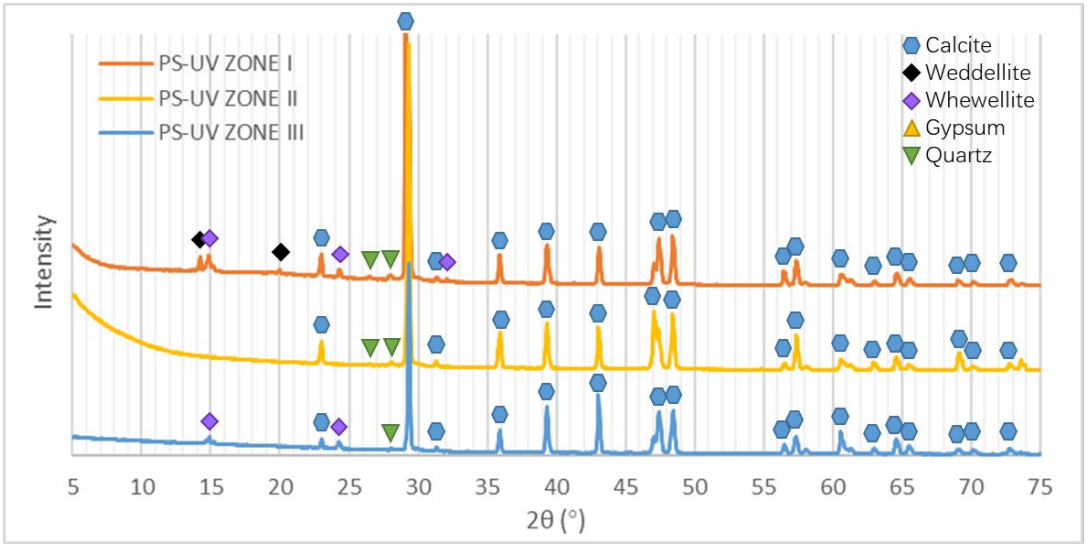

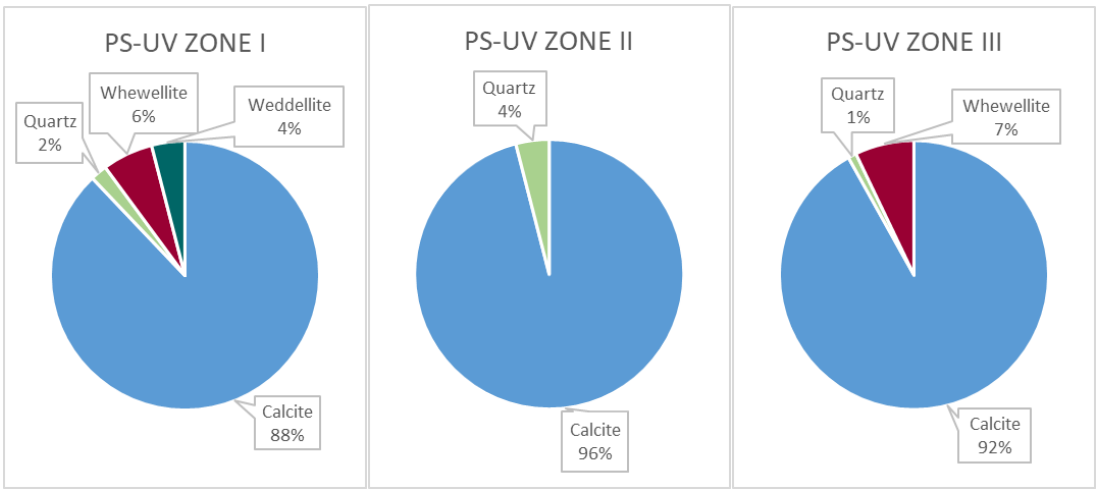

Figure 5.11. XRD and semi-quantitative results of the sample cleaned by ps-UV laser.

SEM photos show microorganism residues still present in gaps and holes in zone I; in zone II no apparent microbial remnants were visible after the treatment, the outline of oolites show higher damage effects caused by the laser ablation probably because they were filled with higher porosity acicular calcite crystals as compared with the sparitic cement; ; on zone III the surface was only partially cleaned as the lichen thallus can still be seen with cortex damaged and revealing the inside of the lichenous structure.

XRD results suggest that on zone I and zone III of the ps-UV laser treated tablet, calcium oxalates are still present: 6% whewellite and 4% weddellite on zone I, 7% whewellite on zone III, indicating the cleaning was not thorough. On zone II there were no oxalates but only calcite and quartz, which complies with the appearance, evidencing the cleaning was more in-depth.

Stone samples treated by picosecond IR laser

The experimental data of the stone sample treated by ps-IR laser is listed below: Figure 5.12 shows the sample before and after treatment, the operating conditions of laser applied on each zone are listed in Table 5.3. Figure 5.13Figure 5.10 presents the OM and SEM images of each zone, and Figure 5.14 presents the XRD results and mineral composition of each treated area.

The most distinguishing feature consists in the treated zones showing different colours as compared with the samples treated by fs-UV laser and ps-UV laser. This effect was also evident under OM and SEM microscopic imaging: non-homogenous whitish hue on a yellowish background, the presence of a white thin surface layer (< 100 um) can be seen from the side view (see Figure 5.13 zone I and zone III). The surface morphology under SEM was more shattered than the ones treated by UV lasers:

for instance, zone I of the ps-IR laser treated sample present many fragments around 20 μm in diameter or less, and the bulk substrate is full of tiny pits (~5 um) (indicated by the white circle in fig. 5.12. In the SEM photo of zone II, marked by the white frame, it could be seen more clearly that those fragments were originally following the morphology of the substrate, indicating they were cracked and then fell off from the bulk substrate. SEM photo of zone III reveals the presence of melting features, collate with the microscopic image, such thing should be the white substance observed on the surface.

The XRD analysis revealed something noteworthy: besides calcite, quartz and whewellite which came from the stone and/or the microbial colonization, portlandite (calcium hydroxide) and lime (calcium oxide) were also found (Figure 5.14). This implies that some of the primary minerals, either calcite or calcium oxalates (or both) underwent thermal decomposition, which means the ps-IR laser led to very high temperature at the stone surface.

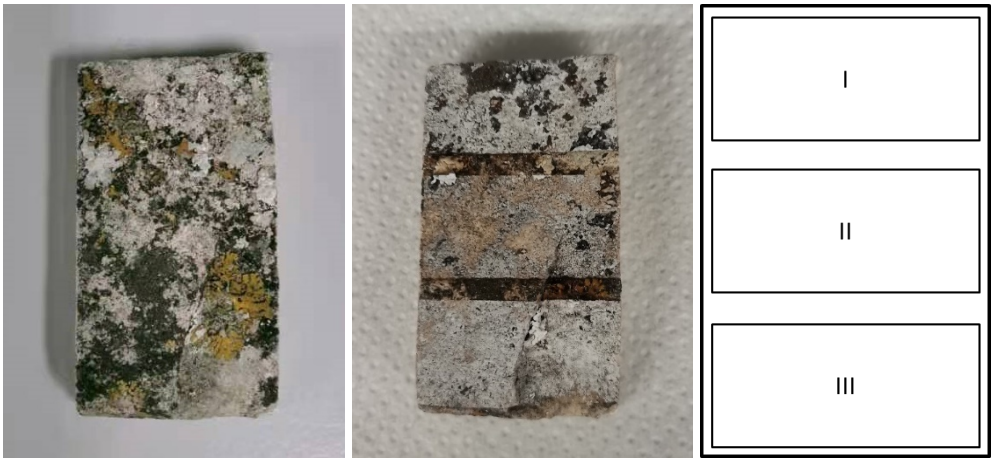

Figure 5.12. Sample tablet for ps-IR laser treatment: before cleaning (left), after cleaning (middle), and three zones with different treatment parameters (right), see also Table 5.3.

Table 5.3. Operation parameters of ps-IR laser for treating the sample.

Treated zone	**Unit**	**I**	**II**	**III**
Pump power	A	9	9	9
Power	W	7.2	7.2	7.2
Frequency	kHz	800	400	800
Energy per pulse	μ J	9.00	18.00	9.00
Fluence per pulse	J/cm^2	0.18	0.37	0.18
Irradiance	GW/cm^2	0.23	0.46	0.23
Scanning speed	mm/s	500	1000	500
Laser dots distance	mm	0.000625	0.0025	0.000625
Scanning lines distance	mm	0.001	0.001	0.002

Average fluence	J/cm^2	1440	1440	720
Scan directions		0º	0º	0º
Repetitions		5	5	3
Total fluence		7200	7200	2700
Laser spots pattern		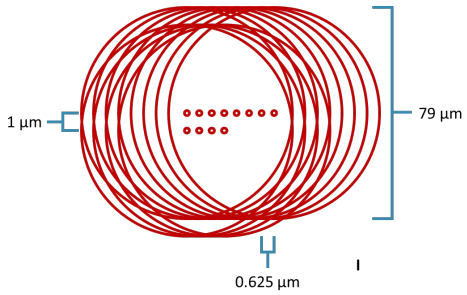 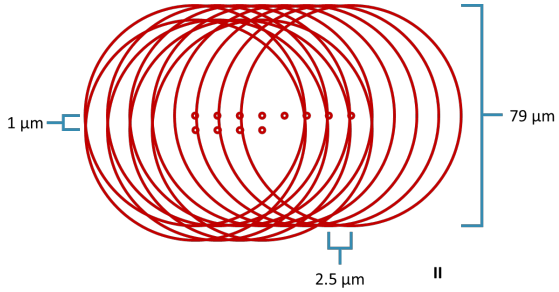 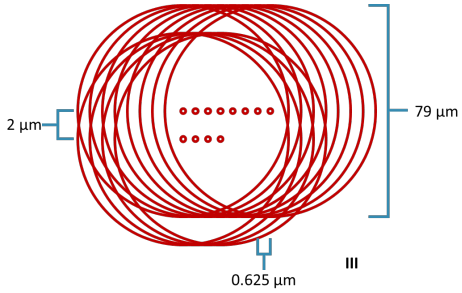		

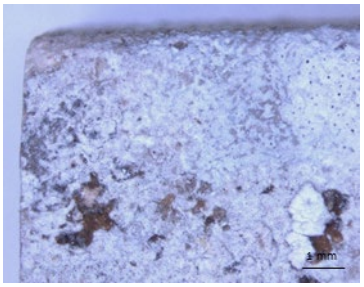
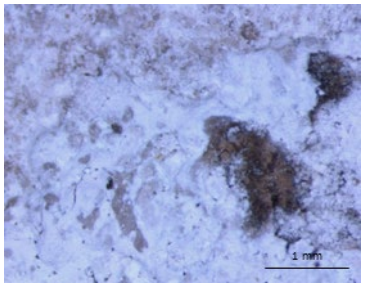
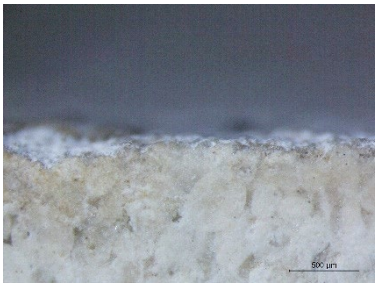

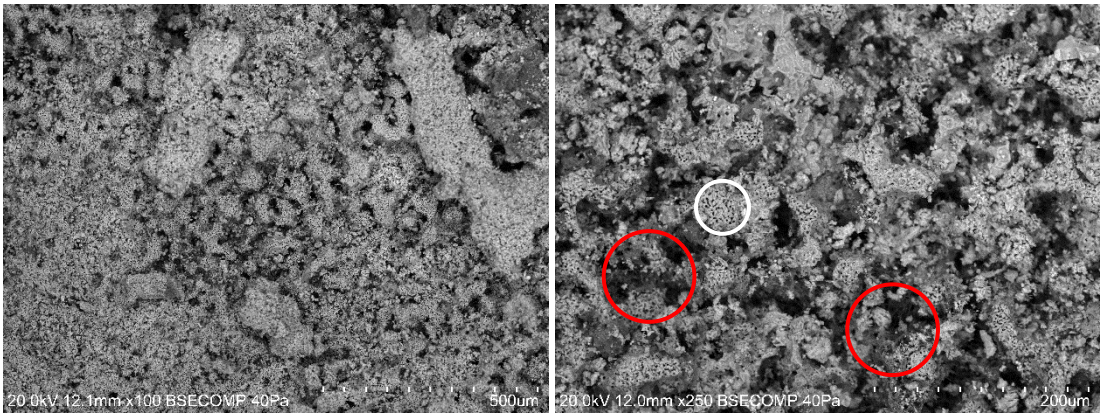

ZONE I (top: OM photos. bottom: SEM images)

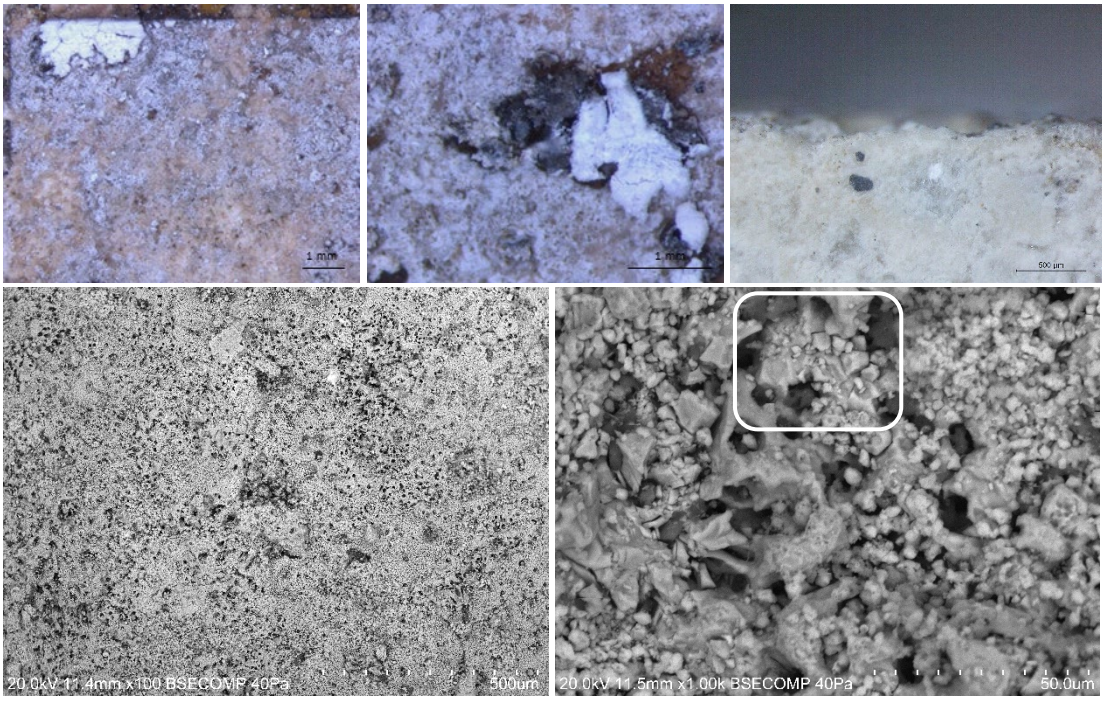

ZONE II (top: OM photos. bottom: SEM images)

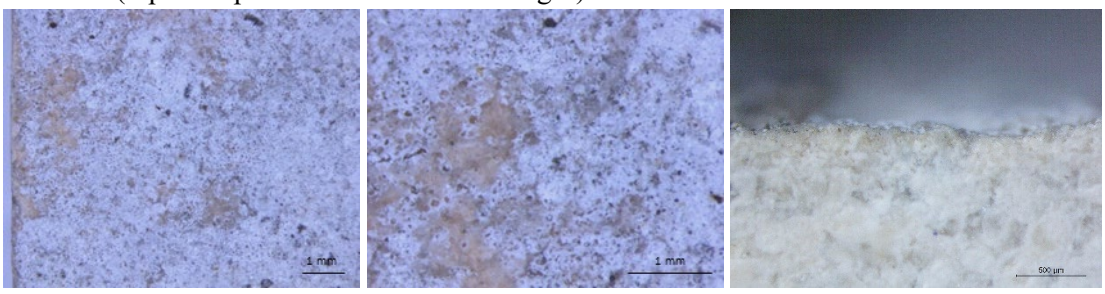

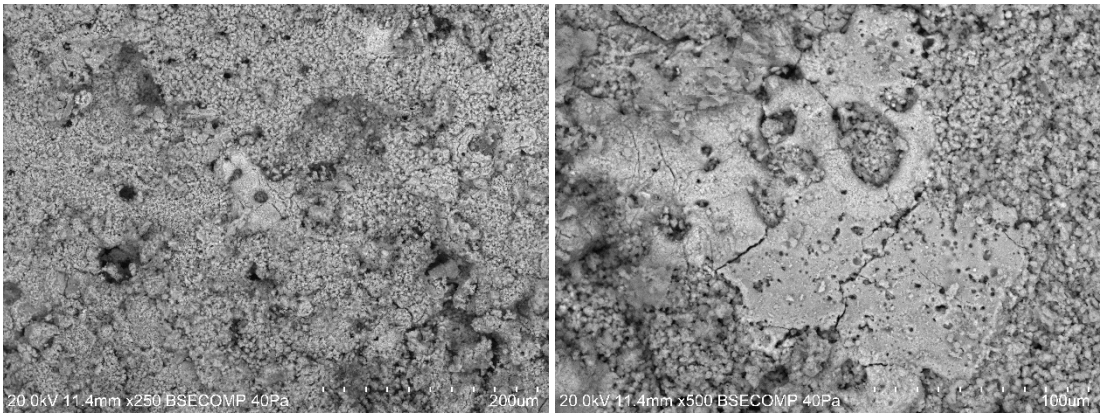

ZONE III (top: OM photos. bottom: SEM images)

Figure 5.13. Om and SEM images of the ps-UV laser cleaned sample surface.

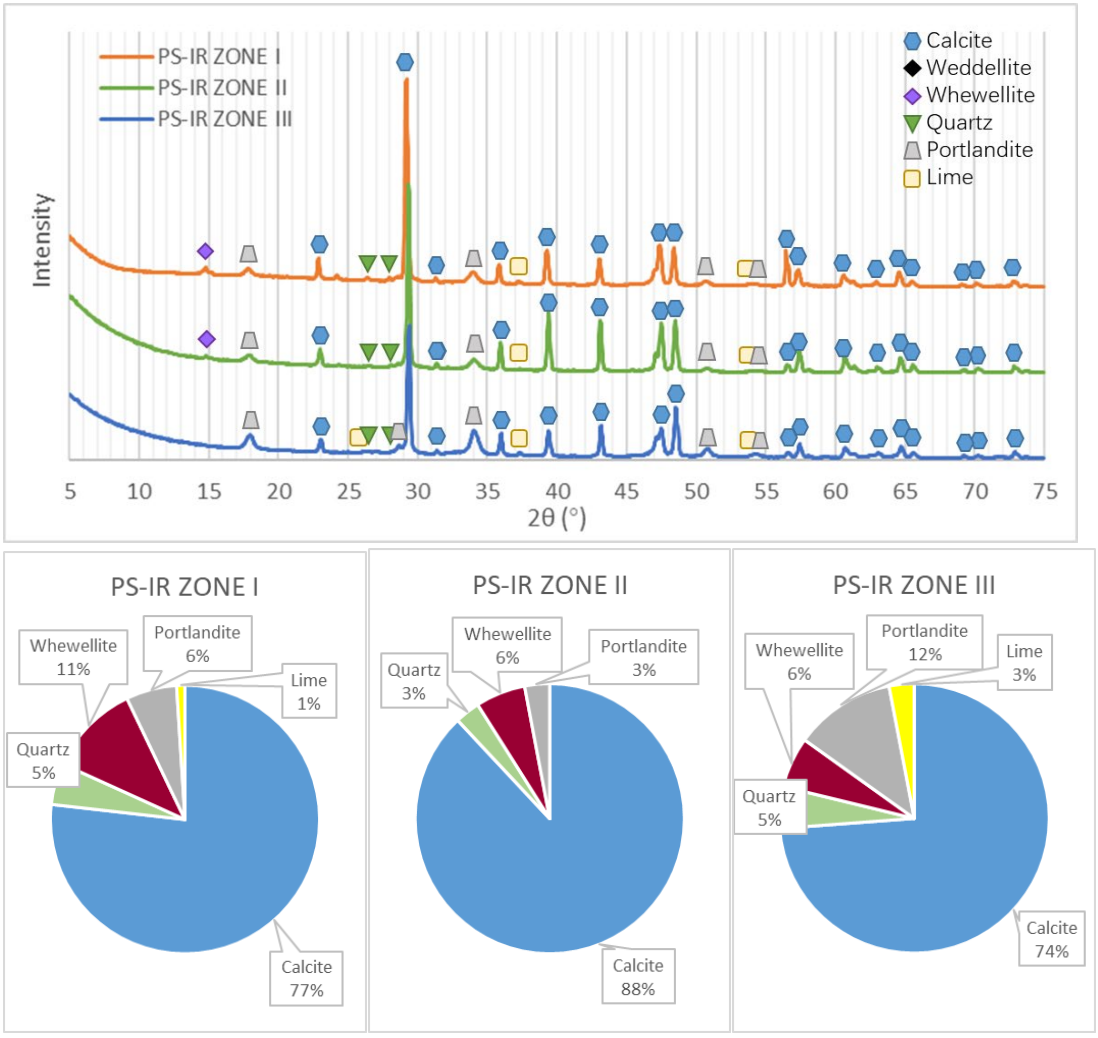

Figure 5.14. XRD and semi-quantification results of the sample cleaned by ps-IR laser.

Weddellite ($CaC_2O_4 \cdot 2H_2O$) starts partially dehydration and transform to whewellite ($CaC_2O_4 \cdot H_2O$) at 120 °C, then completely lose the water and turn to anhydrite calcium oxalate (CaC_2O_4) at 235 °C. As temperature increases, CaC_2O_4 decomposes to $CaCO_3$ at around 425 °C, eventually $CaCO_3$ decompose to lime (CaO) and CO_2 around 700 °C [223] [225] [226], the chemical reaction equation is as follow:

$$CaC_2O_4 \cdot 2H_2O \xrightarrow{\sim 120°C} CaC_2O_4 \cdot H_2O + H_2O$$

$$CaC_2O_4 \cdot H_2O \xrightarrow{\sim 235°C} CaC_2O_4 + H_2O$$

$$CaC_2O_4 + 1/2\ O_2 \xrightarrow{\sim 425°C} CaCO_3 + CO_2$$

$$CaCO_3 \xrightarrow{\sim 700°C} CaO + CO_2$$

$$CaO + H_2O \xrightarrow{moisture} Ca(OH)_2$$

While in the limestone samples investigated here weight loss was observed in the 650 °C to 850 °C temperature range, see *Chapter 1, 1.3.3 Thermogravimetric analysis*,. Calcium oxide is easy to hydrate and convert to calcium hydroxide in moist atmospheric conditions. Thus, the presence of CaO and $Ca(OH)_2$ demonstrates that the temperature during this ps-IR laser ablation reached at least 650 °C or above producing a non-homogenous surface pattern with fragments and pits on the substrate. The recorded presence of whewellite may be explained by two causes: 1) the weddellite dehydrated and transformed into whewellite due to thermal effects [223]; 2) the depth reached by laser cleaning was not sufficient to remove all the microbially precipitated oxalate minerals, even if high temperature was achieved.

Stone samples treated by nanosecond IR laser

The experimental data of the stone sample treated by ns-IR laser is listed below: Figure 5.15 shows the photo of sample before and after treatment, the operating conditions of laser applied on each zone are listed in Table 5.4. Then Figure 5.16Figure 5.10 presents the microscopic and SEM images of each zone, and Figure 5.17 presents the XRD results and mineral composition of each treated zone.

The treated areas once covered with microbial patinas on this sample show the development of an even thicker white surface layer after treatment than those treated by ps-IR laser, especially in zone I. These white layers could be up to 100 μm thick as seen from the side view. In the front view, such layers seem homogeneous with small holes and gaps (50~200 μm) distributed throughout the surface. The surface is more fragmented as evidenced under SEM imaging, implying a more intense thermal physical (cracking) or thermal chemical alteration process by ns-IR laser ablation. This

inference is further confirmed by the XRD results: the amount of portlandite is over 10% and lime was detected on each laser treated areas. No calcium oxalates were left, either because of a deep cleaning achievement or because whewellite and weddellite minerals decomposed into calcite and lime.

Besides the wavelength of lasers, the overlap of laser spots and hatch spacing on are also essential factors that affect temperature on the ablated surface [224]. From Table 5.1, Table 5.2, Table 5.3 and Table 5.4 it could be seen that the ps-IR laser and ns-IR laser had higher overlap of spots than the UV lasers, as well the hatching spaces of IR lasers were closer. That could also contribute to the temperature increase and cause decomposition of carbonate / oxalate stones.

Yet, hyphae of the microorganisms were still found underneath the fragmented mineral grain surface layer (red circle in Figure 5.16 ZONE I), and they were also observed in the ps-IR laser treated sample (red circle in Figure 5.12 ZONE I). Why these organisms were not completely burned is unclear. One interpretation could be that the decomposition reaction of the calcium oxalates and calcite absorbed a large amount of heat energy [226] produced by the IR lasers, this, contrary to expectation, saved the microbes below the stone surface from being burned out.

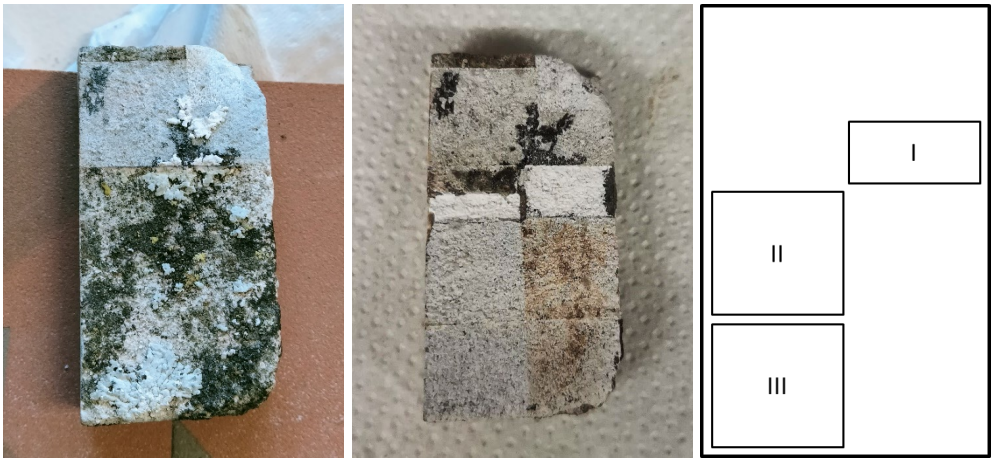

Figure 5.15. Sample tablet for ns-IR laser treatment: before cleaning (left), after cleaning (middle), and three zones with different treating parameters (right).

Table 5.4. Operation parameters of ns-IR laser for treating the sample.

Treated zone	**Unit**	**I**	**II**	**III**
Pulse duration	ns	5	5	5
Power Attenuation		100%	60%	70%
Power	W	30.1	18.1	21.1
Freq	kHz	600	600	600

Energy per pulse	µ J	50.17	30.17	35.17
Fluence per pulse	J/cm^2	1.51	0.92	1.06
Irradiance	GW/cm^2	0.3	0.18	0.21
Scanning speed	mm/s	500	500	500
Laser dots distance	mm	0.0008	0.0008	0.0008
Scanning lines distance	mm	0.0036	0.0036	0.0036
Average fluence	J/cm^2	1672	1003	1171
Scan directions		0º	0º	0º
Repetitions		1	2	2
Total fluence	J/cm^2	1672	2006	2342
Laser spots pattern		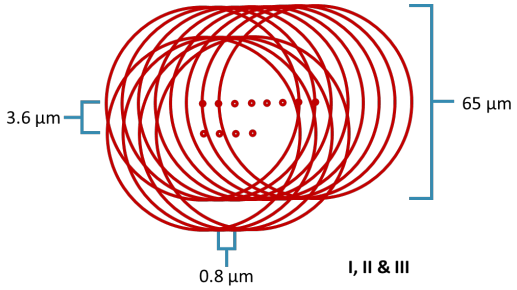		

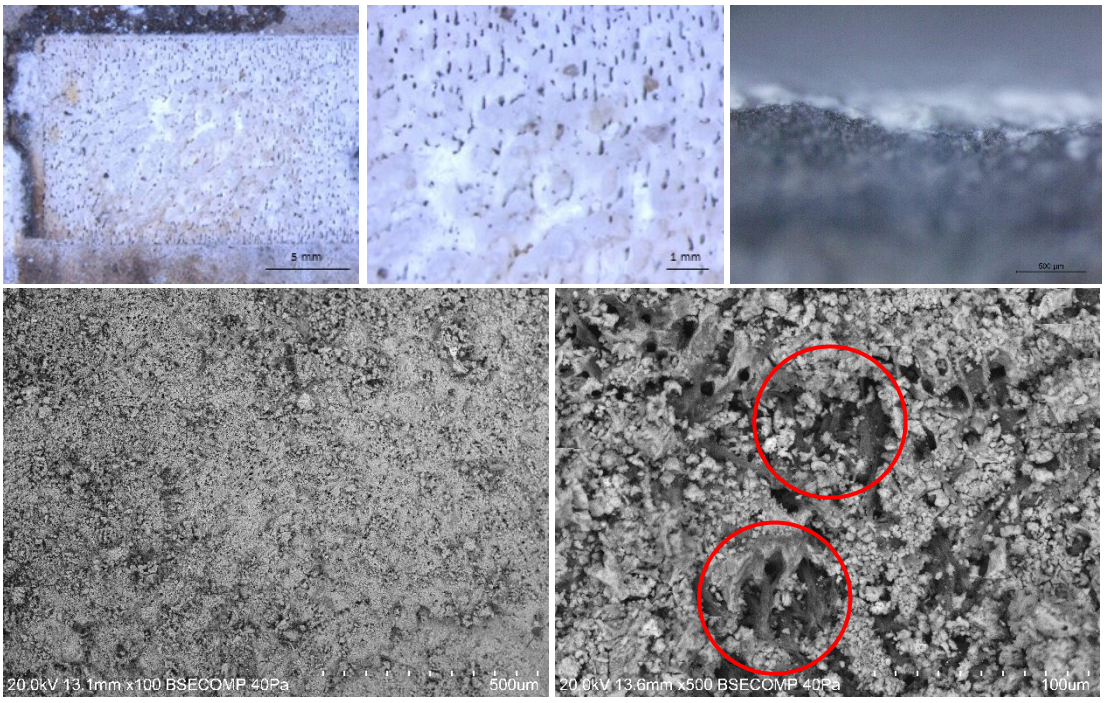

ZONE I (top: OM photos. bottom: SEM images)

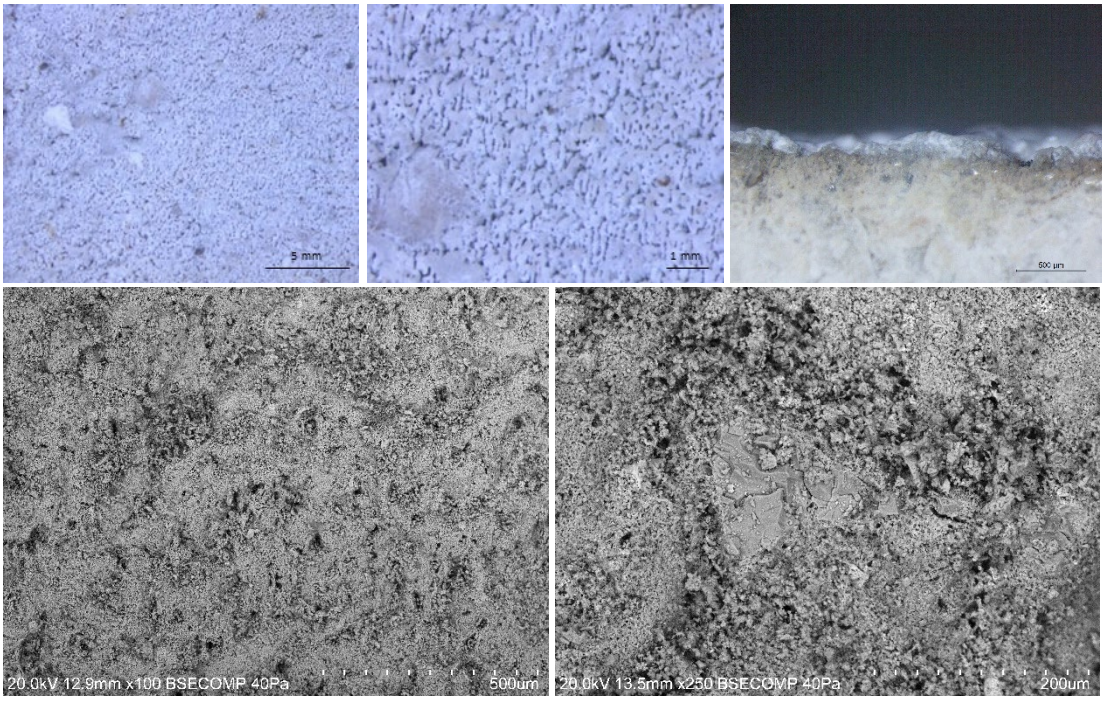

ZONE II (top: OM photos. bottom: SEM images)

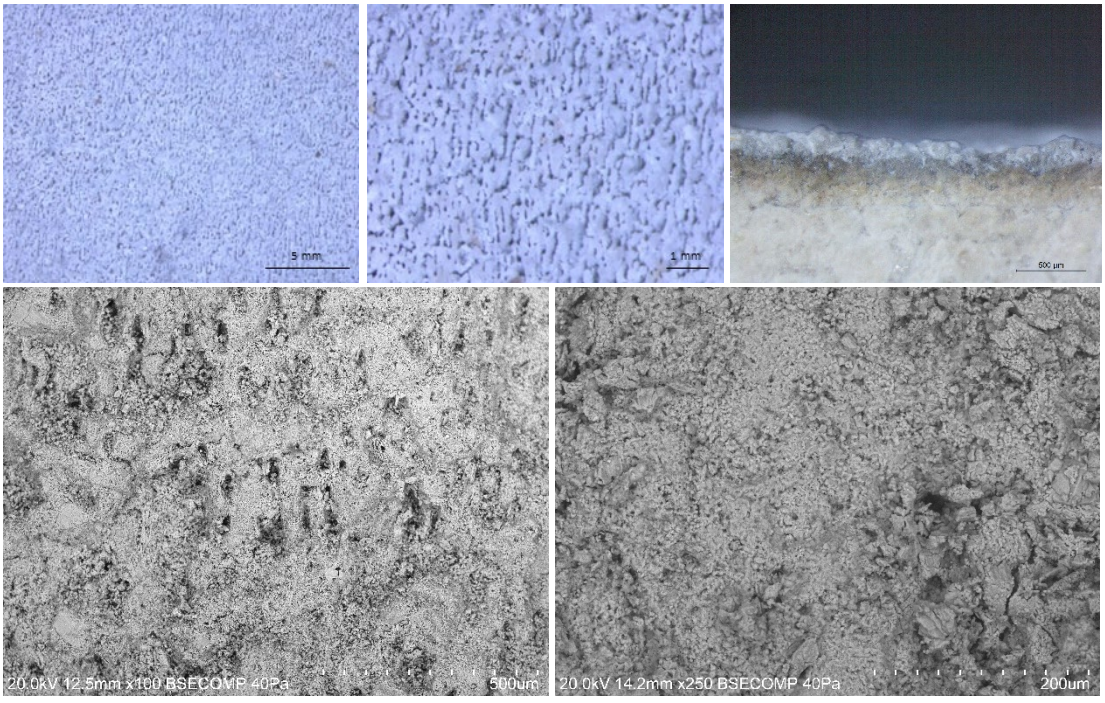

ZONE III (top: OM photos. bottom: SEM images)

Figure 5.16. Optical microscopy and SEM image of the ns-IR laser cleaned sample surface.

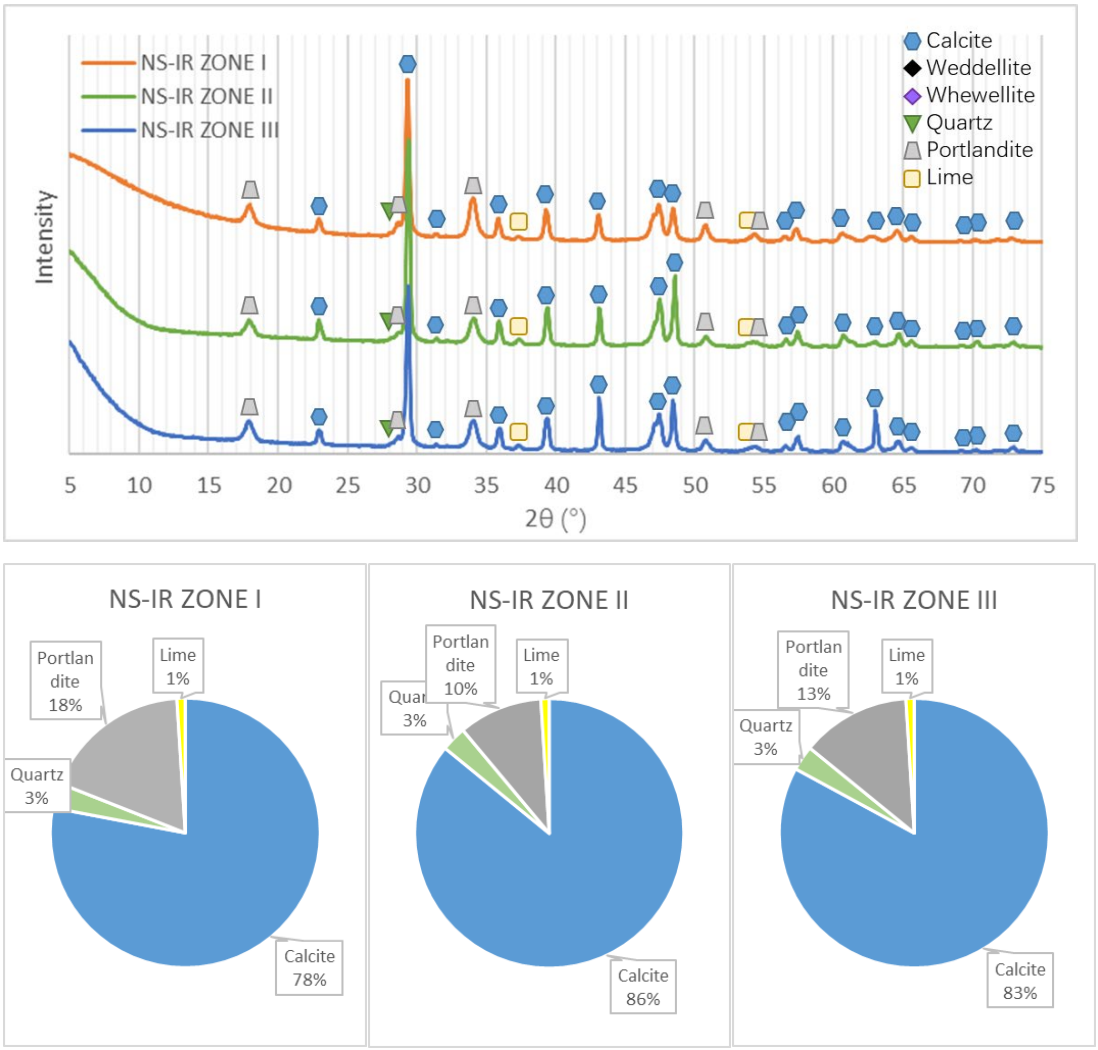

Figure 5.17. XRD and semi-quantification results of the sample cleaned by ns-IR laser.

Cross-section of cleaned areas observed under SEM

A limestone tablet covered by biological/lichenous patinas (sample S, Figure 5.18) was treated using all four types of lasers, then impregnated and cut in order for cross-sections to be observed under SEM.

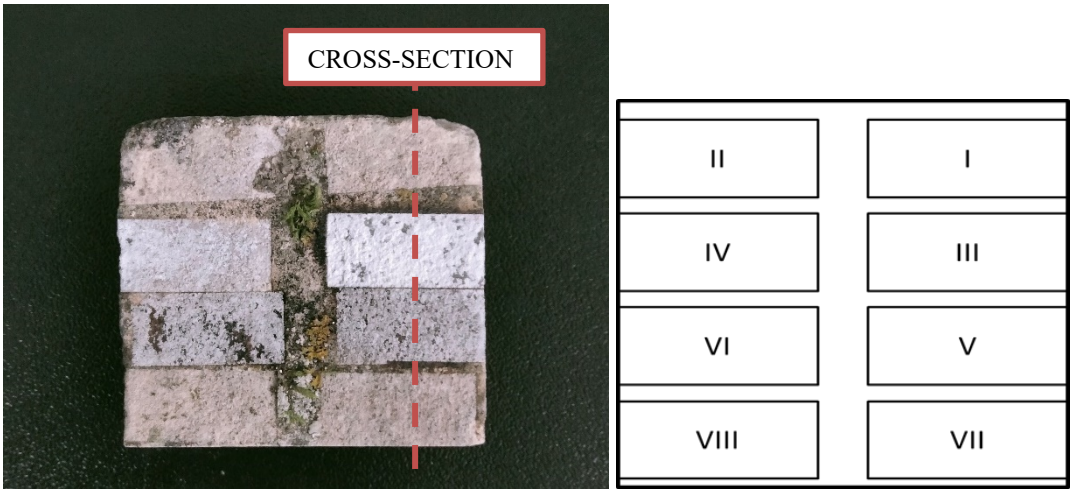

Figure 5.18. Sample S cleaned by various-moded laser for cross-section observation.

Table 5.5. Laser cleaning conditions for sample S.

Treated region	Laser type	Atten / Pump Power	Actual power (W)	Speed (mm/s)	Freq (kHz)	Spacing / Linewidth (um)	Average Fluence (J/cm^2)	Repetition	Total Fluence (J/cm^2)
I	fs-UV	60%	3.244	3000	200	10	10.8	10	108
II	fs-UV	45%	1.749	3000	200	10	5.8	10	58
III	ns-IR	70 %	21.1	500	600	3.6	1171	2	2342
IV	ns-IR	80 %	24.1	500	300	3.6	669	2	1338
V	ps-IR	7.2 A	5.76	2000	600	10	57.6	10	576
VI	ps-IR	7.2 A	5.76	1000	600	5	57.6	5	576
VII	ps-UV	9A	1.79	2000	250	8	11.2	20	224
VIII	ps-UV	9A	1.79	2000	250	8	11.2	10	112

SEM investigation (Figure 5.19), showed that all the stone surfaces treated by all 4 types of lasers were uneven with the development of pitting. For the fs-UV treated sample, pores around 10 μm and cracks hosting microorganism hyphae inside can be seen up to a depth of 200 μm beneath the surface, with narrow fissure penetrated by hyphae almost parallel to the surface also present. For the ns-IR treated region, the number of ditches and cavities are significantly higher than in samples treated by fs-UV laser, with pits at the surface filled with microorganism residues. The areas treated by ps-IR laser showed many cracks 50~100 μm long and ~ 10 μm wide perpendicular to the surface. Such phenomenon is also occurring in sample areas treated by ps-IR laser up to a depth of ~500 μm from the surface. This is probably due to the presence of water contained within the stone porosity (caused by microbial colonization) undergoing thermal expansion by absorbing the IR energy, in turns reaching high temperatures [227]. As demonstrated in the XRD results, the temperature caused by ps-IR laser and ns-IR laser was high enough to decompose calcium oxalates to calcium

oxide, and could therefore cause high water evaporation rates and create porosity. The increase in porosity is deleterious in view of stone conservation since it leads to increased water surface retention as well as to decrease the limestone mechanical strength, leading to further decay by thermal cycles and increased bio-colonization. ps-UV laser ablated region presents no cracking but clusters of pitting holes, which is also be responsible for the increase in surface roughness.

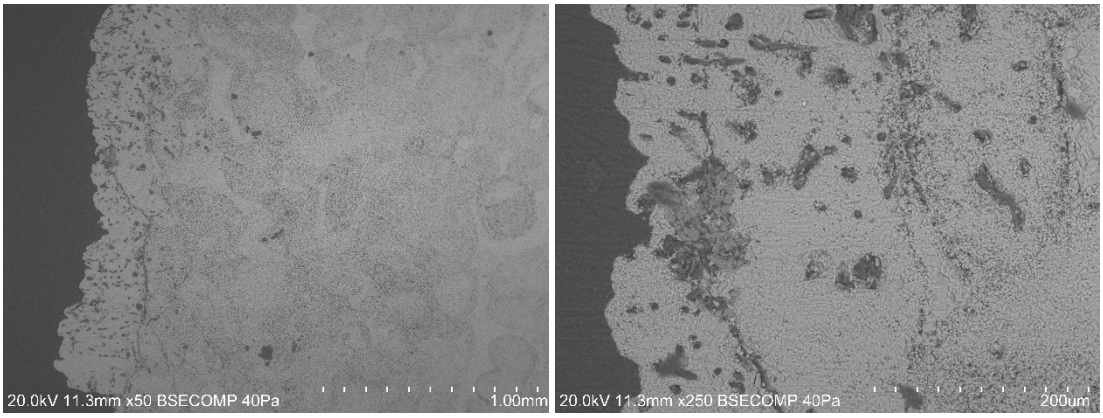

Sample S zone I cleaned by fs-UV laser

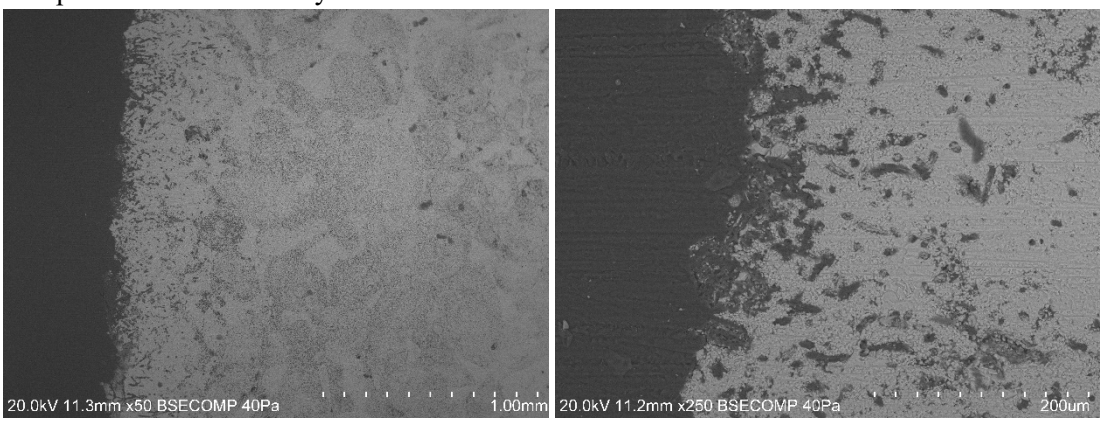

Sample S zone III cleaned by ns-IR laser

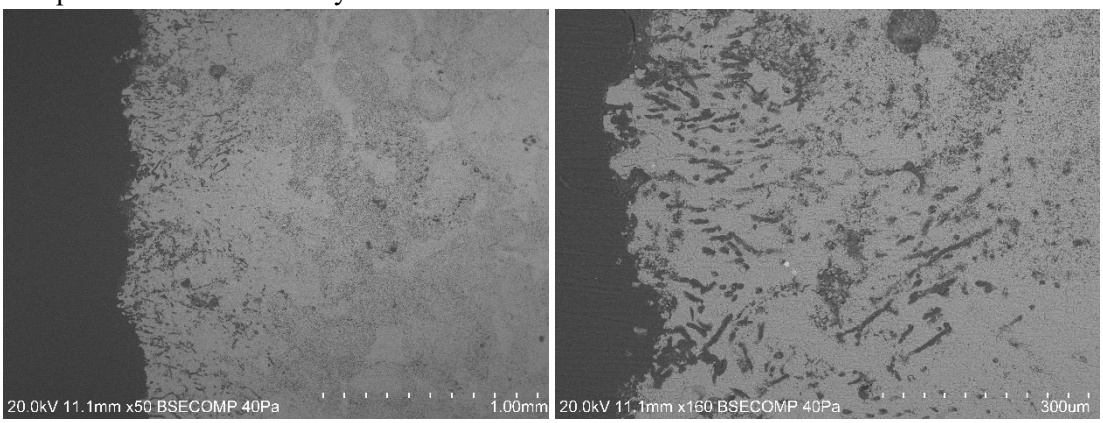

Sample S zone V cleaned by ps-IR laser

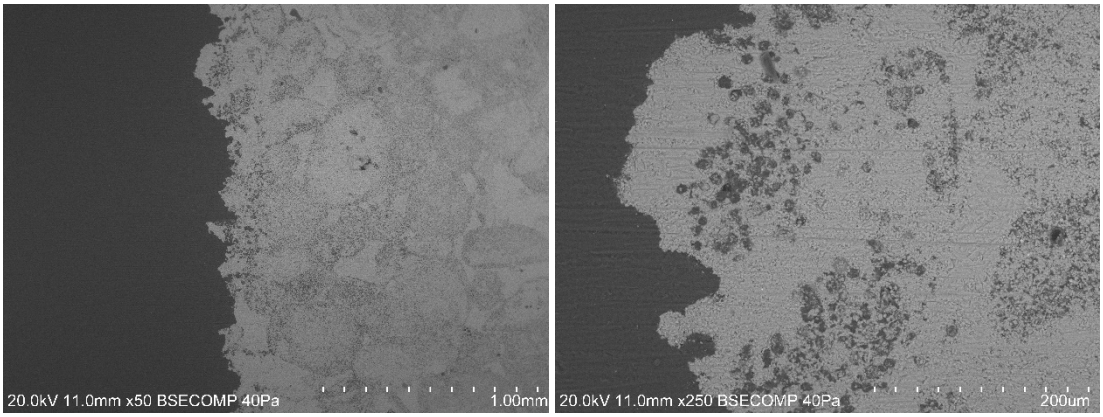

Sample S zone VII cleaned by ps-UV laser

Figure 5.19. SEM of the zones treated by various-mode lasers, cross-sections.

To summarise, the two types of IR lasers used in this research could be considered unsatisfactory considering: a) their damage to the substrate and chemistry alteration on the stone surface caused by high temperatures; b) the incomplete removal of colonising microorganisms. Both fs-UV laser and ps-UV laser performed better on these aspects. It is worth mentioning that none of the lasers tested were able to remove the microorganisms penetrated deeply in the stone (more than 1 mm beneath the surface) as these residues maintained below surface could regrow from the interior of the stone [228]. Thus, regular cleaning should be necessary.

5.3.3 Cleaning effect of lasers applied on natural exposed stone samples

Laser ablation was also applied on the limestone tablets exposed on the roof of the Monastery, see Figure 5.20. Each tablet was divided into four zones and underwent laser ablation using different laser parameters as listed in Table 5.6.

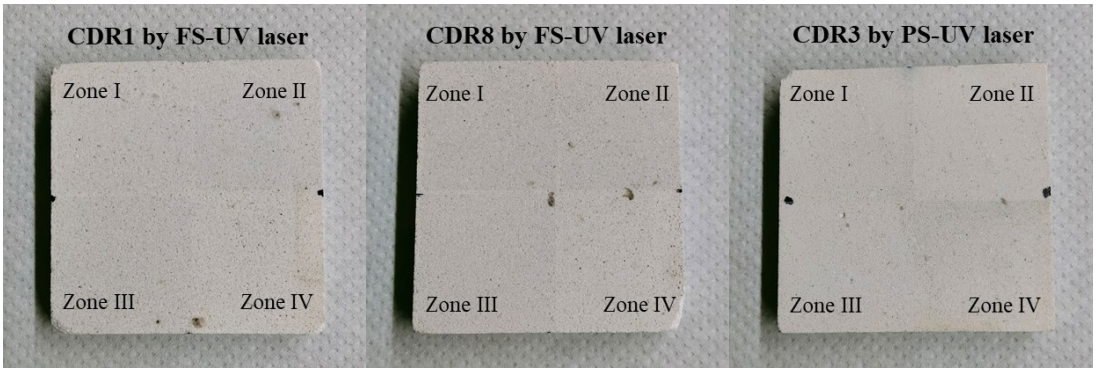

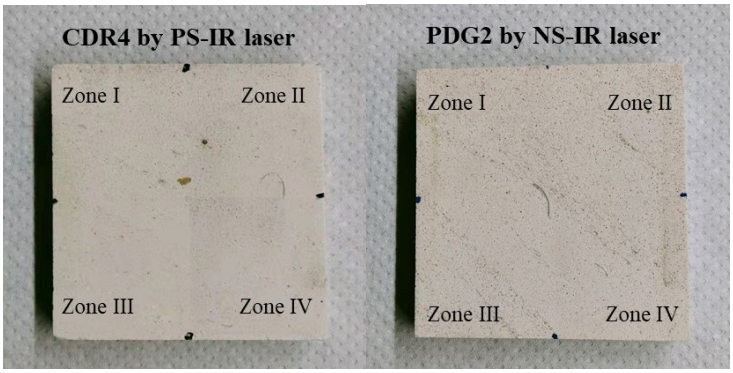

Figure 5.20. Exposed stone samples ablated using various mode lasers with zone IV of each tablet acting as the non-ablated control.

Table 5.6. Operating conditions of various mode lasers applied on the exposed stone tablets.

Sample region	Laser type	Atten / Power	Actual Power (W)	Speed (mm/s)	PPD	Freq (kHz)	Spacing / Linewidth (um)	Average Fluence (J/cm^2)	Repeti -tion
CDR2	Unexposed								
CDR3-IV	Untreated								
CDR1-I	fs-UV	45%	1.749	3000	1	200	0.01	5.9	2
CDR1-II	fs-UV	45%	1.749	1000	3	67	0.015	3.9	2
CDR1-III	fs-UV	45%	1.749	2000	1	200	0.01	8.8	2
CDR8-I	fs-UV	30%	0.638	500	3	67	0.0075	1.42	2
CDR8-II	fs-UV	45%	1.749	500	3	67	0.0075	3.9	2
CDR8-III	fs-UV	45%	1.749	666	3	67	0.010	2.2	2
CDR3-I	ps-UV	9 A	1.79	2000		250	0.008	11.2	5
CDR3-II	ps-UV	9 A	1.79	4000		250	0.016	2.8	5
CDR3-III	ps-UV	9 A	1.79	5000		250	0.020	1.79	5
CDR4-I	ps-IR	9 A	7.2	1000		400	0.001	1440	2
CDR4-II	ps-IR	9 A	7.2	2000		800	0.001	360	2
CDR4-III	ps-IR	9 A	7.2	500		200	0.001	360	2
CDR7-I	ns-IR	50%	15.0	500		300	0.0036	418	1
CDR7-II	ns-IR	25%	7.5	500		300	0.0036	209	1
CDR7-III	ns-IR	75%	22.6	500		300	0.0036	627	1

Figure 5.21 shows the OM and confocal microscopy images of sample CDR3 before and after ps-UV laser treatment. The exposed stone surface displays black fungal spots attached to the substrate (Figure 5.21 a and b), in which white and red represent higher relief while black and blue represent lower relief, those fungus presented as small spots under the confocal microscope (Figure 5.21 c and d); the oolites and their boundaries shew lower altitude due to the material loss caused in the oolites. After laser ablation, the black fungal dots were removed (see Figure 5.21 e – left side), as compared with the untreated side on the right. At higher magnification, the laser ablated

appeared mostly cleaned with only one or two black spots left inside some oolites (Figure 5.21 f), due to the increased penetration ability of the fungus within the highly porous oolitic structure. Seen under confocal microscope, linear ablation marks on the laser cleaned surface can be seen (Figure 5.21 g and h), with the ablated region standing at lower level with respect to the original, non-treated surface (Figure 5.21 i and j).

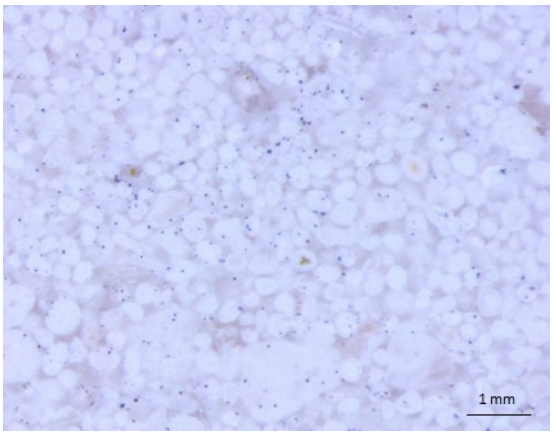

a

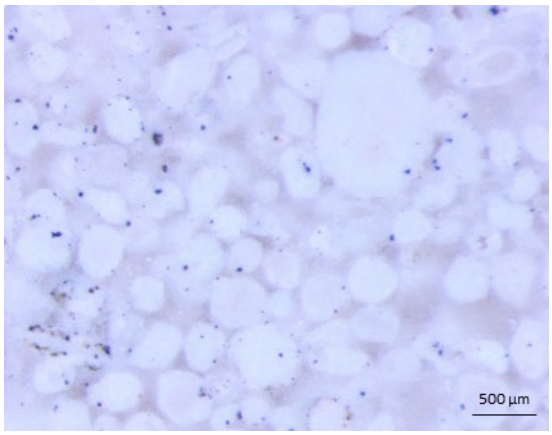

b

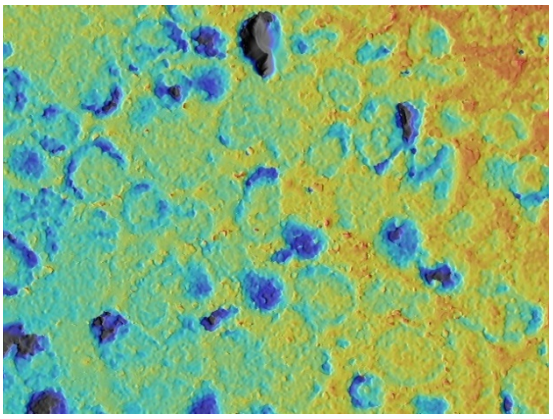

c

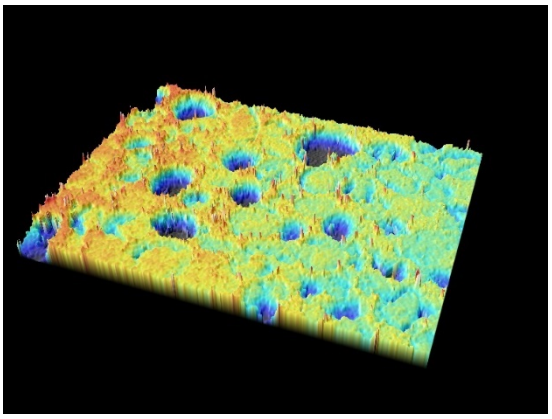

d

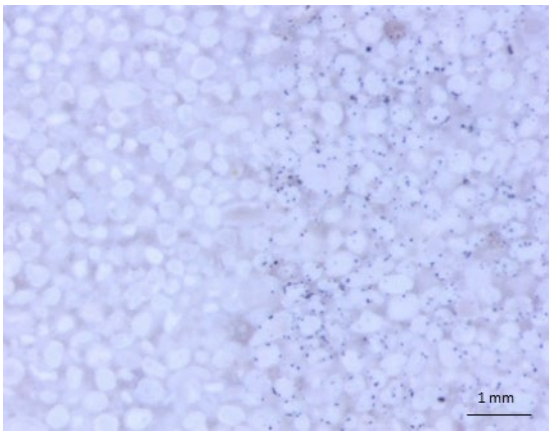

e

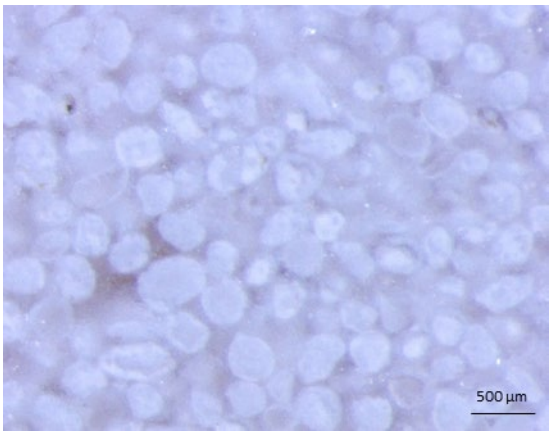

f

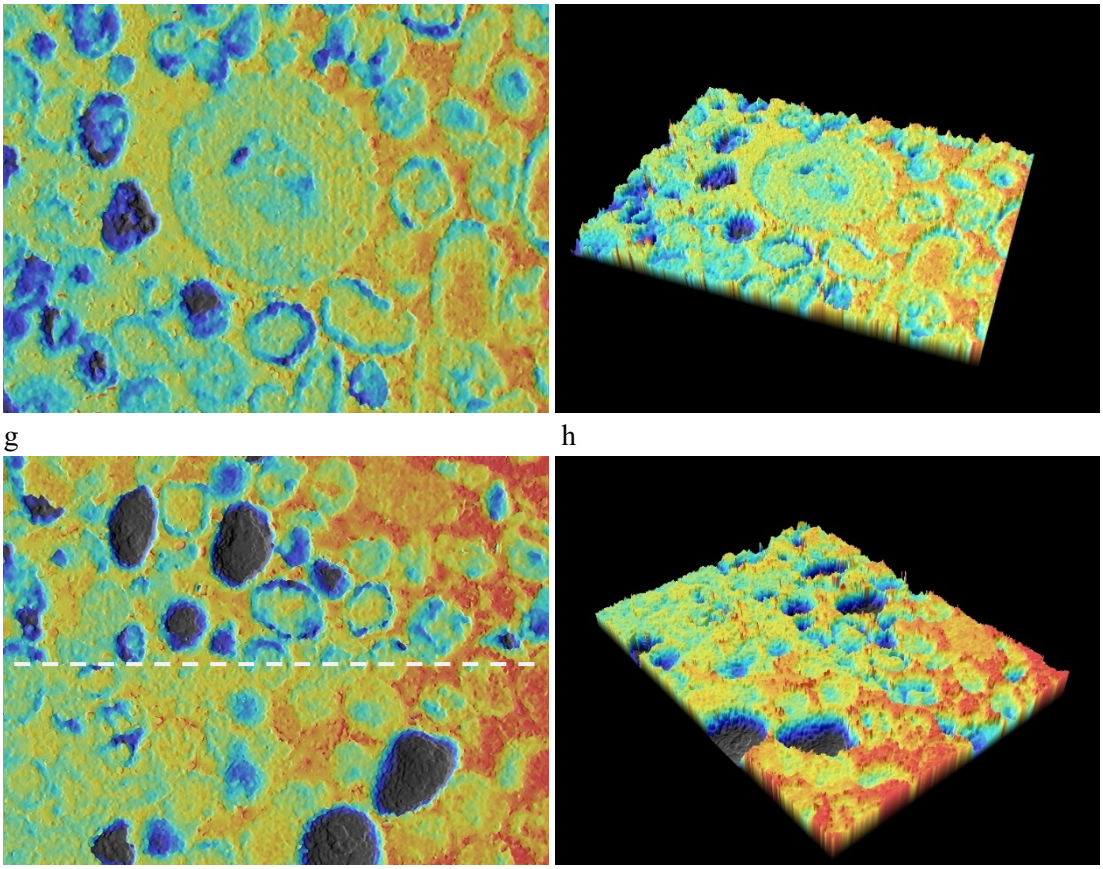

g h

i j

Figure 5.21. Optical microscopy and confocal microscopy (scale -40μm to 40 μm) for the ps-UV laser cleaned exposed sample (CDR3): a) and b). optical microscopy of untreated areas; c) and d) confocal microscopy of untreated areas, 2d and 3d view; e) the boundary between untreated area and laser ablated area; f) the microscopic view inside the laser ablated area; g) and h) confocal microscopy of the laser cleaned area, 2d and 3d view; i) and j) confocal microscopy of the boundary between untreated and laser cleaned areas, 2d and 3d view.

Table 5.7. Roughness, height change and spectrophotometric data (CIELAB system) index of the laser cleaned exposed tablets.

Sample region	**Laser type**	**Height change**	**Roughness *Ra* (μm)**	***L***	***a***	***b***	***C***	***H***
CDR2	Unexposed			89.92	1.98	8.72	8.95	77.18
CDR3-IV	Untreated		7.199	88.11	1.46	7.01	7.16	78.21
CDR1-I	fs-UV	- 5 μm	6.757	87.67	1.57	5.69	5.90	74.57
CDR1-II	fs-UV	- 5 μm	10.862	87.35	1.57	5.58	5.80	74.26
CDR1-III	fs-UV	- 15 μm	10.247	86.47	1.74	6.24	6.47	74.42
CDR8-I	fs-UV	undetectable	7.033	86.45	1.50	5.44	5.65	74.63
CDR8-II	fs-UV	- 4 μm	11.845	86.26	1.73	5.68	5.94	73.06
CDR8-III	fs-UV	- 7 μm	10.021	87.19	1.63	5.84	6.07	74.39

CDR3-I	ps-UV	-10 µm	15.621	87.14	1.41	6.35	6.50	77.47
CDR3-II	ps-UV	-10 µm	7.763	88.65	1.30	6.12	6.26	78.01
CDR3-III	ps-UV	-10 µm	15.910	88.08	1.40	6.46	6.61	77.79
CDR4-I	ps-IR	undetectable	9.649	86.88	1.72	8.79	8.96	78.95
CDR4-II	ps-IR	undetectable	10.046	87.37	1.64	8.15	8.31	78.61
CDR4-III	ps-IR	undetectable	5.709	89.11	1.41	7.53	7.66	79.39
CDR7-I	ns-IR	undetectable	6.164	88.80	1.32	7.36	7.47	79.83
CDR7-II	ns-IR	undetectable	4.307	86.48	1.72	9.42	9.58	79.62
CDR7-III	ns-IR	undetectable	8.153	88.27	1.36	7.79	7.91	80.09

The optical and confocal microscopic photos of all the laser-treated exposed samples are presented in Annex 5B. The roughness, relief change and colorimetry values of the ablated zones are listed in Table 5.7. As observed under OM, the application of both types of UV lasers (femtosecond and picosecond) were successful in achieving a clean surface; on the contrary, the areas treated by both IR lasers (nanosecond and picosecond), though being able to reduce significantly black fungal spots developed at the surface of the limestone, resulted in the creation of yellow-brownish marks on the stone surface (Annex 5B sample CDR4 and PDG2). In terms of surface roughness changes, UV laser ablated areas show more evident surface roughness alteration, particularly evident in oolitic areas where oolites appear in lower relief (Annex 5B sample CDR1 and CDR3) and the surface became more uneven, as also confirmed under confocal microscopy examination: Ra of the areas treated by fs-UV laser and ps-UV laser were found to generally increase with respect to the surface before cleaning, as well as being at higher relief with respect the surfaces treated by ps-IR and ns-IR lasers.

Macroscopically, it can be seen that some treated areas are different in colour and brightness (Figure 5.20). In Table 5.7, such variation was reflected in L and a, b (*CIELAB* system). An interesting result is that, after the fs-UV laser ablation, the brightness of the treated surface became darker, as visible also in Figure 5.20. Using the *CIELAB* standard, *L* of the field unexposed surface was 89.92, after field exposure and before laser treatment it was 88.11, suggesting that the stone became darker during the aging in the outdoor environment under the effect of soiling due to the deposition of particulate pollutants. After ps-IR and ns-IR laser cleaning, some of the regions showed increased the brightness (higher *L* values), such as CDR4-ZONE III (*L* = 89.11), CDR7-ZONE I (*L* =88.80), CDR7-ZONE III (*L* =88.27); however, for all the areas cleaned by fs-UV laser (CDR1 ZONE I, II, III AND CDR8 ZONE I, II, III) there is a decrease in *L* values, it is probably due to the increased roughness and possibly related to the laser fluence [229]. In terms of colour, the samples after field exposure had lower a and b value as compared with the unexposed ones, suggesting that the stone acquired a greener and bluer hues after field exposure (duller, combined with the brightness

reduction). After laser cleaning, colour index a^* of some laser treated areas somewhat recovered the values they had before field exposure, but this change was not present in all samples. Index b^* of the samples treated by IR lasers all showed an increase, some even showing higher values than the original unexposed sample: indicating that the IR laser made the surface turning more yellow. Index b of all the UV laser treated regions were reduced, suggesting that they turned bluer as compared with the IR laser treated ones and the untreated ones.

Another observation is that the regions treated by ps-IR laser and ns-IR laser had no detectable height relief change under the confocal microscopy examination (Annex 5B), unlike the ps-UV and fs-UV laser treated regions, which presented distinct relief reduction indicating loss of stone material from the substrate. The above-mentioned disparity (brightness, roughness and height change) between the surfaces treated by ultraviolet laser and infrared laser proved their different ablation mechanism – laser etching and thermal evaporation, respectively [230].

The Cell Viability Index (CVI) results are shown in Table 5.8. It can be seen that after the laser cleaning, regardless of the operating conditions and/or laser irradiation modes used, the cell viability index values in laser cleaned surfaces showed an overall reduction, demonstrating the effectiveness of all lasers in removing and inactivating microorganisms colonizing the stone. In particular, ns-IR laser cleaned areas showed the lowest CVI values while fs-UV laser cleaned areas showed relatively higher cell viability comparing to other areas, indicating that thermal ablation triggered by the ns-IR laser used in this experiment was more effective as a biocide. This could be explained by microbial contamination having higher absorption in the IR wavelength.

Table 5.8. CVI analysis of the laser cleaned exposed tablets.

Sample region	Laser type	Total fluence (J/cm^2)	Cell viability (%)
CDR2	Unexposed		/
CDR3-IV	Untreated		100 %
CDR8-I	fs-UV	2.84	34.69 %
CDR8-II	fs-UV	7.8	62.77 %
CDR8-III	fs-UV	4.4	78.68 %
CDR3-I	ps-UV	56	20.81 %
CDR3-II	ps-UV	14	3.38 %
CDR3-III	ps-UV	8.9	9.64 %
CDR4-I	ps-IR	2880	26.90 %
CDR4-II	ps-IR	720	17.09 %
CDR4-III	ps-IR	720	37.39 %
CDR7-I	ns-IR	418	3.72 %
CDR7-II	ns-IR	209	1.69 %

CDR7-III	ns-IR	627	13.87 %

5.3.5 Serendipity

Unexpectedly, limestone tablets were found to retain hydrophobicity up to six months after the fs-UV laser treatment (see Figure 5.22). The water contact angle was measured by dripping ~0.05 ml water on the stone surface using a syringe; the untreated original limestone tablet, although polished using 600# sand paper, presented no water repellent properties due to its high natural porosity: the water drop wetted the sample immediately and was absorbed by the tablet within a few seconds once in contact with the surface (Figure 5.22 a). In the case of the fs-UV laser treated sample, the water droplet remained at the surface (Figure 5.22 b). Measured by IMAGEJ software, the contact angle of the water droplet could reach up to ~ 100.3°, demonstrating the surface had been modified from super-hydrophilic (contact angle < 5°) to hydrophobic (contact angle > 90°), see Figure 5.22 c.

In fact, there have been a few studies focusing on improving the hydrophobicity of alumina and silicon surfaces by using CO_2 laser [231] and pulsed nanosecond IR laser [232] respectively, to introduce micro / nano texturing such as dimples, pillars, poles and fibres. In my opinion, this mechanism could also be applied for the stone sample in this research. Under confocal microscope examination, in fact, the hydrophobic area ablated with fs-UV laser presented a pattern somewhat similar to hierarchical topographic structure both on the calcite micrites and inside the oolites (Figure 5.22 d and e). The development of this hierarchical topographic structure on the surface of alloy material has been shown to produce air pockets underneath water droplets, thus decreasing the contact area and causing higher water repellence [233].

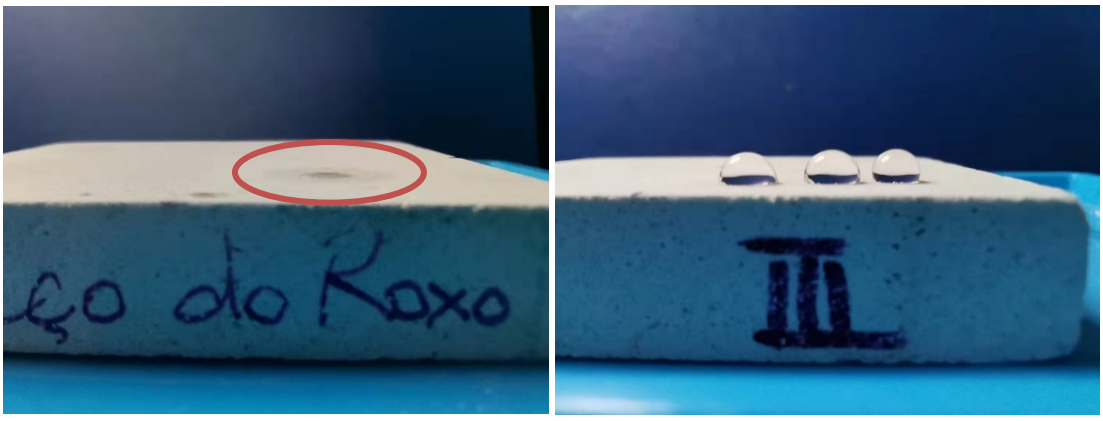

a b

c

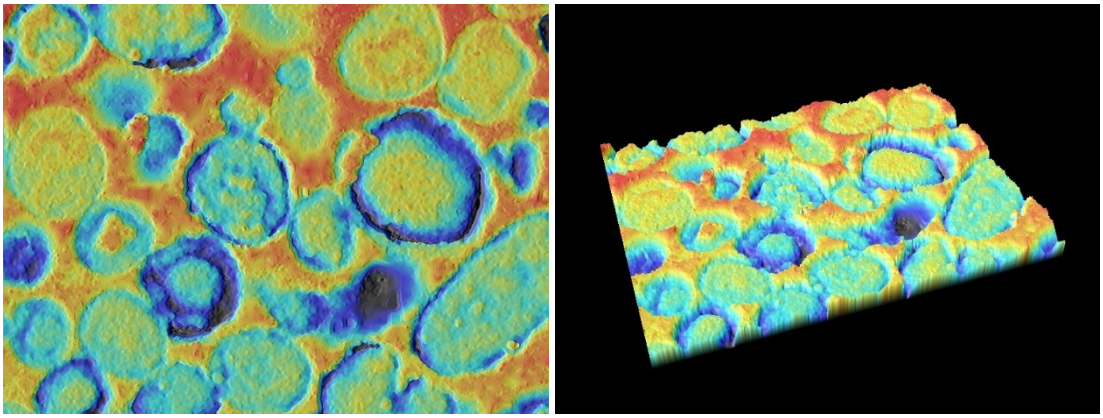

d e

Figure 5.22. Water droplets on the sample treated by fs-UV laser (CDR8): a. on the region without laser treatment, water absorbed immediately by the bulk and left only water stains (in red circle); b. water droplets remained on the laser treated surface; c. the water contact angle of the laser treated surface; d and e. confocal microscopy of this hydrophobic surface area, 2D and 3D view respectively (scale 40 μm to -40 μm).

5.4 Conclusions

Various laser irradiation-modes were tested on two types of samples: a) stone from Batalha Monastery covered by lichenous crusts and; b) stone tablets after 18-months of natural aging under field exposure on the Monastery roof. For the samples exposed outdoor and showing early stages of bio-colonization, all of the four types of lasers experimented in this research, including femtosecond ultraviolet laser, picosecond ultraviolet laser, picosecond infrared laser and nanosecond infrared laser, performed successful cleaning results: black fungal dots developed at their surface were removed and the microorganism cell viability was significantly reduced. On the other hand, it

has to be noted that was that UV-laser ablation led to material loss and left etching marks on the stone surface, thus increasing the surface roughness and leading to surface darkening due the same reason; on the contrast, IR lasers rarely modified the surface morphology and caused no evident material loss, the cleaned surface becoming brighter and yellower. Among all the lasers, nanosecond infrared laser provided the best biocide performance due to the thermal effect it generated.

In order to clean the thick lichenous crusts that could reach ~700 μm on the stone, lasers in different irradiation modes led to different results. Under visual, macroscopic and optical microscopic examination, femtosecond ultraviolet laser and picosecond ultraviolet laser were able to remove the lichen thallus from the colonized limestone without any further assistance, while the infrared lasers left molten substance with non-homogenous whitish hue and black burned powdery fragments on the stone surface. Femtosecond ultraviolet laser proved to be the most effective one in removing all the biologically precipitated calcium oxalates. The two types of infrared lasers lead to chemical alterations on the sample surface due to the high temperature induced by the irradiation: calcium oxalates and calcite decomposed into calcium oxide which reacted with water humidity producing calcium hydroxide) while whewellite was not completely removed. Under SEM investigation, it was seen that even after the lichenous crusts had been removed by UV lasers, numerous pores and cavities cause by lichen roots and fungal hyphae invasion were still visible on the stone substrate, whereas the IR lasers were shown to cause fragmentation of the substrate bulk. The cross-section showed that the microorganisms left were able to re-colonize the stone at depths up to more than 0.5 mm from the stone surface but these remnants were not and would be quite difficult to be cleaned using laser technologies.

Therefore, although the lasers could effectively remove the lichen thallus above the stone surface and in doing so limit progress of the decay process, remnants of endolithic microbes and the perforation morphology caused by previous bio-colonization made it possible for the microorganisms to regrow, suggesting regular laser cleaning is necessary.

An unexpected discovery was that femtosecond ultraviolet laser induced hydrophobic property to the ablated stone surface by morphology alteration. The laser etching produced a surface pattern similar to hierarchical topography passivated bump texture that increased the water contact angle and thus imparting water repellent properties to the originally super-hydrophilic limestone surface. This technique can be promising as a protective method applied for solid artefacts that stand in need of resistance to deterioration related with water contact or absorbance.

Chapter 6

Protective effectiveness of plasma deposited SiO_x thin films on Batalha's oolitic limestone

6.1 Introduction

As a consequence of anthropic activities in urban areas involving the burning of sulphur-containing fossil fuels for domestic and industrial purposes, the emissions of organic and particulate pollutants organic from vehicular traffic, the use of phosphate fertilizers, plus the dry/wet deposition of windborne microorganisms and contaminant particulate and gaseous aerosols, many open-air historical stone monuments have been suffering decay by acid rain attack, surface chemical alteration and biodeterioration, as described in Chapter 2 and Chapter 3. Hence, coating and consolidation for stone conservation have been extensively investigated : coating is to impart water repellency, anti-graffiti or anti-microbial growth properties to the substrate, while consolidation is for filling the pores and cracks in order to restore the mechanical integrity and avoid damages like decohesion and flaking [234][235]. The most widely applied products for these purposes are listed below:

(a) organic polymers – epoxies, polyvinylacetates, polyacrylates, silicones, or a mixture of them. These products have been widely used since the middle of the 20th century, for their ease of application and immediate efficacy. However, through the action of sunlight radiation, these organic consolidants could undergo photo-oxidation and molecular modifications. Take Paraloid B67 and Paraloid B72, two commonly used commercial acrylic polymers for stone restoration as examples [236]:

The methylacrylate and thylmethacrylate units in Paraloid B72 photo-oxidation pathway as follow

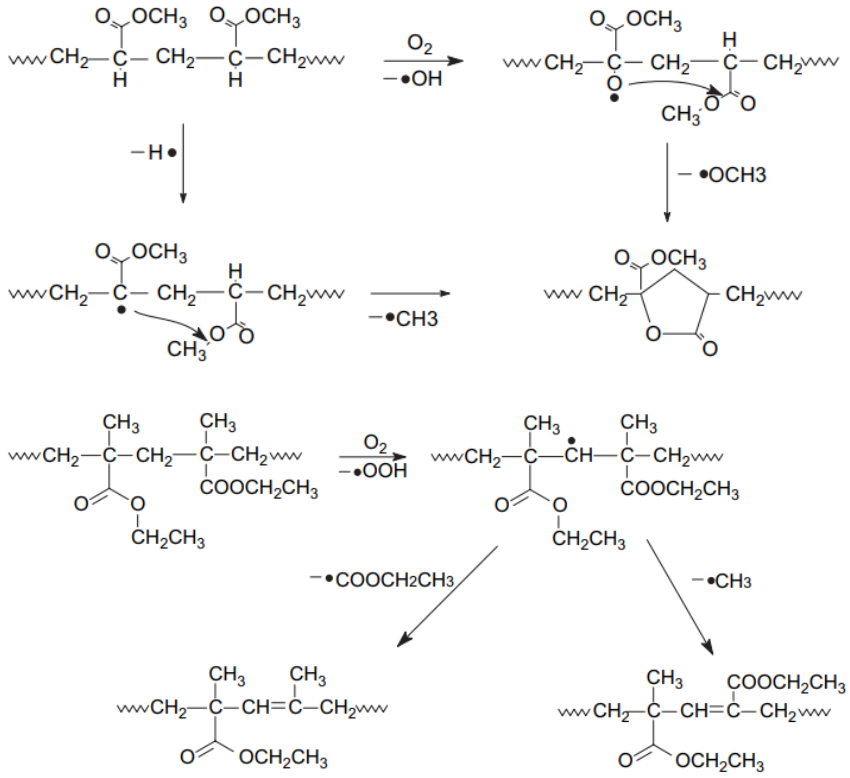

While the photo-oxidative reaction of Paraloid B67 would be

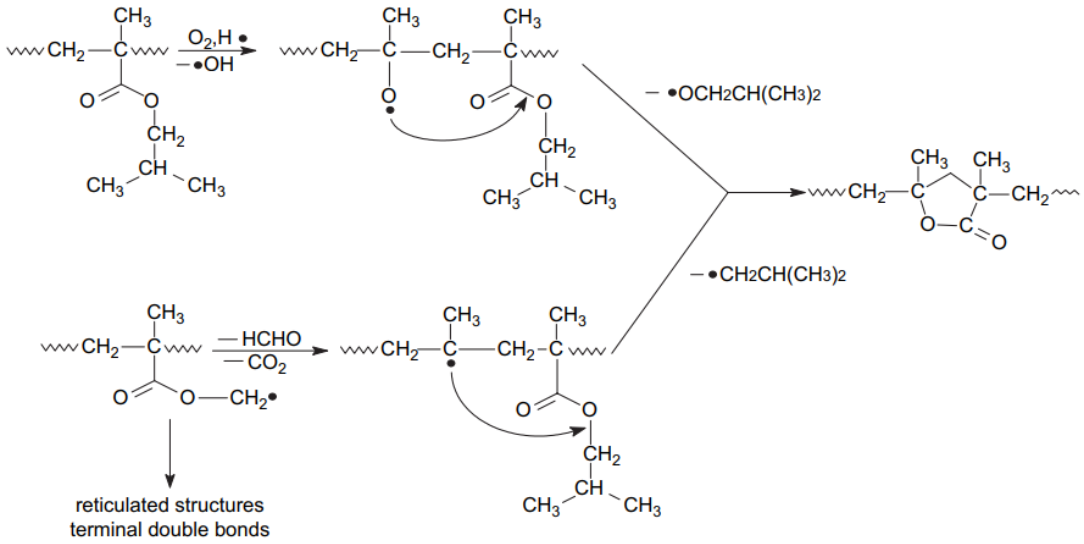

Such modification would form strongly cross-linked structures and their irreversibility makes them difficult to remove, colour changing and loss of conservative properties,

[236]. The worst consequence is that water and soluble salts in porous substrates may induce the onset of salt crystallization decay processes behind the hydrophobic coating layer, thus leading to even further material loss and decay [237] [238]. A Multi layered method which introduces both hydrophobic and hydrophilic layers was proposed by some researchers, to disperse the expansion stress near the interface, in order to prevent the damage caused by wet-dry difference in polymer conservation and salt crystallization [239].

(b) inorganic minerals or emulsions – medium includes carbon hydroxide, barium hydroxide, ammonium oxalate, ammonium phosphate, hydroxyapatite, etc. They have higher physical-chemical compatibility with stone substrates than polymers, and they could act either as consolidants or anti-fungal agents [240]. $Ba(OH)_2$ and $Ca(OH)_2$ based methods are specific for consolidating carbonate stones (i.e., limestone and marble), and they do not harm the substrate. But they do not show high penetration depth and take a long time to convert to $BaCO_3$ and $CaCO_3$ [241]. Actually, lime water suspension has been a traditional stone treatment. AmO_x (ammonium oxalate) could passivate the calcite stone surface by modifying the $CaCO_3$ to pure calcium oxalate, as well by converting $CaSO_4$ into CaC_2O_4, thus acting as a neutral de-sulphating agent [237]. $(NH_4)_2HPO_4$ is similar to AmO_x, but it has much more uniform consolidating effect, thus being considerable for its consolidating efficiency, low colour variation and non-toxicity [242]. Diammonium hydrogen phosphate (DAP) has also been used for consolidation purposes, DAP is able to penetrate into stone at depth more than 2 cm and react with calcite in carbonate stones and forming hydroxyapatite, thus increasing the stone dynamic elastic modulus and tensile strength significantly with the calcium phosphate filling microcracks and stone porosity pores, such reaction is as below and it only took 2 days and can be realized in the field [243].

$$10\ CaCO_3 + 5\ (NH_4)_2HPO_4 \rightarrow Ca_{10}(PO_4, CO_3)_6(OH, CO3)_2 + 5(NH_4)_2CO_3 + 3CO_2 + 2H_2O$$

(c) Tetraethoxysilane (TEOS) and methyltrimethoxysilane (MTMOS) –are the most extensively used as consolidants for stone. TEOS is a popular conservation candidate for its super-hydrophobicity and transparency that does not have any effect on aesthetic appearance of the treated stone [244].

Consolidation of TEOS via hydrolysis are as following [245]:

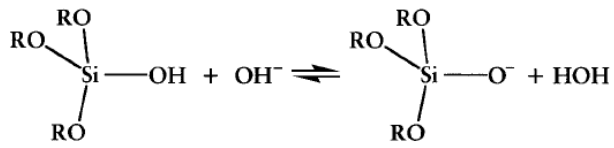

the ethoxy groups (OC_2H_5) are progressively replaced by hydroxyl groups (OH).

When hydroxyl groups of different molecules start to react:

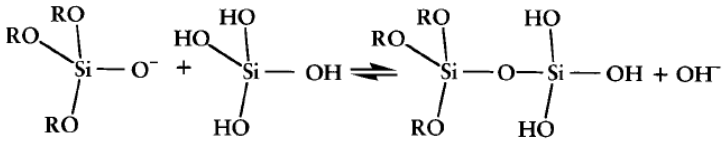

Cross-linking reaction would be:

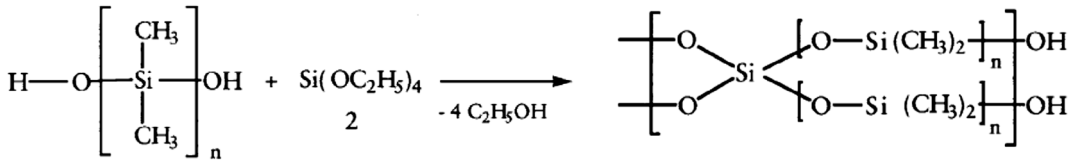

1 2 3

The TEOS is applied first by sol-gel, however due to the developed capillary force, the gel always tends to develop cracks during the drying phase. To avoid the fracturing, various hybrid consolidants based on TEOS had been formulated such as TEOS-HDTMS xerogels, TEOS-colloidal-silica-PDMS-OH, TEOS/PDMS-OH/CTAB, GPTMS mixed with silica nanoparticles and so on [238] [246] [247] [248]. With these modifications, the gel became more stable, and the coating developed improved resistance to acid attack and salt weathering.

During the 90's, it was found that silicate film could be successfully deposited by plasma-enhanced / thermally-activated chemical vaporized deposition (PECVD / TACVD), according to the following reaction [249]:

$$Si(OC_2H_5)_4 + 8\ O_3^+ \rightarrow SiO_2 + 10\ H_2O + 8\ CO_2$$

At that time, substrate heating was required in the deposition to achieve acceptable electrical properties (enough packing density, plasma bombardment) during the process [250] [251]. In the last decade, advancement in organometallic-based PECVD in an atmosphere of oxygen and argon, under capacitively coupled radio frequency plasma power source. In this way, deposition of silicone dioxide film could be operated at low temperatures, i.e., in cold plasma conditions, as opposed to high temperature plasma which is more dangerous, consumes more energy, and cannot be applied in portable system [252] [253].

6.2 Methods and Materials

6.2.1 Limestone tablets preparation and SiO_x thin film deposition

Limestones used in this experiment were collected from the quarries mentioned in *1.2.1 Field investigation and sample collection*. The limestones were then cut to tablets in three sizes: 2.5 x 2.5 x 1 cm, 2.5 x 2.5 x 0.3 cm, 5 x 5 x 1 cm. The limestones were cut to tablets in three sizes: 2.5 x 2.5 x 1 cm, 2.5 x 2.5 x 0.3 cm, 5 x 5 x 1 cm. The surface to be treated was polished with 600# sand paper. The tablets were then washed by water and dried in oven at 60°C. Before deposition, tablets were wipe cleaned by 97% ethanol.

SiO_x thin films were deposited in plasma fed with TEOS in the same capacitively coupled parallel-plate reactor used for bio-incubated and field exposed samples (see section *4.2.3 Plasma etching of bio-incubated and exposed samples*, but it was here operated in deposition mode. An external container of liquid TEOS with heating and flow control system was connected to the chamber. After trial on the Si wafers, the deposition parameters were optimized and used for the TEOS film deposition on stones.

6.2.2 Characterization of the deposited TEOS film on the limestone

Attenuated Total Reflectance-Fourier Transform Infrared Spectroscopy (ATR-FTIR)

The SiO_x coated samples were characterized by ATR-FTIR in order to define the composition of the coating formed on the limestone surface. The instrument and operation parameters are the same as in *Attenuated Total Reflectance-Fourier Transform Infrared Spectroscopy (ATR-FTIR)*.

SEM-EDS

The deposited tablets in the size of 2.5 x 2.5 x 0.3 cm were impregnated with resin and cut for cross-section observation. Consolidating process and SEM-EDS operation condition are the same as in *1.2.2 Thin-section petrography* and *2.2.5 Variable-pressure scanning electron microscopy coupled with energy dispersive spectrometry (VP-SEM + EDS)*.

6.2.3 Resistance test against acid attack, microbial colonization and natural aging

Acid rain attack simulation

This test was conducted by the self-set system shown in Figure 6.2. Sample tablet was set in funnel at tilt angle of 45°, H_2SO_4 solution at pH 3.5 was made dripping on the tablet surface with a flow rate of 5 mL/min. After each 50 mL of acid appliance, the tablet was then left dry in laboratory oven at 60°C for 1 hour, then the acid dripping process was repeated 5 cycles. A total volume of 200 mL sulfuric acid was applied on each sample, then the tablets were dried and observed under SEM and EDS [238]. The sample tablets were then washed by ultrasonic and dried and weighted in order to acquire the weight loss due to acid attack.

Microorganism incubation

Microorganism mixed with cultural media was inoculated on the sample tablets and then incubated for 2 weeks, incubation process and technical parameters were the same as that in *4.2.2 Extraction, cultivation and incubation of microbials.*

Natural aging

Tablets with and without SiO_x thin film coating in the size of 5 x 5 x 1 cm were placed on the roof of the Batalha Monastery facing south (Figure 6.3), from 2021 June 9th to October 10th for 3 months. Then the samples were collected and observed under optical microscope, and evaluated by the spectrophotometer (see *2.2.2 Colour evaluation*) to define the colour change after natural aging.

6.2.4 Property alteration in hydrophobicity and permeability

Water vapor permeability test

For vapor permeability test, limestone tablets with and without SiO_x thin film coatings were fixed and sealed by Parafilm on the top of identical glass containers partially filled with water (making sure that water did not enter into contact with the the tablets' bottom) see Figure 6.1. Then the containers with tablets were placed in an oven at constant temperature of 60°C for 7 days, and weighted every 24 h. Linear regression between weight change and time was made by Excel, the water permeability of each sample was extrapolated by the slope of the accordingly linear function. This method follows the one in articles [254] and [255].

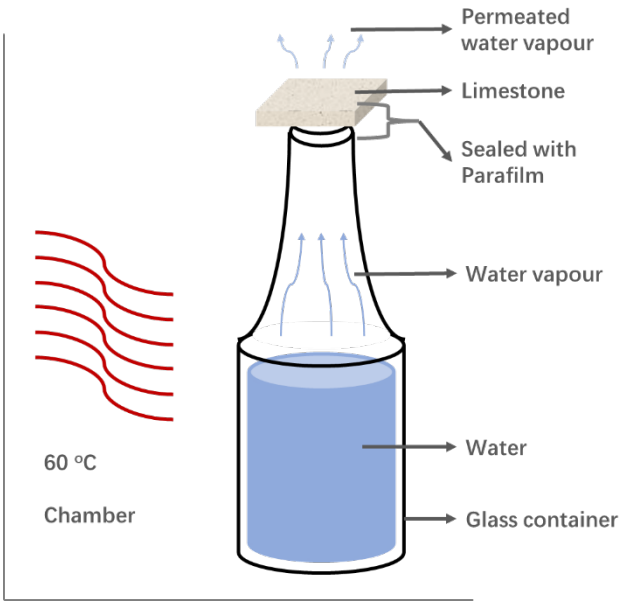

Figure 6.1. Schematic diagram of the experimental sets for water permeability test.

Water contact angle measurements

Water contact angle measurements were conducted using the sessile drop technique at room temperature, with double distilled water (γ = 72.8 mN/m) [256]. The measurement was carried out by a Kruss DSA10 instrument (Hamburg, Germany) equipped with a video camera.

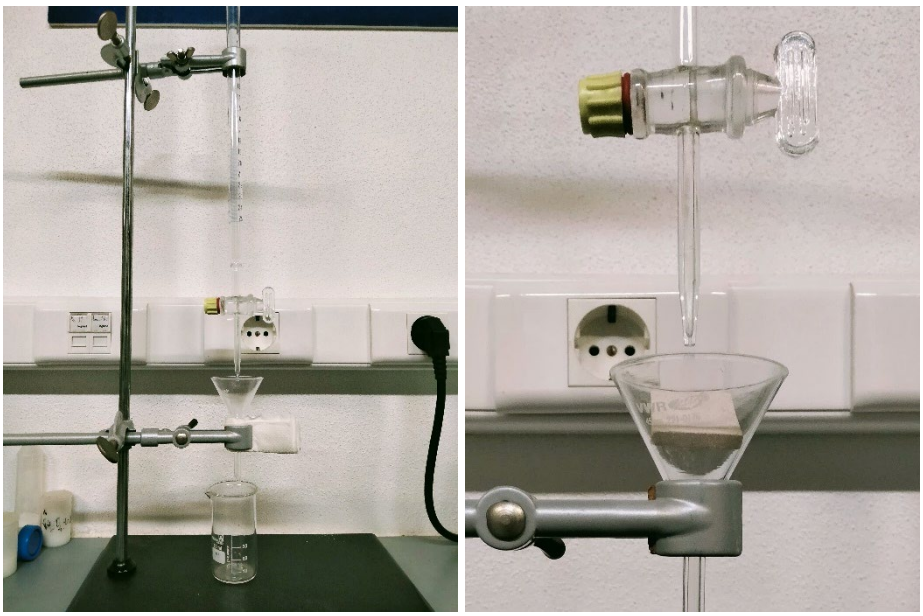

Figure 6.2. System for simulating the acid rain attack.

Figure 6.3. Sample tablets placed on the monastery roof (from left to right, the 1st and 3rd are deposited with SiO_x film, the 2nd and 4th are uncoated).

6.3 Results and Discussion

6.3.1 SiO_x thin film deposition and coating characterization

Firstly, TEOS plasma deposition was carried out on silicon wafer to test the correct parameters. Under SEM and ATR-FTIR examination, a TEOS flow at 1~2 sccm (standard cubic centimeters per minute, or cm^3/min), plasma input power 100~200 W and a working time of 20~40 min were found to be most suitable operating conditions to successfully deposit a Si-O-Si film on the Si wafer surface. In Figure 6.4, it can be seen that as compared with the uncoated wafer, the SiOx coated wafer shows a new band at 785 cm-1 associated with Si-O asymmetric stretching band while the wide band between 870 ~ 1120 cm-1 could be a Gaussian fitting curve of Si-OH stretching, Si-$(CH_2)_n$-Si and Si-O-Si stretching bands. Another band at 1138 cm-1 is likely to be the C-O stretching band [257] [258] [259]. These peaks indicated the presence of the silicate film with incompletely reacted groups.

Under SEM, a homogeneous and compact SiO_x layer can be seen on the silicon wafer surface (Figure 6.5), The thickness of the coating is identical seen from the side, and from the top view appears no gaps even under 1.9k magnification. Under a certain

gas flow (TEOS 2 sccm , Ar 80 sccm, O_2 20 sccm), the thickness of the deposited film is linear correlated with the input power (Figure 6.6).

Hence, in order to obtain a film thickness similar to the one obtained on the silicon wafer, SiO_x were deposited on limestone tablets using different parameters listed in Table 6.1. Then the deposited samples were again characterized by ATR-FTIR and SEM.

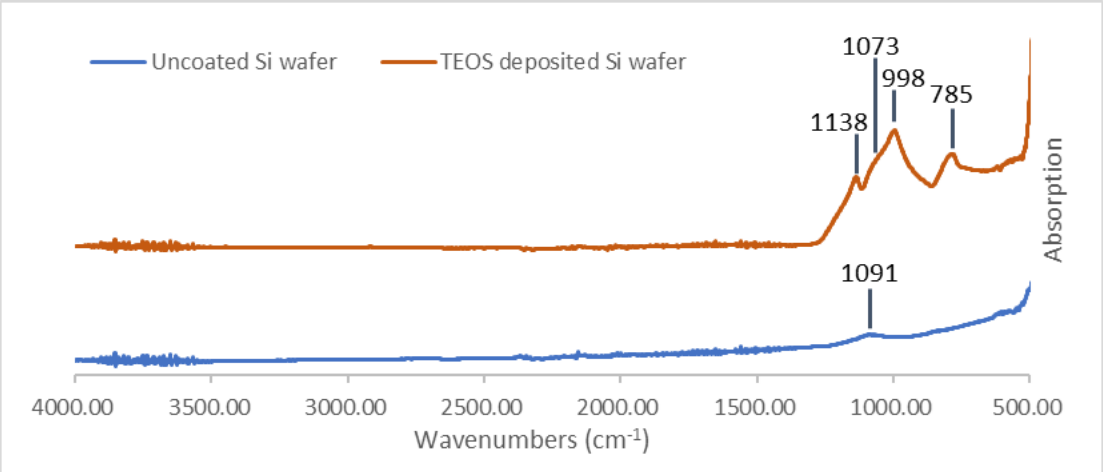

Figure 6.4. ATR-FTIR result of deposited and uncoated Si wafer.

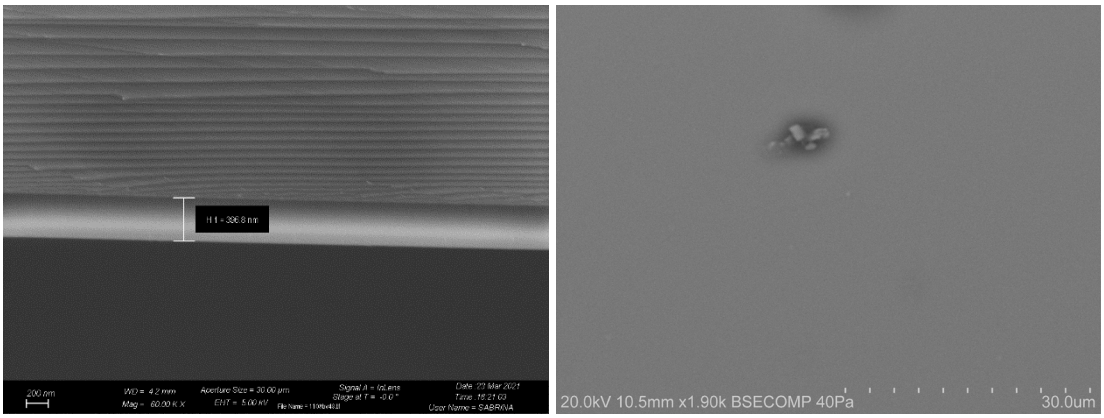

Figure 6.5. SEM of the SiO_x coated Si wafer, side view (left) and top view (right).

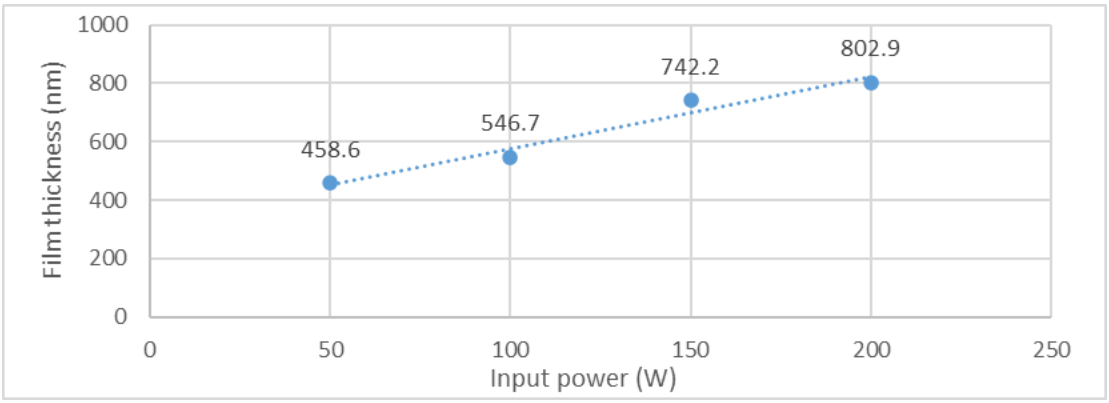

Figure 6.6. Relation between the film thickness and the plasma deposition input power.

Table 6.1. Different parameters used for the deposition of SiO_x thin film.

Group	Deposition parameters			
	Ar / O2 gas flow (sccm)	TEOS flow (sccm)	Input power (W)	Time (min)
A	O_2 20, Ar 80	1 sccm	100 - 7	20
B	O_2 20, Ar 80	2 sccm	100 - 11	40
C	O_2 20, Ar 80	2 sccm	200 - 15	40
D	O_2 20, Ar 80	2 sccm	200 - 11	20
E	O_2 50, Ar 50	2 sccm	200 - 8	40
F	O_2 50, Ar 50	2 sccm	200 - 8	20
ref	-	-	-	-

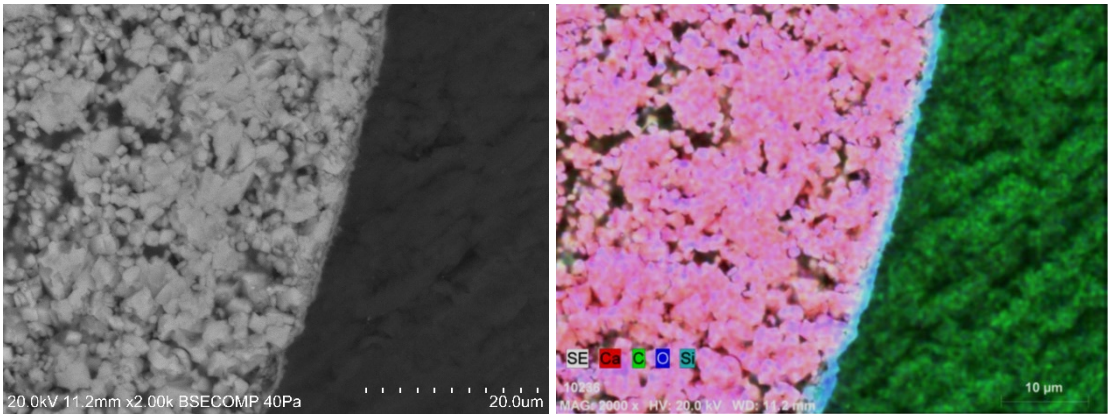

Figure 6.7. SEM image (left) and EDS map (right) of SiO_x thin film deposited on limestone, cross-section view.

It can be seen from the SEM-EDS results (Figure 6.7 and Annex 6A) that the Si-coating could be formed on polished limestone surface successfully. However, the coating thickness is 2~3µm under all deposition conditions, which is much reduced

than that under same conditions on Si wafer. Fortunately, although being thin, the coating is continuous and adapting on the substrates' morphology.

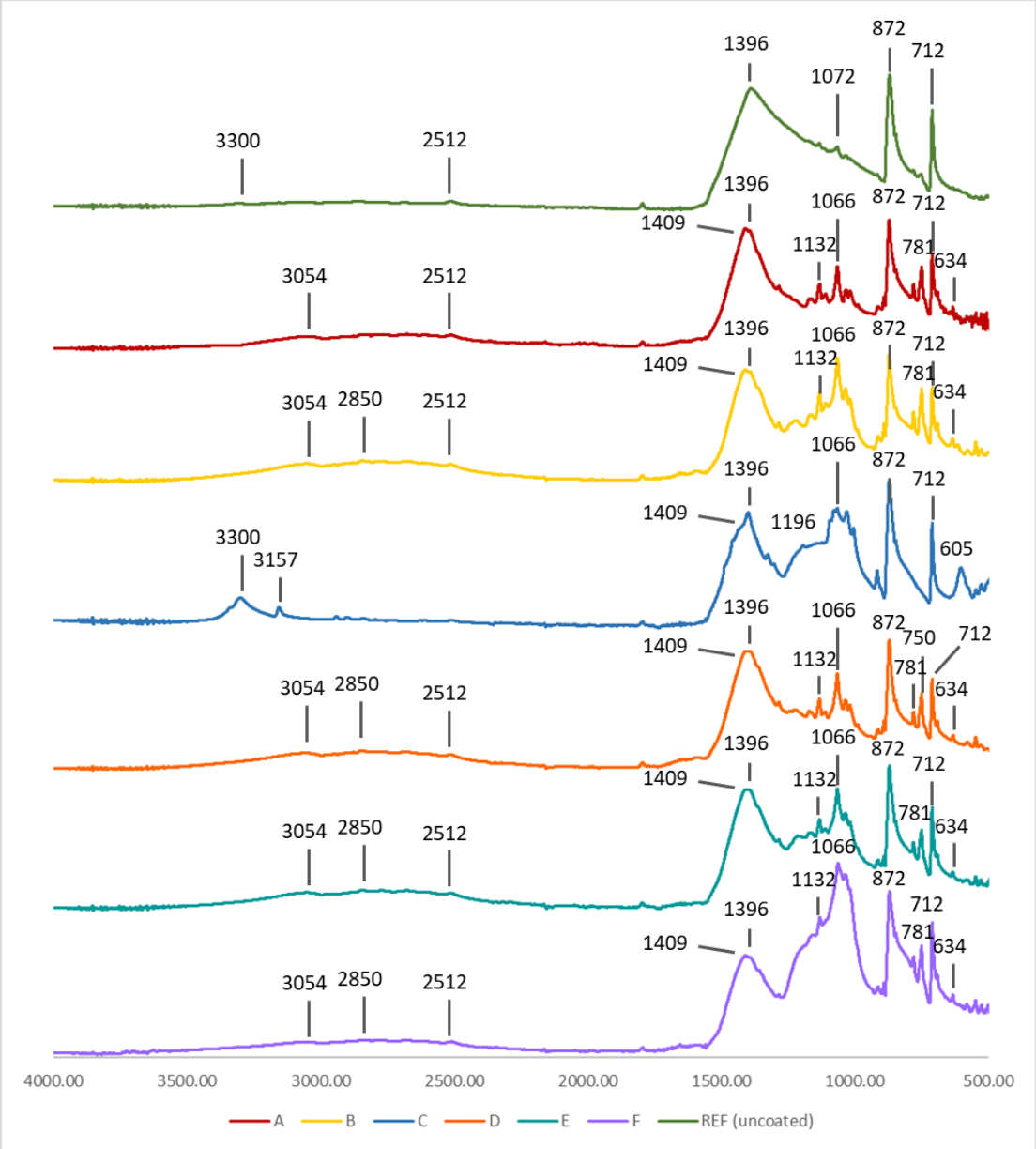

Figure 6.8. ATR-FTIR spectra collected of SiO_x thin film deposited on coated (A,B,C,D,E) and uncoated limestone tablets.

Figure 6.8 shows the ATR-FTIR spectra results of the SiO_x. From the plasma deposited limestone (A, B, C, D, E, F), a broad Si-O symmetric stretching peak at 1066 cm^{-1} was detected. The shallow curve between 3300 ~ 2200 cm^{-1} represents O-H stretching [259]. The peak at 1136 cm^{-1} is associated with the C-O stretching bond,

and the peak at 781 cm^{-1} demonstrated the existence of Si-C bond [260]. This proves the silicate film on the limestone surface, with some of the -OCH_3 groups un-reacted from the TEOS precursor.

6.3.2 Resistance to acid rain

For the uncoated limestones after sulfuric acid accelerated weathering test, the SEM-EDS graphs are shown in Figure 6.9. It can be seen that in the area of calcitic micrite and sparite crystalline cement, voids have appeared, and small crystal grains with diameter < 10 μm were precipitated (a). The outlines of oolites also became discontinuous (b), with some of the oolites even losing their outline (circled by red dash line). EDS mapping (d) showed overlapped distribution of sulphur with the small grains (c), illustrating the precipitation of gypsum crystals (CaSO4 x 2H2O). In the enlarged view of an oolite, small calcite grains inside the oolite have been compacted together (e), and these areas show high counts of S (f), implying the calcite dissolved by sulfuric acid and reacted to form gypsum.

When it comes to the SiO_x coated tablets, sulfuric acid tests led to different results. Figure 6.10 shows that, when the silicate film remained intact (a, b), the distribution of sulphur is scattered and non-aggregated (c, d). In a particular spot where the coating cracked (e, f), S-rich acicular crystals can be seen (circled by yellow dash), (g, h), indicating again the precipitation of gypsum crystals [261]. This proved by contradiction the protective effectiveness of the SiO_x thin film, because where the coating was cracked and lost, the substrate had reacted with the sulfuric acid and produced calcium sulphate, while areas covered by this coating did not show any sulphation reaction.

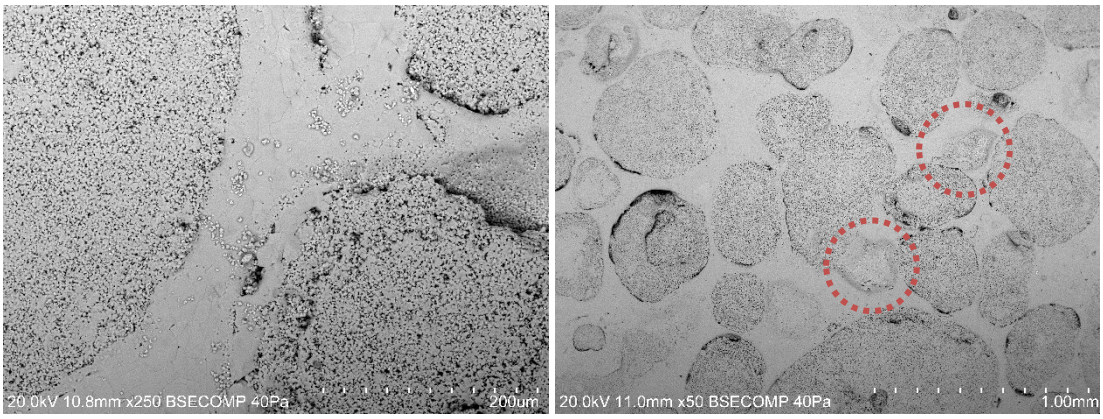

a b

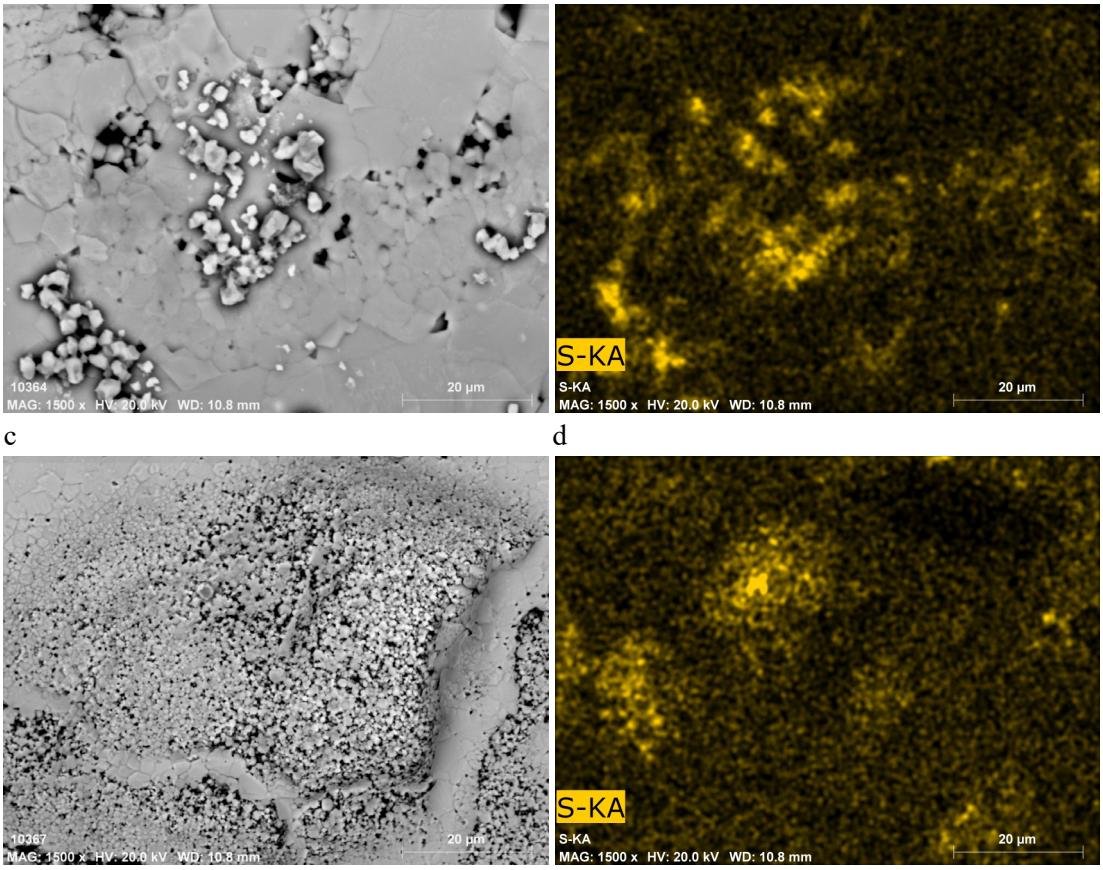

Figure 6.9. SEM-EDS of sulfuric acid attacked limestone without TEOS coating. a, b, c, e. BSE of the surface; d. sulphur element mapping of image c; f. sulphur element mapping of image e.

After ultrasonic cleaning and drying, the sample tablets were then weighted to obtain the mass loss due to acid etching. Without coating, the tablets had lost 0.04 g under the effects of 200 mL H_2SO_4 while in the case of the SiO_x coated tablets, only a weight loss of 0.01~0.02 g was recorded. This demonstrates that the SiO_x film was able to prevent the contact between the limestone and SO_2 acid gas to a certain extent, thus reducing the sulphation and mass loss of $CaCO_3$.

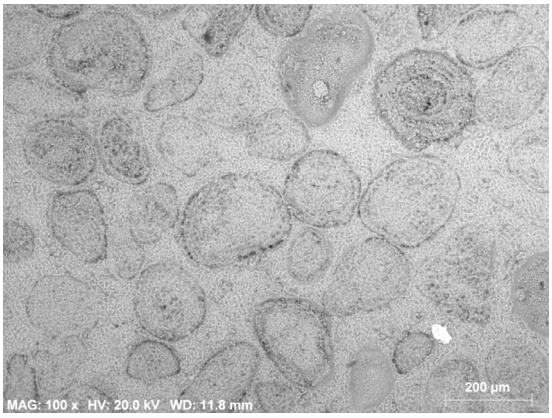
MAG: 100 x HV: 20.0 kV WD: 11.8 mm
200 µm

a

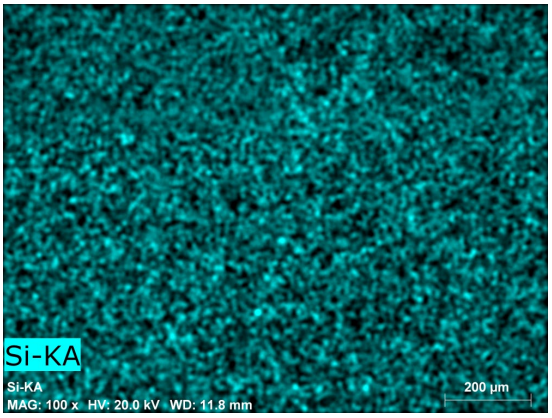
Si-KA
Si-KA
MAG: 100 x HV: 20.0 kV WD: 11.8 mm
200 µm

b

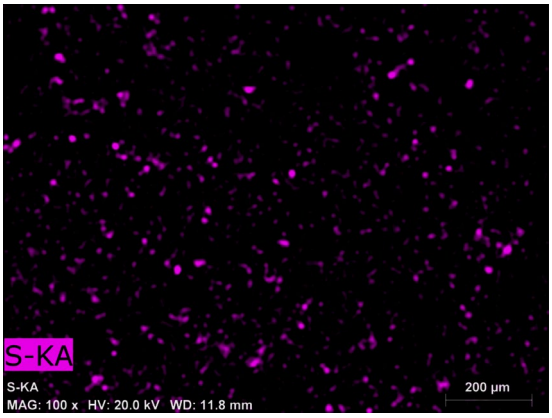
S-KA
S-KA
MAG: 100 x HV: 20.0 kV WD: 11.8 mm
200 µm

c

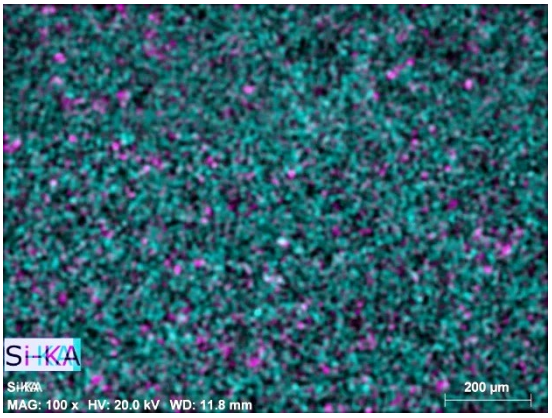
Si-KA
Si-KA
MAG: 100 x HV: 20.0 kV WD: 11.8 mm
200 µm

d

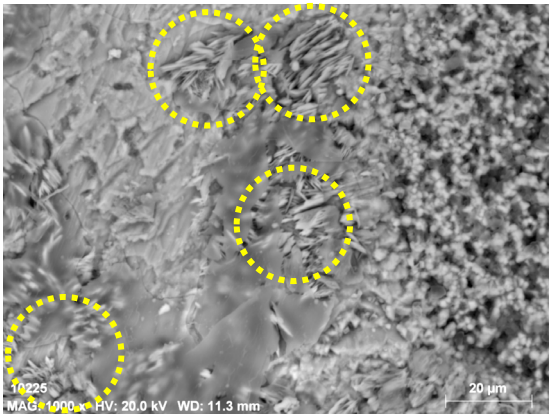
10225
MAG: 1000 x HV: 20.0 kV WD: 11.3 mm
20 µm

e

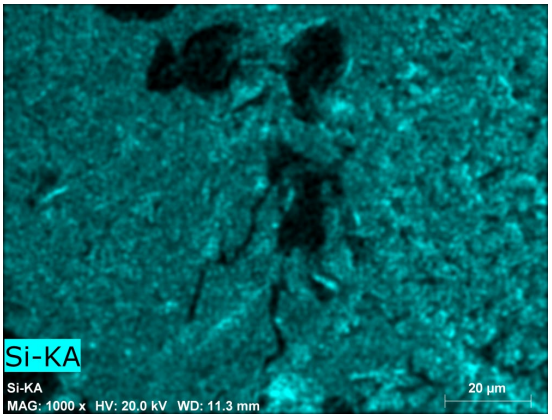
Si-KA
Si-KA
MAG: 1000 x HV: 20.0 kV WD: 11.3 mm
20 µm

f

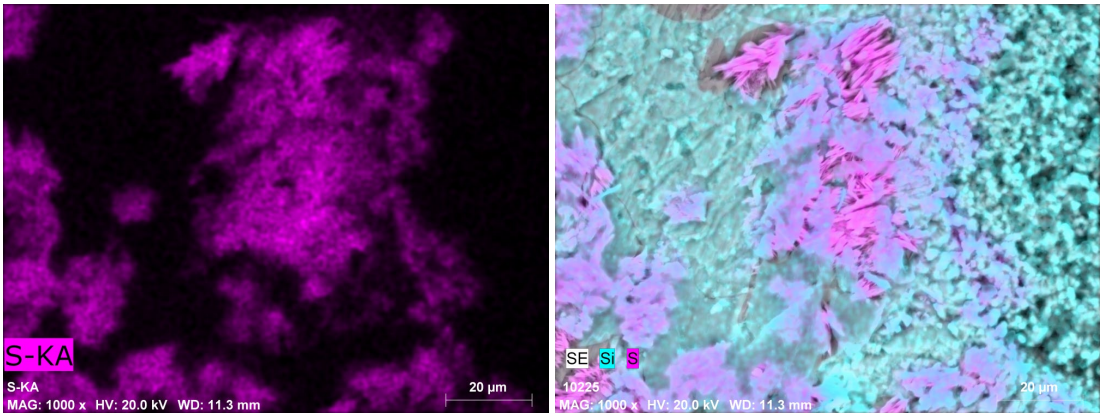

g h

Figure 6.10. SEM-EDS of the SiO_x coated limestone tablets, after sulfuric acid attack. a. an over view of the surface; b, c, d. Si and S element mapping of image a; e. an area where the coating cracked; f, g, h. Si and S element mapping of image e.

Table 6.2. Weight change of the samples before and after the acid attack.

Sample	Original mass (g)	Final mass (g)	Mass change (g)
B	4.70	4.69	0.01
C	5.65	5.63	0.02
D	4.89	4.87	0.02
E	4.45	4.44	0.01
F	4.64	4.62	0.02
REF	4.61	4.57	0.04

6.3.3 Resistance to microbial colonization

The SEM micrographs of microbial incubated samples are shown in Figure 6.11. For limestones without SiO_x coating, after 14-days' incubation, the microorganisms have already aggregated into colonies with size up to 1.0 mm (a). In some areas, the bio-colonization has occupied the whole oolitic framework (b). Wiping the surface with air-laid paper and distilled water, large areas of bio-colonization were removed but a few microbial colonies around 100-200 µm still persisted (c), as well as some bar-shaped fungal spores (d). In the SiO_x coated limestones, in most areas the microorganism turned into agglomeration spots of around 50~100 µm in size (e), big communities also existed in specific zone (f), but they were less concentrated than those found on uncoated limestone (b). After cleaning by wiping the surface with distilled water and air-laid paper, most of the colonies were removed (g) with a few left at the boundary or within of the oolites (h), they are less than 50 µm spots. This is due to the lower microporosity associated with oolitic layering [262]. SiO_x coating might be

absent in some areas where the substrate had hollows and holes due to missing oolite grains (as in Figure 6.14), thus giving opportunity for microorganism colonization. Even so, in general, the SiO_x thin film did reduce the risk of microbial colonization. Nevertheless, bacterial and fungal colonies developed on the surface could be easily wiped away with just distilled water.

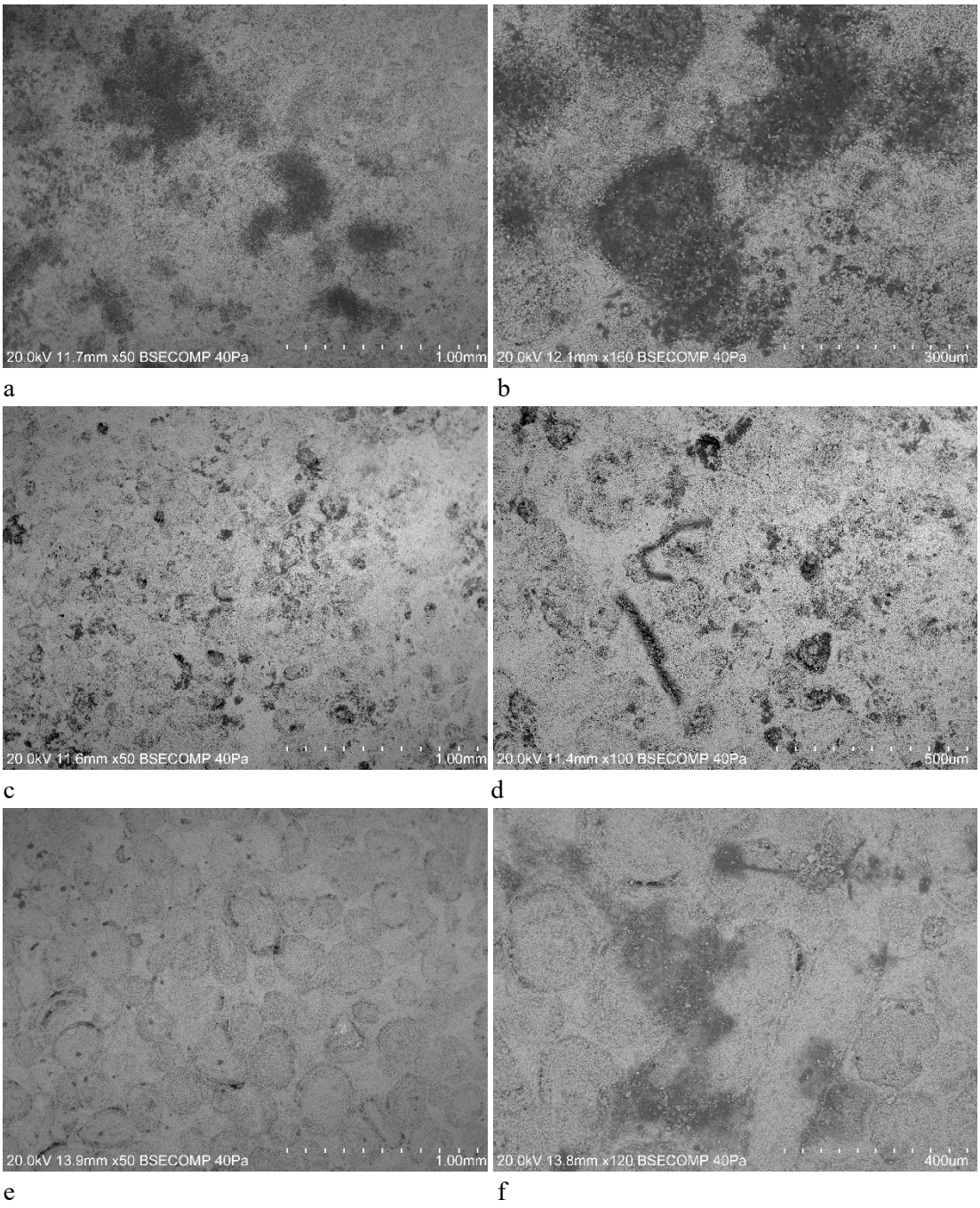

a b

c d

e f

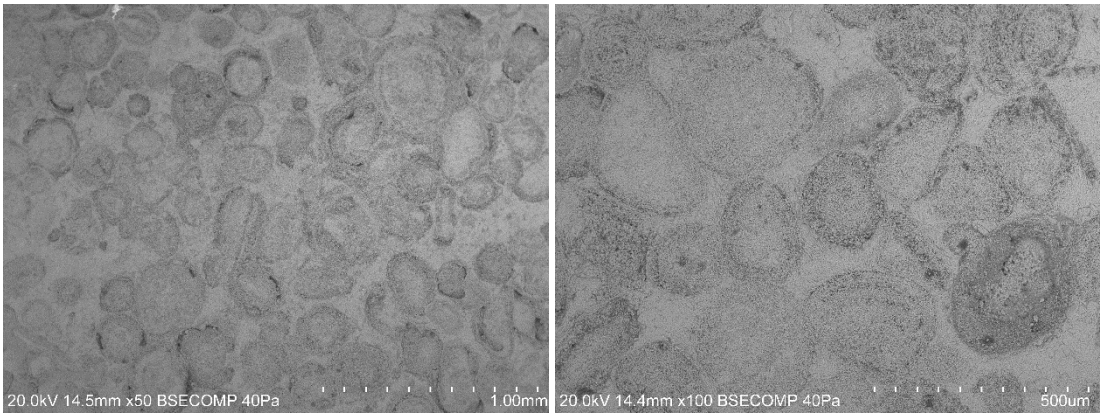

g h

Figure 6.11. SEM of the sample tablets after microbial-incubation. a, b. Undeposited stone after incubation; c, d. undeposited stone with incubation then wiped by airlaid paper with distilled water; e, f. TEOS deposited stone after incubation; g, h. wiped by airlaid paper with distilled water

6.3.4 Outdoor field exposure tests

The tablets exposed on the roof of the Monastery were observed under stereo microscope, see Figure 6.12. On tablets with no SiO_x coating, black spots probably of biological origin had grown intensively on the surface (a, b), the number of these black spots could reach > 30 / mm2; while on the SiO_x coated tablets, the black spots' density is about 5 / mm2 (c, d).

This difference is also reflected in colour, see Table 6.3. In the case of the uncoated tablets, after field exposure the change in lightness ΔL reached -8.68, that is the sample became darker. In the case of SiO_x coated tablets, ΔL was only -0.74, implying the coating was able to significantly preserve the brighter appearance of stone even when exposed in the open environment. According to the red/green and yellow/blue index, the uncoated tablet showed a = 1.79 and b = 7.75, comparing with the SiO_x coated tablet which showed a = 1.46 and b = 6.72, with the uncoated tablet more red and yellow. Hence, when exposed under the solar irradiation, contamination from urban gaseous and particulate air pollutants and microorganisms' colonization, limestone without surface protection would undergo colour changing. It can be deduced that, the red-yellow colour combining with darkening, will end up in the orange – brownish look.

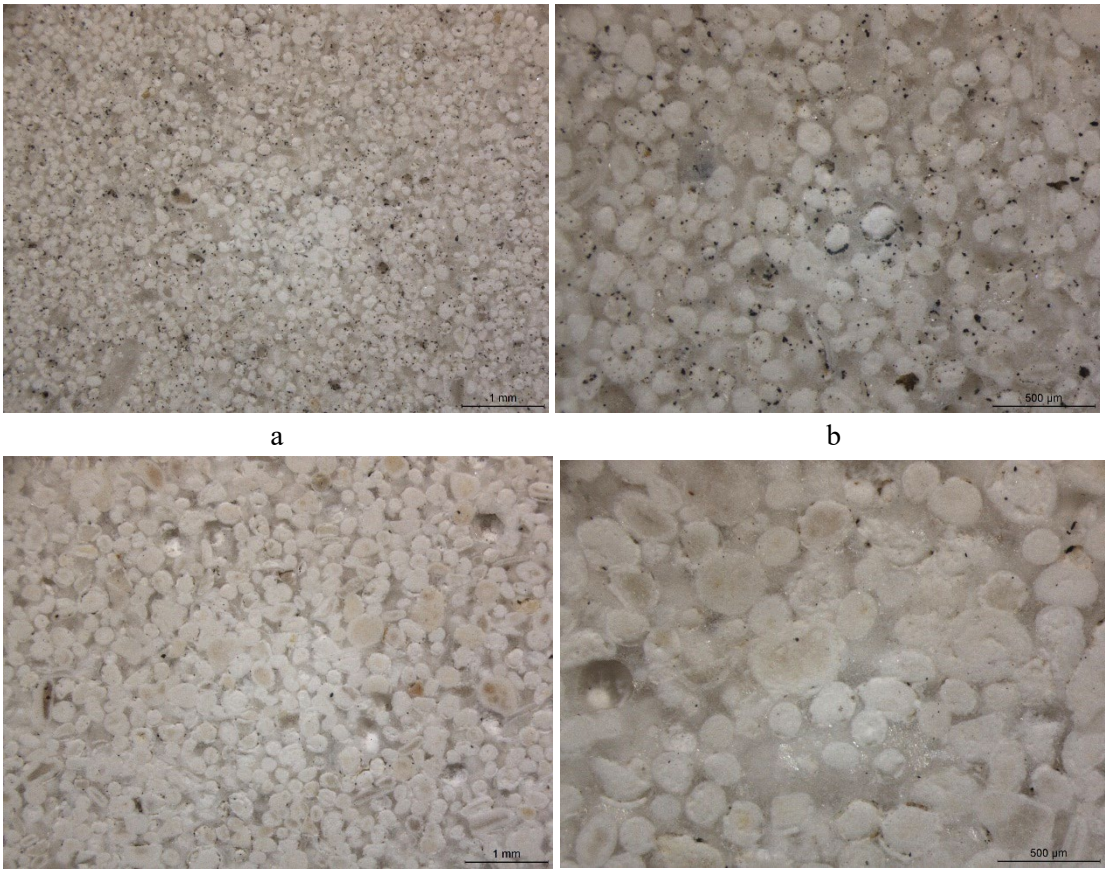

Figure 6.12. Sample tablets after three months of exposure. a, b. sample without SiO_x coating; c, d. sample with SiO_x thin film deposited in condition D.

Table 6.3. L*a*b*C*H* coordinates of the sample tablets before and after expose.

Sample	**CDR quarry stone before exposure**	**CDR9 (uncoated) after exposure**		**CDR10 (SiO_x coated) after exposure**	
	value	value	Δ	value	Δ
L	89.64	80.96	-8.68	88.90	-0.74
a	1.95	1.79	-0.14	1.46	-0.49
b	8.29	7.75	-0.54	6.72	-1.57
C	8.52	7.95	-0.57	6.68	-1.84
H	76.71	77.01	0.30	77.74	1.03

6.3.5 Changes in hydrophobicity and vapour permeability

The water contact angle measurement was not applicable for these samples, because for all samples with and without SiO_x thin film, the water drop was not able to maintain a spherical shape and was absorbed by the substrate within 15 seconds.

Therefore, the deposited coatings did not provide the substrate with water repellent properties.

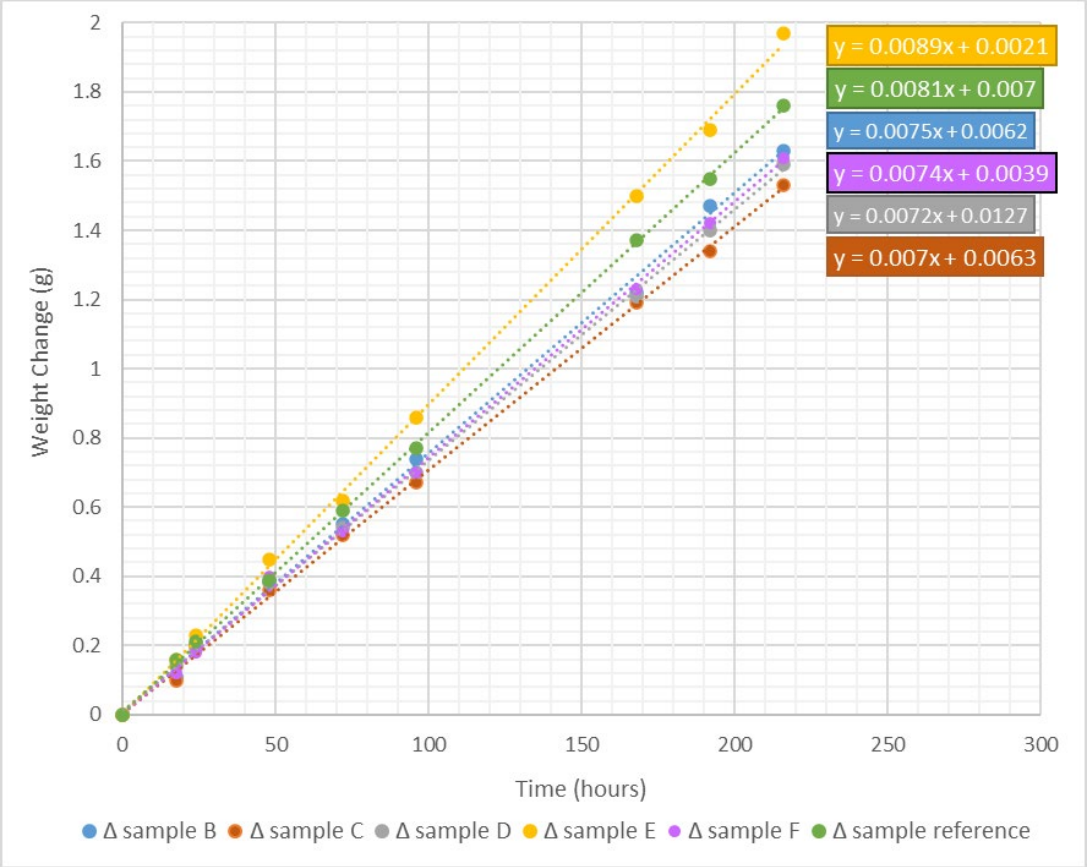

Figure 6.13. Mass loss correlated to time by water vapour permeability.

Table 6.4. Water permeability rate of sample tablets

Sample	Weight loss (g/hour)	Relative permeability rate
B	0.0075	93%
C	0.0070	86%
D	0.0072	89%
E	0.0089	110%
F	0.0074	91%
REF	0.0081	100%

The mass loss due to water vapour permeability with time of each sample – container system is shown in Figure 6.12. Linear regression was made to fit the weight change of each sample, and the corresponding slope represents the vapour permeability rate (gram per hour). In order to obtain the relative ratio of permeability, the value of

each sample has been divided by that of the uncoated sample (REF). It can be seen that all the deposited sample had a permeability rate change less than 14%, among which tablets deposited under condition B and F had only 7% and 9% difference comparing to the uncoated tablet. Sample E showed unexpectedly higher permeability than sample without coating: this might be caused by the presence of fissures or cracks in that tablet.

A strong decrease in water permeability would remarkably increase the risk of water accumulation underneath stone surface, leading to decay caused by dry–wet cycles, freeze–thaw cycles in cold climates [239]. The temperature in Batalha can go below 0 °C during winter monthes, hence, to limit such risk is advisable, especially in the case of monuments and artefacts located outdoor in non-tropical regions. By plasma deposited SiO_x coating, with a water vapour permeability reduced to less than 15% or even to <10%, such changes are acceptable [263].

6.3.6 Durability of the deposited SiO_x thin film

Following the procedure described in *6.3.2 Resistance to acid rain* and *6.3.4 Outdoor field* expos the samples were checked again by SEM-EDS to assess the durability of the SiOx coating (Figure 6.14 and Figure 6.15, respectively). In the case of the acid attacked samples, most part of the SiO_x film remained, except some parts that were lost together with the detached oolites from the limestone substrate. In the case of the outdoor exposed tablets, the coating remained almost intact. However, some material losoccured within the film as can be seen in Figure 6.14 where holes 10~20 μm in size are evident in the Si EDS map.

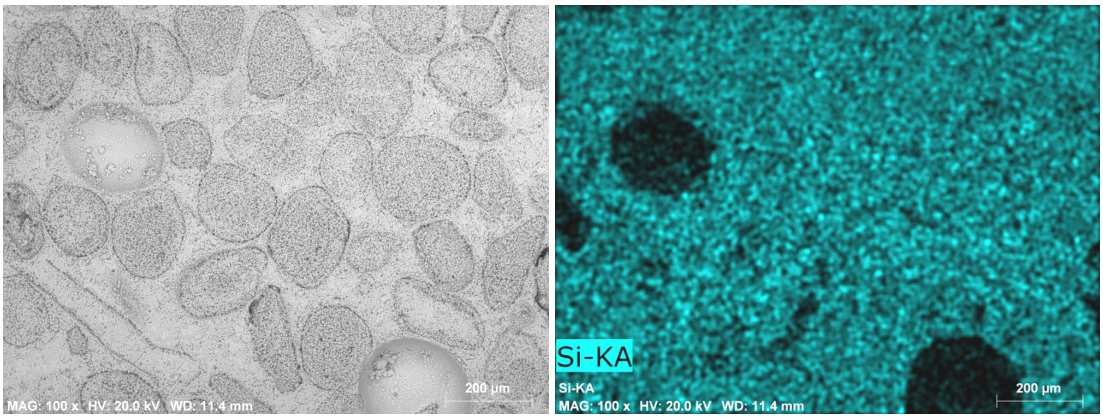

a b

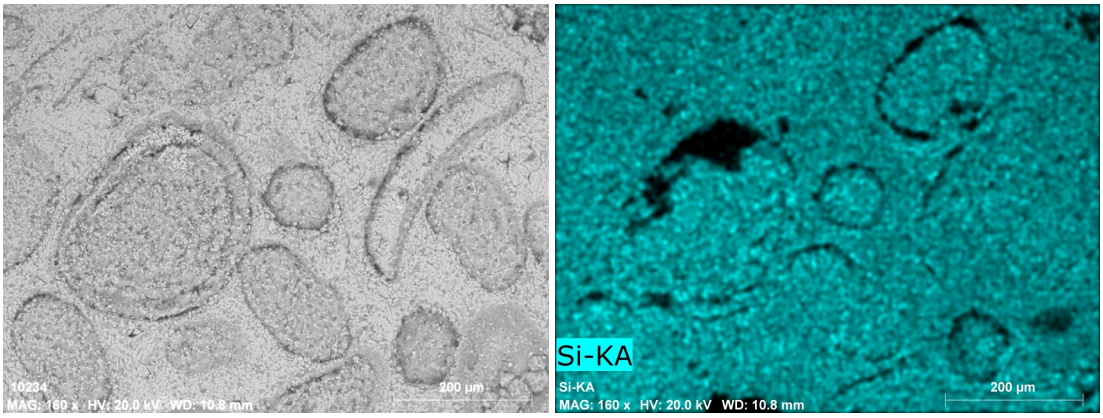

c d

Figure 6.14. SEM-EDS of the acid attacked and ultrasonic cleaned samples. a, c. BSE of the surface; b. Si-element mapping of a; d. Si-element mapping of c.

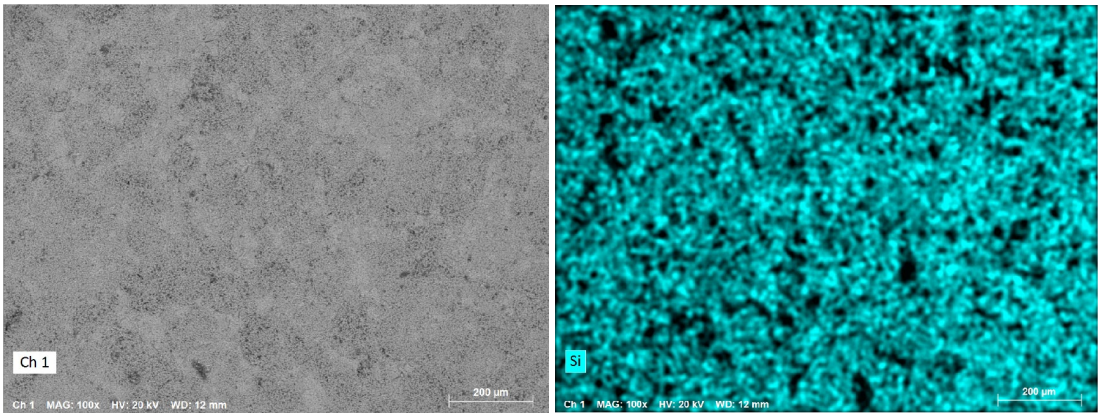

a b

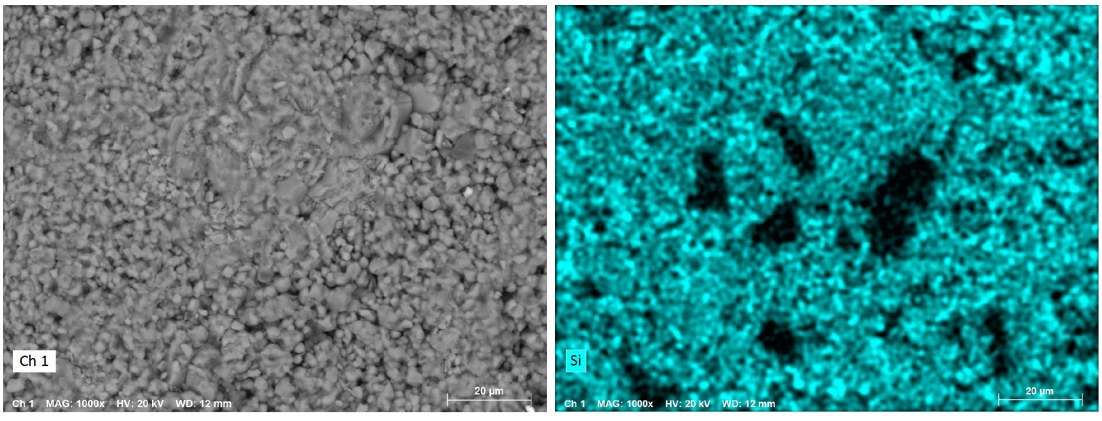

c d

Figure 6.15. SEM-EDS of the exposed samples. a, c. BSE of the surface; b. Si-element mapping of a; d. Si-element mapping of c.

In summary, the plasma deposited SiO_x film offers the following conservation effect: i) prevent the microbial implantation on the stone surface; ii) isolate the substrate from the acid solution attack; iii) maintain the bright appearance of the stone and avert darkening. However, SiO_x thin films deposited via plasma do not behave the same as those consolidate agents do, i.e., such thin film does not fill up the already existed holes or cracks, nor prevent the progression of weathering break down. Therefore, the endurance of this coating also depends on the intrinsic firmness of the substrate material.

6.4 Conclusions

This chapter investigated the conservation effectiveness of plasma deposited SiO_x thin film on the limestone surface used in the Batalha monastery and evaluated their performance after accelerated weathering tests by sulfuric acid attack and microorganism colonization. Water vapour permeability changes brought by the surface coating were also investigated. Results showed a positive effect of the deposited SiO_x coating layer in preventing the contact between acid solutions and the stone substrate, as well as in slowing down microbial colonization and growth. The film did not make noteworthy improvement in hydrophobicity of the stone, but it achieved good result in maintaining its vapour permeability. The durability of such film under various environmental pollutants needs further investigation.

The advantages of SiO_x coating acquired via plasma deposition is correlated to its short consolidation time. Unlike SiO_x coating produced by sol-gel or chemical solution reaction which can take up to months and create fissures, this procedure can obtain a crack-free film as fast as in 20~40 min. Nevertheless, at present the size of the reaction chamber limits the dimension of objects/artefacts that could be treated. On the other hand, in a recent study, the feasibility of using an atmospheric pressure plasma torch to deposit SiO_x thin film from different monomers (TEOS, HMDSO) has been demonstrated [264]. This technique may be proposed for small artefacts made in stone, or even ceramic and other inorganic materials. On a compact and low porosity substrate, SiO_x thin coating could achieve the best performance in terms of materials conservation. Further research aimed at the development of portable plasma instruments that could be used for the deposition of thin SiO_x films on outdoor stone facades and / or statues in Cultural Heritage monuments and buildings are starting to become commercially available.

Summary

This project aims to investigate the application of two innovation technologies – laser cleaning and plasma etching, towards the conservation of bio-deteriorated and weathered building limestone in outdoor cultural heritage assets in urban environments. To this purpose, the Batalha Monastery, one of the most important historical limestone monuments in Batalha county, Leiria district, central region of Portugal, which was built in 14th century using Reguengo Fetal oolitic limestone (Calcarios ooliticos de Reguengo Fetal) and Moleanos limestone (Calcarios de Moleanos) from Jurrasic and showing strong decay patterns at the surface, was selected as the case study of the research. Main objectives of the research were to: a) assess, via the characterization of the weathered building stone of the monastery, the nature and main factors (air pollution versus biogolical attack) responsible for the observed decay patterns; b) compare the efficacy and safety of laser cleaning versus plasma etching in removing decay surface patinas developed on limestone surfaces; c) suggest a conservation protocol for the preservation of the Batalha limestone.

The thesis is divided into six chapters.

The first three chapters (Chapter 1, 2 and 3) focus on the mineralogical and chemical characterization of the building stone material used in the construction of the selected monuments, its decay patterns and its current state of conservation. In particular:

Chapter 1 focuses on the nature and provenance of the limestone used for the construction and restoration of the Batalha Monastery. Through a detailed mineralogical and chemical characterization of the Batalha stone material, the historical quarries which supplied the stone used in the construction of the monastery were identified. Stone samples were collected from the monument (royal cloister, roof, arch, balustrade, and church railing) and from five limestone quarries (Pidiogo, Valinho do Rei, Reguengo do Fetal, Cabeço do Roxo, Outeiro de Sebastiao) in the region surrounding the Batalha county. These stones were investigated by OM, ED-XRF, XRD and TGA. Thin-section observation supplemented the petrographic evidence for the identification: all the stones collected from quarries and the monastery are oolitic

limestones sedimented in middle-late Jurassic. XRD and TGA were used to acquire information on the mineral and chemical composition – they are limestones with high content of calcite and minor quartz. Ca-Sr binary diagrams from the ED-XRF result indicated the source of the samples collected from different parts of the monastery - the monastery baluster was made of stone from the Valinho do Rei or Reguengo do Fetal quarries, whereas part of the church railing, the north-aisle eaves arch and Royal Cloister were made with stone from the Pidiogo or Cabeço do Roxo quarries, while other tested monastery pieces were possibly built with the limestones from the lost quarry Carvalhos.

Chapter 2 focuses on the characterization of orange patinas present at the surface on the external walls and stone ornaments in the monastery, illustrated their differences and the possible formation mechanisms. amples have been investigated by μ-XRD and LV-SEM + EDS. The aim was to determine the composition of the layered patinas, assess whether they have been intentionally applied during restoration interventions or they were naturally formed (either from biological and/or environmental facotrs), and study their degradation patterns. The results revealed that the orange patinas on the window tracery and the ornament showed different compositions and appearance, suggesting distinct formation pathways. Orange patinas on the ornament, which are now showing decay and delamination patterns, mainly consisted of gypsum with hematite as a minor component, implying the possibility of an intentional application of a mixture of ochre and lime as tint plaster. Orange patinas on the window tracery show, instead, the presence of Ca-oxalates, abundant weddellite, and minor whewellite, with minor hematite suggesting the yellowish/orange colour as being due to Ca-oxalate patinas imbedding soil dust airborne particles, suggesting that it was possibly formed naturally either by the chemical attack due to atmospheric air pollutants from traffic exhausts emissions or by bacterial activity. A comparison between this patina and the so-called scialbatura (a surface yellowish coating often found on limestone and marble in ancient monuments in the Mediterranean region) was also made.

Chapter 3 investigates in detail the nature and extent of the widespread microbial colonization affecting the Batalha's limestone surfaces, and the ensuing bio-deterioration processes, revealing how environmental and urban pollution related decay factors may act in synergy with bio-deterioration processes in stone monuments. Stone fragments covered with microbial biofilms and lichenous crusts were investigated using OM, LV-SEM + EDS, and μ-XRD. Microbial samples were collected from the stone surface, cultured, and analysed with NGS metagenomic DNA test to classify the bacterial communities associated with the formation of the biofilms. Particulate air pollutants collected on Pall GN-6 paper filters using an optical particle sizer (OPS) were characterized by SEM-EDS + NGS. The results showed that lichens play a major

role in biodeterioration by promoting both physical and chemical attack on the limestone substrate via hyphae mechanical penetration along calcite inter-crystalline spaces, the dissolution/leaching of calcite minerals, and the precipitation of secondary minerals such as Ca-oxalates within the stone porosity framework. DNA analyses identified the bacterial communities within the biofilms and their relative abundances. Air quality monitoring results suggest that the microbial population colonizing the monastery limestone could at least partially be derived from the dry and wet deposition of airborne biological particles on the stone surfaces and that S, N, and P-rich air pollutants may have provided nutrients and energy for the bacteria communities, thus indirectly facilitating biofilm formation, the growth of a lichenous crusts, and limestone biodeterioration effects.

The last three chapters (Chapters 4, 5 and 6) concentrate on experimental tests aimed at comparing the efficacy of Laser technologies versus Plasma etching in the cleaning and conservation of weathered Batalha limestone samples. In particular:

Chapter 4 describes plasma etching experiments carried out on limestone tablets exposed to accelerated microbial-colonization, the cleaning efficacy was assessed by FTIR, SEM, OM, and CVI-MTT assays. In these tests, it was proved that the plasma was capable to inhibit the bio-colonization process by a) attacking the microorganism cells, thus causing cell disruption and inactivation; b) decomposing the hydro-carbonates, which is the nutrient source as well as the transformation product of microorganisms, in order to eliminate the nutrient supply and chemical support for microbial metabolism and reproduction. At the macroscopic level, detachment of microbial crust was also observed in plasma etched bio-deteriorated limestone surfaces. Plasma etching is therefore regarded as a fast and eco-friendly conservation tool for stone heritage architecture to prevent/reduce the onset of bio-colonization and biodegradation. However, in stones covered by thick lichenous patinas, plasma etching did not prove successful in removing significantly the biological patinas.

Chapter 5 reports on experimental test using four types of lasers (femtosecond UV laser, picosecond UV laser, picosecond IR laser, nanosecond IR laser) in different irradiation modes and pulse duration for ablating the thick lichenous crust originally present on limestones samples from the monastery, as well as from filed exposed stone tablets. Confocal microscope was used to detect the surface roughness change, OM and SEM were used to observe the damage of the lichens, mineral and chemical changes of the limestone induced by laser was investigated with XRD, CVI-MTT assay illustrated the inhibitory effect of bacterial cell viability by laser treatment. Results suggest that femtosecond ultraviolet laser provides the best cleaning result by completely removing the lichen thallus growing on the stone surface without any further intervention such as

chemical alteration or mechanical damages on the substrate. Infrared lasers, instead, produced a thermal effect that led to chemical decomposition and morphology changes on the limestone substrate. Residual fragments of lichens and fungus observed beneath the ablated surface (either by UV lasers or IR lasers) illustrates the difficulty to thoroughly eliminate all endolithic microbes penetrated deeply into the substrate, stressing the need for periodic and regular cleaning sessions. While for field exposed tablets in early stage of bio-colonization, all types of lasers showed biocidal effect, among which ns-IR laser provided the treated area the lowest cell viability, despite the IR lasers left yellow stains on the stone surface. There was also an accidental discovery that fs-UV laser made the limestone surface hydrophobic, this could be a proposing solution for the outdoor artefacts' protection.

Chapter 6 reports on test aimed at assessing the viability of a possible solution for protecting stone artefacts located outdoors from environmental decays: a SiO_x film deposited on stone surface by using TEOS as the reaction precursor and deposited via capacitively coupled parallel-plate plasma. Raman spectrometer proved the existence of the SiO_x coating formed successfully on the limestone, and the thickness of the silicate film was measured by SEM-EDS. By comparing the protective efficacy, coated and uncoated limestone tablets underwent 3-months of field exposure on the roof the Batalha Monastery as well as accelerated aging and cleaning in laboratorial simulation. It was found that the transparent thin SiO_x coating did not significantly influence the water permeability, and this thin film could effectively resist acid rain attack, restrain the colonization of windborne microorganisms, and slow down the darkening of the stone surface. The durability of such film needs further testing, as the plasma deposition protocol is not yet practicable to be applied on vast surfaces in outdoor monuments. Nevertheless, this could be a very promising conservation technique for preserving outdoor stone (or other materials) artworks in limestone monument facades of small-medium dimension.

The cleaning effectiveness of plasma etching and laser cleaning on the limestone of Batalha Monastery was systematically evaluated in the thesis. Main results can be summarised as follows: plasma etching is efficient to remove bio-contamination on stones at incipient stage and is able to decompose carbon-hydroxide substances (used as nutrients by microorganisms) thus inhibiting the growth and reproduction of microorganisms. However, the low-pressure plasma used in this thesis is not capable to clean stones covered by intense microbial colonization, i.e., lichen crusts, fungal colonies, and higher plants. In such cases, laser cleaning seems more efficient as femtosecond UV laser and picosecond UV laser not only ablate the lichen patinas, but also remove calcium oxalate which is a metabolic product by stone inhabiting microorganisms.

Despite the different techniques used for stone cleaning, neither laser nor plasma is able to repair the chemical (dissolution cavities) and physical (cracks and fissures) decay features induced by biodeterioration processes. It is therefore needed to apply preventive conservation methods for stone artefacts that possibly may be exposed to environmental and biological attack. Plasma assisted SiOx thin film surface deposition seems to be a promising solution as it create a transparent, “breathable”, thin surface layer that is capable to effectively protect the stone both from acid rain as well as from microorganism deposition.

The texture of the stone is also a critical factor in determining the decay resistance of the stone. In the Batalha Monastery case study investigated in this thesis, the sedimentary oolitic limestones have intrinsic features that facilitate the decay process. For instance, microporosity differences between the oolitic grains and the sparitic cement in the Batalha limestones seems to be controlling the progression of physical (lichen hyphae penetration) as well as chemical (acid attack) weathering fronts. From the point of view of the mason professionals, limestone can be considered a relatively soft stone comparing to other lithotypes such as metamorphic and igneous stones and that is the reason why it has been so widely used as ornamental stone for sculptures and architectural decorations in Cultural Heritage assets and buildings in Portugal, Europe and worldwide throughout history. Developing proper conservation protocols and methodologies for limestone architectures and artefacts is, therefore an essential topic in cultural heritage research. I hope that the results stemming from this PhD project will be of valuable reference for future research in this field.

Annex

Annex 1A. Optical microscope graphs of limestone thin sections

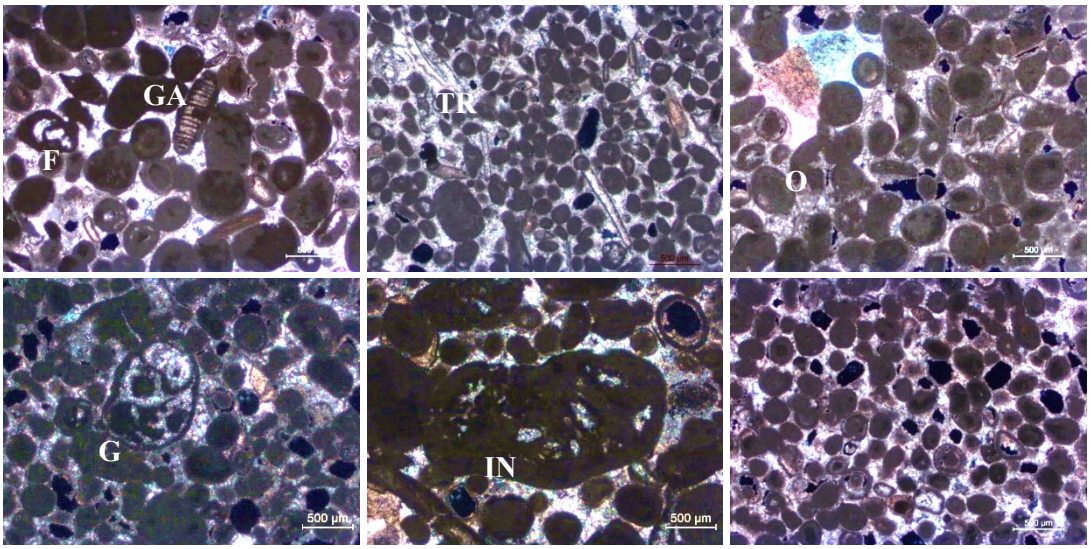

Limestone from Pidiogo quarry (GA=Gymnocodiacean algae, TR=Trilobite, F=Foraminifera, G=Gastrocod, O=Ostracod, IN=Intraclast)

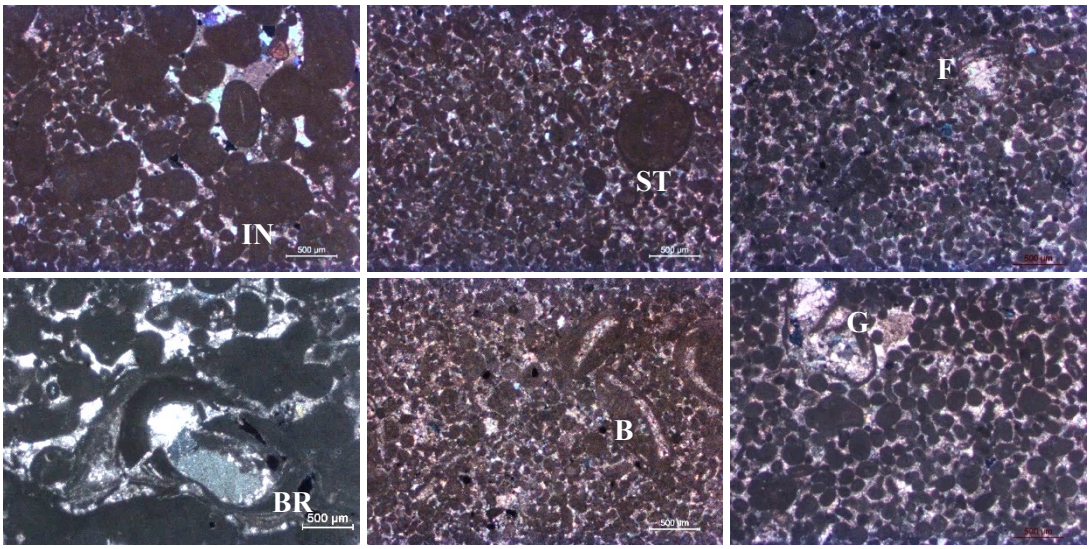

Limestone from Valinho do Rei quarry (F=Foraminifera (trocholina, kurnubia, miliolina), IN=Intraclast, BR=Brachiopod, ST=Styliolinid, B=Bivalve, G=Gastropod)

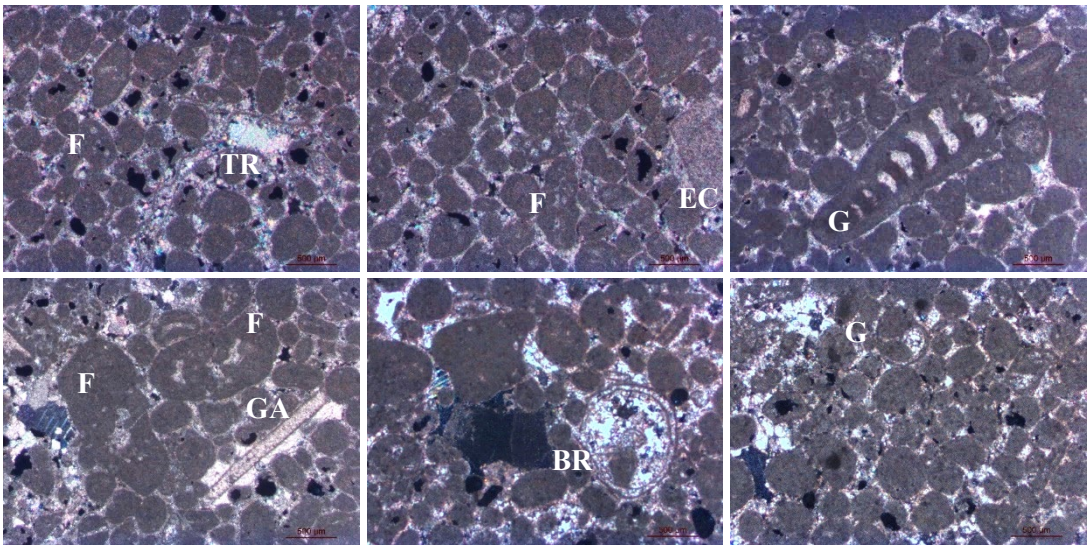

Limestone from Reguengo do Fetal quarry (F=Foraminifera (miliolid, alveospta, haddonia), TR=Trilobite, EC=Echinoderms, G=Gastrapod, BR=Brachiopod)

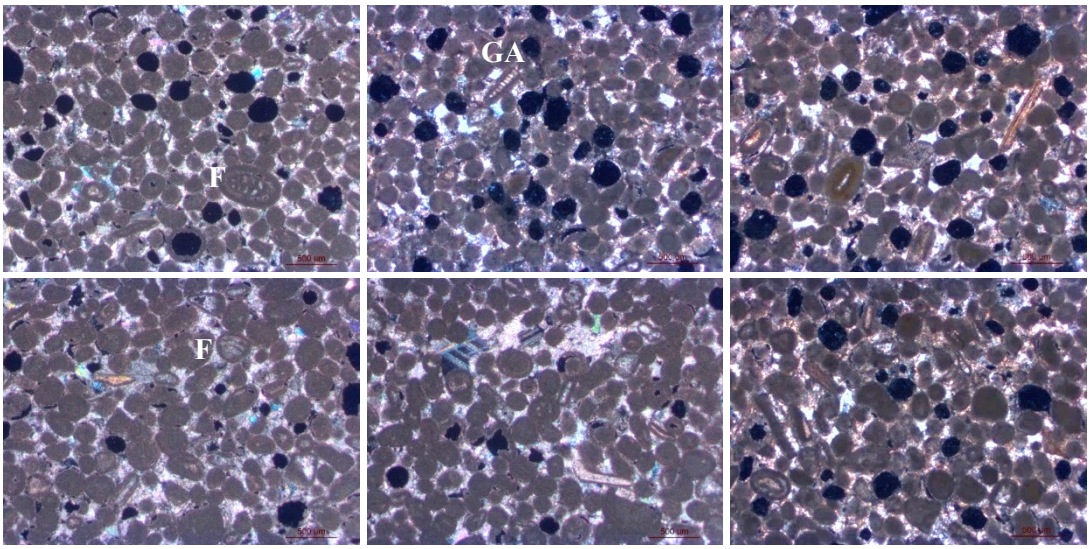

Limestone from Cabeço do Roxo quarry (, GA=Gymnocodiacean algae, F=Foraminifera)

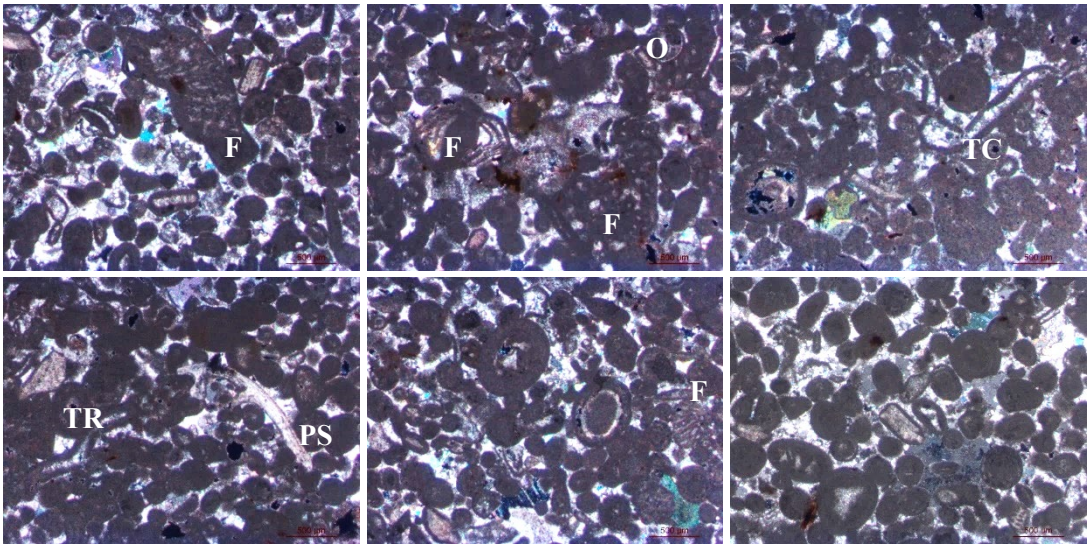

Limestone from Outeiro de Sebastião quarry (PS=Pseudodonezella, O=Ostracod, EC=Echinoderm, F=Foraminifera (kurnubia, lenticulina), TR=Trilobite)

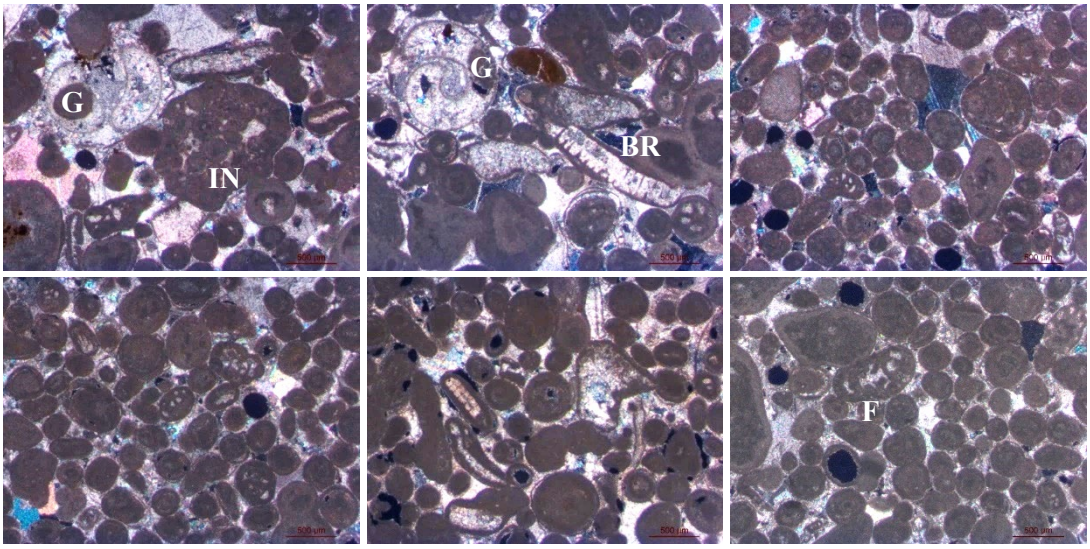

Limestone from Batalha Monastery, royal cloister west gallery (G=Gastropod, GA=Gymnocodiacean algae, B=Bivalve, BR= Brachiopod, F=Foraminifera (miliolid), IN=Intraclast)

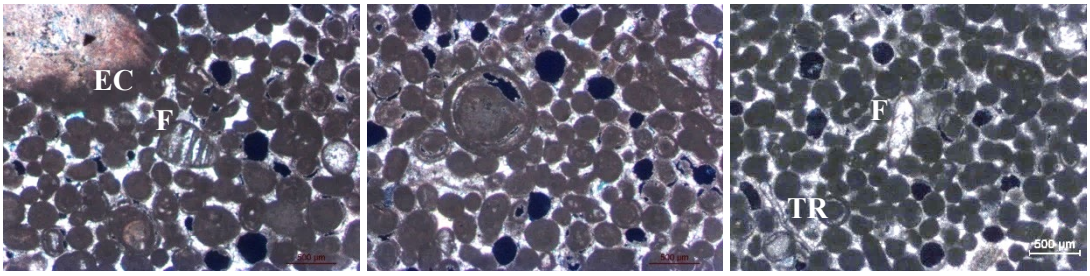

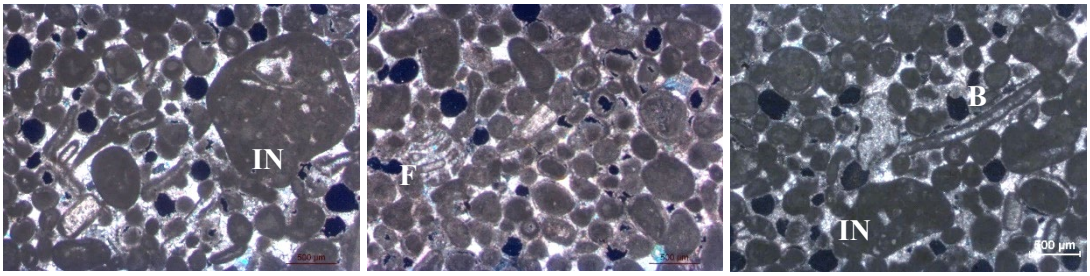

Limestone from Batalha Monastery, north aisle eaves arch (F=Foraminifera (trocholina alpina, miliolina), EC=Echinoderms, IN=Intraclast, TR=Trilobite)

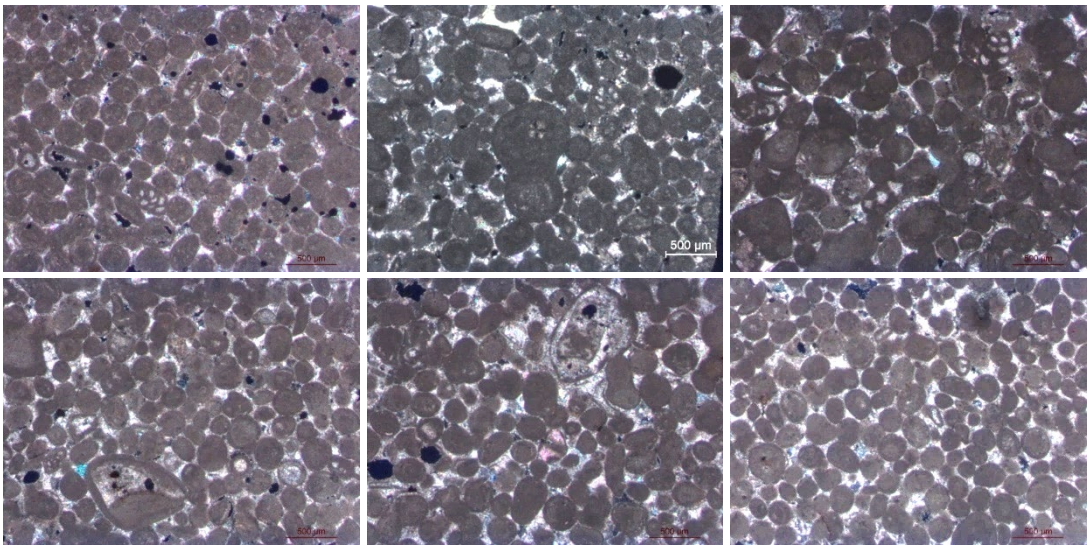

Limestone from Batalha Monastery, roof top (F=Foraminifera)

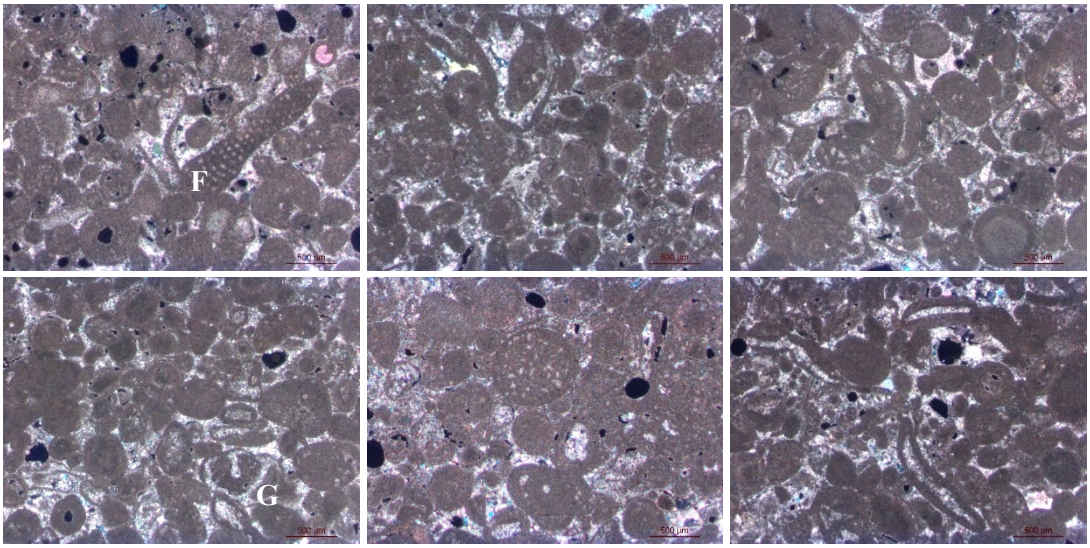

Limestone from Batalha Monastery, church railing 1 (EC=Echinoderm, Gymnocodiacean algae, F=foraminifera (lepidorbitoides))

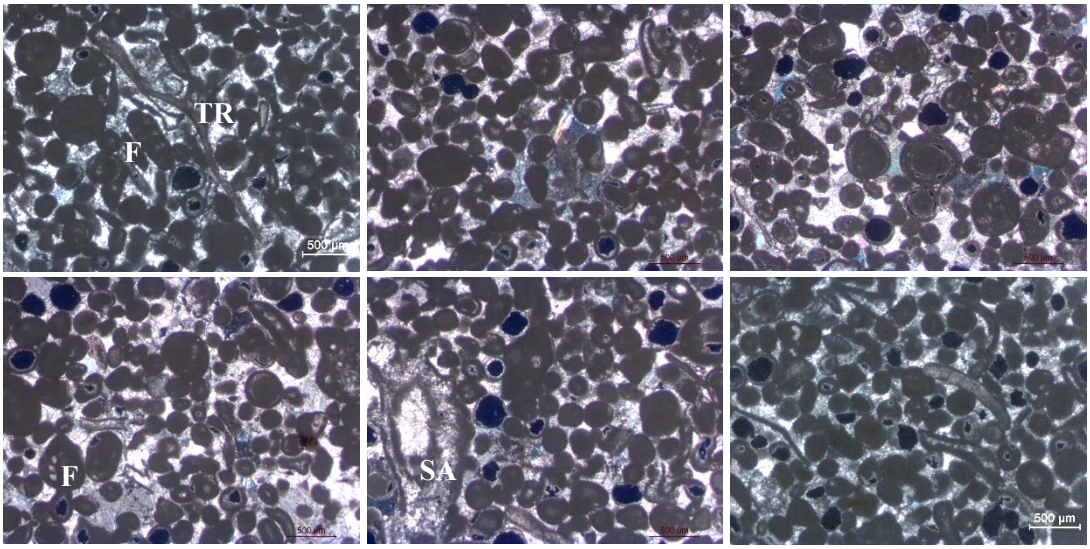

Limestone from Batalha Monastery, church railing 2 (SA=Salpingoporella istriana belongs to Dasyclad Green Algae, F=Foraminifera, TR=Trilobite)

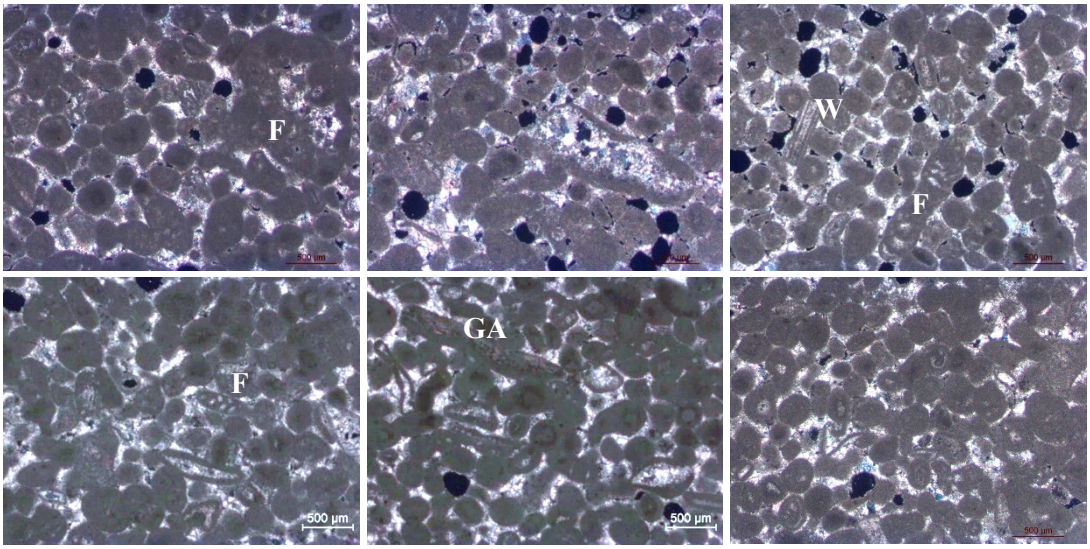

Limestone from Batalha Monastery, baluster (W=Wood, GA=Gymnocodiacean algae, F=Foraminifera)

Annex 1B. XRF results of the limestone samples from different locations (weight percent)

Annex 3A. SEM-EDS picture of tetragonal crystals in the biofilm.

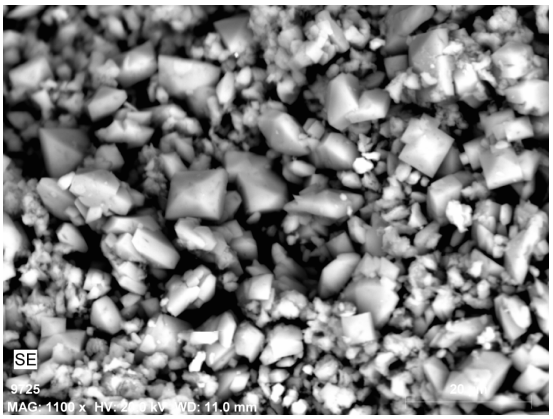

BSE

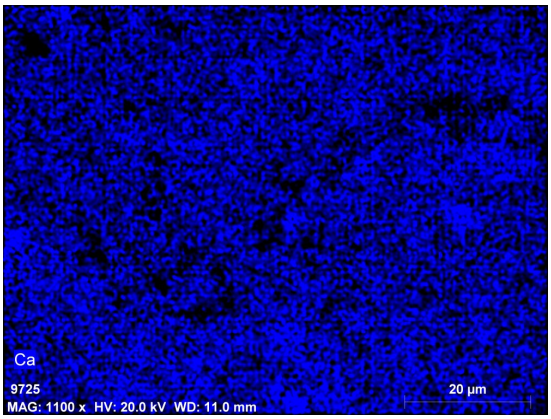

Ca

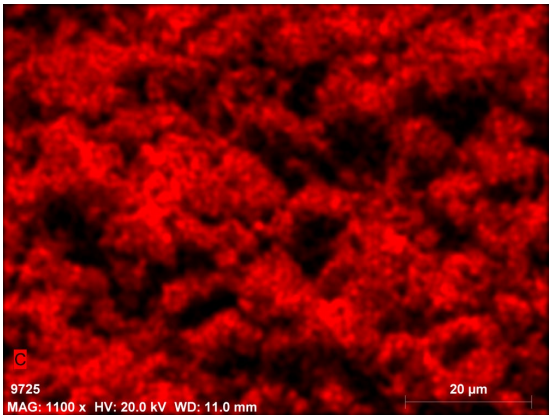

C

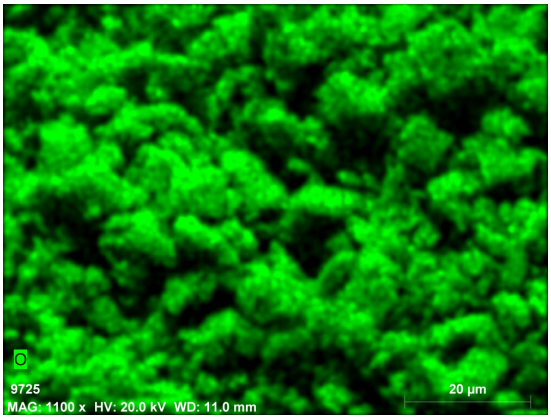

O

Annex 3B. SEM-EDS picture of hyphae cohesive grains.

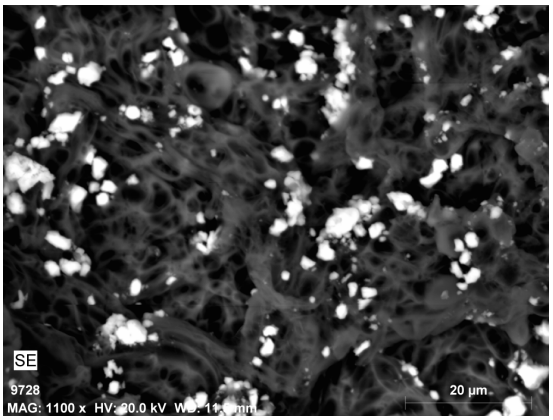

BSE

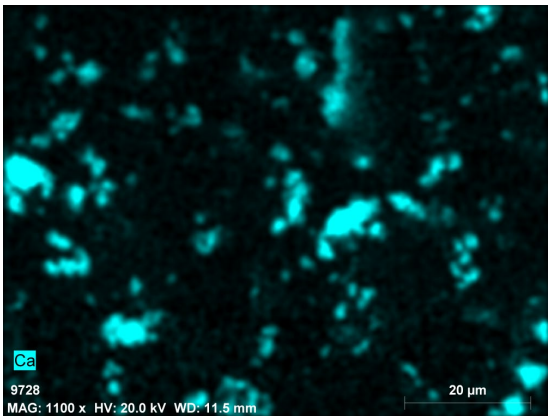

Ca

Annex 3C. SEM-EDS element mapping of a lichen covered area on sample MB-R3.

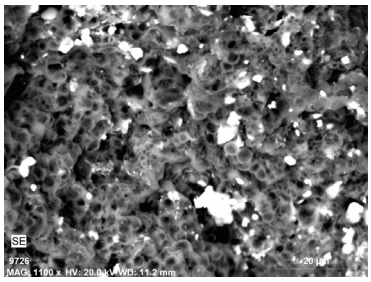

BSE

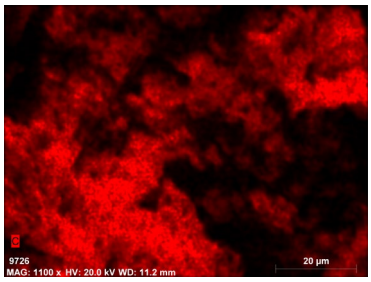

C

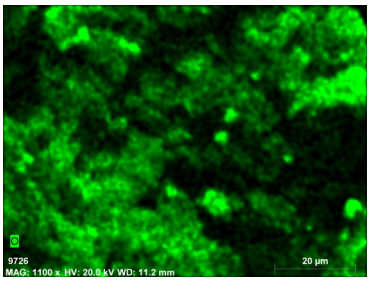

O

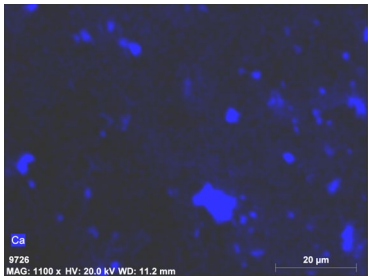

Ca

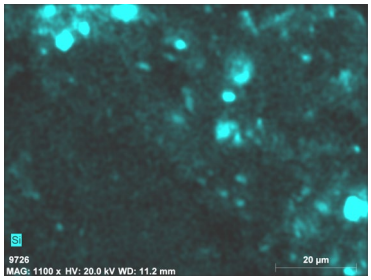

Si

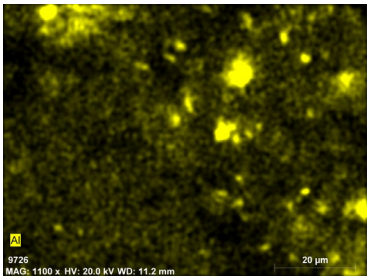

Al

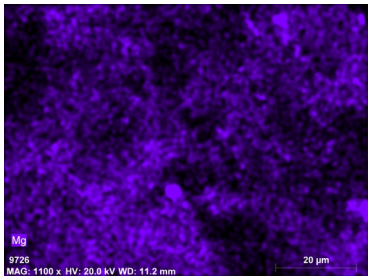

Mg

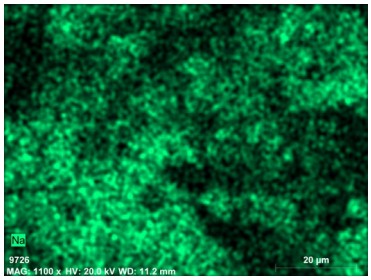

Na

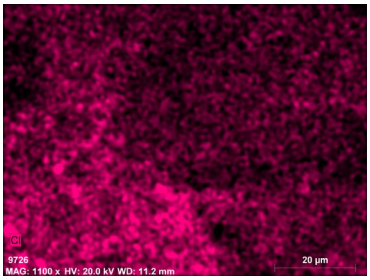

Cl

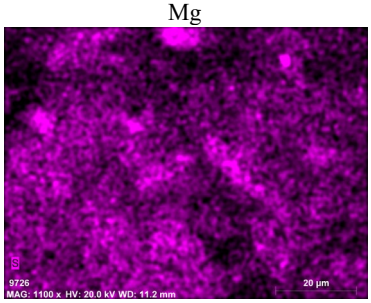

S

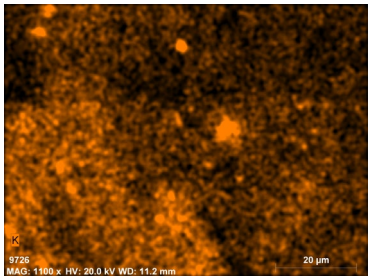

K

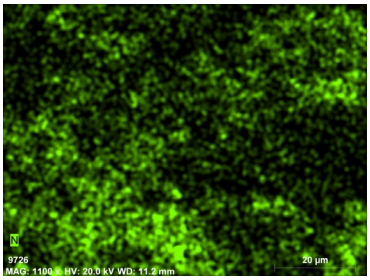

N

Annex 5A. Stone samples with 5*5 mm areas treated by different laser modes.

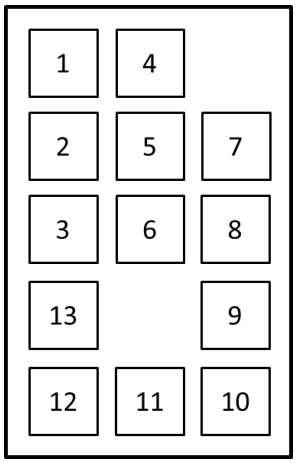

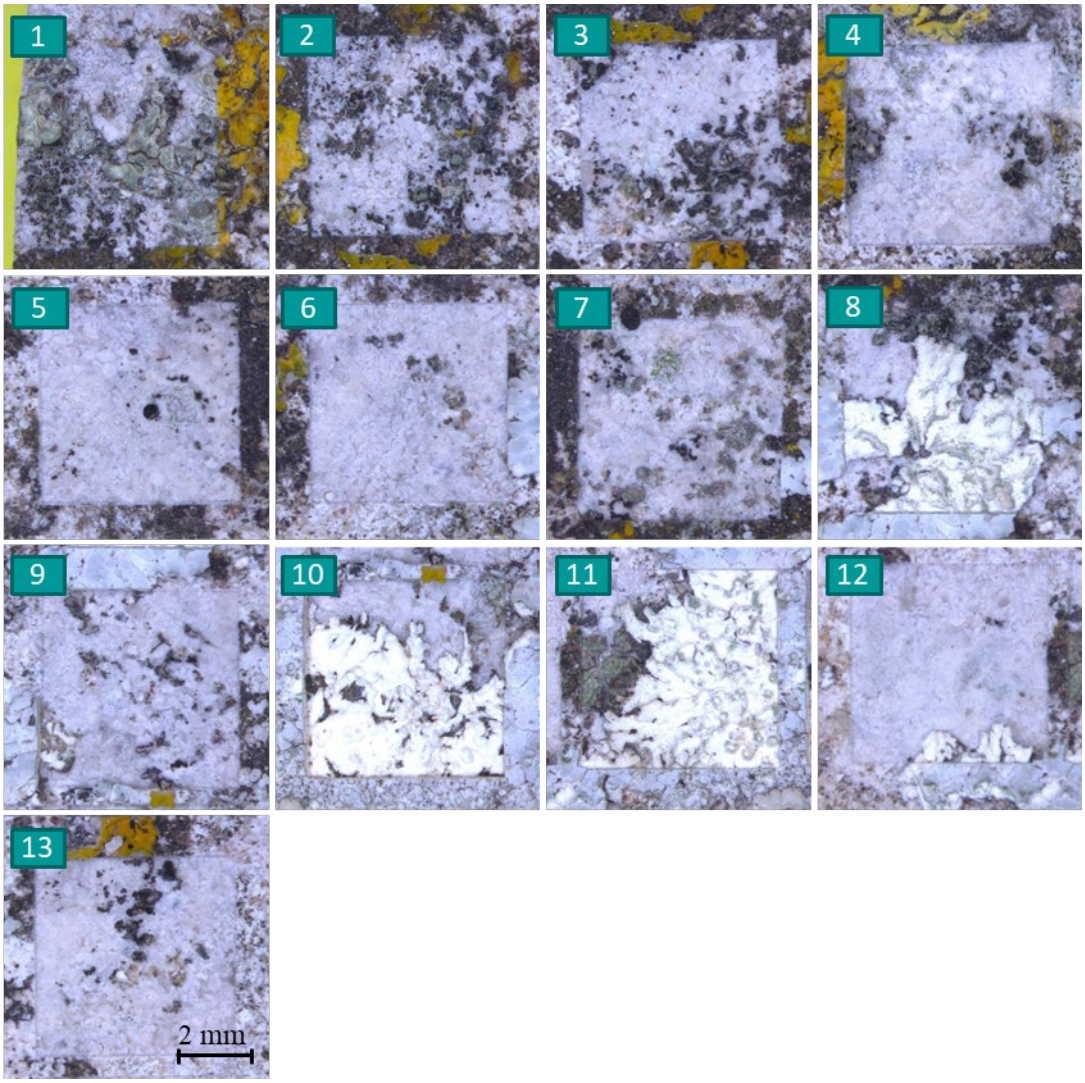

Treated area	Attenuation	Speed (mm/s)	PPD	Frequency (kHz)	Line spacing (mm)	Repititions
1	45%	150	20	10	0.015	10
2	60%+45%	150	20	10	0.015	5+5
3	60%	150	20	10	0.015	10
4	60%	100	20	10	0.015	10
5	60%	3000	1	200	0.015	10
6	60%	1500	2	100	0.015	10
7	60%	750	4	50	0.015	10
8	30%	3000	1	200	0.015	20
9	45%	3000	1	200	0.015	20
10	45%	3000	1	200	0.015	21
11	45%	1500	2	100	0.015	10
12	45%	1500	2	100	0.015	15
13	45%	1000	2	100	0.010	15

(i) Tablet C, treated by fs-UV laser and the operation parameters of each cleaned area

1	2	3
4	5	6
7	8	9
10	11	12
13	14	15

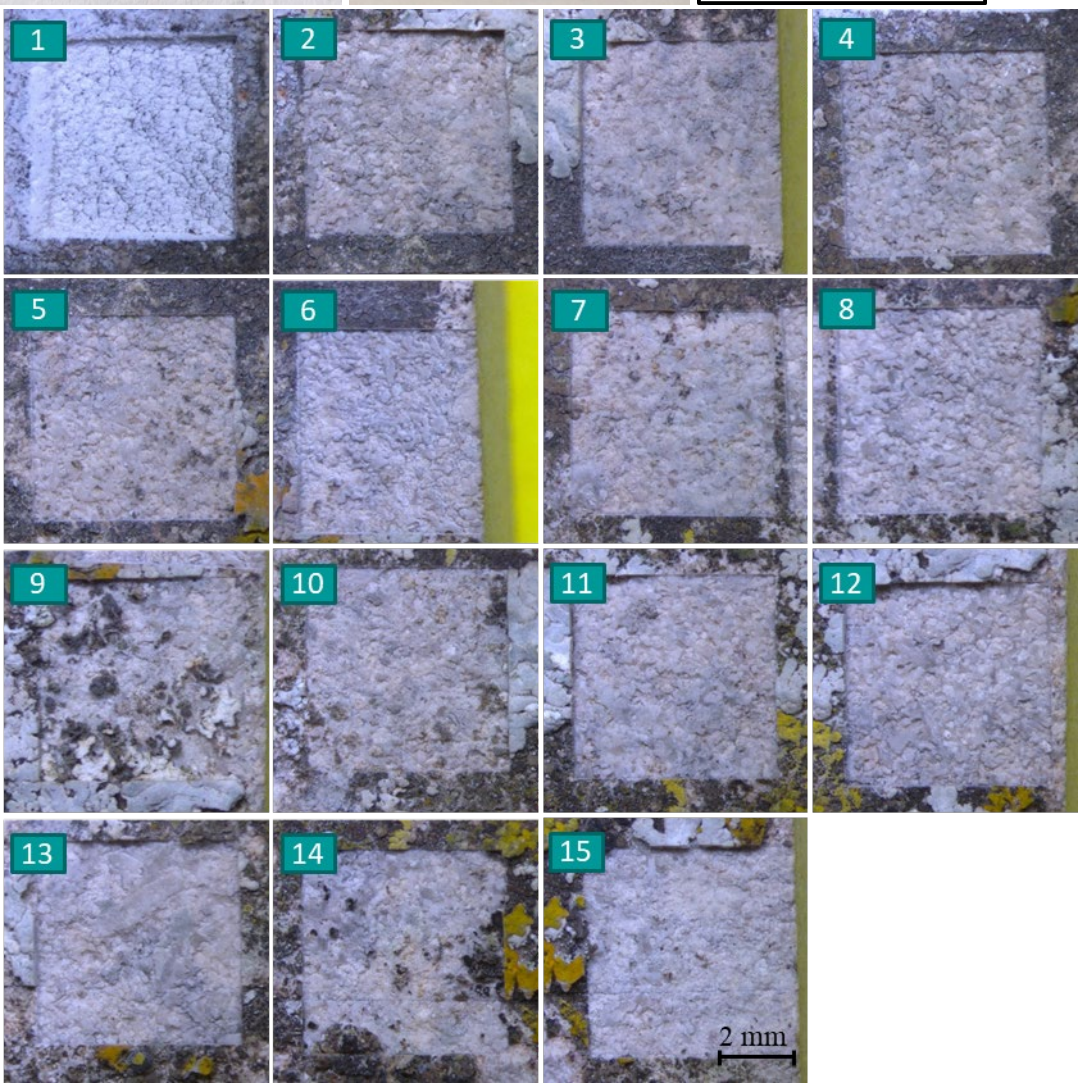

Treated area	Attenuation	Speed (mm/s)	PPD	Frequency (kHz)	Line spacing (mm)	Repititions
1	100%	500	3	67	0.0075	2
2	30%	500	3	67	0.015	10
3	30%	500	3	67	0.0075	5
4	35%	500	3	67	0.0075	5
5	40%	500	3	67	0.0075	5
6	45%	500	3	67	0.0075	2
7	45%	666	3	67	0.010	2
8	45%	666	3	67	0.010	5
9	45%	1332	3	67	0.020	5
10	45%	1332	3	67	0.020	10
11	45%	1332	3	67	0.020	20
12	45%	1199	3	67	0.018	20
13	45%	500	2	100	0.005	5
14	45%	1000	3	67	0.015	15
15	45%	3000	1	200	0.015	100

(ii) Tablet E, treated by fs-UV laser operation parameters of each cleaned area

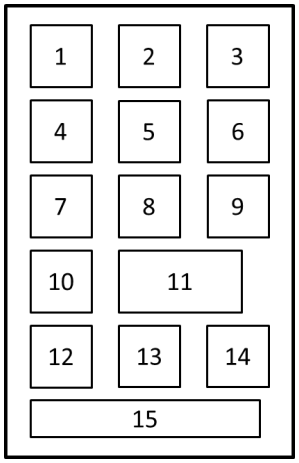
1
2
3
4
5
6
7
8
9
10
11
12
13
14
15

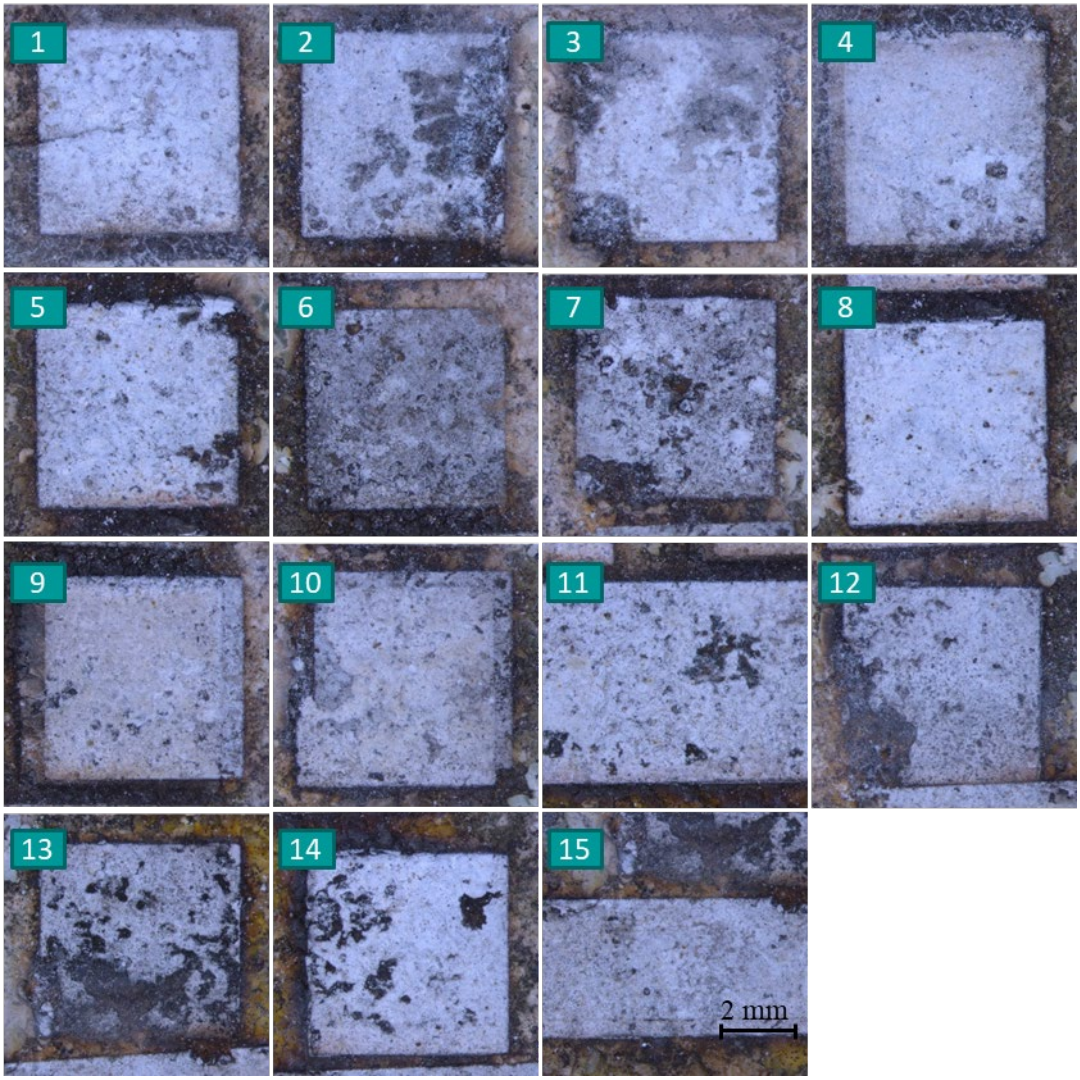
1
2
3
4
5
6
7
8
9
10
11
12
13
14
15
2 mm

Treated area	Pump Power	Frequency (kHZ)	Speed (mm/s)	Line width (mm)	Repititions
1	9A	800	500	0.001	5
2	9A	800	1000	0.001	5
3	9A	800	250	0.001	3
4	9A	800	1000	0.001	3
5	9A	400	1000	0.001	5
6	4.5 A	400	1000	0.001	5
7	6A	400	1000	0.001	5
8	9A	800	500	0.002	3
9	9A	800	500	0.002	1
+	6A	800	500	0.001	1
10	9A	800	1000	0.002	3
+	6A	800	1000	0.001	2
11	9A	800	500	0.002	3
12	9A	800	2000	0.002	3
13	9A	800	3000	0.002	3
14	7.2A	800	500	0.002	3
15	7.2A	800	500	0.002	3

(iii) Tablet G, treated by ps-IR laser operation parameters of each cleaned area

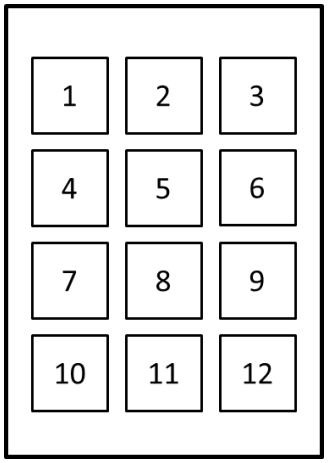
1
2
3
4
5
6
7
8
9
10
11
12

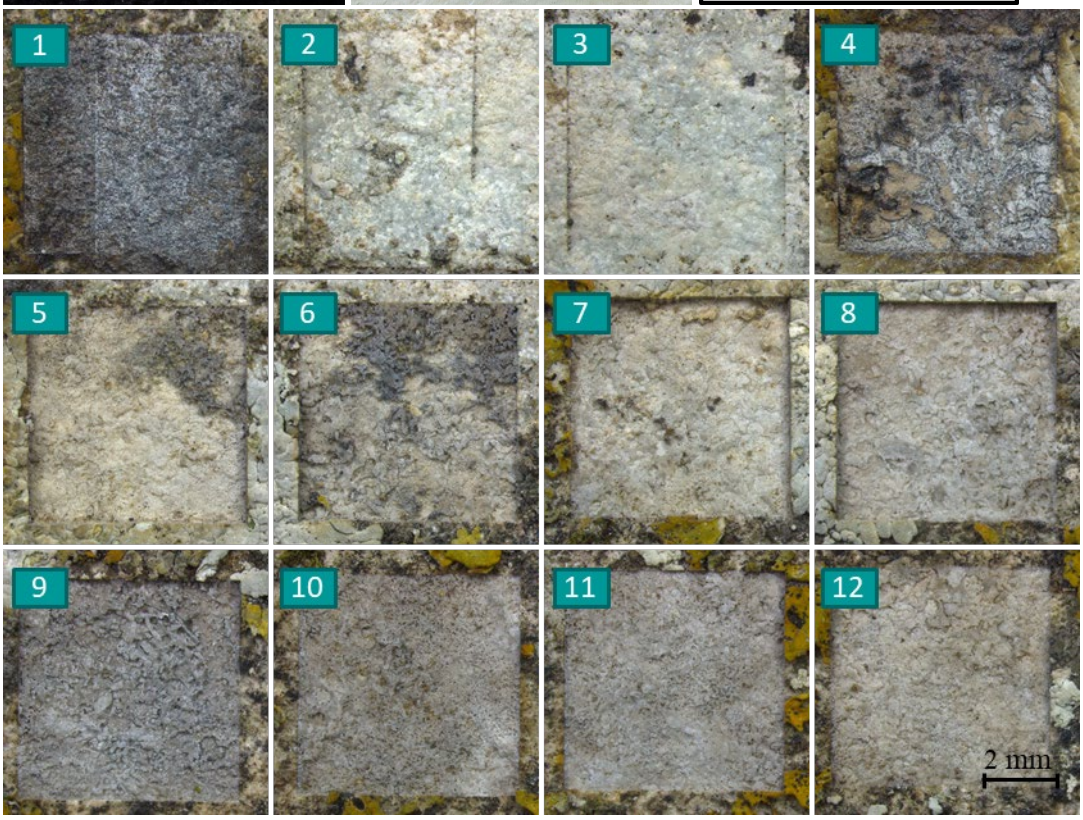
1
2
3
4
5
6
7
8
9
10
11
12
2 mm

Treated area	Pump Power	Frequency (kHZ)	Speed (mm/s)	Line width (mm)	Repititions
1	9A	800	500	0.002	5
2	9A	250	5000	0.020	10
3	9A	250	500	0.016	10
4	9A	800	500	0.002	15
5	9A	250	2000	0.008	20
6	9A	250	2000	0.008	20
7	9A	250	3000	0.012	60
8	9A	250	2000	0.008	80
9	9A	250	1000	0.004	20
10	9A	250	2000	0.008	160
11	9A	250	2000	0.008	200
12	9A	250	2000	0.008	20
+	9A	800	500	0.002	5

(iv) Tablet H, treated by ps-UV operation parameters of each cleaned area

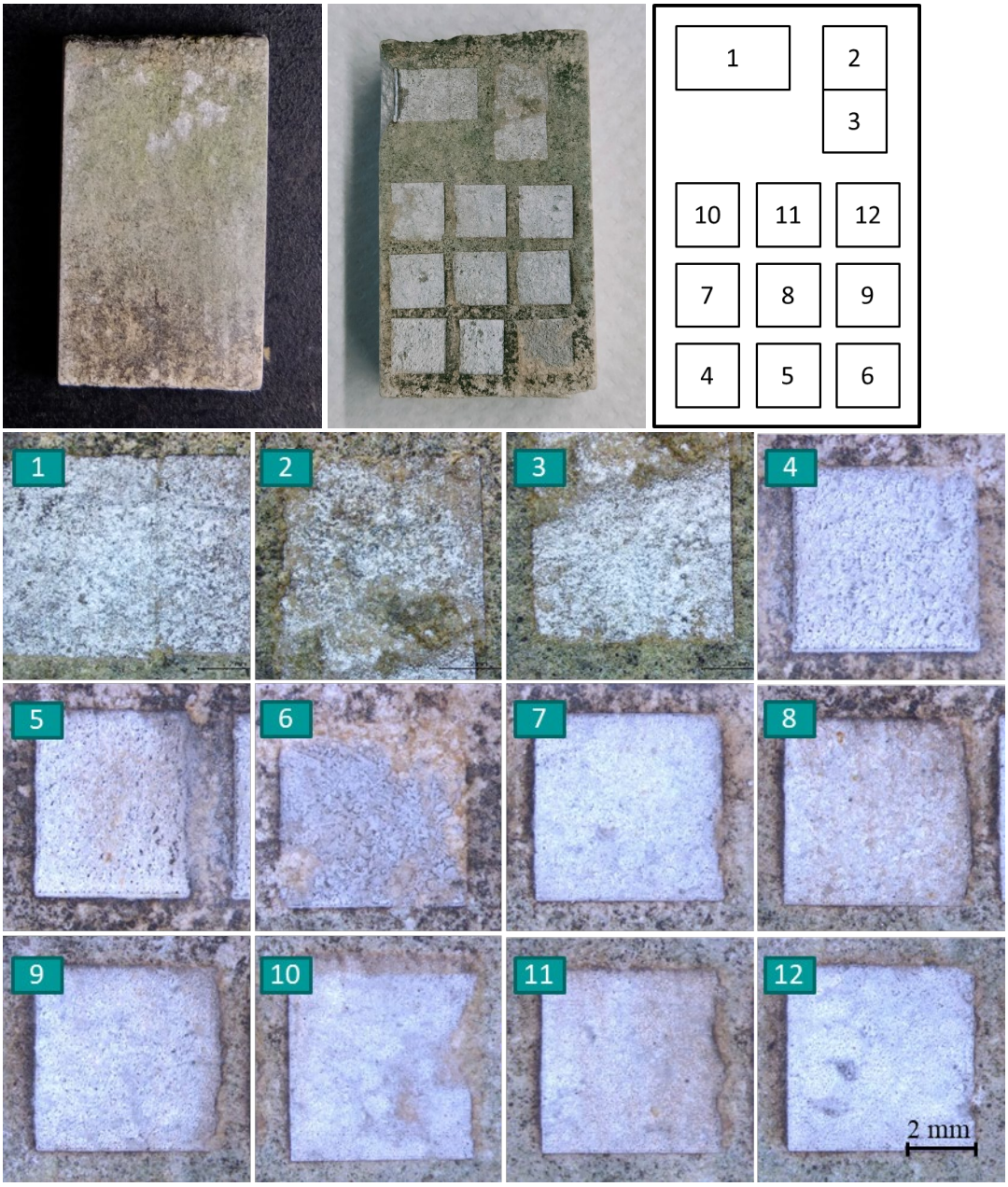
1
2
3
10
11
12
7
8
9
4
5
6
1
2
3
4
5
6
7
8
9
10
11
12
2 mm

Treated area	Attenuation Power	Frequency (kHZ)	Speed (mm/s)	Line width (mm)	Repititions
1	100%				
2	100%	150	200	0.00285	1
3	100%	150	200	0.00285	2
4	100%	600	1000	0.0142	2
5	100%	600	1000	0.0071	1
6	100%	300	1000	0.0071	5
7	80%	300	500	0.0036	2
8	80%	300	500	0.0036	1
9	100%	300	500	0.0036	1
10	70%	300	500	0.0036	3
11	75%	300	500	0.0036	1
12	75%	300	500	0.0036	2

(v) Tablet I, treated by ns-IR operation parameters of each cleaned area

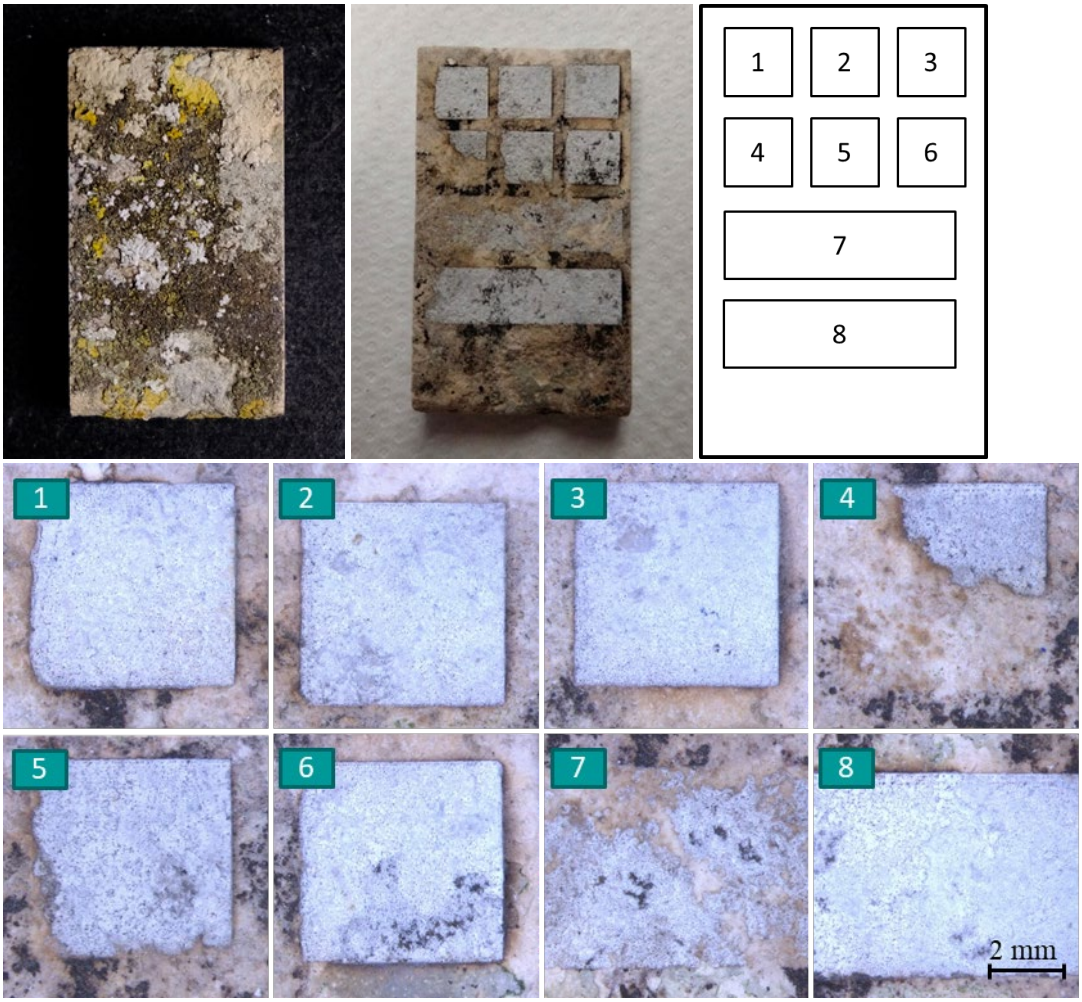

Treated area	Attenuation Power	Frequency (kHZ)	Speed (mm/s)	Line width (mm)	Repititions
1	80%	300	500	0.0036	2
2	75%	300	500	0.0036	2
3	70%	300	500	0.0036	3
4	80%	300	1000	0.0071	2
5	80%	300	750	0.0057	2
6	90%	300	500	0.0036	2
7	75%	300	500	0.0036	2
8	75%	300	500	0.0036	2

(vi) Tablet J, treated by ns-IR laser operation parameters of each cleaned area

Annex 5B. Microscopy and confocal microscopy images of the laser cleaned exposed limestone tablets.

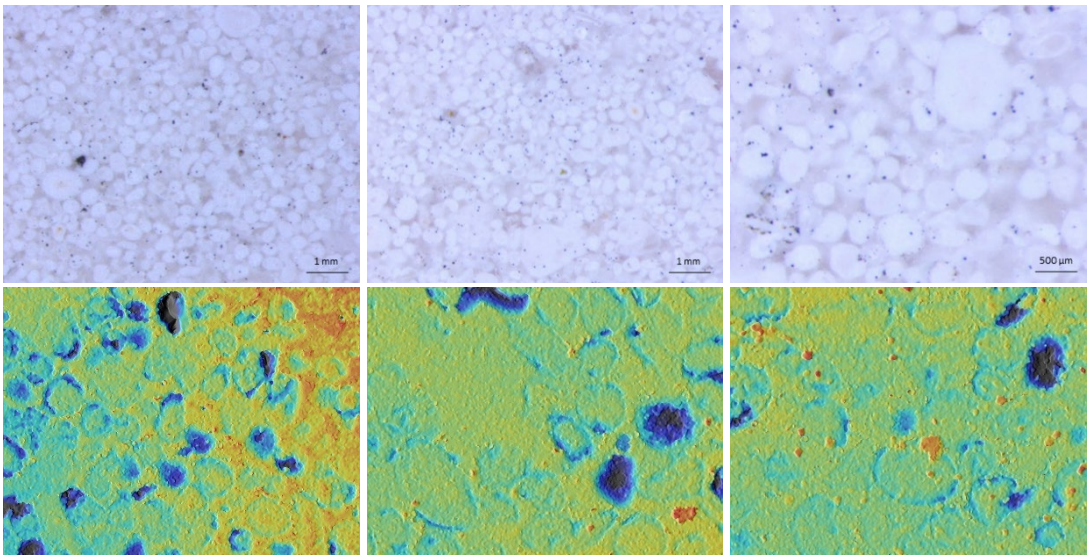

Untreated exposed areas

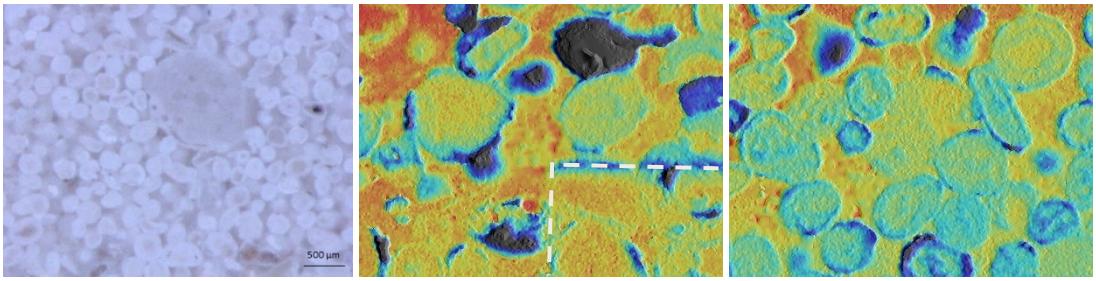

CDR 1 ZONE I cleaned by fs-UV laser (optical, confocal edge, confocal inside)

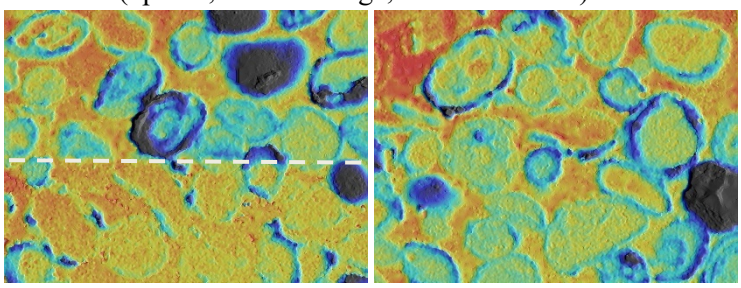

CDR1 ZONE II cleaned by fs-UV laser (optical, confocal edge, confocal inside)

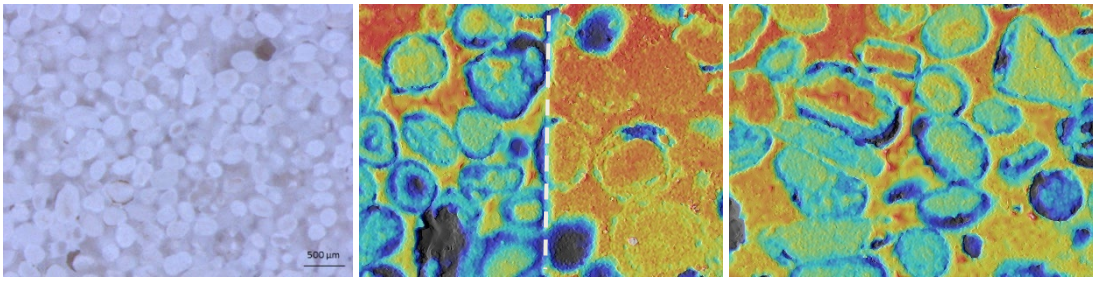

CDR1 ZONE III cleaned by fs-UV laser (optical, confocal edge, confocal inside)

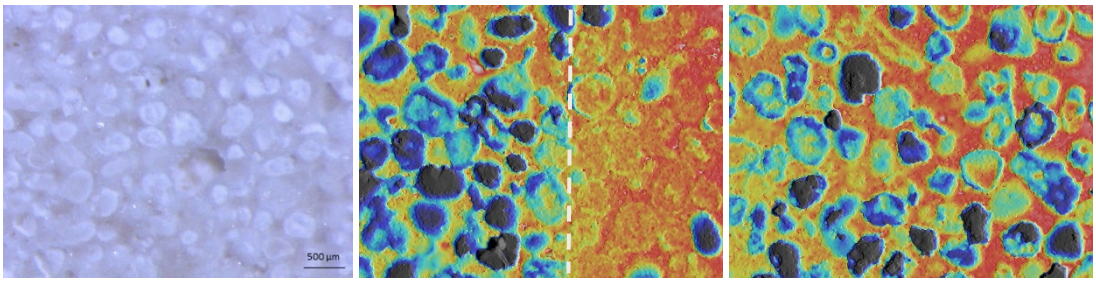

CDR3 ZONE I cleaned by ps-UV laser (optical, confocal edge, confocal inside)

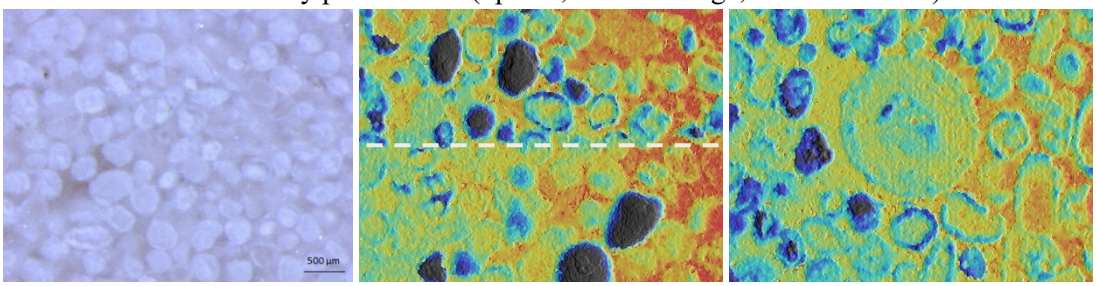

CDR3 ZONE II cleaned by ps-UV laser (optical, confocal edge, confocal inside)

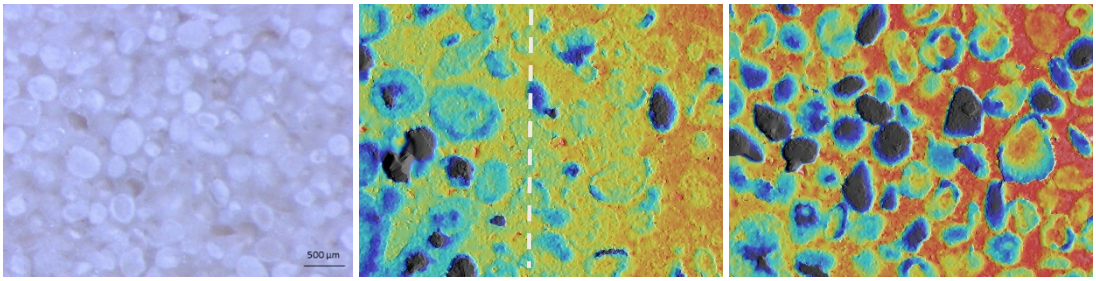

CDR3 ZONE III cleaned by ps-UV laser (optical, confocal edge, confocal inside)

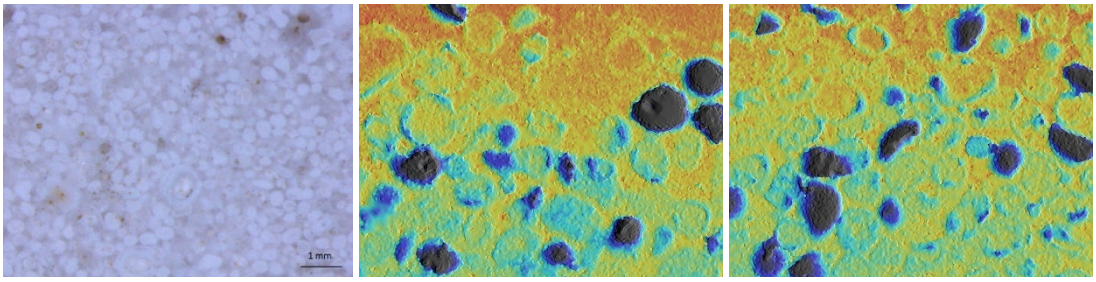

CDR4 ZONE I cleaned by ps-IR laser (optical, confocal edge, confocal inside)

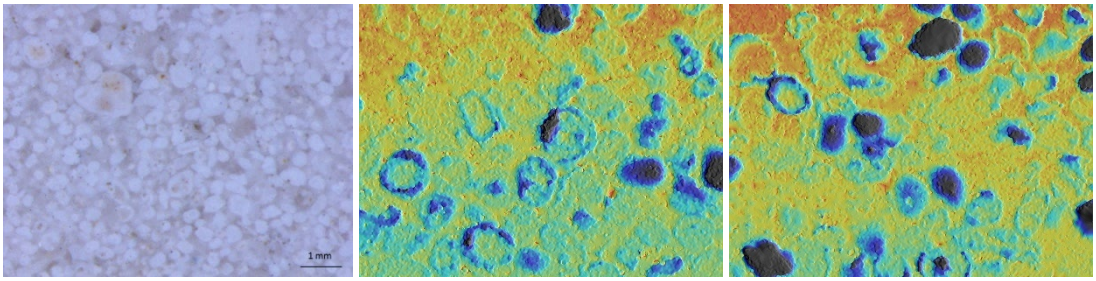

CDR4 ZONE II cleaned by ps-IR laser (optical, confocal edge, confocal inside)

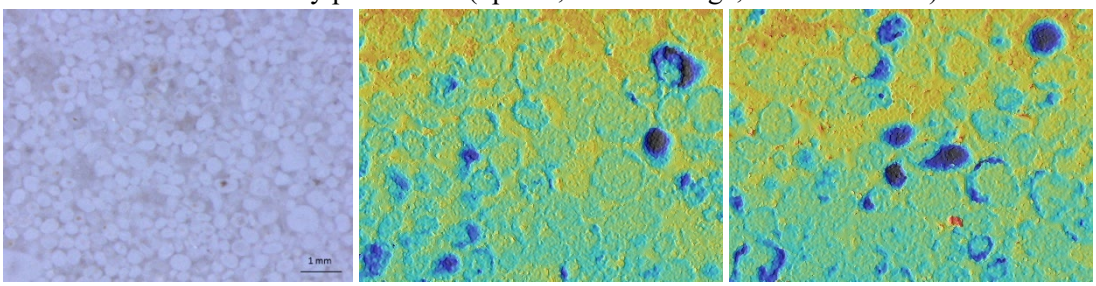

CDR4 ZONE III cleaned by ps-IR laser (optical, confocal edge, confocal inside)

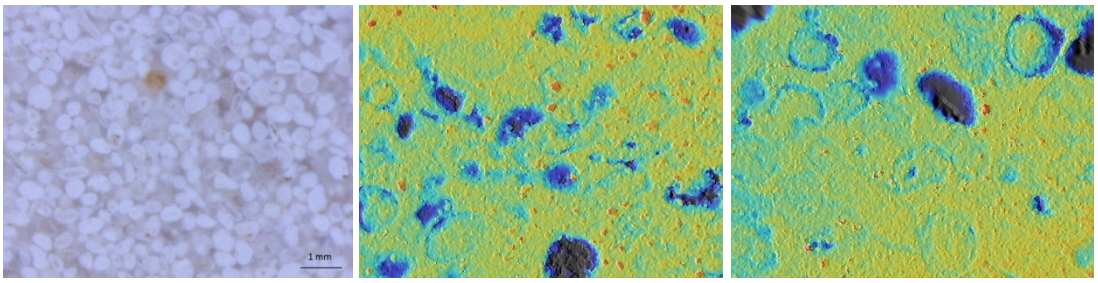

PDG2 ZONE I cleaned by ns-IR laser (optical, confocal edge, confocal inside)

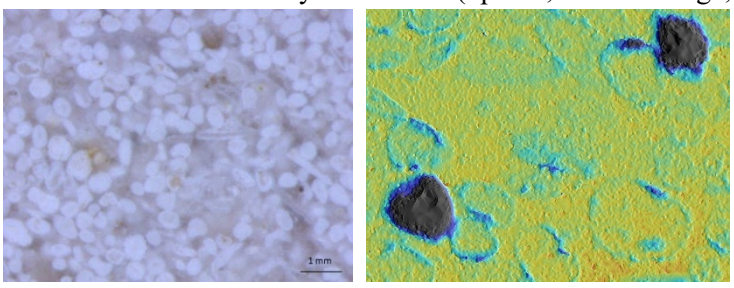

PDG2 ZONE II cleaned by ns-IR laser (optical, confocal inside)

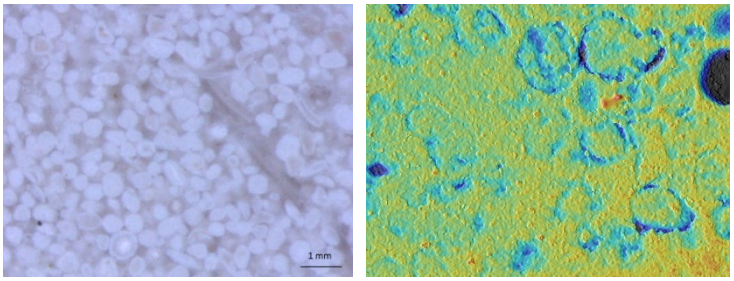

PDG2 ZONE III cleaned by ns-IR laser (optical, confocal inside)

Annex 6A. SEM-EDS of the TEOS deposited tablets, cross section.

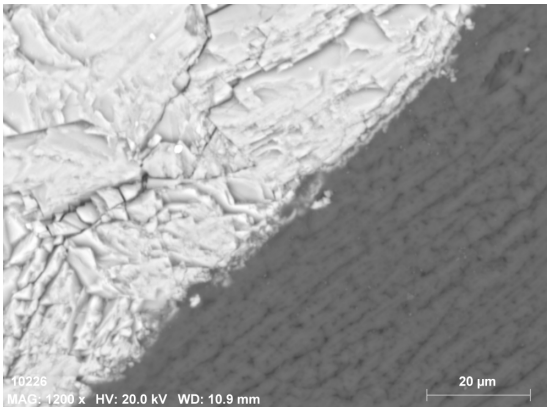

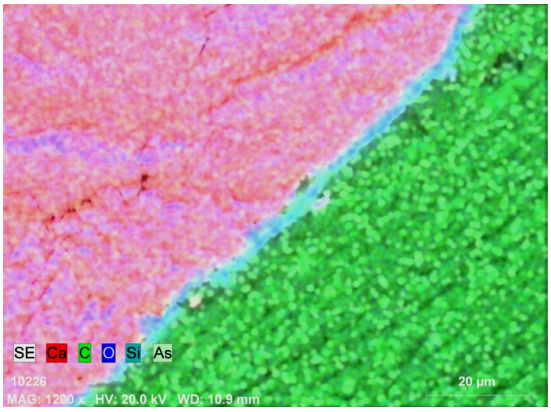

SiO_x coated limestone condition B

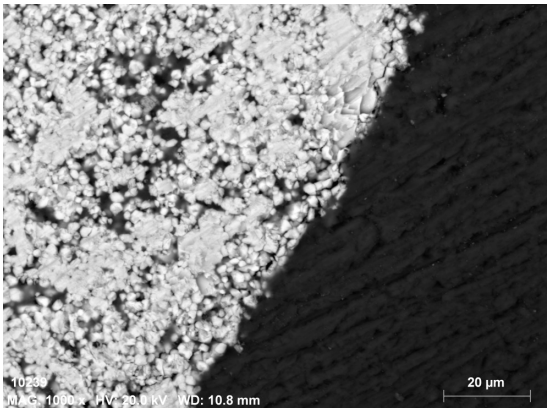

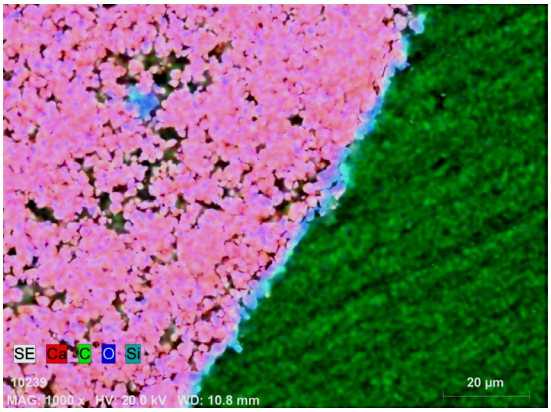

SiO_x coated limestone condition C

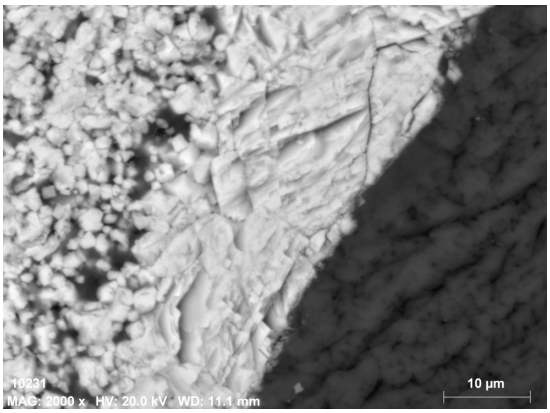

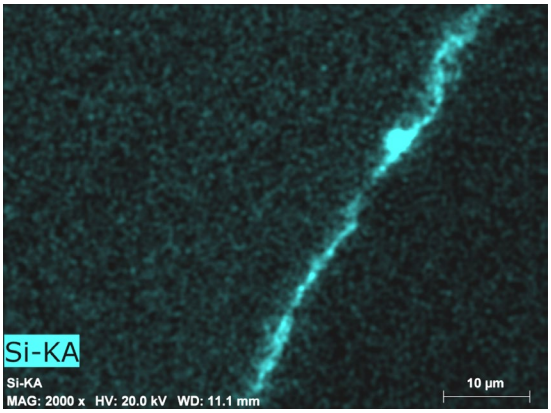

SiO_x coated limestone condition D

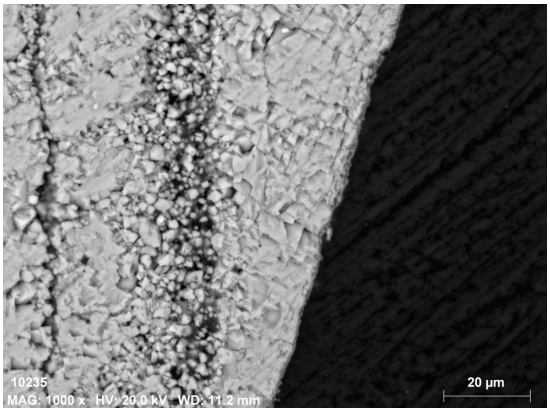

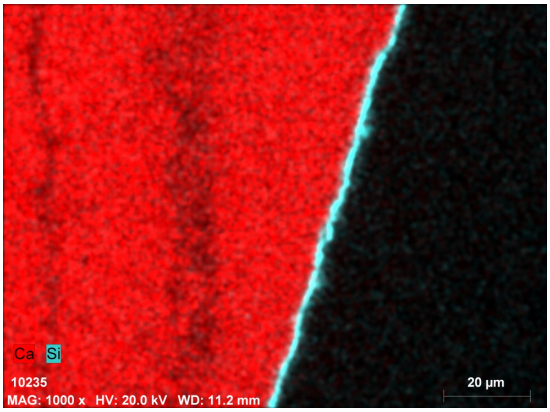

SiO_x coated limestone condition E

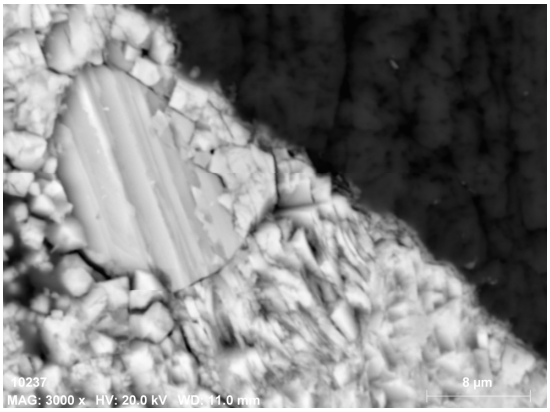

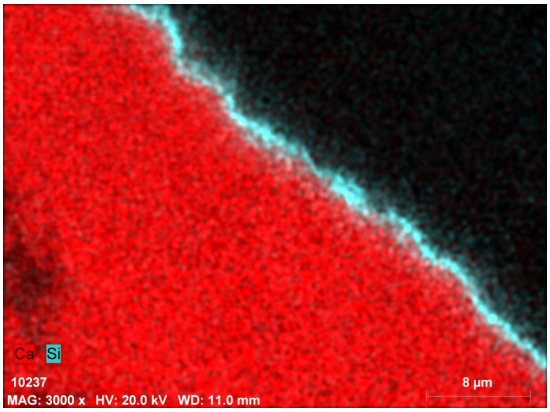

SiO_x coated limestone condition F

References

[1] Ding, Y., Mirao, J., Redol, P., Dias, L., Moita, P., Angelini, E., ... & Schiavon, N. (2021). Provenance study of the limestone used in construction and restoration of the Batalha Monastery (Portugal). *ACTA IMEKO*, *10*(1), 122-128. 10.21014/acta_imeko.v10i1.857

[2] Casal Moura, A.; Carvalho, C.; Almeida, I.; Saúde, J. G.; Farinha Ramos, J.; Augusto, J.; Rodrigues, J. D.; Carvalho, J.; Martins, L.; Matos; M. J.; Machado, M.; Sobreiro, M. J.; Peres, M.; Martins, N.; Bonito, N.; Henriques, P. & Sobreiro, S., 2007. Mármores e Calcários Ornamentais de Portugal. INETI (National Institute of Engineering, Technology and Innovation), ISBN 978- 972-676-204-1. pp. 30.

[3] Miller, A. Z., Leal, N., Laiz, L., Rogerio-Candelera, M. A., Silva, R. J., Dionísio, A., ... & Saiz-Jimenez, C. (2010). Primary bioreceptivity of limestones used in southern European monuments. *Geological Society, London, Special Publications*, *331*(1), 79-92. https://doi.org/10.1144/SP331.6

[4] Carvalho, J. M. F., Manuppella, G., & Moura, A. C. (2003). Portuguese Ornamental Limestones. In *International Symposium on Industrial Minerals and Building Stones, Turkey*.

[5] Carvalho, J. M. (2018). Jointing patterns and tectonic evolution of the Maciço Calcário Estremenho, Lusitanian Basin, Portugal. *Journal of Structural Geology*, *110*, 155-171. https://doi.org/10.1016/j.jsg.2018.03.004

[6] Carvalho, J., Manuppella, G., & Moura, A. C. (2000). Calcários ornamentais portugueses. *Boletim de Minas*, *37*(4), 223-232.

[7] Silva, Z. C. (2019). Lioz—a Royal Stone in Portugal and a Monumental Stone in Colonial Brazil. *Geoheritage*, *11*(1), 165-175. https://doi.org/10.1007/s12371-017-0267-7

[8] Miller, A. Z., Leal, N., Laiz, L., Rogerio-Candelera, M. A., Silva, R. J., Dionísio, A., ... & Saiz-Jimenez, C. (2010). Primary bioreceptivity of limestones used in southern European monuments. *Geological Society, London, Special Publications*, *331*(1), 79-92. https://doi.org/10.1144/SP331.6

[9] Török, Á., & Přikryl, R. (2010). Current methods and future trends in testing, durability analyses and provenance studies of natural stones used in historical monuments. *Engineering Geology*, 115(3-4), 139-142. https://doi.org/10.1016/j.enggeo.2010.07.003

[10] Calça, C. P., & Fairchild, T. R. (2012). Petrographic approach to the study of organic microfossils from the Irati Subgroup (Permian, Parana Basin, Brazil). *Journal of South American Earth Sciences*, *35*, 51-61. https://doi.org/10.1016/j.jsames.2011.10.005

[11] Dreesen, R., & Dusar, M. (2004). Historical building stones in the province of Limburg (NE Belgium): role of petrography in provenance and durability assessment. *Materials Characterization*, *53*(2-4), 273-287. https://doi.org/10.1016/j.matchar.2004.07.001

[12] Šťastná, A., Přikryl, R., & Jehlička, J. (2009). Methodology of analytical study for provenance determination of calcitic, calcite–dolomitic and impure marbles from historical quarries in the Czech Republic. *Journal of Cultural Heritage*, *10*(1), 82-93. https://doi.org/10.1016/j.culher.2008.09.004

[13] Wielgosz-Rondolino, D., Antonelli, F., Bojanowski, M. J., Gładki, M., Göncüoğlu, M. C., & Lazzarini, L. (2020). Improved methodology for identification of Göktepe white marble and the understanding of its use: A comparison with Carrara marble. *Journal of Archaeological Science*, *113*, 105059. https://doi.org/10.1016/j.jas.2019.105059]

[14] Blanc P, Lapuente Mercadal MP, Gutiérrez Garcia-Moreno A. A New Database of the Quantitative Cathodoluminescence of the Main Quarry Marbles Used in Antiquity. *Minerals*. 2020; 10(4):381. https://doi.org/10.3390/min10040381

[15] Shackley, M. S. (1998). Gamma rays, x-rays and stone tools: some recent advances in archaeological geochemistry. *Journal of Archaeological Science*, *25*(3), 259-270. https://doi.org/10.1006/jasc.1997.0247

[16] Saleh, M., Bonizzoni, L., Orsilli, J., Samela, S., Gargano, M., Gallo, S., & Galli, A. (2020). Application of statistical analyses for lapis lazuli stone provenance determination by XRL and XRF. *Microchemical Journal*, *154*, 104655. https://doi.org/10.1016/j.microc.2020.104655

[17] Emami, M., Eslami, M., Fadaei, H., Karami, H. R., & Ahmadi, K. (2018). Mineralogical–geochemical characterization and provenance of the stones used at the Pasargadae Complex in Iran: A new perspective. *Archaeometry*, *60*(6), 1184-1201. https://doi.org/10.1111/arcm.12395

[18] Constantinescu, B., Bugoi, R., & Sziki, G. (2002). Obsidian provenance studies of Transylvania's Neolithic tools using PIXE, micro-PIXE and XRF. *Nuclear Instruments and Methods in Physics Research Section B: Beam Interactions with Materials and Atoms*, *189*(1-4), 373-377. https://doi.org/10.1016/S0168-583X(01)01092-8

[19] Szczepaniak, M., Nawrocka, D., & Mrozek-Wysocka, M. (2008). Applied geology in analytical characterization of stone materials from historical building. *Applied Physics A*, *90*(1), 89-95. https://doi.org/10.1007/s00339-007-4237-9

[20] L. Bianco, Techniques to determine the provenance of limestone used in Neolithic Architecture of Malta, *Romanian Journal of Physics* 62 (2017).: 901. https://www.um.edu.mt/library/oar/bitstream/123456789/20508/1/rjp062_1-2_901.pdf

[21] Vigroux, M., Eslami, J., Beaucour, A. L., Bourges, A., & Noumowe, A. (2021). High temperature behaviour of various natural building stones. *Construction and Building Materials*, *272*, 121629. https://doi.org/10.1016/j.conbuildmat.2020.121629

[22] Calandra, S., Cantisani, E., Vettori, S., Ricci, M., Agostini, B., & Garzonio, C. A. (2022). The San Giovanni Baptistery in Florence (Italy): Assessment of the State of Conservation of Surfaces and Characterization of Stone Materials. *Applied Sciences*, *12*(8), 4050. https://doi.org/10.3390/app12084050

[23] Brilli, M., Conti, L., Giustini, F., Occhiuzzi, M., Pensabene, P., & De Nuccio, M. (2011). Determining the provenance of black limestone artifacts using petrography, isotopes and EPR techniques: the case of the monument of Bocco. *Journal of archaeological science*, *38*(6), 1377-1384. https://doi.org/10.1016/j.jas.2011.02.005

[24] M. Brilli, F. Antonelli, F. Giustini, L. Lazzarini, P. Pensabene, Black limestones used in antiquity: the petrographic, isotopic and EPR database for provenance determination, Journal of Archaeological Science 37 (2010) pp. 994-1005. https://doi.org/10.1016/j.jas.2009.11.032

[25] Miriello, D., Malagodi, M., Ruffolo, S.A. *et al.* Diagnostics, deterioration and provenance of stone materials from the Jefferson Page tomb (Non-Catholic Cemetery of Rome, Italy). *Environ Earth Sci* **60,** 829–836 (2010). https://doi.org/10.1007/s12665-009-0220-4

[26] Dayet, L., Le Bourdonnec, F. X., Daniel, F., Porraz, G., & Texier, P. J. (2016). Ochre provenance and procurement strategies during the middle stone age at Diepkloof Rock Shelter, South Africa. *Archaeometry*, *58*(5), 807-829. https://doi.org/10.1111/arcm.12202

[27] Åberg, G., Löfvendahl, R., Stijfhoorn, D., & Råheim, A. (1995). Provenance and weathering depth of carbonaceous Gotland sandstone by use of carbon and oxygen isotopes. *Atmospheric Environment*, *29*(7), 781-789. https://doi.org/10.1016/1352-2310(94)00324-E

[28] Kuchařová, A., & Přikryl, R. (2017). Mineralogical and geochemical (stable C and O isotopes) variability of marbles from the Moldanubian Zone (Bohemian Massif, Czech Republic): implications for provenance studies. *Environmental Earth Sciences*, *76*(1), 1-20. https://doi.org/10.1007/s12665-016-6348-0

[29] Leng, M. J., Glover, B. W., & Chisholm, J. I. (1999). Nd and Sr isotopes as clastic provenance indicators in the Upper Carboniferous of Britain. *Petroleum Geoscience*, *5*(3), 293-301. https://doi.org/10.1144/petgeo.5.3.293

[30] Attanasio, D. The use of electron spin resonance spectroscopy for determining the provenance of classical marbles. *Appl. Magn. Reson.* **16,** 383–402 (1999). https://doi.org/10.1007/BF03161926

[31] Lynch, S.C., Locock, A.J., Duke, M.J.M. *et al.* Evaluating the applicability of portable-XRF for the characterization of Hokkaido Obsidian sources: a comparison with INAA,

ICP-MS and EPMA. *J Radioanal Nucl Chem* **309,** 257–265 (2016). https://doi.org/10.1007/s10967-016-4766-9

[32] Barone, G., Crupi, V., Longo, F., Majolino, D., Mazzoleni, P., Raneri, S., & Venuti, V. (2014). A multi-technique approach for the characterization of decorative stones and non-destructive method for the discrimination of similar rocks. *X-Ray Spectrometry*, *43*(2), 83-92. https://doi.org/10.1002/xrs.2520

[33] Juárez-Rodríguez, O., Argote-Espino, D., Santos-Ramírez, M., & López-García, P. (2018). Portable XRF analysis for the identification of raw materials of the Red Jaguar sculpture in Chichén Itzá, Mexico. *Quaternary International*, *483*, 148-159. https://doi.org/10.1016/j.quaint.2017.09.012

[34] Saleh, M., Bonizzoni, L., Orsilli, J., Samela, S., Gargano, M., Gallo, S., & Galli, A. (2020). Application of statistical analyses for lapis lazuli stone provenance determination by XRL and XRF. *Microchemical Journal*, *154*, 104655. https://doi.org/10.1016/j.microc.2020.104655

[35] Bowitz, J., Ehling, A. Non-destructive infrared analyses: a method for provenance analyses of sandstones. *Environ Geol* **56,** 623–630 (2008). https://doi.org/10.1007/s00254-008-1361-6

[36] Szakmány, G., Kasztovszky, Z., Szilágyi, V., Starnini, E., Friedel, O., & Biró, K. T. (2011). Discrimination of prehistoric polished stone tools from Hungary with non-destructive chemical Prompt Gamma Activation Analyses (PGAA). *European Journal of Mineralogy*, *23*(6), 883-893. https://doi.org/10.1127/0935-1221/2011/0023-2148

[37] Columbu, S., Gaviano, E., Costamagna, L. G., & Fancello, D. (2021). Mineralogical-petrographic and physical-mechanical features of the construction stones in Punic and Roman temples of Antas (SW Sardinia, Italy): Provenance of the raw materials and conservation state. *Minerals*, *11*(9), 964. https://doi.org/10.3390/min11090964

[38] Sammarco, M., Margiotta, S., Foresi, L. M., & Ceraudo, G. (2015). Characterization and provenance of building materials from the Roman Pier at San Cataldo (Lecce, Southern Apulia, Italy): a lithostratigraphical and micropaleonthological approach. *Mediterranean Archaeology and Archaeometry*, *15*(2), 101-112. http://doi.org/10.5281/zenodo.16604

[39] Mota-López, M. I., Fort, R., Álvarez de Buergo, M., & Pizzo, A. (2020). Provenance analysis of the granitic ashlars used in the construction of the Roman theatre in Emerita Augusta (Merida, Spain). *Archaeological and Anthropological Sciences*, *12*(10), 1-21. https://doi.org/10.1007/s12520-020-01192-1

[40] Malfilatre, C., Boulvais, P., Dabard, M. P., Bourquin, S., Hallot, E., Pallix, D., & Gapais, D. (2012). Petrographical and geochemical characterization of Comblanchien limestone (Bourgogne, France): A fingerprint of the building stone provenance. *Comptes Rendus Geoscience*, *344*(1), 14-24. https://doi.org/10.1016/j.crte.2011.12.002

[41] J. C. V. Da Silva, The Monastery of Batalha, Scala Books, London, 2007, ISBN 978-1857593822.

[42] B. T. Gemeda, R. Lahoz, A. T. Caldeira, N. Schiavon, Efficacy of laser cleaning in the removal of biological patina on the volcanic scoria of the rock-hewn churches of Lalibela, Ethiopia, Environmental Earth Sciences 77 (2018) p. 36. https://doi.org/10.1007/s12665-017-7223-3

[43] N. Schiavon, A. Candeias, T. Ferreira, M. Da Conceiçao Lopes, A. Carneiro, T. Calligaro, J. Mirao, A combined multi-analytical approach for the study of Roman glass from south-west Iberia: synchrotron μ-XRF, external-PIXE/PIGE and BSEM–EDS, Archaeometry 54 (2012) pp. 974-996. https://doi.org/10.1111/j.1475-4754.2012.00662.x

[44] L. Aires-Barros, As Rochas dos Monumentos Portugueses: Tipologias e Patologias, Volume II, Instituto Português do Património Arquitectónico, Lisbon, 2001, ISBN 9789728087814.

[45] Edital n.º 03/2017/g.A.P. Sítio de interesse municipal da pedreira histórica de Valinho do Rei e sítio de interesse municipal da pedreira histórica de Pidiogo – criação de zona especial de proteção (zep).

[46] C. M. Soares, O Restauro do Mosteiro da Batalha: Pedreiras Históricas, Estaleiro de Obras e Mestres Canteiros, Magno Ed., Leiria, 2001. ISBN 9789728345280.

[47] C. R. Hubbard, E. H. Evans, D. K. Smith, The reference intensity ratio, I/Ic, for computer simulated powder patterns, Journal of Applied Crystallography 9 (1976) pp. 169-174. https://doi.org/10.1107/S0021889876010807

[48] J. Lasne, A. Noblet, C. Szopa, R. Navarro-González, M. Cabane, O. Poch, F. Stalport, P. François, S. K. Atreya, and P. Coll, Oxidants at the surface of Mars: a review in light of recent exploration results, Astrobiology 16 (2016) pp. 977-996. https://doi.org/10.1089/ast.2016.1502

[49] M. Beltrame, M. Liberato, J. Mirão, H. Santos, P. Barrulas, F. Branco, Gonçalves, L., A. Candeias, Schiavon, N, Islamic and post Islamic ceramics from the town of Santarém (Portugal): the continuity of ceramic technology in a transforming society, Journal of Archaeological Science: Reports 23 (2019) pp. 910-928. https://doi.org/10.1016/j.jasrep.2018.11.029

[50] E. Flügel, Fossils in thin section: it is not that difficult, in: Microfacies of Carbonate Rocks. E. Flügel (editor). Springer, Berlin, Heidelberg, 2004, ISBN 978-3-662-08726-8, pp. 399-574. https://doi.org/10.1007/978-3-642-03796-2_10

[51] E. Flügel, Microfacies of Carbonate Rocks: Analysis, Interpretation and Application, Springer Science & Business Media, Berlin, 2013, ISBN 978-3-662-08726-8.

[52] E. Flügel, Microfacies data: matrix and grains, in: Microfacies of Carbonate Rocks. E. Flügel (editor). Springer, Berlin, Heidelberg, 2004, ISBN 978-3-662-08726-8, pp. 73-176

[53] C. Solak, K. Taslı, H. Koç, Biostratigraphy and facies analysis of the Upper Cretaceous–Danian platform carbonate succession in the Kuyucak area, western Central Taurides, S

Turkey, Cretaceous Research 79 (2017) pp. 43-63. https://doi.org/10.1016/j.cretres.2017.06.019

[54] D. Ivanova, B. Kołodziej, E. Koleva-Rekalova, E. Roniewicz, Oxfordian to Valanginian palaeoenvironmental evolution on the western Moesian Carbonate Platform: a case study from SW Bulgaria, Annales Societatis Geologorum Poloniae 78 (2008) pp. 65-90.

[55] S. W. Lokier, M. Al Junaibi, The petrographic description of carbonate facies: are we all speaking the same language?, Sedimentology 63 (2016) pp. 1843-1885. https://doi.org/10.1111/sed.12293

[56] Ghabezloo, S., Sulem, J., Guédon, S., & Martineau, F. (2009). Effective stress law for the permeability of a limestone. *International Journal of Rock Mechanics and Mining Sciences*, *46*(2), 297-306. https://doi.org/10.1016/j.ijrmms.2008.05.006

[57] Carta Geologica de Portugal, 1:50,000, Sheet 27-A Vila Nova de Ourém, Instituto Geológico e Mineiro, Departamento de Geologia, Lisbon, 1998.

[58] F. de Souza, S. R. Bragança, Thermogravimetric analysis of limestones with different contents of MgO and microstructural characterization in oxy-combustion, Thermochimica Acta 561 (2013) pp. 19-25. https://doi.org/10.1016/j.tca.2013.03.006

[59] Kusiorowski, R., Zaremba, T., Piotrowski, J. *et al.* Thermal decomposition of asbestos-containing materials. *J Therm Anal Calorim* **113,** 179–188 (2013). https://doi.org/10.1007/s10973-013-3038-y

[60] Mohammed, S., Elhem, G., & Mekki, B. (2016). Valorization of pozzolanicity of Algerian clay: optimization of the heat treatment and mechanical characteristics of the involved cement mortars. *Applied Clay Science*, *132*, 711-721. https://doi.org/10.1016/j.clay.2016.08.027

[61] M. Mohamed, S. Yusup, S. Maitra, Decomposition study of calcium carbonate in cockle shell, Journal of Engineering Science and Technology 7 (2012) pp. 1-10.

[62] D. Xu, H. Wei, Y. Luo, The influence of grain size on decomposition reaction of limestone in dispersing state, Journal of Wuhan University of Technology-Mater. Sci. Ed. 19 (2004) pp. 1-5. https://doi.org/10.1007/BF02841354

[63] Chabas, A., & Lefevre, R. A. (2000). Chemistry and microscopy of atmospheric particulates at Delos (Cyclades–Greece). *Atmospheric environment*, *34*(2), 225-238. https://doi.org/10.1016/S1352-2310(99)00255-1

[64] Baker, P. A., Gieskes, J. M., & Elderfield, H. (1982). Diagenesis of carbonates in deep-sea sediments; evidence from Sr/Ca ratios and interstitial dissolved Sr (super 2+) data. *Journal of Sedimentary Research*, *52*(1), 71-82. https://doi.org/10.1306/212F7EE1-2B24-11D7-8648000102C1865D

[65] Lau, K. V., Maher, K., Brown, S. T., Jost, A. B., Altıner, D., DePaolo, D. J., ... & Payne, J. L. (2017). The influence of seawater carbonate chemistry, mineralogy, and diagenesis

on calcium isotope variations in Lower-Middle Triassic carbonate rocks. *Chemical Geology*, *471*, 13-37. https://doi.org/10.1016/j.chemgeo.2017.09.006

[66] Stoll, H. M., & Schrag, D. P. (2001). Sr/Ca variations in Cretaceous carbonates: relation to productivity and sea level changes. *Palaeogeography, Palaeoclimatology, Palaeoecology*, *168*(3-4), 311-336. https://doi.org/10.1016/S0031-0182(01)00205-X

[67] Margolis, S. V., & Showers, W. (1988). Weathering characteristics, age, and provenance determinations on ancient Greek and Roman marble artifacts. In *Classical Marble: Geochemistry, Technology, Trade* (pp. 233-242). Springer, Dordrecht. https://doi.org/10.1007/978-94-015-7795-3_26

[68] L. Lazzarini, G. Moschini, B. M. Stievano, A contribution to the identification of Italian, Greek and Anatolian marbles through a petrological study and the evaluation of calcium/strontium ratio, Archaeometry 22 (1980) pp. 173-183. https://doi.org/10.1111/j.1475-4754.1980.tb00940.x

[69] Hardie, L. A. (1996). Secular variation in seawater chemistry: An explanation for the coupled secular variation in the mineralogies of marine limestones and potash evaporites over the past 600 my. *Geology*, *24*(3), 279-283. https://doi.org/10.1130/0091-7613(1996)024<0279:SVISCA>2.3.CO;2

[70] Ehinola, O. A., Ejeh, O. I., & Oderinde, O. J. (2016). Geochemical characterization of the Paleocene Ewekoro limestone formation, SW Nigeria: implications for provenance, diagenesis and depositional environment. *Geomaterials*, *6*(03), 61. http://doi.org/10.4236/gm.2016.63006

[71] Riding, R., & Liang, L. (2005). Seawater chemistry control of marine limestone accumulation over the past 550 million years. *Revista Española de Micropaleontología*, *37*(1), 1-11.

[72] Lowenstein, T. K., Timofeeff, M. N., Brennan, S. T., Hardie, L. A., & Demicco, R. V. (2001). Oscillations in Phanerozoic seawater chemistry: Evidence from fluid inclusions. *Science*, *294*(5544), 1086-1088. DOI: 10.1126/science.1064280

[73] Han, G., & Liu, C. Q. (2004). Water geochemistry controlled by carbonate dissolution: a study of the river waters draining karst-dominated terrain, Guizhou Province, China. *Chemical Geology*, *204*(1-2), 1-21. https://doi.org/10.1016/j.chemgeo.2003.09.009

[74] Lowenstein, T. K., Hardie, L. A., Timofeeff, M. N., & Demicco, R. V. (2003). Secular variation in seawater chemistry and the origin of calcium chloride basinal brines. *Geology*, *31*(10), 857-860. https://doi.org/10.1130/G19728R.1

[75] Karmann, I., Cruz Jr, F. W., Viana Jr, O., & Burns, S. J. (2007). Climate influence on geochemistry parameters of waters from Santana–Pérolas cave system, Brazil. *Chemical Geology*, *244*(1-2), 232-247. https://doi.org/10.1016/j.chemgeo.2007.06.029

[76] Huh, Y., Panteleyev, G., Babich, D., Zaitsev, A., & Edmond, J. M. (1998). The fluvial geochemistry of the rivers of Eastern Siberia: II. Tributaries of the Lena, Omoloy, Yana, Indigirka, Kolyma, and Anadyr draining the collisional/accretionary zone of the

Verkhoyansk and Cherskiy ranges. *Geochimica et cosmochimica acta*, *62*(12), 2053-2075. https://doi.org/10.1016/S0016-7037(98)00127-6

[77] Wüst, R. A., & Schlüchter, C. (2000). The origin of soluble salts in rocks of the Thebes mountains, Egypt: The damage potential to ancient Egyptian wall art. *Journal of Archaeological Science*, *27*(12), 1161-1172. https://doi.org/10.1006/jasc.1999.0550

[78] El-Gohary, M.A. A holistic approach to the assessment of the groundwater destructive effects on stone decay in Edfu temple using AAS, SEM-EDX and XRD. *Environ Earth Sci* **75,** 13 (2016). https://doi.org/10.1007/s12665-015-4849-x

[79] Friedman, G. M., & Sanders, J. E. (1967). Origin and occurrence of dolostones. In *Developments in sedimentology* (Vol. 9, pp. 267-348). Elsevier. https://doi.org/10.1016/S0070-4571(08)71114-2

[80] Gebelein, C. D., & Hoffman, P. (1973). Algal origin of dolomite laminations in stromatolitic limestone. *Journal of Sedimentary Research*, *43*(3).

[81] Carvalho, J. M., & Lisboa, J. V. (2018). Ornamental stone potential areas for land use planning: a case study in a limestone massif from Portugal. *Environmental earth sciences*, *77*(5), 1-13. https://doi.org/10.1007/s12665-018-7382-x

[82] E. K. Bartle, R. J. Watling, Provenance determination of oriental porcelain using laser ablation-inductively coupled plasma-mass spectrometry (LA-ICP-MS), Journal of Forensic Sciences 52 (2007) pp. 341-348. https://doi.org/10.1111/j.1556-4029.2006.00364.x

[83] Z. Vangelatos, M. Delagrammatikas, O. Papadopoulou, P. Vassiliou, Computational modelling of the mechanical behaviour of the Pentelic marble-steel clamp system on the structures of the Athens Acropolis, Proc. of the 2019 IMEKO TC-4 International Conference on Metrology for Archaeology and Cultural Heritage Florence, Italy, 4 – 6 December 2019, pp. 516-521

[84] M. Kyritsis-Spinoulas, Z. Vangelatos, P. Vassiliou, D. Manolakos, M. Delagrammatikas, O. Papadopoulou, Steel clamps from the Acropolis: some old, some new and some digital, Proc. of the 5th International Conference on Corrosion Mitigation and Surface Protection Technologies, Luxor, Egypt, 11 – 18 December 2016, pp. 11-18.

[85] Ding, Y., Redol, P., Angelini, E., Mirão, J., & Schiavon, N. (2021). Surface orange patinas on the limestone of the Batalha Monastery (Portugal): characterization and decay patterns. *Environmental Science and Pollution Research*, 1-11. https://doi.org/10.1515/rbm-2001-5594

[86] Rattazzi, A., Camaiti, M., & Salvioni, D. (1996). The statues of the apostles from the main doorway of the church of the Monastery of Batalha (Portugal): analysis of degradation forms in relation to ancient treatments. In *Proceedings of the 8th International Congress on Deterioration and Conservation of Stone, J. Riederer, Editor, Möller Druck und Verlag, Berlin* (pp. 101-108).

[87] Aires-Barros, L., Basto, M. J., Dionísio, A., & Charola, A. E. (2001). Orange coloured surface deposits on stones from the Monastery of Batalha (Portugal) and from nearby

historic quarries: characteristics and origins. *International Journal for Restoration of Buildings and Monuments*, *7*(5), 491-506. https://doi.org/10.1515/rbm-2001-5594

[88] Lazzarini, L., & Salvadori, O. (1989). A reassessment of the formation of the patina called scialbatura. *Studies in conservation*, *34*(1), 20-26. https://doi.org/10.1179/sic.1989.34.1.20

[89] Del Monte, M., & Sabbioni, C. (1987). A study of the patina called 'scialbatura'on imperial Roman marbles. *Studies in Conservation*, *32*(3), 114-121. https://doi.org/10.1179/sic.1987.32.3.114

[90] Del Monte, M., Sabbioni, C., & Zappia, G. (1987). The origin of calcium oxalates on historical buildings, monuments and natural outcrops. *Science of the Total Environment*, *67*(1), 17-39.

[91] Schiavon, N. (2007) Kaolinization of Granite in an Urban Environment. *Environmental Geology, 52*(*2)*, 399-407. https://doi.org/10.1007/s00254-006-0473-0

[92] Rosado, T., Silva, M., Galvão, A., Mirao. J., Candeias, A. & Caldeira, A.T.C. A first insight on the biodegradation of limestone: the case of the World Heritage Convent of Christ. *Appl. Phys. A* **122,** 1012 (2016). https://doi.org/10.1007/s00339-016-0525-6

[93] Camuffo, D. (1993). Reconstructing the climate and the air pollution of Rome during the life of the Trajan Column. *Science of the total environment*, *128*(2-3), 205-226. https://doi.org/10.1016/0048-9697(93)90220-Z

[94] Kawamura, K., & Kaplan, I. R. (1987). Motor exhaust emissions as a primary source for dicarboxylic acids in Los Angeles ambient air. *Environmental science & technology*, *21*(1), 105-110.

[95] Franzini, M., Gratziu, C., & Wicks, E. (1984). Patine ad ossalato di calcio su monumenti marmorei. *Societa Italiana di Mineralogia e Petrologia, 39*(1), 59-70.

[96] Demitry, L. (1988). The conservation of the Stadium of Domizian in Rome. In VIth International Congress on Deterioration and Conservation of Stone, Torun, 12-14 September 1988. Proceedings (pp. 748-756).

[97] Fassina, V. (1995). New findings on past treatments carried out on stone and marble monuments' surfaces. *Science of the total environment*, *167*(1-3), 185-203. https://doi.org/10.1016/0048-9697(95)04580-T

[98] Hubbard, C. R., & Snyder, R. L. (1988). RIR-measurement and use in quantitative XRD. *Powder Diffraction*, *3*(2), 74-77. https://doi.org/10.1017/S0885715600013257

[99] Veiga, A., Mirão, J., Candeias, A. J., Simões Rodrigues, P., Martins Teixeira, D., Muralha, V. S., & Ginja Teixeira, J. (2014). Pigment analysis of Portuguese portrait miniatures of 17th and 18th centuries by Raman Microscopy and SEM-EDS. *Journal of Raman* Spectroscopy, 45(10), 947-957. https://doi.org/10.1002/jrs.4570

[100] Arandigoyen, M., & Alvarez, J. I. (2006). Blended pastes of cement and lime: Pore structure and capillary porosity. *Applied surface science*, *252*(23), 8077-8085. https://doi.org/10.1016/j.apsusc.2005.10.019

[101] Danin, A., & Caneva, G. (1990). Deterioration of limestone walls in Jerusalem and marble monuments in Rome caused by cyanobacteria and cyanophilous lichens. *International biodeterioration*, *26*(6), 397-417. https://doi.org/10.1016/0265-3036(90)90004-Q

[102] Uetake, J., Naganuma, T., Hebsgaard, M. B., Kanda, H., & Kohshima, S. (2010). Communities of algae and cyanobacteria on glaciers in west Greenland. *Polar Science*, *4*(1), 71-80. https://doi.org/10.1016/j.polar.2010.03.002

[103] Collepardi, M. (1999). Thaumasite formation and deterioration in historic buildings. Cement and Concrete Composites, 21(2), 147-154. https://doi.org/10.1016/S0958-9465(98)00044-4

[104] Perdikatsis, V., & Brecoulaki, H. (2008). The use of red and yellow ochres as painting materials in Ancient Macedonia. BAR International Series, 1746, 559.

[105] Martin-Gil, J., Ramos-Sánchez, M. D. C., & Martín-Gil, F. J. (1999). Ancient pastes for stone protection against environmental agents. *Studies in conservation*, *44*(1), 58-62. https://doi.org/10.1179/sic.1999.44.1.58

[106] Ion, R. M., Teodorescu, S., Ştirbescu, R. M., Bucurică, I. A., Dulamă, I. D., & Ion, M. L. (2017). Calcium oxalate on limestone surface of heritage buildings. In Key Engineering Materials (Vol. 750, pp. 129-134). Trans Tech Publications Ltd. https://doi.org/10.4028/www.scientific.net/KEM.750.129

[107] Palmieri, F., Estoppey, A., House, G. L., Lohberger, A., Bindschedler, S., Chain, P. S., & Junier, P. (2019). Oxalic acid, a molecule at the crossroads of bacterial-fungal interactions. *Advances in applied microbiology*, *106*, 49-77.

[108] Hess, D., Coker, D. J., Loutsch, J. M., & Russ, J. (2008). Production of oxalates in vitro by microbes isolated from rock surfaces with prehistoric paints in the lower Pecos region, Texas. Geoarchaeology: An International Journal, 23(1), 3-11. https://doi.org/10.1002/gea.20208

[109] Cheng, C., Wang, Q., He, L., & Sheng, X. (2017). Change in mineral weathering behaviors of a bacterium Chitinophaga jiangningensis JN53 under different nutrition conditions. Journal of basic microbiology, 57(4), 293-301. https://doi.org/10.1002/jobm.201600652

[110] Ding, Y., Salvador, C. S. C., Caldeira, A. T., Angelini, E., & Schiavon, N. (2021). Biodegradation and Microbial Contamination of Limestone Surfaces: An Experimental Study from Batalha Monastery, Portugal. Corrosion and Materials Degradation, 2(1), 31-45. https://doi.org/10.3390/cmd2010002

[111] Marques, M. (2018 Jan 10), Desvio do trânsito é a melhor solução para o Mosteiro da Batalha. *Diário de Notícias.* https://www.dn.pt/portugal/populacao-esta-contra-barreiras-junto-ao-mosteiro-da-batalha-e-pede-isencao-de-portagens-9028235.html

[112] Duffy, A. P., & Perry, S. H. (1996). The mechanisms and causes of Portland Limestone decay-A Case Study. In 8th International Congress on Deterioration and Conservation of stone (Vol. 1, pp. 135-145).

[113] Rodriguez-Navarro, C., & Doehne, E. (1999). Salt weathering: influence of evaporation rate, supersaturation and crystallization pattern. Earth Surface Processes and Landforms: The Journal of the British Geomorphological Research Group, 24(3), 191-209. https://doi.org/10.1002/(SICI)1096-9837(199903)24:3<191::AID-ESP942>3.0.CO;2-G

[114] Schiavon, N. (2002) Biodeterioration of calcareous and granitic building stones in urban environments", Natural Stone, Weathering Phenomena, Conservation Strategies and Case Studies, S. Siegesmund, T. Weiss, A. Vollbrecht https://doi.org/10.1144/GSL.SP.2002.205.01.15

[115] Sánchez, J. S., Alves, C. A. S., Romaní, J. V., & Mosquera, D. F. (2009). Origin of gypsum-rich coatings on historic buildings. Water, air, and soil pollution, 204(1-4), 53. https://doi.org/10.1007/s11270-009-0025-9

[116] Ahmadjian, V. Resynthesis of lichens. In *The lichens*; Elsevier Inc.; Academic Press: Cambridge, MA, USA, 1973; pp. 565–579, http://doi.org/10.1016/B978-0-12-044950-7.50023-4

[117] Warscheid, T.; Braams, J. Biodeterioration of stone: A review. *Int. Biodeterior. Biodegrad.* **2000**, *46*, 343–368, http://doi.org/10.1016/S0964-8305(00)00109-8

[118] Grube, M.; Cernava, T.; Soh, J.; Fuchs, S.; Aschenbrenner, I.; Lassek, C.; Wegner, U.; Becher, D.; Riedel, K.; Sensen, C.W.; et al. Exploring functional contexts of symbiotic sustain within lichen-associated bacteria by comparative omics. *ISME J.* **2015**, *9*, 412–424, http://doi.org/10.1038/ismej.2014.138

[119] Trovão, J.; Portugal, A.; Soares, F.; Paiva, D.S.; Mesquita, N.; Coelho, C.; Pinheiro, A.C.; Catarino, L.; Gil, F.; Tiago, I. Fungal diversity and distribution across distinct biodeterioration phenomena in limestone walls of the old cathedral of Coimbra, UNESCO World Heritage Site. *Int. Biodeterior. Biodegrad.* **2019**, *142*, 91–102, http://doi.org/10.1016/j.ibiod.2019.05.008

[120] Pinheiro, A.C.; Mesquita, N.; Trovão, J.; Soares, F.; Tiago, I.; Coelho, C.; Carvalho, H.P.; Gil, F.; Catarino, L.; Piñar, G.; et al. Limestone biodeterioration: A review on the Portuguese cultural heritage scenario. *J. Cult. Herit.* **2019**, *36*, 275–285, http://doi.org/10.1016/j.culher.2018.07.008

[121] Macedo, M.F.; Miller, A.Z.; Dionísio, A.; Saiz-Jimenez, C. Biodiversity of cyanobacteria and green algae on monuments in the Mediterranean Basin: An overview. *Microbiology* **2009**, *155*, 3476–3490, http://doi.org/10.1099/mic.0.032508-0

[122] Prada, J.L.; Pugés, M.; Rocabayera, R. Estudio de las patologias del Retablo del Altar Mayor de la Sé da Guarda. *Património Estudos*; Instituto Português do Património Arquitectónico: Lisbon, Portugal; p. 70.

[123] Ascaso, C.; Wierzchos, J.; Delgado Rodrigues, J.; Aires-Barros, L.; Henriques, F.; Charola, A.E. Endolithic microorganisms in the biodeterioration of the tower of Belem. *Int. Z. FürBauinstandsetz.* **1998**, *4*, 627–640. https://doi.org/10.1515/rbm-1998-5321

[124] Ascaso, C.; Wierzchos, J.; Souza-Egipsy, V.; De los Rıos, A.; Rodrigues, J.D. In situ evaluation of the biodeteriorating action of microorganisms and the effects of biocides

on carbonate rock of the Jeronimos Monastery (Lisbon). *Int. Biodeterior. Biodegrad.* **2002**, *49*, 1–12. https://doi.org/10.1016/S0964-8305(01)00097-X

[125] Mateus, D.M.; Silva, R.B.; Costa, F.M.; Coroado, J.P. Diversidade microbiológica do edifício da Sacristia Incompleta do Convento de Cristo, em Tomar, e avaliação do seu controlo por biocidas. *Conserv. Património* **2013**, *17*, 11–17.

[126] Schiavon, N.; Chiavari, G.; Schiavon, G.; Fabbri, D. Nature and decay effects of urban soiling on granitic building stones. *Sci. Total Environ.* **1995**, *167*, 87–101. https://doi.org/10.1016/0048-9697(95)04572-I

[127] Schiavon, N. Biodeterioration of calcareous and granitic building stones in urban environments. *Geol. Soc. Lond. Spec. Publ.* **2002**, *205*, 195–205. https://doi.org/10.1144/GSL.SP.2002.205.01.15

[128] Ortega-Morales, O.; Montero-Muñoz, J.L.; Neto, J.A.B.; Beech, I.B.; Sunner, J.; Gaylarde, C. Deterioration and microbial colonization of cultural heritage stone buildings in polluted and unpolluted tropical and subtropical climates: A meta-analysis. *Int. Biodeterior. Biodegrad.* **2019**, *143*, 104734. https://doi.org/10.1016/j.ibiod.2019.104734

[129] Ding, Y.; Mirão, J.; Redol, P.; Dias, L.; Moita, P.; Angelini, E.; Grassini, S.; Schiavon, N. A combined petrographic and geochemical metrological approach to assess the provenance of the building limestone used in the Batalha Monastery (Portugal). In *Metrology for Archaeology and Cultural Heritage*; Battisti, V., Gallo, V., Eds.; Florence, Italy. IMEKO **2019**; p. 338.

[130] Dias, L.; Rosado, T.; Coelho, A.; Barrulas, P.; Lopes, L.; Moita, P.; Candeias, A.; Mirão, J.; Caldeira, A.T. Natural limestone discolouration triggered by microbial activity—A contribution. *AIMS Microbiol.* **2018**, *4*, 594, https://doi.org/10.3934/microbiol.2018.4.594

[131] Rosado, T.; Dias, L.; Lança, M.; Nogueira, C.; Santos, R.; Martins, M.R.; Candeias, A.; Mirão, J.; Caldeira, A.T. Assessment of microbiota present on a Portuguese historical stone convent using high-throughput sequencing approaches. *MicrobiologyOpen* **2020**, *9*, 1067–1084. https://doi.org/10.1002/mbo3.1030

[132] Dias, L.; Rosado, T.; Candeias, A.; Mirão, J.; Caldeira, A.T. A change in composition, a change in colour: The case of limestone sculptures from the Portuguese National Museum of Ancient Art. *J. Cult. Herit.* **2020**, *42*, 255–262. https://doi.org/10.1016/j.culher.2019.07.025

[133] Mifsud, S.; Lanfranco, E.; Fiorentino, J.; Mifsud, S.D. An Updated Flora of Selmunett (St. Paul's Island) including Mosses and Lichens. *XJENZA* **2016**, *4*, 142–159.

[134] Lisci, M.; Monte, M.; Pacini, E. Lichens and higher plants on stone: A review. *Int. Biodeterior. Biodegrad.* **2003**, *51*, 1–17, https://doi.org/10.1016/S0964-8305(02)00071-9

[135] Sayer, J.A.; Kierans, M.; Gadd, G.M. Solubilisation of some naturally occurring metal-bearing minerals, limescale and lead phosphate by Aspergillus niger. *FEMS Microbiol. Lett.* **1997**, *154*, 29–35. https://doi.org/10.1111/j.1574-6968.1997.tb12620.x

[136] Gharieb, M.M.; Sayer, J.A.; Gadd, G.M. Solubilization of natural gypsum (CaSO4. 2H2O) and the formation of calcium oxalate by Aspergillus niger and Serpula himantioides. *Mycol. Res.* **1998**, *102*, 825–830. https://doi.org/10.1017/S0953756297005510

[137] Scheerer, S.; Ortega-Morales, O.; Gaylarde, C. Microbial deterioration of stone monuments—an updated overview. *Adv. Appl. Microbiol.* **2009**, *66*, 97–139. https://doi.org/10.1016/S0065-2164(08)00805-8

[138] Shi, J.; Wang, N.; Gao, H.; Baker, A.; Yao, X.; Zhang, D. Phosphorus solubility in aerosol particles related to particle sources and atmospheric acidification in Asian continental outflow. *Atmos. Chem. Phys.* **2019**, *19*, 847–860. https://doi.org/10.5194/acp-19-847-2019

[139] Leiva, D.; Clavero-León, C.; Carú, M.; Orlando, J. Intrinsic factors of Peltigera lichens influence the structure of the associated soil bacterial microbiota. *FEMS Microbiol. Ecol.* **2016**, *92*, fiw178, http://doi.org/10.1093/femsec/fiw178

[140] Ryan, R.P.; Germaine, K.; Franks, A.; Ryan, D.J.; Dowling, D.N. Bacterial endophytes: Recent developments and applications. *FEMS Microbiol. Lett.* **2008**, *278*, 1–9, http://doi.org/10.1111/j.1574-6968.2007.00918.x

[141] Bates, S.T.; Cropsey, G.W.; Caporaso, J.G.; Knight, R.; Fierer, N. Bacterial communities associated with the lichen symbiosis. *Appl. Environ. Microbiol.* **2011**, *77*, 1309–1314, http://doi.org/10.1128/AEM.02257-10

[142] Pankratov, T.A.; Dedysh, S.N.; Zavarzin, G.A. The leading role of actinobacteria in aerobic cellulose degradation in Sphagnum peat bogs. *Dokl. Biol. Sci.* **2006**, *410*, 428–430, http://doi.org/10.1134/S0012496606050243

[143] Sierra, M.A.; Danko, D.C.; Sandoval, T.A.; Pishchany, G.; Moncada, B.; Kolter, R.; Mason, C.E.; Zambrano, M.M. The microbiomes of seven lichen genera reveal host specificity, a reduced core community and potential as source of antimicrobials. *Front. Microbiol.* **2020**, *11*, 398, http://doi.org/10.3389/fmicb.2020.00398

[144] Bjelland, T.; Grube, M.; Hoem, S.; Jorgensen, S.L.; Daae, F.L.; Thorseth, I.H.; Øvreås, L. Microbial metacommunities in the lichen–rock habitat. *Environ. Microbiol. Rep.* **2011**, *3*, 434–442, http://doi.org/10.1111/j.1758-2229.2010.00206.x

[145] Lee, Y.M.; Kim, E.H.; Lee, H.K.; Hong, S.G. Biodiversity and physiological characteristics of Antarctic and Arctic lichens-associated bacteria. *World J. Microbiol. Biotechnol.* **2014**, *30*, 2711–2721. https://doi.org/10.1007/s11274-014-1695-z

[146] Özvan, A.; Dinçer, İ.; Akın, M.; Oyan, V.; Tapan, M. Experimental studies on ignimbrite and the effect of lichens and capillarity on the deterioration of Seljuk Gravestones. *Eng. Geol.* **2015**, *185*, 81–95, http://doi.org/10.1016/j.enggeo.2014.12.001

[147] Ding, Y., Caldeira, A. T., Salvador, C., Grassini, S., Angelini, E., & Schiavon, N. (2021). The inhibition of biodegradation on building limestone by plasma etching. *ACTA IMEKO*, *10*(3), 209-217. http://dx.doi.org/10.21014/acta_imeko.v10i3.1162

[148] Schiavon, N., Chiavari, G., & Fabbri, D. (2004). Soiling of limestone in an urban environment characterized by heavy vehicular exhaust emissions. *Environmental Geology*, *46*(3), 448-455. http://doi.org/10.1007/s00254-004-1046-8

[149] Caldeira, A. T., Schiavon, N., Mauran, G., Salvador, C., Rosado, T., Mirão, J., & Candeias, A. (2021). On the Biodiversity and Biodeteriogenic Activity of Microbial Communities Present in the Hypogenic Environment of the Escoural Cave, Alentejo, Portugal. *Coatings*, *11*(2), 209. http://doi.org/10.3390/coatings11020209

[150] Ding, Y., Salvador, C. S. C., Caldeira, A. T., Angelini, E., & Schiavon, N. (2021). Biodegradation and microbial contamination of limestone surfaces: an experimental study from Batalha Monastery, Portugal. *Corrosion and Materials Degradation*, *2*(1), 31-45. https://doi.org/10.3390/cmd2010002

[151] Gemeda, B. T., Lahoz, R., Caldeira, A. T., & Schiavon, N. (2018). Efficacy of laser cleaning in the removal of biological patina on the volcanic scoria of the rock-hewn churches of Lalibela, Ethiopia. *Environmental Earth Sciences*, *77*(2), 1-12. https://doi.org/10.1007/s12665-017-7223-3

[152] Tiňo, R., Vizárová, K., & Krčma, F. (2019). Plasma surface cleaning of cultural heritage objects. In *Nanotechnologies and Nanomaterials for Diagnostic, Conservation and Restoration of Cultural Heritage* (pp. 239-275). Elsevier. https://doi.org/10.1016/B978-0-12-813910-3.00011-2

[153] Rutledge, S. K., Banks, B. A., & Cales, M. (1995). Atomic oxygen treatment for non-contact removal of organic protective coatings from painting surfaces. *MRS Online Proceedings Library*, *352*(1), 161-166. https://doi.org/10.1557/PROC-352-161

[154] Voltolina, S., Aibéo, C., Cavallin, T., Egel, E., Favaro, M., Kamenova, V., ... & Patelli, A. (2013). Assessment of atmospheric plasma torches for cleaning architectural surfaces. *Built Herit*, *4*, 1051-1057.

[155] Voltolina, S., Nodari, L., Aibeo, C., Egel, E., Pamplona, M., Simon, S., ... & Patelli, A. (2016). Assessment of plasma torches as innovative tool for cleaning of historical stone materials. *Journal of Cultural Heritage*, *22*, 940-950. http://doi.org/10.1016/j.culher.2016.05.001

[156] Grassini, S., Angelini, E., d'Agostino, R., Palumbo, F., & Ingo, G. M. (2007). Advanced plasma treatment for cleaning and protecting precious metal artefacts. In *Strategies for saving our cultural heritage. Proceedings of the international conference on conservation strategies for saving indoor metallic collections, Cairo. TEI of Athens, Athens* (pp. 127-131).

[157] Belkind, A., & Gershman, S. (2008). Plasma cleaning of surfaces. *Vacuum Coating and Technology November*, 46-57.

[158] Yang, L., Chen, J., Gao, J., & Guo, Y. (2009). Plasma sterilization using the RF glow discharge. *Applied Surface Science*, *255*(22), 8960-8964.http://doi.org/10.1016/j.apsusc.2009.03.026

[159] Lu, X., Laroussi, M., & Puech, V. (2012). On atmospheric-pressure non-equilibrium plasma jets and plasma bullets. *Plasma Sources Science and Technology*, *21*(3), 034005. http://doi.org/10.1088/0963-0252/21/3/034005

[160] Pflugfelder, C., Mainusch, N., Hammer, I., & Viöl, W. (2007). Cleaning of wall paintings and architectural surfaces by plasma. *Plasma Processes and Polymers*, *4*(S1), S516-S521. https://doi.org/10.1002/ppap.200731218

[161] Tendero, C., Tixier, C., Tristant, P., Desmaison, J., & Leprince, P. (2006). Atmospheric pressure plasmas: A review. *Spectrochimica Acta Part B: Atomic Spectroscopy*, *61*(1), 2-30. https://doi.org/10.1016/j.sab.2005.10.003

[162] El-Gohary, M., & Metawa, A. (2016). CLEANING OF ARCHITECTURAL BRICKS USING RF PLASMA. I. METALLIC STAINS. *International Journal of Conservation Science*, *7*(3).

[163] Fricke, K., Koban, I., Tresp, H., Jablonowski, L., Schröder, K., Kramer, A., ... & Kocher, T. (2012). Atmospheric pressure plasma: a high-performance tool for the efficient removal of biofilms. https://doi.org/10.1371/journal.pone.0042539

[164] Huttenlochner, K., Müller-Renno, C., Ziegler, C., Merz, R., Merz, B., Kopnarski, M., ... & Ulber, R. (2017). Removing biofilms from stainless steel without changing surface properties relevant for bacterial attachment. *Biointerphases*, *12*(2), 02C404. https://doi.org/10.1116/1.4982196

[165] Xu, Z., Shen, J., Cheng, C., Hu, S., Lan, Y., & Chu, P. K. (2017). In vitro antimicrobial effects and mechanism of atmospheric-pressure He/O2 plasma jet on Staphylococcus aureus biofilm. *Journal of Physics D: Applied Physics*, *50*(10), 105201. http://doi.org/10.1088/1361-6463/aa593

[166] Lombardo, L., Donato, N., Grassini, S., Gullino, A., Moulaee, K., Neri, G., & Parvis, M. (2020). High sensitive and selective minisensor for acetone monitoring. *IEEE Transactions on Instrumentation and Measurement*, *69*(6), 3308-3316. http://doi.org/10.1109/TIM.2020.2967161

[167] Noè, C., Tonda-Turo, C., Carmagnola, I., Hakkarainen, M., & Sangermano, M. (2021). UV-Cured Biodegradable Methacrylated Starch-Based Coatings. *Coatings*, *11*(2), 127. https://doi.org/10.3390/coatings11020127

[168] Rosado, T. I. S. (2014). *New methodologies for the characterisation and biodegradation assessment of mural paintings* (Doctoral dissertation, Universidade de Evora (Portugal)).

[169] Dias, L., Rosado, T., Coelho, A., Barrulas, P., Lopes, L., Moita, P., ... & Caldeira, A. T. (2018). Natural limestone discolouration triggered by microbial activity—a contribution. *AIMS microbiology*, *4*(4), 594. http://doi.org/10.3934/microbiol.2018.4.594

[170] Stanienda-Pilecki, K. J. (2019). The importance of Fourier-Transform Infrared Spectroscopy in the identification of carbonate phases differentiated in magnesium content. 34(6) (2019), pp. 32-42.

[171] Ortega-Zavala, Dulce Esmeralda, et al. "An initial study on alkali activated limestone binders." *Cement and Concrete Research* 120 (2019): 267-278. http://doi.org/10.1016/j.cemconres.2019.04.002

[172] Ramasamy, V., et al. "FTIR-characterisation and thermal analysis of natural calcite and aragonite." *Indian Journal of Physics* 77 (2003): 443-450.

[173] Anjos, Ofélia, et al. "Application of FTIR-ATR spectroscopy to the quantification of sugar in honey." *Food chemistry* 169 (2015): 218-223. http://doi.org/10.1016/j.foodchem.2014.07.138

[174] Mail, Mohd Hafiz, et al. "FTIR and elementary analysis of Trigona honey, Apis honey and adulterated honey mixtures." *Biomedical and Pharmacology Journal* 12.04 (2019): 2011-2017. http://doi.org/10.13005/bpj/1833

[175] Kozłowicz, Katarzyna, et al. "Identification of sugars and phenolic compounds in honey powders with the use of GC–MS, FTIR spectroscopy, and X-ray diffraction." *Scientific Reports* 10.1 (2020): 1-10. http://doi.org/10.1038/s41598-020-73306-7

[176] Zanini, A., Trafeli, V., & Bartoli, L. (2018, June). The laser as a tool for the cleaning of Cultural Heritage. In *IOP Conference Series: Materials Science and Engineering* (Vol. 364, No. 1, p. 012078). IOP Publishing.

[177] Sanjeevan, P., & Klemm, A. (2005, November). A review of laser technique application in cleaning process of porous construction materials. In *PRoBE conference*.

[178] Siano, S., Giamello, M., Bartoli, L., Mencaglia, A., Parfenov, V., & Salimbeni, R. (2008). Laser cleaning of stone by different laser pulse duration and wavelength. *Laser physics*, *18*(1), 27-36. https://doi.org/10.1134/S1054660X08010064

[179] Weber, R., Graf, T., Berger, P., Onuseit, V., Wiedenmann, M., Freitag, C., & Feuer, A. (2014). Heat accumulation during pulsed laser materials processing. *Optics express*, *22*(9), 11312-11324. https://doi.org/10.1364/OE.22.011312

[180] Maingi, E. M., Alonso, M. P., Angurel, L. A., Rahman, M. A., Chapoulie, R., Dubernet, S., & de la Fuente, G. F. (2022). Historical stained-glass window laser preservation: The heat accumulation challenge. *Boletín de la Sociedad Española de Cerámica y Vidrio*. https://doi.org/10.1016/j.bsecv.2021.12.003

[181] Pereira-Pardo, L., & Korenberg, C. (2018). The use of erbium lasers for the conservation of cultural heritage. A review. *Journal of Cultural Heritage*, *31*, 236-247. https://doi.org/10.1016/j.culher.2017.10.007

[182] Shaikh, N. M., Hafeez, S., Rashid, B., & Baig, M. A. (2007). Spectroscopic studies of laser induced aluminum plasma using fundamental, second and third harmonics of a Nd: YAG laser. *The European Physical Journal D*, *44*(2), 371-379. https://doi.org/10.1140/epjd/e2007-00188-3

[183] Pereira-Pardo, L., & Korenberg, C. (2018). The use of erbium lasers for the conservation of cultural heritage. A review. *Journal of Cultural Heritage*, *31*, 236-247. https://doi.org/10.1016/j.culher.2017.10.007

[184] Bertasa, M., & Korenberg, C. (2022). Successes and challenges in laser cleaning metal artefacts: A review. *Journal of Cultural Heritage*, *53*, 100-117. https://doi.org/10.1016/j.culher.2021.10.010

[185] Liu, J., Wu, J., Chen, H., Chen, Y., Wang, Z., Ma, C., & Zhang, H. (2021). Short-pulsed Raman fiber laser and its dynamics. *SCIENCE CHINA Physics, Mechanics & Astronomy*, *64*(1), 1-21. https://doi.org/10.1007/s11433-020-1591-2

[186] Liu, X., Popa, D., & Akhmediev, N. (2019). Revealing the transition dynamics from Q switching to mode locking in a soliton laser. *Physical review letters*, *123*(9), 093901. https://doi.org/10.1103/PhysRevLett.123.093901

[187] Yang, C., Guo, J., Wei, P., Wan, H., Xu, J., & Wang, J. (2016). Dynamic properties of a pulse-pumped fiber laser with a short, high-gain cavity. *Optical Fiber Technology*, *31*, 61-64. https://doi.org/10.1016/j.yofte.2016.05.010

[188] Braslavsky, S. E. (2007). Glossary of terms used in photochemistry, (IUPAC Recommendations 2006). *Pure and Applied Chemistry*, *79*(3), 293-465. https://doi.org/10.1351/pac200779030293

[189] Lazzarini, L., Marchesini, L., & Asmus, J. F. (1973). Lasers for the cleaning of statuary: initial results and potentialities. *Journal of Vacuum Science and Technology*, *10*(6), 1039-1043. https://doi.org/10.1116/1.1318462

[190] Scholten, H., Schipper, D., Ligterink, F. J., Pedersoli, J. L., Rudolph, P., Kautek, W., ... & Hua-Ströfer, H. Y. (2005). Laser cleaning investigations of paper models and original objects with Nd: YAG and KrF laser systems. In *Lasers in the Conservation of Artworks* (pp. 11-18). Springer, Berlin, Heidelberg. https://doi.org/10.1007/3-540-27176-7_2

[191] Pilch, E., Pentzien, S., Mädebach, H., & Kautek, W. (2005). Anti-fungal laser treatment of paper: a model study with a laser wavelength of 532 nm. In *Lasers in the Conservation of Artworks* (pp. 19-27). Springer, Berlin, Heidelberg. https://doi.org/10.1007/3-540-27176-7_3

[192] Burmester, T., Meier, M., Haferkamp, H., Barcikowski, S., Bunte, J., & Ostendorf, A. (2005). Femtosecond laser cleaning of metallic cultural heritage and antique artworks. In *Lasers in the Conservation of Artworks* (pp. 61-69). Springer, Berlin, Heidelberg. https://doi.org/10.1007/3-540-27176-7_8

[193] Lorusso, A., Nassisi, V., Buccolieri, A., Buccolieri, G., Castellano, A., Leo, L. S., ... & Borrielli, A. (2008). Laser ablation threshold of cultural heritage metals. *Radiation Effects & Defects in Solids*, *163*(4-6), 325-329. https://doi.org/10.1080/10420150701777611

[194] Dickmann, K., Hildenhagen, J., Studer, J., & Müsch, E. (2005). Archaeological ironwork: removal of corrosion layers by Nd: YAG-laser. In *Lasers in the Conservation*

of Artworks (pp. 71-77). Springer, Berlin, Heidelberg. https://doi.org/10.1007/3-540-27176-7_9

[195] Ristic, S., Polic-Radovanovic, S., Katavic, B., Nikolic, Z., Ristic, O., & Pačevski, A. (2012). Some experimental results of ruby laser beam interaction with Neolithic ceramics from Stubline, Serbia. *Lasers in engineering*, *23*(5), 403.

[196] Pena-Poza, J., Ascaso, C., Sanz, M., Pérez-Ortega, S., Oujja, M., Wierzchos, J., ... & García-Heras, M. (2018). Effect of biological colonization on ceramic roofing tiles by lichens and a combined laser and biocide procedure for its removal. *International Biodeterioration & Biodegradation*, *126*, 86-94. https://doi.org/10.1016/j.ibiod.2017.10.003

[197] Polić, S., Ristić, S., Stašić, J., Trtica, M., & Radojković, B. (2015). Studies of the Iranian medieval ceramics surface modified by pulsed tea CO2 and Nd: YAG lasers. *Ceramics International*, *41*(1), 85-100. https://doi.org/10.1016/j.ceramint.2014.08.036

[198] Striova, J., Castellucci, E., Sansonetti, A., Camaiti, M., Matteini, M., Decruz, A., ... & Colombini, M. P. (2010, December). Free-running Er: YAG laser cleaning of mural painting specimens treated with linseed oil,'Beverone'and Paraloid B72. In *Proceedings of the International Conference on Lasers in the Conservation of Artworks VIII (LACONA VIII), Taylor & Francis* (pp. 85-92).

[199] Striova, J., Salvadori, B., Fontana, R., Sansonetti, A., Barucci, M., Pampaloni, E., ... & Colombini, M. P. (2015). Optical and spectroscopic tools for evaluating Er: YAG laser removal of shellac varnish. *Studies in Conservation*, *60*(sup1), S91-S96. https://doi.org/10.1179/0039363015Z.000000000213

[200] Elhagrassy, A. F., Hakeem, A., & Alhagrassy, A. F. (2018). Comparative study of biological cleaning and laser techniques for conservation of weathered stone in Failaka island, Kuwait. *Sci. Cult*, *4*, 43-50. http://doi.org/10.5281/zenodo.1214561

[201] Pouli, P., Papakonstantinou, E., Frantzikinaki, K., Panou, A., Frantzi, G., Vasiliadis, C., & Fotakis, C. (2016). The two-wavelength laser cleaning methodology; theoretical background and examples from its application on CH objects and monuments with emphasis to the Athens Acropolis sculptures. *Heritage Science*, *4*(1), 1-11. https://doi.org/10.1186/s40494-016-0077-2

[202] Tzortzakis, S., Anglos, D., & Gray, D. (2006). Ultraviolet laser filaments for remote laser-induced breakdown spectroscopy (LIBS) analysis: applications in cultural heritage monitoring. *Optics letters*, *31*(8), 1139-1141. https://doi.org/10.1364/OL.31.001139

[203] Tornari, V., Bernikola, E., Hatzigiannakis, K., Melessanaki, K., & Pouli, P. (2013). Synchronized deformation monitoring in laser cleaning: an application for cultural heritage conservation. *Universal Journal of Physics and Application*, *1*(2), 149-159. https://doi.org/10.13189/ujpa.2013.010215

[204] Salimbeni, R., Pini, R., & Siano, S. (2001). Achievement of optimum laser cleaning in the restoration of artworks: expected improvements by on-line optical

diagnostics. *Spectrochimica Acta Part B: Atomic Spectroscopy*, *56*(6), 877-885. https://doi.org/10.1016/S0584-8547(01)00197-5

[205] Tserevelakis, G. J., Pozo-Antonio, J. S., Siozos, P., Rivas, T., Pouli, P., & Zacharakis, G. (2019). On-line photoacoustic monitoring of laser cleaning on stone: Evaluation of cleaning effectiveness and detection of potential damage to the substrate. *Journal of Cultural Heritage*, *35*, 108-115. https://doi.org/10.1016/j.culher.2018.05.014

[206] Strlič, M., Šelih, V. S., Kolar, J., Kočar, D., Pihlar, B., Ostrowski, R., ... & Johansson, L. S. (2005). Optimisation and on-line acoustic monitoring of laser cleaning of soiled paper. *Applied Physics A*, *81*(5), 943-951. https://doi.org/10.1007/s00339-005-3268-3

[207] Jankowska, M., & Śliwiński, G. (2003). Acoustic monitoring for the laser cleaning of sandstone. *Journal of Cultural Heritage*, *4*, 65-71. https://doi.org/10.1016/S1296-2074(02)01230-X

[208] DeCruz, A., Wolbarsht, M. L., Andreotti, A., Colombini, M. P., Pinna, D., & Culberson, C. F. (2009). Investigation of the Er: YAG laser at 2.94 μm to remove lichens growing on stone. *Studies in Conservation*, *54*(4), 268-277. https://doi.org/10.1179/sic.2009.54.4.268

[209] Speranza, M., Sanz, M., Oujja, M., De los Rios, A., Wierzchos, J., Pérez-Ortega, S., ... & Ascaso, C. (2013). Nd-YAG laser irradiation damages to Verrucaria nigrescens. *International Biodeterioration & Biodegradation*, *84*, 281-290. https://doi.org/10.1016/j.ibiod.2012.02.010

[210] Barreiro, P., González, P., & Pozo-Antonio, J. S. (2019). IR irradiation to remove a sub-aerial biofilm from granitic stones using two different laser systems: An Nd: YAG (1064 nm) and an Er: YAG (2940 nm). *Science of The Total Environment*, *688*, 632-641. https://doi.org/10.1016/j.scitotenv.2019.06.306

[211] Sanz, M., Oujja, M., Ascaso, C., de los Ríos, A., Pérez-Ortega, S., Souza-Egipsy, V., ... & Castillejo, M. (2015). Infrared and ultraviolet laser removal of crustose lichens on dolomite heritage stone. *Applied Surface Science*, *346*, 248-255. https://doi.org/10.1016/j.apsusc.2015.04.013

[212] Sanz, M., Oujja, M., Ascaso, C., Pérez-Ortega, S., Souza-Egipsy, V., Fort, R., ... & Castillejo, M. (2017). Influence of wavelength on the laser removal of lichens colonizing heritage stone. *Applied Surface Science*, *399*, 758-768. https://doi.org/10.1016/j.apsusc.2016.12.032

[213] Rivas, T., Pozo-Antonio, J. S., de Silanes, M. L., Ramil, A., & López, A. J. (2018). Laser versus scalpel cleaning of crustose lichens on granite. *Applied Surface Science*, *440*, 467-476. https://doi.org/10.1016/j.apsusc.2018.01.167

[214] [Rivas, T., Lopez, A. J., Ramil, A., Pozo, S., Fiorucci, M. P., de Silanes, M. L., ... & Moreno, P. (2013). Comparative study of ornamental granite cleaning using femtosecond and nanosecond pulsed lasers. *Applied surface science*, *278*, 226-233. https://doi.org/10.1016/j.apsusc.2012.12.038

[215] Pouli, P., Oujja, M., & Castillejo, M. (2012). Practical issues in laser cleaning of stone and painted artefacts: optimisation procedures and side effects. *Applied Physics A*, *106*(2), 447-464. https://doi.org/10.1007/s00339-011-6696-2

[216] J.M. Liu, Simple technique for measurements of pulsed Gaussian-beam spot sizes, Opt. Lett. 7 (1982) 196–198.

[217] Maingi, E. M., Alonso, M. P., Angurel, L. A., Rahman, M. A., Chapoulie, R., Dubernet, S., & de la Fuente, G. F. (2022). Historical stained-glass window laser preservation: the heat accumulation challenge. *Boletín de la Sociedad Española de Cerámica y Vidrio*, *61*, S69-S82. https://doi.org/10.1016/j.bsecv.2021.12.003

[218] Mora, M., Amaveda, H., Porta-Velilla, L., de la Fuente, G. F., Martínez, E., & Angurel, L. A. (2021). Improved Copper–Epoxy Adhesion by Laser Micro-and Nano-Structuring of Copper Surface for Thermal Applications. *Polymers*, *13*(11), 1721. https://doi.org/10.3390/polym13111721

[219] Goodenough, U., & Roth, R. (2021). Lichen 2. Constituents. *Algal Research*, *58*, 102356. https://doi.org/10.1016/j.algal.2021.102356

[220] Bosch-Roig, P., Lustrato, G., Zanardini, E., & Ranalli, G. (2015). Biocleaning of Cultural Heritage stone surfaces and frescoes: which delivery system can be the most appropriate?. *Annals of microbiology*, *65*(3), 1227-1241. https://doi.org/10.1007/s13213-014-0938-4

[221] Gadd, G. M., & Dyer, T. D. (2017). Bioprotection of the built environment and cultural heritage. *Microbial biotechnology*, *10*(5), 1152-1156. https://doi.org/10.1111/1751-7915.12750

[222] Rivas, T., Pozo-Antonio, J. S., de Silanes, M. L., Ramil, A., & López, A. J. (2018). Laser versus scalpel cleaning of crustose lichens on granite. *Applied Surface Science*, *440*, 467-476. https://doi.org/10.1016/j.apsusc.2018.01.167

[223] Frost, R. L., & Weier, M. L. (2004). Thermal treatment of whewellite—a thermal analysis and Raman spectroscopic study. *Thermochimica Acta*, *409*(1), 79-85. https://doi.org/10.1016/S0040-6031(03)00332-0

[224] Nazami, G. R., & Sahoo, S. (2020). Influence of hatch spacing and laser spot overlapping on heat transfer during laser powder bed fusion of aluminum alloy. *Journal of Laser Applications*, *32*(4), 042007. https://doi.org/10.2351/7.0000157

[225] Kloprogge, J. T. (2017). Infrared and Raman spectroscopy of minerals and inorganic materials. https://doi.org/10.1016/B978-0-12-409547-2.12154-7

[226] Gadalla, A. M. (1984). Kinetics of the decomposition of hydrated oxalates of calcium and magnesium in air. *Thermochimica acta*, *74*(1-3), 255-272. https://doi.org/10.1016/0040-6031(84)80027-1

[227] Fried, N. M. (2018). Recent advances in infrared laser lithotripsy. *Biomedical optics express*, *9*(9), 4552-4568. http://doi.org/10.1364/boe.9.004552

[228] McNamara, C. J., & Mitchell, R. (2005). Microbial deterioration of historic stone. *Frontiers in Ecology and the Environment*, *3*(8), 445-451. https://doi.org/10.2307/3868661

[229] Suriano, R., Kuznetsov, A., Eaton, S. M., Kiyan, R., Cerullo, G., Osellame, R., ... & Turri, S. (2011). Femtosecond laser ablation of polymeric substrates for the fabrication of microfluidic channels. *Applied Surface Science*, *257*(14), 6243-6250. https://doi.org/10.1016/j.apsusc.2011.02.053

[230] Dowding, C. (2010). Laser ablation. In *Advances in Laser Materials Processing* (pp. 575-628). Woodhead Publishing. https://doi.org/10.1533/9781845699819.7.575

[231] Yilbas, B. S., Khaled, M., Abu-Dheir, N., Aqeeli, N., & Furquan, S. Z. (2013). Laser texturing of alumina surface for improved hydrophobicity. *Applied surface science*, *286*, 161-170. https://doi.org/10.1016/j.apsusc.2013.09.040

[232] Rico, V. J., López-Santos, C., Villagrá, M., Espinós, J. P., de la Fuente, G. F., Angurel, L. A., ... & González-Elipe, A. R. (2019). Hydrophobicity, freezing delay, and morphology of laser-treated aluminum surfaces. *Langmuir*, *35*(19), 6483-6491. https://doi.org/10.1021/acs.langmuir.9b00457

[233] Yang, Z., Tian, Y., Zhao, Y., & Yang, C. (2019). Study on the fabrication of super-hydrophobic surface on Inconel alloy via nanosecond laser ablation. *Materials*, *12*(2), 278. **https://doi.org/10.3390/ma12020278**

[234] Price, C. A., & Doehne, E. (2011). Stone conservation: an overview of current research.

[235] Favaro, M., Tomasin, P., Ossola, F., & Vigato, P. A. (2008). A novel approach to consolidation of historical limestone: the calcium alkoxides. *Applied Organometallic Chemistry*, *22*(12), 698-704. https://doi.org/10.1002/aoc.1462

[236] Favaro, M., Mendichi, R., Ossola, F., Russo, U., Simon, S., Tomasin, P., & Vigato, P. A. (2006). Evaluation of polymers for conservation treatments of outdoor exposed stone monuments. Part I: Photo-oxidative weathering. *Polymer Degradation and Stability*, *91*(12), 3083-3096. https://doi.org/10.1016/j.polymdegradstab.2006.08.012

[237] Matteini, M. (2008). Inorganic treatments for the consolidation and protection of stone artefacts. *Conservation science in cultural heritage*, *8*, 13-27. https://doi.org/10.6092/issn.1973-9494/1393

[238] Xu, F., Li, D., Zhang, H., & Peng, W. (2012). TEOS/HDTMS inorganic–organic hybrid compound used for stone protection. *Journal of sol-gel science and technology*, *61*(2), 429-435. https://doi.org/10.1007/s10971-011-2643-0

[239] Zhang, H., Liu, Q., Liu, T., & Zhang, B. (2013). The preservation damage of hydrophobic polymer coating materials in conservation of stone relics. *Progress in Organic Coatings*, *76*(7-8), 1127-1134. https://doi.org/10.1016/j.porgcoat.2013.03.018

[240] Sierra-Fernandez, A., Gomez-Villalba, L. S., De la Rosa-García, S. C., Gomez-Cornelio, S., Quintana, P., Rabanal, M. E., & Fort, R. (2018). Inorganic nanomaterials for the consolidation and antifungal protection of stone heritage. In *Advanced materials for the*

conservation of stone (pp. 125-149). Springer, Cham. https://doi.org/10.1007/978-3-319-72260-3_6

[241] Croveri, P., Dei, L., Giorgi, R., & Salvadori, B. (2004, June). Consolidation of Globigerina limestone (Malta) by means of inorganic treatments: preliminary results. In *Proc. 10th Int. Congress on Deterioration and Conservation of Stone, Edited by D. Kwiatowski & R. Lofvendahl, Stockholm* (pp. 463-470).

[242] Matteini, M., Rescic, S., Fratini, F., & Botticelli, G. (2011). Ammonium phosphates as consolidating agents for carbonatic stone materials used in architecture and cultural heritage: Preliminary research. *International Journal of Architectural Heritage*, *5*(6), 717-736. https://doi.org/10.1080/15583058.2010.495445

[243] Sassoni, E., Naidu, S., & Scherer, G. W. (2011). The use of hydroxyapatite as a new inorganic consolidant for damaged carbonate stones. *Journal of Cultural Heritage*, *12*(4), 346-355. https://doi.org/10.1016/j.culher.2011.02.005

[244] Adamopoulos FG, Vouvoudi EC, Pavlidou E, Achilias DS, Karapanagiotis I. TEOS-Based Superhydrophobic Coating for the Protection of Stone-Built Cultural Heritage. *Coatings*. 2021; 11(2):135. https://doi.org/10.3390/coatings11020135

[245] Wheeler, G. (2005). *Alkoxysilanes and the Consolidation of Stone*. Getty Publications.

[246] Salazar-Hernández, C., Alquiza, M. J. P., Salgado, P., & Cervantes, J. (2010). TEOS–colloidal silica–PDMS-OH hybrid formulation used for stone consolidation. *Applied Organometallic Chemistry*, *24*(6), 481-488. https://doi.org/10.1002/aoc.1646

[247] Liu, Y., & Liu, J. (2016). Synthesis of TEOS/PDMS-OH/CTAB composite coating material as a new stone consolidant formulation. *Construction and Building Materials*, *122*, 90-94. https://doi.org/10.1016/j.conbuildmat.2016.06.069

[248] Kim, E. K., Won, J., Do, J. Y., Kim, S. D., & Kang, Y. S. (2009). Effects of silica nanoparticle and GPTMS addition on TEOS-based stone consolidants. *Journal of Cultural Heritage*, *10*(2), 214-221. https://doi.org/10.1016/j.culher.2008.07.008

[249] Nguyen, S., Dobuzinsky, D., Harmon, D., Gleason, R., & Fridmann, S. (1990). Reaction Mechanisms of Plasma-and Thermal-Assisted Chemical Vapor Deposition of Tetraethylorthosilicate Oxide Films. *Journal of The Electrochemical Society*, *137*(7), 2209.

[250] Martinu, L., & Poitras, D. (2000). Plasma deposition of optical films and coatings: A review. *Journal of Vacuum Science & Technology A: Vacuum, Surfaces, and Films*, *18*(6), 2619-2645. https://doi.org/10.1116/1.1314395

[251] Tochitani, G., Shimozuma, M., & Tagashira, H. (1993). Deposition of silicon oxide films from TEOS by low frequency plasma chemical vapor deposition. *Journal of Vacuum Science & Technology A: Vacuum, Surfaces, and Films*, *11*(2), 400-405. https://doi.org/10.1116/1.578743

[252] Juárez, H., Pacio, M., Díaz, T., Rosendo, E., Garcia, G., García, A., ... & Escalante, G. (2009, May). Low temperature deposition: properties of SiO2 films from TEOS and

ozone by APCVD system. In *Journal of Physics: Conference Series* (Vol. 167, No. 1, p. 012020). IOP Publishing.

[253] Abbasi-Firouzjah, M., Hosseini, S. I., Shariat, M., & Shokri, B. (2013). The effect of TEOS plasma parameters on the silicon dioxide deposition mechanisms. *Journal of non-crystalline solids*, *368*, 86-92. https://doi.org/10.1016/j.jnoncrysol.2013.03.008

[254] Tsakalof, A., Manoudis, P., Karapanagiotis, I., Chryssoulakis, I., & Panayiotou, C. (2007). Assessment of synthetic polymeric coatings for the protection and preservation of stone monuments. *Journal of Cultural Heritage*, *8*(1), 69-72. https://doi.org/10.1016/j.culher.2006.06.007

[255] Adamopoulos, F. G., Vouvoudi, E. C., Pavlidou, E., Achilias, D. S., & Karapanagiotis, I. (2021). TEOS-Based Superhydrophobic Coating for the Protection of Stone-Built Cultural Heritage. *Coatings*, *11*(2), 135. https://doi.org/10.3390/coatings11020135

[256] Noè C, Tonda-Turo C, Carmagnola I, Hakkarainen M, Sangermano M. UV-Cured Biodegradable Methacrylated Starch-Based Coatings. *Coatings*. 2021; 11(2):127. https://doi.org/10.3390/coatings11020127

[257] Abbasi-Firouzjah, M., Hosseini, S. I., Shariat, M., & Shokri, B. (2013). The effect of TEOS plasma parameters on the silicon dioxide deposition mechanisms. *Journal of non-crystalline solids*, *368*, 86-92. https://doi.org/10.1016/j.jnoncrysol.2013.03.008

[258] Hamelmann, F., Heinzmann, U., Szekeres, A., Kirov, N., & Nikolova, T. (2005). Deposition of silicon oxide thin films in TEOS with addition of oxygen to the plasma ambient: IR spectra analysis. *Journal of Optoelectronics and Advanced Materials*, *7*(1), 389-392.

[259] Deshmukh, S. C., & Aydil, E. S. (1995). Investigation of SiO2 plasma enhanced chemical vapor deposition through tetraethoxysilane using attenuated total reflection Fourier transform infrared spectroscopy. *Journal of Vacuum Science & Technology A: Vacuum, Surfaces, and Films*, *13*(5), 2355-2367. https://doi.org/10.1116/1.579521

[260] Yan, H., Yuanhao, W., & Hongxing, Y. (2015). TEOS/silane-coupling agent composed double layers structure: a novel super-hydrophilic surface. *Energy Procedia*, *75*, 349-354. https://doi.org/10.1016/j.apenergy.2015.09.097

[261] Mahmoud, M. H. H., Rashad, M. M., Ibrahim, I. A., & Abdel-Aal, E. A. (2004). Crystal modification of calcium sulphate dihydrate in the presence of some surface-active agents. *Journal of colloid and interface science*, *270*(1), 99-105. 10.1016/j.jcis.2003.09.023

[262] Schiavon, N. (1991). Gypsum crust formation and "stratigraphy" in weathered building limestones: a SEM study of stone decay in the UK. In *Science, Technology and European Cultural Heritage* (pp. 447-451). Butterworth-Heinemann. https://doi.org/10.1016/B978-0-7506-0237-2.50064-2

[263] Lettieri, M., Masieri, M., Morelli, A., Pipoli, M., & Frigione, M. (2018). Oleo/hydrophobic coatings containing nano-particles for the protection of stone

materials having different porosity. Coatings, 8(12), 429. https://doi.org/10.3390/coatings8120429

[264] Jeckell, Z., Patel, D., Herschberg, A., Choi, T., Barlaz, D., Bonova, L., ... & Ruzic, D. (2021). Silicon Dioxide Deposited Using Atmospheric Pressure Plasma Chemical Vapor Deposition for Improved Adhesion and Water Intrusion Resistance for Lightweight Manufacturing. *Surfaces and Interfaces*, *23*, 100989. https://doi.org/10.1016/j.surfin.2021.100989

[265]